

厚生労働科学研究費補助金
労災疾病臨床研究事業

悪性胸膜中皮腫に対するヒト化抗 CD26 抗体と
免疫チェックポイント阻害薬との革新的併用療法の開発

令和4年度 総括・分担研究報告書

研究代表者 森本 幾夫

令和5(2023)年3月

目 次

I. 総括研究報告

悪性胸膜中皮腫に対するヒト化抗 CD26 抗体と免疫チェックポイント阻害薬との革新的併用療法の開発
..... 1

研究代表者 森本 幾夫
順天堂大学大学院医学研究科 免疫病・がん先端治療学講座 特任教授

II. 分担研究報告

1. ヒト免疫化マウスを用いたヒト化 CD26 抗体と抗 PD-1 抗体との併用療法の
抗腫瘍作用メカニズムの解析
..... 9

研究代表者 森本 幾夫
順天堂大学大学院医学研究科 免疫病・がん先端治療学講座 特任教授

研究分担者 波多野 良
順天堂大学大学院医学研究科 免疫病・がん先端治療学講座 特任准教授

研究分担者 岸本 卓巳
独立行政法人労働者健康安全機構
アスベスト疾患研究・研修センター 所長

研究分担者 山田 健人
埼玉医科大学医学部 病理学 教授

研究協力者 伊藤 匠
順天堂大学大学院医学研究科 免疫病・がん先端治療学講座 特任助教

研究協力者 金子 有太郎
ワイズ・エー・シー株式会社 代表取締役 CEO
近畿大学 客員教授 (元)

2. ヒト化 CD26 抗体の有効性予測バイオマーカーの探索：
国内第 I/II 相臨床試験検体における発現評価
..... 19

研究代表者 森本 幾夫
順天堂大学大学院医学研究科 免疫病・がん先端治療学講座 特任教授

研究分担者 波多野 良
順天堂大学大学院医学研究科 免疫病・がん先端治療学講座 特任准教授

研究分担者 山田 健人
埼玉医科大学医学部 病理学 教授

研究分担者 岸本 卓巳
独立行政法人労働者健康安全機構
アスベスト疾患研究・研修センター 所長

研究協力者 伊藤 匠
順天堂大学大学院医学研究科 免疫病・がん先端治療学講座 特任助教

研究協力者 藤本 伸一
岡山労災病院 腫瘍内科部長

研究協力者 青江 啓介
山口宇部医療センター 腫瘍内科 内科系診療部長

Ⅲ. 研究成果の刊行に関する一覧表・・・・・・・・・・・・・・・・・・25

Ⅳ. 研究成果の刊行物・別刷

I. 総括研究報告

労災疾病臨床研究事業費補助金
総括研究報告書
悪性胸膜中皮腫に対するヒト化抗 CD26 抗体と
免疫チェックポイント阻害薬との革新的併用療法の開発

研究代表者 森本 幾夫 順天堂大学大学院医学研究科
免疫病・がん先端治療学講座 特任教授

研究要旨

悪性胸膜中皮腫はアスベストばく露によって起こる難治性悪性腫瘍だが、満足できる治療法はなく、新たな治療法の確立が望まれる。われわれはヒト化 CD26 抗体 YS110 を開発し、国内でも悪性中皮腫に対する第 I/II 相臨床試験を実施した。2019 年中に第 II 相臨床試験の最終患者への投与が終了し、結果の集計が完了したところだが、安全性が確認され、フランスでの第 I 相臨床試験と同等の有効性を示唆する結果が得られている。

治療抵抗性の悪性中皮腫患者に対して、CD26 抗体単剤でも高い割合で Stable Disease・Partial Response となり抗腫瘍効果は認められたが、より長期間抗腫瘍効果を発揮し、無増悪生存期間を与えられる本抗体を用いた新たな併用療法の開発も重要な課題である。そこで、ヒト免疫化マウスを用いたヒト悪性中皮腫細胞株担がんモデルを確立し、YS110 と PD-1 抗体との併用効果を検討した結果、それぞれの単剤よりも強い相乗効果が認められるデータを得た。YS110 と PD-1 抗体を併用すると腫瘍の周囲に浸潤するヒト CD4 T 細胞・CD8 T 細胞がともに増加し、特に CD8 T 細胞だけでなく CD4 T 細胞の浸潤も促進することが重要である可能性が考えられた。

国内第 I/II 相臨床試験の患者から提供を受けた腫瘍病理組織から腫瘍部分を切り出し、マイクロアレイ解析を行うことで、CD26 抗体の有効性予測バイオマーカーの探索を試みた。CD26 抗体の抗腫瘍効果が Progressive Disease であった 4 症例と比較して Stable Disease であった 3 症例で共通して発現が高い遺伝子、発現が低い遺伝子の絞り込みを行い、見出した候補分子の悪性中皮腫における発現を免疫組織染色で評価できる最適染色条件を決定した。国内臨床試験検体での染色を行ったが、SD/PD 症例間で認められた mRNA レベルでの発現量の違いをより明瞭に反映する免疫組織染色以外の評価方法についても今後並行して検討する。

研究分担者

岸本 卓巳：独立行政法人労働者健康安全
機構 アスベスト疾患研究・
研修センター 所長

山田 健人：埼玉医科大学医学部 病理学
教授

波多野 良：順天堂大学大学院医学研究科
免疫病・がん先端治療学講座
特任准教授

研究協力者

藤本 伸一：岡山労災病院 腫瘍内科部長

青江 啓介：山口宇部医療センター 腫瘍
内科 内科系診療部長

伊藤 匠：順天堂大学大学院医学研究科
免疫病・がん先端治療学講座
特任助教

大沼 圭：順天堂大学大学院医学研究科
免疫病・がん先端治療学講座
非常勤講師

金子 有太郎：ワイズ・エー・シー株式
会社 代表取締役 CEO
近畿大学 客員教授(元)

A. 研究目的

悪性中皮腫はアスベスト暴露により発症する難治性がんであり、予後は極めて不良で労災疾病行政上も大きな問題となっている。

研究代表者は CD26 の抗体開発、cDNA の単離を世界に先駆けて行い(Immunol Rev 1998)、30 年に渡り CD26 研究を続け、特に CD26 のヒト免疫及びがんにおける機能、臨床応用の研究で世界をリードしている。抗腫瘍効果の強いヒト化 CD26 抗体を開発し、悪性中皮腫における CD26 の発現、抗体の抗腫瘍作用機構を明らかにしてきた(Clin Cancer Res 2007, PLoS One 2013, Nat Immunol 2015)。フランスにて治療抵抗性の悪性中皮腫を中心とした計 33 例に First-in-Human 第 I 相臨床試験を実施し、**安全性が確認され、有効**

性を示唆するデータも得られた(Br J Cancer 2017)。本邦でも治療抵抗性の悪性中皮腫に対する第 I 相臨床試験を開始し(第 1~3 コホート)、2018 年に全 9 例への投与が終了した(Lung Cancer 2019)。本結果から抗体推奨用量を 6mg/kg とし、第 II 相臨床試験も 2019 年中に全 31 例への投与が終了した。国内臨床試験でもフランスでの臨床試験と同等の有効性を示す結果が得られている(論文投稿中)。重要なことに、CD26 抗体ではフランスでの臨床試験 33 例、国内での臨床試験 40 例中、**免疫チェックポイント阻害薬(ICI)で報告されているような自己免疫疾患様の有害事象はなく、安全性が証明**されている。特記すべきは、国内臨床試験 40 例中、PD-1 抗体(Nivolumab (Nivo))無効例が 13 例含まれており、うち評価可能 11 例中 Partial Response (PR)が 1 例・Stable Disease (SD)が 7 例・Progressive Disease (PD)が 3 例で、72.7% (8/11)が PR・SD であり、CD26 抗体が **ICI 抵抗性患者にも有効である可能性が示唆**された。近年、CTLA-4 抗体、PD-1 抗体などの ICI の登場は、特に悪性黒色腫や肺癌などの領域で治療に変革をもたらした。本邦でも治療抵抗性の悪性中皮腫 31 例に対する Nivo の第 II 相臨床試験で無増悪生存期間(PFS) 6.1 ヶ月と突出して良好な結果が得られているが、欧米での治療抵抗性悪性中皮腫に対する臨床試験では、PD-1 抗体は Nivo, Pembrolizumab とともに単剤では PFS 2.6-4.5 ヶ月ほどで、Nivo と CTLA-4 抗体の併用でも悪性中皮腫 38 例で PFS 6.2 ヶ月である(Front Oncol 2020)。このように一般的に併用療法では単剤よりも PFS は向上するものの副作用出現率も上昇するため、更なる治療手段の改善が必要である。ヒト化 CD26 抗体の国内臨床試験でも全 40 例中 Nivo 抵抗性再発例が 13 例被験者となっており、ICI の治療抵抗性患者の治療をいかに向上させるかも今後、克服すべき課題といえる。

以上から、ヒト化 CD26 抗体単剤でも有効性を示す結果は得られているが、**多くの悪性中皮腫患者に、より長期間抗腫瘍効果を**

発揮できる、有効かつ安全な新規治療法の確立を最終的な目標とし、CD26 抗体と ICI との併用療法の開発を行う。

(1)ヒト免疫化マウスを作製し、このマウスを用いた悪性中皮腫担癌モデルにおいてヒト化 CD26 抗体と PD-1 抗体との併用効果を検討する。

(2)中皮腫病理組織を用いて腫瘍部位を切り出し、DNA マイクロアレイ解析を行う。SD 症例と PD 症例との遺伝子発現の比較から CD26 抗体の有効性予測バイオマーカーを絞り込み、候補分子の悪性中皮腫における発現を免疫組織染色で評価する。

B. 研究方法

各分担研究報告書に著述

(倫理面への配慮)

ヒト臍帯血 CD34 陽性造血幹細胞および成人健常者の末梢血を用いた研究については、森本が講座責任者である順天堂大学大学院医学研究科で本研究を行うための研究計画書等を倫理審査委員会へ提出し、承認を得ている(順大医倫第 2020280 号, 2020291 号)。また、ヒト化 CD26 抗体の国内第 I/II 相臨床試験の患者検体を用いたバイオマーカー探索研究については、臨床試験審査委員会、各治験実施施設内の治験審査委員会にて、試験の実施と合わせてバイオマーカー探索用採血・腫瘍組織検体の提供について協議され、実施承認を取得済みである。研究対象者に対する人的擁護上の配慮及び研究により研究対象者が受ける不利益、利益等の説明を行い、書面でのインフォームド・コンセントを得ている。

動物実験の実施はいわゆる 3R に基づいて行い、順天堂大学医学部実験動物委員会に実験計画書を提出し審議の上、承認されている(承認番号: 2022239)。

C. 研究結果

1) ヒト化 CD26 抗体と PD-1 抗体との併用効果の検討

ヒト化 CD26 抗体はマウス CD26 には結合しないため、ヒトの悪性中皮腫を用いる必要があり、PD-1 抗体との併用効果を検討するためには、ヒト免疫細胞が生着したヒト免疫化マウスを作製する必要がある。そこで、重度の免疫不全マウスである NOG マウスに低線量の放射線を照射し、ヒトの造血幹細胞を尾静脈より移植した。

悪性中皮腫細胞株 H226(上皮型)および JMN(肉腫型)は、マウス体内でヒト T 細胞の細胞数が増えてくる造血幹細胞移植 13 週目にマウスの側腹部に皮下移入した。

H226 および JMN をヒト免疫化マウスに皮下移入して 5 週間経過し、小さな腫瘍形成を確認した時点から、control human IgG₁、ヒト化 CD26 抗体単独、mouse anti-human PD-1 mAb (以下、PD-1 抗体)単独、ヒト化 CD26 抗体と PD-1 抗体の併用をそれぞれ 200μg/dose で週 3 回投与を続けた。腫瘍サイズを週に 2 回採寸した結果、control 抗体投与群と比較して、CD26 抗体単独(YS alone)、PD-1 抗体単独(PD1 alone)それぞれで腫瘍増殖の抑制が見られたが、併用投与群(YS+PD1)ではさらに腫瘍サイズが小さいことが示された。JMN と比較して H226 の方が併用投与の効果が顕著で、5 匹中 3 匹は腫瘍サイズが縮小した。

2) 腫瘍浸潤リンパ球の解析

H226 及び JMN をヒト免疫化マウスに皮下移入して 9 週間後に皮下の腫瘍を回収して一部は病理学的解析とフローサイトメトリーによる腫瘍浸潤リンパ球(TIL)の割合の

解析を行い、残りは TIL の精製に用いてフェノタイプの解析、mRNA 発現解析を行った。CD26 抗体単独または CD26 抗体と PD-1 抗体の併用投与群では、脾臓のヒト CD4 T 細胞・CD8 T 細胞、腫瘍内ヒト CD4 T 細胞・CD8 T 細胞のいずれも細胞膜上の CD26 の発現が顕著に低下していることが示された。

フローサイトメトリーにはマウスに投与しているヒト化 CD26 抗体とはエピトープが異なる CD26 抗体を使用しているため、ヒト化 CD26 抗体が結合することで細胞膜上から細胞内への CD26 分子の移行が起こっていることが予想される。また、脾臓の T 細胞だけでなく、腫瘍内の T 細胞でも同様の変化が見られたことから、マウスに投与した CD26 抗体は腫瘍周囲に浸潤する T 細胞にも結合していると考えられる。同様に、細胞膜上の PD-1 の発現も解析した結果、PD-1 抗体単独または CD26 抗体と PD-1 抗体の併用投与群では、脾臓のヒト CD4 T 細胞・CD8 T 細胞、腫瘍内ヒト CD4 T 細胞・CD8 T 細胞のいずれも細胞膜上の PD-1 の発現も顕著に低下していることが示された。

腫瘍内に浸潤したヒト CD4 T 細胞と CD8 T 細胞の細胞数と割合の解析を行った。肉腫型の JMN では、CD26 抗体と PD-1 抗体の併用投与により、腫瘍内のヒト CD8 T 細胞の割合が control IgG 投与群と比べて有意に増加した($p=0.019$)。一方で、JMN よりもよい強い抗腫瘍効果が認められた上皮型の H226 では、CD26 抗体と PD-1 抗体の併用投与により、腫瘍内のヒト CD8 T 細胞の割合が control IgG 投与群と比べて有意に増加するとともに($p=0.040$)、ヒト CD4 T 細胞の割合もいずれの群と比べても有意に増加し

ていた。CD8 T 細胞だけでなく CD4 T 細胞の浸潤を促進することは、腫瘍免疫を亢進するうえで重要であることが示唆された。

3) 国内第 I/II 相臨床試験患者の腫瘍病理組織の遺伝子発現解析

本パートの目的は、ヒト化 CD26 抗体療法が有効な患者を選択できるバイオマーカーを探索することである。CD26 抗体の国内臨床試験で腫瘍病理組織のバイオマーカー解析に同意が得られたのは、第 I 相が全 9 例中 2 例、第 II 相が全 31 例中 21 例の計 23 例(23/40)であった。

同意が得られた 23 例中、性別・組織型・Nivolumab 投与の有無が同じ条件で、SD 症例と PD 症例を 3 例以上取れるのは、「男性・上皮型・Nivolumab 投与無し」(SD 6 例/PD 4 例)のみであったため、その条件で無増悪生存期間 PFS が長い SD 3 例と PD 4 例から腫瘍部位を切り出し、DNA マイクロアレイ解析を行った。

SD 群 3 例と PD 群 4 例との間で遺伝子発現の群比較を行い、PD 群と比較して SD 群で高発現している遺伝子群と SD 群と比較して PD 群で高発現している遺伝子群をヒートマップにまとめた(2021 年度 労災疾病臨床研究事業費補助金 研究報告書に記載)。

SD 症例では抗線維化、炎症亢進、増殖・代謝亢進に関わる遺伝子の発現が高く、SD 症例 3 例に共通して PD 症例よりも顕著に発現が高い遺伝子 X を見出した。また、PD 症例では腫瘍部位を切り出して遺伝子発現解析を行ったものの、骨格筋や横紋筋、筋収縮、筋線維芽細胞に関係する遺伝子の発現が高く、PD 症例 4 例に共通して SD 症例よりも

顕著に発現が高い遺伝子 Y を見出した。

長期間 PFS が持続する CD26 抗体有効例と PD 症例とを判別できるバイオマーカー候補分子として特に X と Y に着目し、悪性中皮腫組織の免疫染色に最適な抗体、及び、染色条件(抗体濃度や抗原賦活化条件)の検討を行い、最適条件を決定したところである。

D. 考察

ヒト化 CD26 抗体の副作用が少ない利点を活かした新たな併用療法を開発するために、ヒト免疫化マウスを用いたヒト悪性中皮腫株担がんモデルにて、ヒト化 CD26 抗体と PD-1 抗体との併用療法の抗腫瘍作用メカニズムの解析を行った。

CD26 は腫瘍だけでなく T 細胞にも発現しており、近年の研究から CD26 抗体の抗腫瘍作用はがんへの直接的な影響だけでなく、T 細胞を介した腫瘍免疫への影響もあることが強く示唆される。CD26 はヒト T 細胞に活性化シグナルを伝達する T 細胞共刺激分子でもあり、ヒト化 CD26 抗体は CD26 のリガンドである caveolin-1 と CD26 との結合、つまりは T 細胞への CD26 共刺激シグナルの伝達をブロックする。一方で、マウス T 細胞の CD26 は共刺激分子として機能しない。また、ヒト T 細胞では CD26 は強陽性・弱陽性・陰性の三相性パターンを示すのに対し、マウス T 細胞は一律に弱陽性である。T 細胞以外の免疫細胞における CD26 の発現も、ヒトとマウスとでは異なる。このように、T 細胞における機能や免疫細胞における発現パターンなどがヒトとマウスとでは大きく異なるため、CD26 抗体の腫瘍免疫への影響を解析するにはヒト免疫系での解析が不可欠である。また、ICI が抗腫瘍効果を

を発揮するためにも、T 細胞を中心とした免疫系の存在が不可欠であり、ヒト化 CD26 抗体と ICI との併用効果を検討する実験にはヒト免疫化マウスを用いる必要がある。しかしながら、ヒト免疫化マウスを用いた担がんモデルには問題点も存在する。一つは、免疫細胞がヒト臍帯血造血幹細胞由来の HLA を発現しているのに対し、ヒト腫瘍細胞株は異なる HLA を発現しているため、同種異系 (allogeneic) の T 細胞応答を見ることになり、本来のがん抗原特異的な応答とは異なる。また、ヒト免疫細胞の組成に関しても、今回のモデルではヒト T 細胞と B 細胞はマウス体内で十分な生着が認められるが、ヒト NK 細胞や抗原提示細胞を含む骨髄系免疫細胞の生着率は非常に低い。この問題を解決するために、ヒト IL-2, IL-15, IL-3, GM-CSF などの遺伝子を強制発現させた NOG マウスが樹立・市販されつつあるが、現時点ではヒトの造血幹細胞から全ての免疫細胞を発生・分化させることはできず、また、線維芽細胞など腫瘍周囲の間質はマウス由来の細胞であることなど、ヒトのがん微小環境をマウスで再現することは不可能に近い。

マウス担がんモデルで餌と一緒に DPP4 inhibitor (Sitagliptin) を食べさせることで、CXCR3 陽性の CD4 T 細胞、CD8 T 細胞、NK 細胞や CCR3 陽性の好酸球ががん細胞周囲により集積し、腫瘍免疫の亢進に働くことが報告された(Nat Immunol 2015, 2019)。フランス及び国内のヒト化 CD26 抗体の臨床試験の結果から、CD26 抗体を投与すると血清中の可溶性 CD26 量が低下し、それに伴い DPP4 酵素活性も低下する(Br J Cancer 2017, Biomark Res 2021)。このことから、CD26 抗体を投与した場合において

も、がん細胞周囲に集積する免疫細胞数の増加が起こる可能性が考えられる。しかしながら、ヒト化 CD26 抗体はマウス CD26 には結合しないため、今回の担がんモデルにおいて、血清中の可溶性ヒト CD26 量は CD26 抗体投与によって 7 割近く低下したが、可溶性マウス CD26 量には影響しなかった。マウス CD26 にも DPP4 酵素活性があるため、ヒトとマウスの CD26 由来 DPP4 酵素活性の合計では CD26 抗体を投与しても 5 割程度の低下に留まっており、がん患者に CD26 抗体を投与した場合ほどこのモデルでは DPP4 酵素活性低下作用は期待できない。今回のモデルでも、CD26 抗体と PD-1 抗体との併用投与により腫瘍内に浸潤するヒト CD4 T 細胞・CD8 T 細胞の増加が認められたが、これは PD-1 抗体によるヒト T 細胞の活性化と CD26 抗体による浸潤促進効果が関与していると予想される。

ヒト化 CD26 抗体の予後・治療効果予測バイオマーカーを探索するために、CD26 抗体の国内第 I/II 相臨床試験患者の腫瘍病理組織を用いて、SD 症例 3 例と PD 症例 4 例の DNA マイクロアレイ解析を行い、SD 症例で共通して発現が高い遺伝子、または、PD 症例で共通して発現が高い遺伝子の絞り込みを行った。

SD 症例群と PD 症例群との間で mRNA レベルでの発現量に顕著な差が見られた遺伝子 X と遺伝子 Y に着目し、腫瘍病理組織の免疫染色による発現評価を行っているが、現時点で SD 症例と PD 症例との間に DNA マイクロアレイでの結果ほど明瞭な差が認められない症例も見られている。免疫組織染色はホルマリン固定された組織のタンパクレベルでの発現を評価する方法として重宝

されるが、mRNA 発現とタンパク質発現が必ずしも一致しないことや、免疫組織染色の感度あるいは定量性が低い問題もあるため、今後は腫瘍組織における遺伝子 X と Y の mRNA レベルでの発現を In Situ Hybridization で評価する方法や、血清や胸水中の遺伝子 X と Y のタンパク量を ELISA で定量する方法なども並行して検討していく予定である。

E. 結論

ヒト悪性中皮腫細胞株 H226 と JMN を皮下移入する担がんモデルにおいて、ヒト化 CD26 抗体と PD-1 抗体との併用効果を検討した結果、それぞれの単剤よりも強い腫瘍増殖抑制効果が見られることが示された。CD26 抗体は CD26 陽性がん細胞に直接作用するとともに、ヒト T 細胞とがん細胞膜上の CD26 発現・可溶性 CD26 量を低下させることで DPP4 酵素活性低下にも働くことを示した。

ヒト化 CD26 抗体の国内第 I/II 相臨床試験患者の SD 症例 3 例と PD 症例 4 例の DNA マイクロアレイ解析を行った。その結果、mRNA レベルにおいて SD 症例で共通して発現が顕著に高い遺伝子 X と PD 症例で共通して発現が顕著に高い遺伝子 Y を見出し、悪性中皮腫組織におけるそれらの発現評価を行える最適染色条件を決定した。

F. 健康危険情報

現時点では特記すべき健康危険情報はない。

G. 今後の展望

悪性中皮腫細胞株を皮下移入する今回の

モデルと並行して、より患者のがん細胞の特性を維持していると考えられる悪性中皮腫の患者腫瘍移植(PDX; Patient-derived xenograft)モデルにおいても併用効果の有効性を検討する。

CD26 抗体療法が有効な患者を選択できるバイオマーカーを同定できれば、PD-1 抗体が有効であった悪性中皮腫患者、無効であった悪性中皮腫患者それぞれで、有効性予測バイオマーカーの陽性率を解析することで、CD26 抗体と PD-1 抗体との併用療法が期待できる患者、PD-1 抗体が無効でも CD26 抗体による治療が期待できる患者の割合を予測することへの応用も期待される。

H. 研究発表

1. 論文発表

- 1) Kobayashi S, Fugo K, Hatano R, Yamazaki K, Morimoto C, Terawaki H. Anti-glomerular basement membrane disease concomitant with MPO-ANCA positivity concurrent with high serum levels of interleukin-26 following coronavirus disease 2019 vaccination. Intern Med. in press. doi: 10.2169/internalmedicine.
- 2) Santos MF, Rappa G, Fontana S, Karbanova J, Aalam F, Tai D, Li Z, Pucci M, Alessandro R, Morimoto C, Corbeil D, Lorico A. Anti-Human CD9 Fab Fragment Antibody Blocks the Extracellular Vesicle-Mediated Increase in Malignancy of Colon Cancer Cells. Cells. 2022;11(16):2474.
- 3) Hatano R, Itoh T, Otsuka H, Saeki H, Yamamoto A, Song D, Shirakawa Y, Iyama S, Sato T, Iwao N, Harada N, Aune TM, Dang NH, Kaneko Y, Yamada T, Morimoto C, Ohnuma K. Humanized anti-IL-26 monoclonal antibody as a novel targeted therapy for chronic graft-versus-host disease. Am J Transplant. 2022;22(12):2804-2820.
- 4) Komiya E, Tominaga M, Hatano R, Kamikubo Y, Toyama S, Sakairi H, Honda K, Itoh T, Kamata Y, Tsurumachi M, Kishi R, Ohnuma K, Sakurai T, Morimoto C, Takamori K. Peripheral endomorphins drive mechanical alloknosis under the enzymatic control of CD26/DPPIV. J Allergy Clin Immunol. 2022;149(3):1085-1096
- 5) Fujiwara Y, Takahashi Y, Okada M, Kishimoto T, Kondo S, Fujikawa K, Hayama M, Sugeno M, Ueda S, Komuro K, Lanasa M, Nakano T. Phase 1 Study of Tremelimumab Monotherapy or in Combination with Durvalumab in Japanese Patients with Advanced Solid Tumors or Malignant Mesothelioma. Oncologist. 2022;27(9):e703-722
- 6) Kishimoto T, Kato K, Ashizawa K, Kurihara Y, Tokuyama T, Sakai F. A retrospective study on radiological findings of diffuse pleural thickening with benign asbestos pleural effusion in Japanese cases. Ind Health. 2022;60(5):429-435
- 7) Hayashi H, Ashizawa K, Takahashi M, Kato K, Arakawa H, Kishimoto T, Otsuka Y, Noma S, Honda S. The diagnosis of early pneumoconiosis in dust-exposed workers: comparison of chest radiography and computed tomography. Acta Radiol. 2022;63(7):909-913
- 8) Okatama M, Fujimori K, Sato M, Samata K, Kurita K, Sugiyama H, Ichikawa D, Matsushita M, Suto Y, Iwasaki G, Yamada

T, Kiuchi F, Hirao M, Kunieda H, Yamazaki K, Hattori Y. GTN057, a komaroviquinone derivative, induced myeloma cells' death in vivo and inhibited c-MET tyrosine kinase. Cancer Medicine. in press

- 9) Tsuchiya, T, Saisho Y, Inaishi J, Sasaki H, Sato M, Nishikawa M, Masugi Y, Yamada T, Itoh H. Increased alpha cell to beta cell ratio in patients with pancreatic cancer. Endocr J. 2022;69(12):1407-1414

2. 著書

なし

3. 学会発表

- 1) Shirakawa Y, Hatano R, Itoh T, Otsuka H, Okumura K, Morimoto C. IL-26 facilitates cartilage destruction and infiltration of inflammatory cells into synovium in a collagen induced arthritis model. 第 51 回日本免疫学会学術集会, 熊本, 2022 年 12 月 8 日
- 2) 岸本卓巳、藤本伸一、水橋啓一、三浦元彦、小澤聡子、加藤勝也. 良性石綿胸水の認定基準に関する研究 -前向き調査結果について-. 第 70 回日本職業・災害医学会学術大会, Web 開催, 2022 年 11 月 5 日
- 3) 岸本卓巳、宮原甚平、妹尾純江. 石綿肺がん認定のための肺内石綿繊維計測の意義. 第 63 回日本肺癌学会学術集会, 福岡(ハイブリッド開催), 2022 年 12 月 1 日
- 4) 林睦、間所裕子、坂元亨宇、山田健人. CD26 陽性がんに対する新規抗体-抗が

ん剤結合分子ADCの開発. 第111回日本病理学会総会, 神戸, 2022 年 4 月 16 日

- 5) 政岡秀彦、稲田博輝、細沼沙紀、土居美枝子、金野美年子、金玲、山口浩、石澤圭介、山田健人、佐々木惇. 原発性腹膜癌(高異型度漿液性癌)の一例. 第 63 回日本臨床細胞学会総会(春期大会), 東京, 2022 年 6 月 12 日
- 6) 竹ノ谷隆、古川貴久、山田健人、川井田みほ、清川駿樹、浅田祐介、尾戸一平、矢部信成、大住幸司、村井信二. リンパ節転移が認められた腫瘍径 1cm 未満の直腸神経内分泌腫瘍(NET-G2)の1例. 第 44 回日本癌局所療法研究会, 大阪, 2022 年 7 月 1 日

I. 知的財産権の出願・登録状況(予定を含む)

1. 特許取得
- 1) 発明者: 森本幾夫, 波多野良, 大沼圭, 金子有太郎. 発明の名称: 抗 CD26 抗体と免疫チェックポイント阻害剤との併用療法. 出願日: 2022 年 5 月 27 日. 出願番号: 特願 PCT/JP2022/021738. 出願人: ワイズ・エー・シー株式会社、学校法人順天堂
2. 実用新案登録
- なし
3. その他
- なし

II. 分担研究報告

労災疾病臨床研究事業費補助金
分担研究報告書

ヒト免疫化マウスを用いたヒト化 CD26 抗体と抗 PD-1 抗体との併用療法の
抗腫瘍作用メカニズムの解析

研究代表者	森本 幾夫	順天堂大学大学院医学研究科 免疫病・がん先端治療学講座 特任教授
研究分担者	波多野 良	順天堂大学大学院医学研究科 免疫病・がん先端治療学講座 特任准教授
研究分担者	岸本 卓巳	独立行政法人労働者健康安全機構 アスベスト疾患研究・研修センター 所長
研究分担者	山田 健人	埼玉医科大学医学部 病理学 教授
研究協力者	伊藤 匠	順天堂大学大学院医学研究科 免疫病・がん先端治療学講座 特任助教
研究協力者	金子有太郎	ワイズ・エー・シー株式会社 代表取締役 CEO 近畿大学 客員教授(元)

研究要旨

悪性胸膜中皮腫はアスベストばく露によって起こる難治性悪性腫瘍だが、満足できる治療はなく、新たな治療法の確立が望まれる。われわれは悪性胸膜中皮腫に発現する CD26 に着目し、ヒト化 CD26 抗体 YS110 を開発した。フランスにて悪性中皮腫を中心とした第 I 相臨床試験を、国内でも悪性中皮腫に対する第 I/II 相臨床試験を実施した。2019 年中に第 II 相臨床試験の最終患者への投与が終了し、結果の集計が完了したところだが、安全性が確認され、フランスでの第 I 相臨床試験と同等の有効性を示唆する結果が得られている。治療抵抗性の悪性中皮腫患者に対して、CD26 抗体単剤でも高い割合で Stable Disease・Partial Response となり抗腫瘍効果は認められたが、より長期間抗腫瘍効果を発揮し、無増悪生存期間を与えられる本抗体を用いた新たな併用療法の開発も重要な課題である。そこで、ヒト免疫化マウスを用いたヒト悪性中皮腫細胞株担がんモデルを確立し、YS110 と PD-1 抗体との併用効果を検討した結果、それぞれの単剤よりも強い相乗効果が認められるデータを得た。YS110 と PD-1 抗体を併用すると腫瘍の周囲に浸潤するヒト CD4 T 細胞・CD8 T 細胞がともに増加し、特に CD8 T 細胞だけでなく CD4 T 細胞の浸潤も促進することが重要である可能性が考えられた。

A. 研究目的

悪性胸膜中皮腫はアスベストばく露によって起こる胸膜中皮由来の難治性悪性腫瘍である。アスベストばく露から発症までの潜伏期間は約 30-50 年とされ、日本を含め中国やインドなどアジア・中東では患者数が今後さらに増加すると考えられている。予後は極めて悪く、現時点で満足できる治療成績ではなく、新たな治療法の確立が望まれる。われわれは、新規治療標的分子として悪性中皮腫細胞に発現する CD26 に着目し、ヒト化 CD26 抗体を開発してフランスにて悪性中皮腫を中心に First-in-Human 第 I 相臨床試験を行った。Infusion reaction (急性輸注反応)を除いて特記すべき副作用もなく、安全性が確認されるとともに、抗がん剤抵抗性の悪性中皮腫患者 19 例中 10 例が modified RESIST 評価で Stable Disease (SD)となり、そのうち 5 例は 6 ヶ月以上、最長で 399 日 SD が持続し、有効性を示唆する結果も得られた(Br J Cancer. 2017)。

本邦でも抗がん剤抵抗性の悪性中皮腫に対する第 I/II 相臨床試験を実施し、第 I 相は 1~3 コホート各 3 例ずつの計 9 例、第 II 相は 31 例に投与を行い、2019 年中に第 II 相の最終患者への投与が終了した。第 I/II 相で計 40 例に投与を行い、抗がん剤抵抗性の悪性中皮腫患者に対して高い割合で抗腫瘍効果が認められるも、完全奏功(Complete Response: CR)はなく、より長期間抗腫瘍効果を発揮し、無増悪生存期間を与えられる本抗体を用いた新たな併用療法の開発も重要な課題である。

我々はこれまでにヒト化 CD26 抗体の抗腫瘍作用メカニズムとして、抗体医薬特有の抗体依存性細胞傷害(ADCC)活性に加え、が

ん細胞の細胞膜上の CD26 に抗体が結合することによる直接的な増殖抑制作用を明らかにしてきた(Clin Cancer Res. 2001, Immunology. 2002, Clin Cancer Res. 2007, PLoS One. 2013)。また、CD26 抗体は、CD26 分子が有する DPP4 酵素活性には直接影響しないが、細胞膜上の CD26 分子の数や体液中に膜から切断された形で存在する soluble CD26 の数を減少させるため、CD26 抗体を投与すると DPP4 酵素活性も結果的に低下する。近年の知見から、DPP4 酵素活性を阻害すると DPP4 によるケモカインの切断と活性低下が妨げられ、腫瘍周囲に浸潤する免疫細胞が増加する、すなわち腫瘍免疫亢進に働くことが強く示唆され(Nat Immunol. 2015, 2019)、CD26 抗体は多様なメカニズムを介して抗腫瘍効果を発揮していると考えられる。特記すべきは、国内第 I/II 相臨床試験 40 例の中には PD-1 抗体 Nivolumab 無効例が 13 例含まれており、それらの患者に対しても同様に高い割合で抗腫瘍効果が認められたことから、CD26 抗体は免疫チェックポイント阻害薬(ICI)抵抗性の患者にも有効であること、ICI とは異なるメカニズムで抗腫瘍効果を発揮することが強く示唆された。

そこで、副作用が非常に少ない CD26 抗体の利点を活かした他の分子標的薬、特に ICI との併用療法を開発すべく、ヒト化 CD26 抗体と PD-1 抗体との併用効果を検討した。ICI が抗腫瘍効果を発揮するためには T 細胞を中心とした免疫細胞が不可欠であり、マウスに同系のマウス腫瘍株を移入する担癌モデルがよく用いられる。一方で、CD26 抗体が抗腫瘍効果を発揮するためにはヒト CD26 分子上の結合部位も重要であ

り(Clin Cancer Res. 2007)、ヒトとマウスとでは免疫系における CD26 の機能も大きく異なることから(Immunol Rev. 1998)、ヒト化 CD26 抗体のデータ取得にはヒト腫瘍株並びにヒト免疫系での解析が必須である。以上の理由から、ヒト免疫化マウスを作製し、このマウスを用いた悪性中皮腫株担がんモデルにおいてヒト化 CD26 抗体と PD-1 抗体との併用効果を検討した。

B. 研究方法

1) 細胞

ヒト悪性中皮腫細胞株 H226(上皮型)と JMN(肉腫型)は、10% FBS を添加した RPMI1640 培地中で 37°C, 5% CO₂ 環境下で培養した。ヒト臍帯血 CD34 陽性造血幹細胞は RIKEN BioResource Center から購入した。

2) マウス

NOD/Shi-scid, IL-2R γ KO Jic (NOD.Cg-Prkdc^{scid} Il2rg^{tm1Sug/ShiJic})マウス(以下、NOG マウス)は In-Vivo Science Inc.から購入した。マウスは順天堂大学の specific pathogen free (SPF)施設で飼育した。

3) 抗体と試薬

Flow cytometry には下記のヒト抗原特異抗体を用いた。BUV395-labeled anti-CD3 mAb (clone SK7), PE-labeled anti-CD26 mAb (clone M-A261) 及び APC-R700-labeled anti-CD4 (clone RPA-T4)は BD Biosciences から購入した。Brilliant Violet 421-labeled anti-CD45 mAb (clone HI30), Brilliant Violet 510-labeled anti-CD14 mAb (clone M5E2), Brilliant Violet

605-labeled anti-CD11c mAb (clone 3.9), FITC-labeled anti-CD11b mAb (clone ICRF44), PerCP/Cy5.5-labeled anti-CD8 mAb (clone RPA-T8), PE/Cy7-labeled anti-CD56 mAb (clone 5.1H11), APC-labeled anti-CD19 mAb (clone 4G7)及び APC/Fire 750-labeled anti-mouse CD45 mAb (clone 30-F11)及び抗体の非特異的な結合をブロックするための Human TruStain FcX, TruStain FcX (anti-mouse CD16/32)は BioLegend から購入した。また、Brilliant Violet 同士の非特異的な結合を抑えるための Brilliant Stain Buffer plus は BD Biosciences から購入した。

4) ヒト免疫化マウスを用いた担癌モデル

NOG マウスに低線量(100cGy)で放射線照射し、翌日ヒト臍帯血 CD34 陽性造血幹細胞 1x10⁵ cells を尾静脈内から移入した。ヒト造血幹細胞を移入して 5 週, 9 週, 13 週, 17 週後にマウス尾静脈から経時的に採血を行い、ヒト免疫細胞の生着を確認した。ヒト造血幹細胞を移植して 13 週後のヒト T 細胞が生着したマウスに、JMN または H226 の細胞懸濁液と Matrigel を 1:1 混合して 1 匹あたり 1x10⁶ cells ずつ側腹部に皮下移入した。JMN または H226 を皮下移入して 5 週間経過し、小さな腫瘍形成を確認した時点から、control human IgG1 (Bio X Cell), ヒト化 CD26 抗体(Y's AC Co., Ltd)単独, mouse anti-human PD-1 mAb (Bio X Cell; clone J116)単独, ヒト化 CD26 抗体と PD-1 抗体の併用をそれぞれ 200 μ g/dose で週 3 回投与を続けた。腫瘍サイズは週に 2 回採寸し、JMN または H226 移入 9 週間後にマウスを解剖し、皮下の腫瘍を回収して重量を測定し

た。腫瘍の一部は病理解析のために 10%ホルマリンで固定し、残りは Liberase TL Research Grade (Roche) 0.25mg/ml で酵素処理を行い、DNase I (Roche)存在下で組織を破碎して腫瘍組織中の細胞を得た。腫瘍内浸潤リンパ球の解析では、MagniSort Human CD3 Positive Selection Kit (invitrogen) 及び EasySep Magnet (STEMCELL)を用いてリンパ球精製を行った。また、腫瘍内浸潤リンパ球との性質比較のために、脾臓のリンパ球解析も行った。

5) フローサイトメトリー

マウス体内のヒト免疫細胞の生着を確認するために、マウスの尾静脈から採血して得た末梢血を、Human と Mouse に対する TruStain FcX を両方添加し、蛍光色素標識抗体で染色した後、BD FACS Lysing Solution (BD Biosciences)にて溶血と固定処理を行い、洗浄した後、BD LSRFortessa (BD Biosciences)で測定を行い、得られたデータを FlowJo (BD Biosciences)で解析した。

6) マウス血清中の可溶性ヒト CD26 値とマウス CD26 値、及びその DPP4 酵素活性値の測定

ヒト免疫化マウスに JMN または H226 を皮下移入して 5 週間後から抗体投与を開始し、9 週間後にマウスを解剖する際、採血して血清を保存した。

マウス血清中の可溶性ヒト CD26 値の測定は、研究代表者森本が開発した、ヒト化 CD26 抗体とはエピトープがそれぞれ異なる mouse anti-human CD26 mAb 2 クローン (clone 5F8 と 9C11)を用いた sandwich ELISA により行った。可溶性マウス CD26

値の測定は、Mouse DPPIV/CD26 DuoSet ELISA (R&D Systems)を用いて行った。マイクロプレートリーダー(Bio-Rad)で吸光値を測定し、得られたデータを Microplate Manager 6 (Bio-Rad)で解析した。

(倫理面への配慮)

ヒト臍帯血 CD34 陽性造血幹細胞を用いた研究については、森本が講座責任者である順天堂大学大学院医学研究科で本研究を行うための研究計画書等を倫理審査委員会へ提出し、承認を得ている(順大医倫第 2020280 号)。動物実験の実施はいわゆる 3R に基づいて行い、順天堂大学医学部実験動物委員会に実験計画書を提出し審議の上、承認されている(承認番号: 2022239)。

C. 研究結果

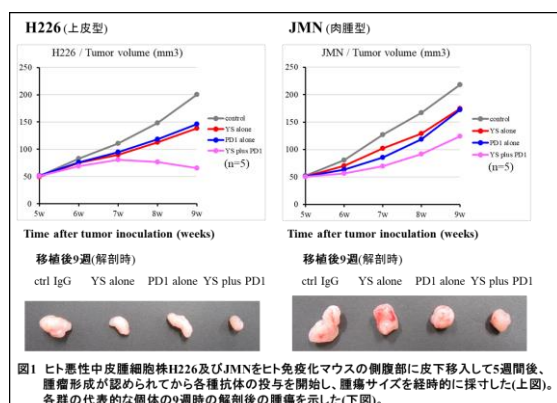
1) ヒト化 CD26 抗体と PD-1 抗体との併用効果の検討

ヒト化 CD26 抗体はマウス CD26 には結合しないため、ヒトの悪性中皮腫を用いる必要があり、PD-1 抗体との併用効果を検討するためには、ヒト免疫細胞が生着したヒト免疫化マウスを作製する必要がある。そこで、重度の免疫不全マウスである NOG マウスに低線量の放射線を照射し、ヒトの造血幹細胞を尾静脈より移植した。ヒト造血幹細胞を移植して 10 週間経過するまではマウスの血中のヒト免疫細胞の約 90%が B 細胞(CD19 陽性)で、10 週以降はヒト CD4 T 細胞(CD3 陽性 CD4 陽性)・CD8 T 細胞(CD3 陽性 CD8 陽性)の割合が徐々に増えていき 13 週目ではヒトの血球細胞の約 10-15%が T 細胞、17 週目では約 25-35%が T 細胞であることが確認された(2021 年度 労災疾病臨床研究事業

費補助金 研究報告書に記載)。

悪性中皮腫細胞株 H226(上皮型)および JMN(肉腫型)は、in vivo での増殖が非常に遅く、マウスの皮下に移入してから腫瘍を形成するまでに 5-6 週間かかるため、マウス体内でヒト T 細胞の細胞数が増えてくる造血幹細胞移植 13 週目に悪性中皮腫細胞株を皮下移入することとした。

H226 および JMN をヒト免疫化マウスの側腹部に皮下移入して 5 週間経過し、小さな腫瘍形成を確認した時点から、control human IgG₁, ヒト化 CD26 抗体単独, mouse anti-human PD-1 mAb (以下、PD-1 抗体)単独, ヒト化 CD26 抗体と PD-1 抗体の併用をそれぞれ 200μg/dose で週 3 回投与を続けた。腫瘍サイズを週に 2 回採寸した結果、control 抗体投与群と比較して、CD26 抗体単独(YS alone)、PD-1 抗体単独(PD1 alone)それぞれで腫瘍増殖の抑制が見られたが、併用投与群(YS+PD1)ではさらに腫瘍サイズが小さいことが示された(図 1)。JMN と比較して H226 の方が併用投与の効果が顕著で、5 匹中 3 匹は腫瘍サイズが縮小した(データ未掲載)。



2) 腫瘍浸潤リンパ球の解析

H226 及び JMN をヒト免疫化マウスに皮下移入して 9 週間後にマウスを解剖し、皮

下の腫瘍を回収して一部は病理学的解析とフローサイトメトリーによる腫瘍浸潤リンパ球(TIL)の割合の解析を行い、残りは TIL の精製に用いてフェノタイプの解析、mRNA 発現解析を行った。

まず腫瘍内ヒト CD4 T 細胞・CD8 T 細胞の細胞膜上の CD26 と PD-1 の発現の解析を行った。比較対照として脾臓のヒト CD4 T 細胞・CD8 T 細胞でも同様の解析も行った。CD26 抗体単独または CD26 抗体と PD-1 抗体の併用投与群では、脾臓のヒト CD4 T 細胞・CD8 T 細胞、腫瘍内ヒト CD4 T 細胞・CD8 T 細胞のいずれも細胞膜上の CD26 の発現が顕著に低下していることが示された(データ未掲載)。フローサイトメトリーにはマウスに投与しているヒト化 CD26 抗体とはエピトープが異なる CD26 抗体を使用しているため、ヒト化 CD26 抗体が結合することで細胞膜上から細胞内への CD26 分子の移行が起こっていることが予想される。また、脾臓の T 細胞だけでなく、腫瘍内の T 細胞でも同様の変化が見られたことから、マウスに投与した CD26 抗体は腫瘍周囲に浸潤する T 細胞にも結合していると考えられる。同様に、細胞膜上の PD-1 の発現も解析した結果、PD-1 抗体単独または CD26 抗体と PD-1 抗体の併用投与群では、脾臓のヒト CD4 T 細胞・CD8 T 細胞、腫瘍内ヒト CD4 T 細胞・CD8 T 細胞のいずれも細胞膜上の PD-1 の発現も顕著に低下していることが示された(データ未掲載)。フローサイトメトリーにはマウスに投与している PD-1 抗体とはエピトープが異なる PD-1 抗体を使用しているため、CD26 と同様に PD-1 でも PD-1 抗体が結合することで細胞膜上から細胞内への PD-1 分子の移行が起こっていること、

PD-1抗体は腫瘍周囲に浸潤するT細胞にも結合していることが考えられる。

次に、腫瘍内に浸潤したヒト CD4 T細胞と CD8 T細胞の細胞数と割合の解析を行った。肉腫型の JMN では、CD26抗体と PD-1抗体の併用投与により、腫瘍内のヒト CD8 T細胞の割合が control IgG 投与群と比べて有意に増加した($p=0.019$) (図 2 右)。一方で、JMN よりもよい強い抗腫瘍効果が認められた上皮型の H226 では、CD26抗体と PD-1抗体の併用投与により、腫瘍内のヒト CD8 T細胞の割合が control IgG 投与群と比べて有意に増加するとともに($p=0.040$)、ヒト CD4 T細胞の割合もいずれの群と比べても有意に増加していた(図 2 左)。特に、図 2 左中、赤丸で表示した個体は併用投与によって腫瘍サイズが縮小していった個体を示しており、ヒト CD4 T細胞の浸潤が顕著に増加した個体であったことから、CD8 T細胞だけでなく CD4 T細胞の浸潤を促進することは、腫瘍免疫を亢進するうえで重要であることが示唆された。腫瘍内に浸潤したヒト CD4 T細胞・CD8 T細胞の絶対数においても同様の結果であった(データ未掲載)。

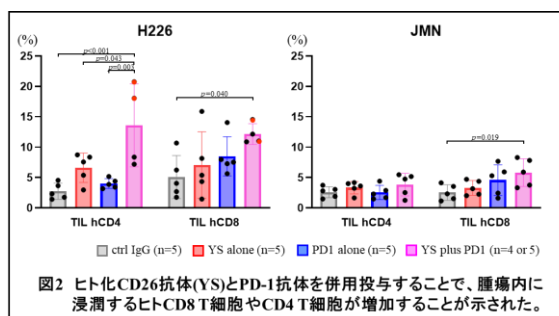


図2 ヒト化CD26抗体(YS)とPD-1抗体を併用投与することで、腫瘍内に浸潤するヒトCD8 T細胞やCD4 T細胞が増加することが示された。

現在、腫瘍組織における Ki-67 陽性の増殖期にあるがん細胞の数や、cleaved caspase-3やcleaved PARP陽性のアポトーシスを起こしたがん細胞の数の評価を行っている。また、腫瘍内に浸潤したヒト CD4 T

細胞・CD8 T細胞のエフェクター機能を中心としたフェノタイプ解析も行っており、CD26抗体とPD1抗体との抗腫瘍作用メカニズムの違いについてより詳細に解析し、併用効果の有効性を実証する。

D. 考察

ヒト化 CD26 抗体の副作用が少ない利点を活かした新たな併用療法を開発するために、ヒト免疫化マウスを用いたヒト悪性中皮腫株担がんモデルにて、ヒト化 CD26 抗体と PD-1 抗体との併用療法の抗腫瘍作用メカニズムの解析を行った。

マウスと MHC のハプロタイプを揃えたマウスがん細胞株を移入した担がんモデルでは、がん免疫系が同種同系となり、がん抗原に特異的な免疫応答を解析することができる。より疾患の病態を模倣したモデルの方が望ましいことは言うまでもないが、CD26 分子の研究ではマウスの免疫系を用いることができない理由が複数存在する。

CD26 は腫瘍だけでなく T細胞にも発現しており、近年の研究から CD26 抗体の抗腫瘍作用はがんへの直接的な影響だけでなく、T細胞を介した腫瘍免疫への影響も強く示唆される。CD26 はヒト T細胞に活性化シグナルを伝達する T細胞共刺激分子でもあり、ヒト化 CD26 抗体は CD26 のリガンドである caveolin-1 と CD26 との結合、つまりは T細胞への CD26 共刺激シグナルの伝達をブロックする。一方で、マウス T細胞の CD26 は共刺激分子として機能しない。また、ヒト T細胞では CD26 は強陽性・弱陽性・陰性の三相性パターンを示すのに対し、マウス T細胞は一律に弱陽性である。T細胞以外の免疫細胞における CD26

の発現も、ヒトとマウスとは異なる。このように、T細胞における機能や免疫細胞における発現パターンなどがヒトとマウスとは大きく異なるため、CD26抗体の腫瘍免疫への影響を解析するにはヒト免疫系での解析が不可欠である。また、ICIが抗腫瘍効果を発揮するためにも、T細胞を中心とした免疫系の存在が不可欠であり、ヒト化CD26抗体とICIとの併用効果を検討する実験にはヒト免疫化マウスを用いる必要がある。

CD26抗体が抗腫瘍効果を発揮するうえで、抗体がCD26分子上のどの部位に結合するか(エピトープ)が重要であり、CD26抗体の抗腫瘍効果のデータを取得するには、抗マウスCD26抗体ではなく、臨床応用を目標としたヒト化CD26抗体を用いることが不可欠である。ヒト化CD26抗体YS110はマウスCD26には交差性を示さず全く結合しないことから、ヒトCD26を発現したがん細胞を用いた実験系が不可欠になる。

以上の理由から、CD26抗体とPD-1抗体との併用効果のデータを取得するには、ヒト免疫系での実験が必要だが、ヒト免疫化マウスを用いた担がんモデルには問題点も存在する。一つは、免疫細胞がヒト臍帯血造血幹細胞由来のHLAを発現しているのに対し、ヒト腫瘍細胞株は異なるHLAを発現しているため、同種異系(allogeneic)のT細胞応答を見ることになり、本来のがん抗原特異的な応答とは異なる。また、ヒト免疫細胞の組成に関しても、今回のモデルではヒトT細胞とB細胞はマウス体内で十分な生着が認められるが、ヒトNK細胞や抗原提示細胞を含む骨髓系免疫細胞の生着率は非常に低い。この問題を解決するために、ヒトIL-2, IL-15, IL-3, GM-CSFなどの遺伝子を強制

発現させたNOGマウスが樹立・市販されつつあるが、現時点ではヒトの造血幹細胞から全ての免疫細胞を発生・分化させることはできず、また、線維芽細胞など腫瘍周囲の間質はマウス由来の細胞であることなど、ヒトのがん微小環境をマウスで再現することは不可能に近い。

近年、マウス担がんモデルで餌と一緒にDPP4 inhibitor (Sitagliptin)を食べさせることで、CXCR3陽性のCD4 T細胞、CD8 T細胞、NK細胞やCCR3陽性の好酸球ががん細胞周囲により集積し、腫瘍免疫の亢進に働くことが報告された(Nat Immunol. 2015, 2019)。フランス及び国内のヒト化CD26抗体の臨床試験の結果から、CD26抗体を投与すると血清中の可溶性CD26量が低下し、それに伴いDPP4酵素活性も低下する(Br J Cancer. 2017, Biomark Res. 2021)。このことから、CD26抗体を投与した場合においても、がん細胞周囲に集積する免疫細胞数の増加が起こる可能性が考えられる。しかしながら、ヒト化CD26抗体はマウスCD26には結合しないため、今回の担がんモデルにおいて、血清中の可溶性ヒトCD26量はCD26抗体投与によって7割近く低下したが、可溶性マウスCD26量には影響しなかった(データ未掲載)。マウスCD26にもDPP4酵素活性があるため、ヒトとマウスのCD26由来DPP4酵素活性の合計ではCD26抗体を投与しても5割程度の低下に留まっており、がん患者にCD26抗体を投与した場合ほどこのモデルではDPP4酵素活性低下作用は期待できない。今回のモデルでも、CD26抗体とPD-1抗体との併用投与により腫瘍内に浸潤するヒトCD4 T細胞・CD8 T細胞の増加が認められたが(図2)、これはPD-1抗

体によるヒト T 細胞の活性化と CD26 抗体による浸潤促進効果が関与していると予想される。がん患者に対して両剤の併用投与を行った場合では抗腫瘍免疫増強作用がより強いことが期待される。

E. 結論

ヒト T 細胞と B 細胞が十分に生着した免疫化マウスの作製に成功し、ヒト悪性中皮腫細胞株 H226 と JMN を皮下移入する担がんモデルにおいて、ヒト化 CD26 抗体と PD-1 抗体との併用効果を検討した結果、それぞれの単剤よりも強い腫瘍増殖抑制効果が見られることが示された。CD26 抗体は CD26 陽性がん細胞に直接作用するとともに、ヒト T 細胞とがん細胞膜上の CD26 発現・可溶性 CD26 量を低下させることで DPP4 酵素活性低下にも働くことを示した。

F. 今後の展望

悪性中皮腫細胞株を皮下移入する今回のモデルと並行して、より患者のがん細胞の特性を維持していると考えられる悪性中皮腫の患者腫瘍移植 (PDX; Patient-derived xenograft) モデルにおいても併用効果の有効性を検討する。

G. 研究発表

1. 論文発表

1) Kobayashi S, Fugo K, Hatano R, Yamazaki K, Morimoto C, Terawaki H. Anti-glomerular basement membrane disease concomitant with MPO-ANCA positivity concurrent with high serum levels of interleukin-26 following coronavirus disease 2019 vaccination. Intern Med. in press. doi: 10.2169/internalmedicine.

- 2) Santos MF, Rappa G, Fontana S, Karbanova J, Aalam F, Tai D, Li Z, Pucci M, Alessandro R, Morimoto C, Corbeil D, Lorico A. Anti-Human CD9 Fab Fragment Antibody Blocks the Extracellular Vesicle-Mediated Increase in Malignancy of Colon Cancer Cells. *Cells*. 2022;11(16):2474.
- 3) Hatano R, Itoh T, Otsuka H, Saeki H, Yamamoto A, Song D, Shirakawa Y, Iyama S, Sato T, Iwao N, Harada N, Aune TM, Dang NH, Kaneko Y, Yamada T, Morimoto C, Ohnuma K. Humanized anti-IL-26 monoclonal antibody as a novel targeted therapy for chronic graft-versus-host disease. *Am J Transplant*. 2022;22(12):2804-2820.
- 4) Komiya E, Tominaga M, Hatano R, kamikubo Y, Toyama S, Sakairi H, Honda K, Itoh T, Kamata Y, Tsurumachi M, Kishi R, Ohnuma K, Sakurai T, Morimoto C, Takamori K. Peripheral endomorphins drive mechanical alloknesis under the enzymatic control of CD26/DPPIV. *J Allergy Clin Immunol*. 2022;149(3):1085-1096
- 5) Fujiwara Y, Takahashi Y, Okada M, Kishimoto T, Kondo S, Fujikawa K, Hayama M, Sugeno M, Ueda S, Komuro K, Lanasa M, Nakano T. Phase 1 Study of Tremelimumab Monotherapy or in Combination with Durvalumab in Japanese Patients with Advanced Solid Tumors or Malignant Mesothelioma. *Oncologist*. 2022;27(9): e703-722
- 6) Kishimoto T, Kato K, Ashizawa K, Kurihara Y, Tokuyama T, Sakai F. A retrospective study on radiological findings of diffuse pleural thickening with benign

asbestos pleural effusion in Japanese cases.
Ind Health. 2022;60(5):429-435

- 7) Hayashi H, Ashizawa K, Takahashi M, Kato K, Arakawa H, Kishimoto T, Otsuka Y, Noma S, Honda S. The diagnosis of early pneumoconiosis in dust-exposed workers: comparison of chest radiography and computed tomography. Acta Radiol. 2022;63(7):909-913
- 8) Okatama M, Fujimori K, Sato M, Samata K, Kurita K, Sugiyama H, Ichikawa D, Matsushita M, Suto Y, Iwasaki G, Yamada T, Kiuchi F, Hirao M, Kunieda H, Yamazaki K, Hattori Y. GTN057, a komaroviquinone derivative, induced myeloma cells' death in vivo and inhibited c-MET tyrosine kinase. Cancer Medicine. in press
- 9) Tsuchiya, T, Saisho Y, Inaishi J, Sasaki H, Sato M, Nishikawa M, Masugi Y, Yamada T, Itoh H. Increased alpha cell to beta cell ratio in patients with pancreatic cancer. Endocr J. 2022;69(12):1407-1414

2. 著書

なし

3. 学会発表

- 1) Shirakawa Y, Hatano R, Itoh T, Otsuka H, Okumura K, Morimoto C. IL-26 facilitates cartilage destruction and infiltration of inflammatory cells into synovium in a collagen induced arthritis model. 第 51 回日本免疫学会学術集会, 熊本, 2022 年 12 月 8 日
- 2) 岸本卓巳、藤本伸一、水橋啓一、三浦元

彦、小澤聡子、加藤勝也. 良性石綿胸水の認定基準に関する研究 ー前向き調査結果についてー. 第 70 回日本職業・災害医学会学術大会, Web 開催, 2022 年 11 月 5 日

- 3) 岸本卓巳、宮原甚平、妹尾純江. 石綿肺がん認定のための肺内石綿繊維計測の意義. 第 63 回日本肺癌学会学術集会, 福岡(ハイブリッド開催), 2022 年 12 月 1 日
- 4) 林睦、間所裕子、坂元亨宇、山田健人. CD26 陽性がんに対する新規抗体-抗がん剤結合分子 ADC の開発. 第 111 回日本病理学会総会, 神戸, 2022 年 4 月 16 日
- 5) 政岡秀彦、稲田博輝、細沼沙紀、土居美枝子、金野美年子、金玲、山口浩、石澤圭介、山田健人、佐々木惇. 原発性腹膜癌 (高異型度漿液性癌) の一例. 第 63 回日本臨床細胞学会総会 (春期大会), 東京, 2022 年 6 月 12 日
- 6) 竹ノ谷隆、古川貴久、山田健人、川井田みほ、清川駿樹、浅田祐介、尾戸一平、矢部信成、大住幸司、村井信二. リンパ節転移が認められた腫瘍径 1cm 未満の直腸神経内分泌腫瘍 (NET-G2) の 1 例. 第 44 回日本癌局所療法研究会, 大阪, 2022 年 7 月 1 日

H. 知的財産権の出願・登録状況 (予定を含む)

1. 特許取得

- 1) 発明者: 森本幾夫, 波多野良, 大沼圭, 金子有太郎. 発明の名称: 抗 CD26 抗体と免疫チェックポイント阻害剤との併用療法. 出願日: 2022 年 5 月 27 日. 出願番号: 特願 PCT/JP2022/021738. 出願人: ワイズ・エー・シー株式会社、学校法人

順天堂

2. 実用新案登録
なし
3. その他
なし

労災疾病臨床研究事業費補助金

分担研究報告書

ヒト化 CD26 抗体の有効性予測バイオマーカーの探索：

国内第 I/II 相臨床試験検体における発現評価

研究代表者	森本 幾夫	順天堂大学大学院医学研究科 免疫病・がん先端治療学講座 特任教授
研究分担者	波多野 良	順天堂大学大学院医学研究科 免疫病・がん先端治療学講座 特任准教授
研究分担者	山田 健人	埼玉医科大学医学部 病理学 教授
研究分担者	岸本 卓巳	独立行政法人労働者健康安全機構 アスベスト疾患研究・研修センター 所長
研究協力者	伊藤 匠	順天堂大学大学院医学研究科 免疫病・がん先端治療学講座 特任助教
研究協力者	藤本 伸一	岡山労災病院 腫瘍内科部長
研究協力者	青江 啓介	山口宇部医療センター 腫瘍内科 内科系診療部長

研究要旨

悪性胸膜中皮腫はアスベストばく露によって起こる難治性悪性腫瘍であり、現時点で満足できる治療法はなく、新たな治療法の確立が望まれる。われわれは、悪性胸膜中皮腫に発現する CD26 に着目し、ヒト化 CD26 抗体を開発しフランスにて第 I 相臨床試験を、2017 年から国内で悪性中皮腫に対する第 I/II 相臨床試験を開始した。安全性が確認され治療薬としての有効性を示唆する結果も得られ、2019 年中に第 I 相 9 例・第 II 相 31 例(計 40 例)への投与が終了し、結果を集計が完了した。昨年度は、国内第 I/II 相臨床試験の患者から提供を受けた腫瘍病理組織から腫瘍部分を切り出し、RNA 抽出と DNA マイクロアレイ解析を行うことで、CD26 抗体の有効性予測バイオマーカーの探索を試みた。CD26 抗体の抗腫瘍効果が Progressive Disease(PD)であった 4 症例と比較して Stable Disease(SD)であった 3 症例で共通して発現が高い遺伝子、発現が低い遺伝子の絞り込みを行い、CD26 抗体の有効性予測バイオマーカー候補を見出した。今年度は、見出した候補分子の悪性中皮腫における発現を免疫組織染色で評価できる最適染色条件の決定と、国内臨床試験検体での染色を行ったが、SD/PD 症例間で認められた mRNA レベルでの発現量の違いをより明瞭に反映する免疫組織染色以外の評価方法についても検討する予定である。

A. 研究目的

悪性胸膜中皮腫はアスベストばく露によって起こる胸膜中皮由来の難治性悪性腫瘍

である。予後は極めて悪く、手術療法、化学療法、放射線療法などが行われるが、いずれも満足できる治療成績ではなく、新たな治療

法の確立が望まれる。われわれは、新規治療標的分子として悪性中皮腫細胞に発現する CD26 に着目し、ヒト化 CD26 抗体を開発してフランスにて悪性中皮腫を中心に First-in-Human 第 I 相臨床試験を行った。

このフランスでの結果を受け、どの患者に CD26 抗体療法が有効なのか、治療効果や予後を予測できるバイオマーカーの探索が課題として挙げられた。このことは、本抗体療法がより安全かつ効果的に行われるうえで極めて重要であり、かつ、抗体療法適用患者を適切に選択できれば期待していた治療効果が得られない患者にまで高額な医療費負担を強いることがなくなり、労災補償行政にも貢献できる。

そこで、本抗体の予後・治療効果予測バイオマーカーを同定するために、2017 年から本邦で開始した治療抵抗性(標準治療で Progressive Disease (PD))の悪性胸膜中皮腫に対するヒト化 CD26 抗体の第 I/II 相臨床試験患者の(1)中皮腫病理組織、(2)血清、(3)末梢血リンパ球を用いた解析に取り組んできた。

昨年度は、(1)中皮腫病理組織を用いて、腫瘍部位の切り出し、RNA 抽出、DNA マイクロアレイ解析を行い、Stable Disease (SD)症例と PD 症例との遺伝子発現の比較から CD26 抗体の有効性予測バイオマーカーの絞り込みを行った。今年度は、見出した候補分子の悪性中皮腫における発現を免疫組織染色で評価できる最適染色条件の決定と、国内臨床試験検体での染色を行った。

B. 研究方法

1) 腫瘍病理組織

ヒト化 CD26 抗体の悪性胸膜中皮腫に対

する国内第 I/II 相臨床試験は第 I 相が全 9 例、第 II 相が全 31 例で行われたが、その中で腫瘍病理組織のバイオマーカー探索に同意が得られたのは、第 I 相が 2 例、第 II 相が 21 例の計 23 例であった。抗がん剤治療や抗 PD-1 抗体 Nivolumab 治療を開始する前に採取された悪性中皮腫組織をホルマリン固定して作製されたパラフィンブロックの組織切片の提供を受け、マイクロダイセクションにより腫瘍部分の切り出しを行った。

2) DNA マイクロアレイ解析

ホルマリン固定・パラフィン包埋された悪性中皮腫組織からマイクロダイセクションで切り出した腫瘍部位を溶解し、miRNeasy FFPE Kit (QIAGEN)を用いて Total RNA 抽出を行った。全 7 サンプルの中で最も得られた RNA 量が少なかったサンプルに合わせて RNA 44ng から TransPlex Whole Transcriptome Amplification Kit (Sigma-Aldrich) と Titanium Taq DNA Polymerase (Clontech)を用いて cDNA の合成と増幅を行った。SureTag DNA Labeling Kit (Agilent Technologies)を用いて cDNA の断片化、DNA の Cy3 標識、精製を行った後、SurePrint G3 Human GE マイクロアレイ 8 x 60K Ver 3.0 (Design ID:072363) (Agilent Technologies)を用いて DNA マイクロアレイ解析を行った。

3) 免疫組織染色

悪性中皮腫病理組織スライドをオートクレーブで賦活化し、2.5%正常ウマ血清にてブロッキングした後、遺伝子 X と Y に対する一次抗体で反応させ、洗浄後に二次抗体ペルオキシダーゼ結合抗 Rabbit IgG 抗体

(ImmPRESS 社制)と反応させ、洗浄した後、ジアミノベンチジンにて発色させた。染色標本は2名の病理医が個別に観察し、++、+、+/-、- の四段階で評価を行った。

(倫理面への配慮)

ヒト化 CD26 抗体の国内第 I/II 相臨床試験の患者検体を用いたバイオマーカー探索研究については、臨床試験審査委員会、各治験実施施設内の治験審査委員会にて、試験の実施と合わせてバイオマーカー探索用採血・腫瘍組織検体の提供について協議され、実施承認を取得済みである。検体の提供を受ける際には、研究対象者に対する人的擁護上の配慮及び研究により研究対象者が受ける不利益、利益等の説明を行い、書面でのインフォームド・コンセントを得ている。

C. 研究結果

1) 国内第 I/II 相臨床試験患者の腫瘍病理組織の遺伝子発現解析

本パートの目的は、ヒト化 CD26 抗体療法が有効な患者を選択できるバイオマーカーを探索することである。CD26 抗体の国内臨床試験で腫瘍病理組織のバイオマーカー解析に同意が得られたのは、第 I 相が全 9 例中 2 例、第 II 相が全 31 例中 21 例の計 23 例(23/40)であった。DNA マイクロアレイ解析を行う際に、考慮すべき事項として性別・組織型・抗 PD-1 抗体 Nivolumab 投与の有無が挙げられる。同意が得られた 23 例中、性別・組織型・Nivolumab 投与の有無が同じ条件で、SD 症例と PD 症例を 3 例以上取れるのは、「男性・上皮型・Nivolumab 投与無し」(SD 6 例/PD 4 例)のみであったため、その条件で無増悪生存期間 PFS が長い SD

3 例と PD 4 例から腫瘍部位を切り出し、DNA マイクロアレイ解析を行った。

SD 群 3 例と PD 群 4 例との間で遺伝子発現の群比較を行い、PD 群と比較して SD 群で高発現している遺伝子群と SD 群と比較して PD 群で高発現している遺伝子群をヒートマップにまとめた(2021 年度 労災疾病臨床研究事業費補助金 研究報告書に記載)。図 1 に PD 症例と比較して SD 症例で発現が高かった遺伝子を、図 2 に SD 症例と比較して PD 症例で発現が高かった遺伝子を示す。

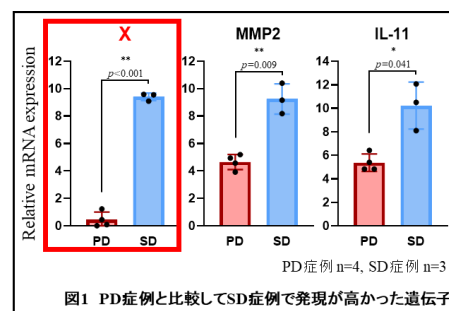


図1 PD症例と比較してSD症例で発現が高かった遺伝子

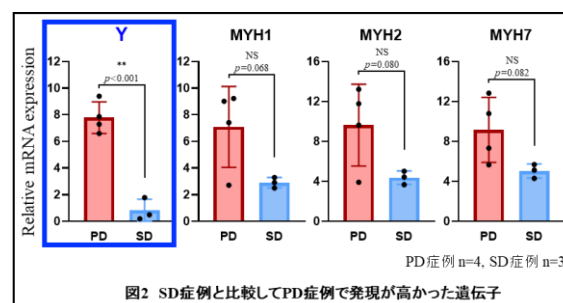


図2 SD症例と比較してPD症例で発現が高かった遺伝子

SD 症例では抗線維化、炎症亢進、増殖・代謝亢進に関わる遺伝子の発現が高く、SD 症例 3 例に共通して PD 症例よりも顕著に発現が高い遺伝子 X を見出した(図 1)。また、PD 症例では腫瘍部位を切り出して遺伝子発現解析を行ったものの、骨格筋や横紋筋、筋収縮、筋線維芽細胞に関係する遺伝子の発現が高く、PD 症例 4 例に共通して SD 症例よりも顕著に発現が高い遺伝子 Y を見出し

た(図 2)。

長期間 PFS が持続する CD26 抗体有効例と PD 症例とを判別できるバイオマーカー候補分子として特に X と Y に着目し、悪性中皮腫組織の免疫染色に最適な抗体、及び、染色条件(抗体濃度や抗原賦活化条件)の検討を行い、最適条件を決定したところである。現在、ヒト化 CD26 抗体の国内第 I/II 相臨床試験患者の腫瘍病理組織の免疫染色を行っており、CD26 抗体療法が特に有効な症例と有効ではない PD 症例との判別に有用か評価を行っている。

D. 考察

ヒト化 CD26 抗体の予後・治療効果予測バイオマーカーを探索するために、CD26 抗体の国内第 I/II 相臨床試験患者の腫瘍病理組織を用いて、SD 症例 3 例と PD 症例 4 例の DNA マイクロアレイ解析を行い、SD 症例で共通して発現が高い遺伝子、または、PD 症例で共通して発現が高い遺伝子の絞り込みを行った。

SD 症例群と PD 症例群との間で mRNA レベルでの発現量に顕著な差が見られた遺伝子 X と遺伝子 Y に着目し、腫瘍病理組織の免疫染色による発現評価を行っているが、現時点で SD 症例と PD 症例との間に DNA マイクロアレイでの結果ほど明瞭な差が認められない症例も見られている(データ未掲載)。免疫組織染色はホルマリン固定された組織のタンパクレベルでの発現を評価する方法として重宝されるが、mRNA 発現とタンパク質発現が必ずしも一致しないことや、免疫組織染色の感度あるいは定量性が低い問題もあるため、今後は腫瘍組織における遺伝子 X と Y の mRNA レベルでの発現を In

Situ Hybridization で評価する方法や、血清や胸水中の遺伝子 X と Y のタンパク量を ELISA で定量する方法なども並行して検討していく予定である。

これらの遺伝子を高発現する症例では何故 CD26 抗体が有効なのか無効なのかを解明することで、CD26 抗体の抗腫瘍作用メカニズムの更なる解明や、CD26 抗体による治療効果がより期待できる併用療法の開発にも繋がることが期待される。

E. 結論

ヒト化 CD26 抗体の国内第 I/II 相臨床試験患者の悪性中皮腫組織から腫瘍部位を切り出し、得られた微量の Total RNA を用いて SD 症例 3 例と PD 症例 4 例の DNA マイクロアレイ解析を行った。その結果、mRNA レベルにおいて SD 症例で共通して発現が顕著に高い遺伝子 X と PD 症例で共通して発現が顕著に高い遺伝子 Y を見出し、悪性中皮腫組織におけるそれらの発現評価を行える最適染色条件を決定した。

F. 今後の展望

今回見出した遺伝子 X と Y の発現量を評価する方法に関して、免疫組織染色以外の方法も並行して模索する必要があるが、CD26 抗体療法が有効な患者を選択できるバイオマーカーを同定できれば、PD-1 抗体が有効であった悪性中皮腫患者、無効であった悪性中皮腫患者それぞれで、有効性予測バイオマーカーの陽性率を解析することで、CD26 抗体と PD-1 抗体との併用療法が期待できる患者、PD-1 抗体が無効でも CD26 抗体による治療が期待できる患者の割合を予測することへの応用も期待される。

G. 研究発表

1. 論文発表

- 1) Kobayashi S, Fugo K, Hatano R, Yamazaki K, Morimoto C, Terawaki H. Anti- glomerular basement membrane disease concomitant with MPO-ANCA positivity concurrent with high serum levels of interleukin-26 following coronavirus disease 2019 vaccination. Intern Med. in press. doi: 10.2169/internalmedicine.
- 2) Santos MF, Rappa G, Fontana S, Karbanova J, Aalam F, Tai D, Li Z, Pucci M, Alessandro R, Morimoto C, Corbeil D, Lorico A. Anti-Human CD9 Fab Fragment Antibody Blocks the Extracellular Vesicle- Mediated Increase in Malignancy of Colon Cancer Cells. Cells. 2022;11(16):2474.
- 3) Hatano R, Itoh T, Otsuka H, Saeki H, Yamamoto A, Song D, Shirakawa Y, Iyama S, Sato T, Iwao N, Harada N, Aune TM, Dang NH, Kaneko Y, Yamada T, Morimoto C, Ohnuma K. Humanized anti-IL-26 monoclonal antibody as a novel targeted therapy for chronic graft-versus-host disease. Am J Transplant. 2022;22(12): 2804-2820.
- 4) Komiya E, Tominaga M, Hatano R, kamikubo Y, Toyama S, Sakairi H, Honda K, Itoh T, Kamata Y, Tsurumachi M, Kishi R, Ohnuma K, Sakurai T, Morimoto C, Takamori K. Peripheral endomorphins drive mechanical allodynia under the enzymatic control of CD26/DPPIV. J Allergy Clin Immunol. 2022;149(3): 1085-1096
- 5) Fujiwara Y, Takahashi Y, Okada M, Kishimoto T, Kondo S, Fujikawa K, Hayama M, Sugeno M, Ueda S, Komuro K, Lanasa M, Nakano T. Phase 1 Study of Tremelimumab Monotherapy or in Combination with Durvalumab in Japanese Patients with Advanced Solid Tumors or Malignant Mesothelioma. Oncologist. 2022;27(9):e703-722
- 6) Kishimoto T, Kato K, Ashizawa K, Kurihara Y, Tokuyama T, Sakai F. A retrospective study on radiological findings of diffuse pleural thickening with benign asbestos pleural effusion in Japanese cases. Ind Health. 2022;60(5):429-435
- 7) Hayashi H, Ashizawa K, Takahashi M, Kato K, Arakawa H, Kishimoto T, Otsuka Y, Noma S, Honda S. The diagnosis of early pneumoconiosis in dust-exposed workers: comparison of chest radiography and computed tomography. Acta Radiol. 2022;63(7):909-913
- 8) Okatama M, Fujimori K, Sato M, Samata K, Kurita K, Sugiyama H, Ichikawa D, Matsushita M, Suto Y, Iwasaki G, Yamada T, Kiuchi F, Hirao M, Kunieda H, Yamazaki K, Hattori Y. GTN057, a komaroviquinone derivative, induced myeloma cells' death in vivo and inhibited c-MET

tyrosine kinase. Cancer Medicine. in press

- 9) Tsuchiya, T, Saisho Y, Inaishi J, Sasaki H, Sato M, Nishikawa M, Masugi Y, Yamada T, Itoh H. Increased alpha cell to beta cell ratio in patients with pancreatic cancer. Endocr J. 2022;69(12):1407-1414

2. 著書

なし

3. 学会発表

- 1) Shirakawa Y, Hatano R, Itoh T, Otsuka H, Okumura K, Morimoto C. IL-26 facilitates cartilage destruction and infiltration of inflammatory cells into synovium in a collagen induced arthritis model. 第 51 回日本免疫学会学術集会, 熊本, 2022 年 12 月 8 日
- 2) 岸本卓巳、藤本伸一、水橋啓一、三浦元彦、小澤聡子、加藤勝也. 良性石綿胸水の認定基準に関する研究 -前向き調査結果について-. 第 70 回日本職業・災害医学会学術大会, Web 開催, 2022 年 11 月 5 日
- 3) 岸本卓巳、宮原甚平、妹尾純江. 石綿肺がん認定のための肺内石綿繊維計測の意義. 第 63 回日本肺癌学会学術集会, 福岡(ハイブリッド開催), 2022 年 12 月 1 日
- 4) 林睦、間所裕子、坂元亨宇、山田健人. CD26 陽性がんに対する新規抗体-抗がん剤結合分子ADCの開発. 第111回日本病理学会総会, 神戸, 2022 年 4 月 16 日
- 5) 政岡秀彦、稲田博輝、細沼沙紀、土居美

枝子、金野美年子、金玲、山口浩、石澤圭介、山田健人、佐々木惇. 原発性腹膜癌(高異型度漿液性癌)の一例. 第 63 回日本臨床細胞学会総会(春期大会), 東京, 2022 年 6 月 12 日

- 6) 竹ノ谷隆、古川貴久、山田健人、川井田みほ、清川駿樹、浅田祐介、尾戸一平、矢部信成、大住幸司、村井信二. リンパ節転移が認められた腫瘍径 1cm 未満の直腸神経内分泌腫瘍(NET-G2)の1例. 第 44 回日本癌局所療法研究会, 大阪, 2022 年 7 月 1 日

H. 知的財産権の出願・登録状況(予定を含む)

1. 特許取得

- 1) 発明者: 森本幾夫, 波多野良, 大沼圭, 金子有太郎. 発明の名称: 抗 CD26 抗体と免疫チェックポイント阻害剤との併用療法. 出願日:2022 年 5 月 27 日. 出願番号: 特願 PCT/JP2022/021738. 出願人: ワイズ・エー・シー株式会社、学校法人順天堂

2. 実用新案登録

なし

3. その他

なし

Ⅲ. 研究成果の刊行に関する一覧表

研究成果の刊行に関する一覧表

雑誌

発表者氏名	論文タイトル名	発表誌名	巻号	ページ	出版年
Kobayashi S, Fugo K, Hatano R, Yamazaki K, Morimoto C, Terawaki H.	Anti-glomerular basement membrane disease concomitant with MPO-ANCA positivity concurrent with high serum levels of interleukin-26 following coronavirus disease2019 vaccination.	Intern Med.			(in press)
Santos MF, Rappaport A, Fontana S, Karbanova J, Aalam F, Tai D, Li Z, Pucci M, Alessandro R, Morimoto C, Corbeil D, Lorico A.	Anti-Human CD9 Fab Fragment Antibody Blocks the Extracellular Vesicle-Mediated Increase in Malignancy of Colon Cancer Cells.	Cells.	11(16)	2474	2022
Hatano R, Itoh T, Otsuka H, Saeki H, Yamamoto A, Song D, Shirakawa Y, Iyama S, Satoh T, Iwao N, Harada N, Aune TM, Dang NH, Kaneko Y, Yamada T, Morimoto C, Ohnuma K.	Humanized anti-IL-26 monoclonal antibody as a novel targeted therapy for chronic graft-versus-host disease.	Am J Transplant.	22(12)	2804-2820	2022
Komiya E, Tomiyaga M, Hatano R, Kamikubo Y, Toyama S, Sakairi H, Honda K, Itoh T, Kamata Y, Tsurumachi M, Kishida R, Ohnuma K, Sakurai T, Morimoto C, Takamori K.	Peripheral endomorphins drive mechanical allodynia under the enzymatic control of CD26/DPPIV.	J Allergy Clin Immunol.	149(3)	1085-1096	2022
Fujiwara Y, Takahashi Y, Okada M, Kishimoto T, Kondo S, Fujikawa K, Hayama M, Sugeno M, Ueda S, Komuro K, Lanasa M, Nakano T.	Phase 1 Study of Tremelimumab Monotherapy or in Combination with Durvalumab in Japanese Patients with Advanced Solid Tumors or Malignant Mesothelioma.	Oncologist.	27(9)	e703-722	2022

発表者氏名	論文タイトル名	発表誌名	巻号	ページ	出版年
Kishimoto T, Kato K, Ashizawa K, Kurihara Y, Tokuyama T, Sakai F.	A retrospective study on radiological findings of diffuse pleural thickening with benign asbestos pleural effusion in Japanese cases.	Ind Health.	60(5):	429-435	2022
Hayashi H, Ashizawa K, Takahashi M, Kato K, Arakawa H, Kishimoto T, Otsuka Y, Nomura S, Honda S.	The diagnosis of early pneumoconiosis in dust-exposed workers: comparison of chest radiography and computed tomography.	Acta Radiol.	63(7):	909-913	2022
Okatama M, Fujimori K, Sato M, Samata K, Kurita K, Sugiyama H, Ichikawa D, Matsushita M, Suto Y, Iwasaki G, Yamada T, Kiuchi F, Hirao M, Kunieda H, Yamazaki K, Hattori Y.	GTN057, a komaroviquinone derivative, induced myeloma cells' death in vivo and inhibited c-MET tyrosine kinase.	Cancer Medicine			(in press)
Tsuchiya T, Saisho Y, Inaishi J, Sasaki H, Sato M, Nishikawa M, Masugi Y, Yamada T, Itoh H.	Increased alpha cell to beta cell ratio in patients with pancreatic cancer.	Endocr J.	69(12)	1407-1414	2022

IV. 研究成果の別刷

[CASE REPORT]

Anti-glomerular Basement Membrane Disease Concomitant with MPO-ANCA Positivity Concurrent with High Serum Levels of Interleukin-26 Following Coronavirus Disease 2019 Vaccination

Seiji Kobayashi¹, Kazunori Fugo², Ryo Hatano³, Kazuto Yamazaki², Chikao Morimoto³ and Hiroyuki Terawaki¹

Abstract:

As coronavirus disease 2019 (COVID-19) vaccine booster campaigns progress worldwide, new reports of complications following COVID-19 vaccination have emerged. We herein report a case of new-onset anti-glomerular basement membrane (GBM) disease concomitant with myeloperoxidase-antineutrophil cytoplasmic antibody positivity concurrent with high levels of interleukin (IL)-26 following the second dose of the Pfizer-BioNTech COVID-19 vaccine. The temporal association with vaccination in this case suggests that an enhanced neutrophilic immune response through IL-26 may have triggered necrotizing glomerulonephritis and a T-cell-mediated immune response to GBMs, leading to the development of anti-GBM antibodies, with an enhanced B-cell response after the vaccination triggering anti-GBM IgG and the onset of anti-GBM disease.

Key words: Anti-GBM disease, ANCA-associated glomerulonephritis, IL-26, mRNA-based COVID-19 vaccine, pharmacovigilance

(Intern Med Advance Publication)

(DOI: 10.2169/internalmedicine.1027-22)

Introduction

As coronavirus disease 2019 (COVID-19) vaccine booster campaigns progress worldwide, new reports of adverse events following mRNA-based COVID-19 vaccination have emerged, such as cases of anti-glomerular basement membrane (GBM) disease or anti-neutrophil cytoplasmic antibody (ANCA)-associated vasculitis (AAV) (1, 2). The pathogenesis of anti-GBM disease has been well defined at the molecular level, but the factors that initiate the autoimmune process remain unclear (3).

AAV is a multisystem autoimmune disease, with neutrophil extracellular traps (NETs) involved in its pathogenesis (4). Interleukin (IL)-26 is a member of the IL-10 family of cytokines that participates in inflammatory signaling through directly binding DNA to facilitate cellular transduc-

tion and intracellular inflammation signaling (5). Recently, it has been shown that IL-26 binds to NETs to induce the secretion of inflammatory cytokines (IL-1 β and IL-6) and chemokines (IL-8) by myeloid cells in ANCA-associated glomerulonephritis (6).

We herein report a case of new-onset anti-GBM disease concomitant with myeloperoxidase (MPO)-ANCA positivity with high levels of serum IL-26 following the receipt of the second dose of the Pfizer-BioNTech COVID-19 vaccine.

Case Report

A 67-year-old man with a history of pulmonary tuberculosis at 25 years old was admitted with a fever and anuria 6 weeks after his second vaccination. He had reported protracted systemic reactions with a low-grade fever and gross hematuria two weeks after the first dose. He received a sec-

¹Division of Nephrology, Department of Internal Medicine, Teikyo University Chiba Medical Center, Japan, ²Department of Pathology, Teikyo University Chiba Medical Center, Japan and ³Department of Therapy Development and Innovation for Immune Disorders and Cancers, Graduate School of Medicine, Juntendo University, Japan

Received: September 20, 2022; Accepted: December 12, 2022; Advance Publication by J-STAGE: February 1, 2023

Correspondence to Dr. Seiji Kobayashi, kobayashi.seiji.oh@teikyo-u.ac.jp

ond dose three weeks after the first dose. One month after the second dose, he developed a fever, anasarca, and anuria, which lasted over the next two weeks. He had received 6 months of chemotherapy for the treatment of pulmonary tuberculosis at 25 years old. There was no history of smoking or medication use, including propylthiouracil. Results of annual medical reviews had been normal, with serum creatinine levels of 0.6 mg/dL and normal urinalysis findings.

On admission, his blood pressure was 162/98 mmHg, and a physical examination revealed generalized edema. Laboratory tests revealed a white blood cell (WBC) count of 12,900/mm³, serum creatinine of 14.6 mg/dL, and albumin of 1.6 g/dL. A serologic evaluation revealed a C-reactive protein level of 37.0 mg/dL, positive anti-GBM IgG (>3,500 U/mL, reference range 3.0> U/mL), positive MPO-ANCA IgG (268 U/mL, reference range 3.5> U/mL), and positive IFN- γ release assays for tuberculosis. The levels of complement C3 and C4 were within the reference ranges, and testing for proteinase 3-ANCA, anti-nuclear antibody, hepatitis B virus, hepatitis C virus were negative. Polymerase chain reaction and serology testing for SARS-CoV-2 were also negative. A urinalysis revealed blood (3+) and protein (3+) at 4,377 mg/dL, and urine microscopy showed >100 red blood cells per high-power field (>10% dysmorphic) and 100 WBCs per high-power field with granular casts. Computed tomography of the chest revealed nodules in the apex segment of the right upper lobe and bilateral mild pleural effusion, without pulmonary involvement. Three sputum smear examinations with Ziehl-Neelsen staining for the diagnosis of tuberculosis over a three-day period were negative. In addition, there were no negative culture results for those sputum specimens.

A kidney biopsy was performed 52 days after the second vaccination. Light microscopy of the kidney biopsy specimen showed cellular crescents and fibrinoid necrosis involving 43 of 45 glomeruli, with CD4 T cells and macrophages scattered throughout the glomeruli. Cortical tubules displayed diffuse acute epithelial injury with interstitial inflammation. Interstitial fibrosis and tubular atrophy were moderate. Immunofluorescence showed linear staining of GBMs for IgG1. Electron microscopy revealed disruption of GBMs and diffuse effacement of podocyte foot processes without immune complex-mediated deposits, leading to a diagnosis of anti-GBM glomerulonephritis (Fig. 1). Further investigations revealed a high serum IL-26 level of 517.1 pg/mL on an enzyme-linked immunosorbent assay (reference range: not detectable), IL-1 β of 34.5 pg/mL, IL-6 of 1,577.9 pg/mL, tumor necrosis factor- α (TNF- α) of 300.6 pg/mL, granulocyte colony-stimulating factor (G-CSF) of 126.6 pg/mL, IL-8 of 615.4 pg/mL, and chemokine (C-X-C motif) ligand (CXCL) 1 of 1,480.9 pg/mL using the Bio Plex multi-plex system (Bio-Rad Laboratories, Inc. Hercules, CA, USA). He carried human leukocyte antigen (HLA) DRB1*04:03 and DRB1*14:05 alleles.

Intravenous methylprednisolone 1 g daily for 3 days was initiated the day after the kidney biopsy followed by oral

prednisolone 1 mg/kg daily. Ten days after admission, he was treated with 2 doses of rituximab at 375 mg/m² once a week. Hemodialysis was initiated on day 2 after admission. Prednisolone was tapered by 0.1 mg/kg/day weekly, and the patient was discharged after 50 days in hospital. The patient received 300 mg of isoniazid daily for latent tuberculosis infection over 9 months from the start of treatment for anti-GBM disease. Currently, he continues maintenance hemodialysis while on oral prednisolone at 10 mg/day. Nine months after discharge, neither pulmonary involvement nor relapse occurred, with serum levels of anti-GBM IgG, MPO-ANCA and inflammatory cytokines/chemokines, including IL-26, gradually decreasing or resolving (Fig. 2).

Discussion

Several recent case reports have described the new onset of anti-GBM disease or AAV following COVID-19 vaccination (2, 7, 8). However, the mechanism concerning the contribution of the mRNA-based vaccines to these diseases remains unknown. To our knowledge, this is the first report of anti-GBM disease concomitant with ANCA positivity accompanied by a high serum IL-26 level following the second dose of the Pfizer-BioNTech COVID-19 vaccine. The temporal association with vaccination in this case suggests that an enhanced neutrophilic immune response through IL-26 may have triggered necrotizing glomerulonephritis and a T-cell-mediated immune response to GBMs, leading to the development of anti-GBM antibodies, with an enhanced B-cell response after the vaccination triggering anti-GBM IgG and the onset of anti-GBM disease (Fig. 3).

The possible mechanisms underlying the new-onset adverse effects following mRNA-based COVID-19 vaccination reportedly include molecular mimicry, vaccine adjuvants, and polyclonal activation followed by the production of particular autoantibodies. Recently, Ventura et al. reported that 2 out of 35 patients who developed ANCA after SARS-CoV-2 vaccination developed ANCA and AAV after receiving the first dose of the Pfizer-BioNTech COVID-19 vaccine. One of the two cases developed ANCA six days after the first dose (9). A secondary effect from the polyclonal activation induced by the vaccine may be attributable to the production of ANCA by potential autoreactive clones specific for MPO. AAV has been known to occur under a variety of circumstances, including with infections (4, 10). Certain infectious agents such as *Mycobacterium tuberculosis* may lead to development of ANCA (11, 12). In our case, latent MPO-ANCA, which might have developed following pulmonary tuberculosis, may have been enhanced following receipt of the SARS-CoV-2 mRNA vaccine, potentially triggering ANCA-associated glomerulonephritis. Whether or not our case can be attributed to pulmonary tuberculosis-induced ANCA is speculative but intriguing and warrants further investigation, given emerging cases of vaccination-induced AAV.

IL-26 directly binds neutrophil-derived extracellular DNA

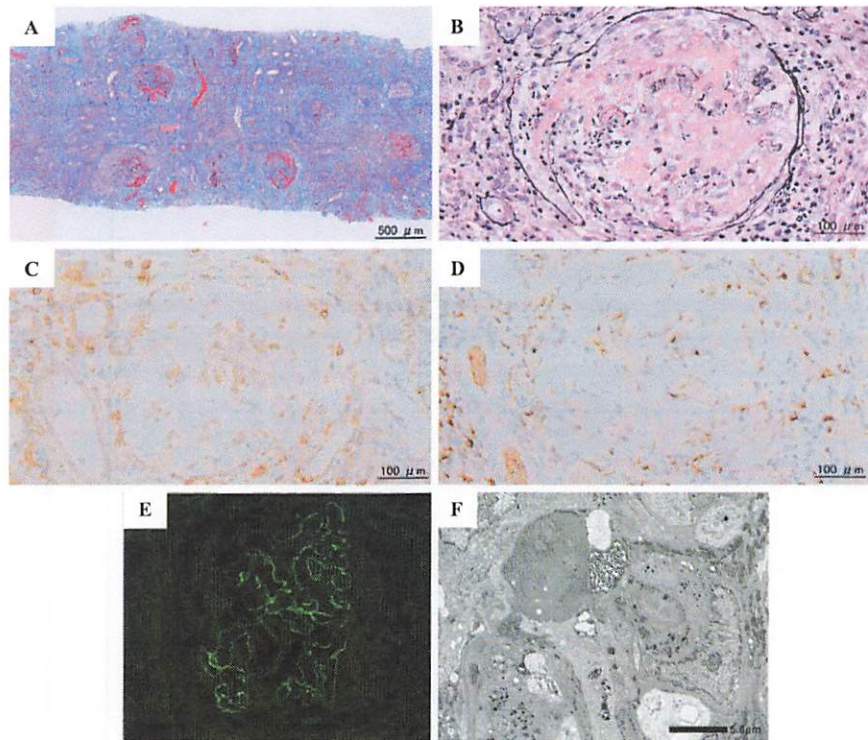


Figure 1. Kidney biopsy findings. Light microscopy of (A) the renal cortex showing multiple glomeruli with fibrinoid necrosis and crescentic formations associated with rupture of Bowman's capsule (Masson trichrome, original magnification $\times 40$) and of (B) a representative glomerulus showing fibrinoid necrosis, a circumferential cellular crescent, and destruction of the glomerular tuft and Bowman's capsule with leukocytes, including neutrophils (Jones methenamine silver, original magnification $\times 200$). Immunohistochemical staining for (C) CD4 and (D) CD68 showing scattered CD4 T cells and macrophages throughout the glomeruli as well as adjacent tubules and interstitium (original magnification $\times 200$, respectively). Immunofluorescence for (E) IgG1 of glomeruli showing global linear staining along glomerular basement membranes (original magnification $\times 200$). (F) Electron microscopy of the glomerulus showing disruption of the glomerular basement membranes, diffuse foot process effacement, and the absence of electron-dense deposits (original magnification, $\times 6,000$).

to facilitate intracellular inflammation signaling in a stimulator of interferon genes (STING)- and inflammasome-dependent manner (5). It is possible that an enhanced neutrophilic immune response through IL-26 after the vaccination may have been responsible for the ANCA-associated glomerulonephritis in our case. Recently, Poli et al. demonstrated that IL-26 is one of the most significant inflammatory mediators in active AAV (6). High levels of IL-26 are detected in the sera of active AAV patients with glomerulonephritis. Furthermore, IL-26 binds to NETs, and IL-26-DNA complexes induce secretion of inflammatory cytokines (TNF- α , IL-1 β , IL-6, and G-CSF) and chemokines (IL-8 and CXCL1) by myeloid cells in the crescentic necrotizing lesions of ANCA-associated glomerulonephritis (6). In our case, IL-26 may have potentiated the recruitment of immune cells to the necrotizing lesions through inflammatory cytokines and chemokines, leading to ANCA-associated glomerulonephritis.

Anti-GBM disease is caused by autoimmunity to the $\alpha 3$ chain of type IV collagen of GBM. Susceptibility to anti-

GBM disease is strongly associated with HLA-DRB1 genes, for which HLA-DRB1*15 and DRB1*04 are particularly responsible (13). In our case, the T-cell-mediated immune response to peptides derived from the ruptured GBM through HLA-DR4 from HLA DRB1*04:03 on antigen-presenting cells may have induced the development of anti-GBM antibodies. Furthermore, the vaccine is supposed to elicit CD4 cytokine responses involving type 1 helper T cells (14). It is possible that the enhanced B-cell response after the second dose of the vaccine was responsible for triggering the extremely high titers of anti-GBM IgG1 and the subsequent onset of anti-GBM disease.

Whether AAV predisposes patients to the development of anti-GBM disease or if ANCA positivity occurs in the course of anti-GBM disease is unclear at present (15). Patients with anti-GBM disease may be classified into at least two clusters based on clinical presentation: older adults presenting with kidney involvement alone with a high proportion of ANCA positivity and younger individuals with pulmonary involvement and a lower proportion of double posi-

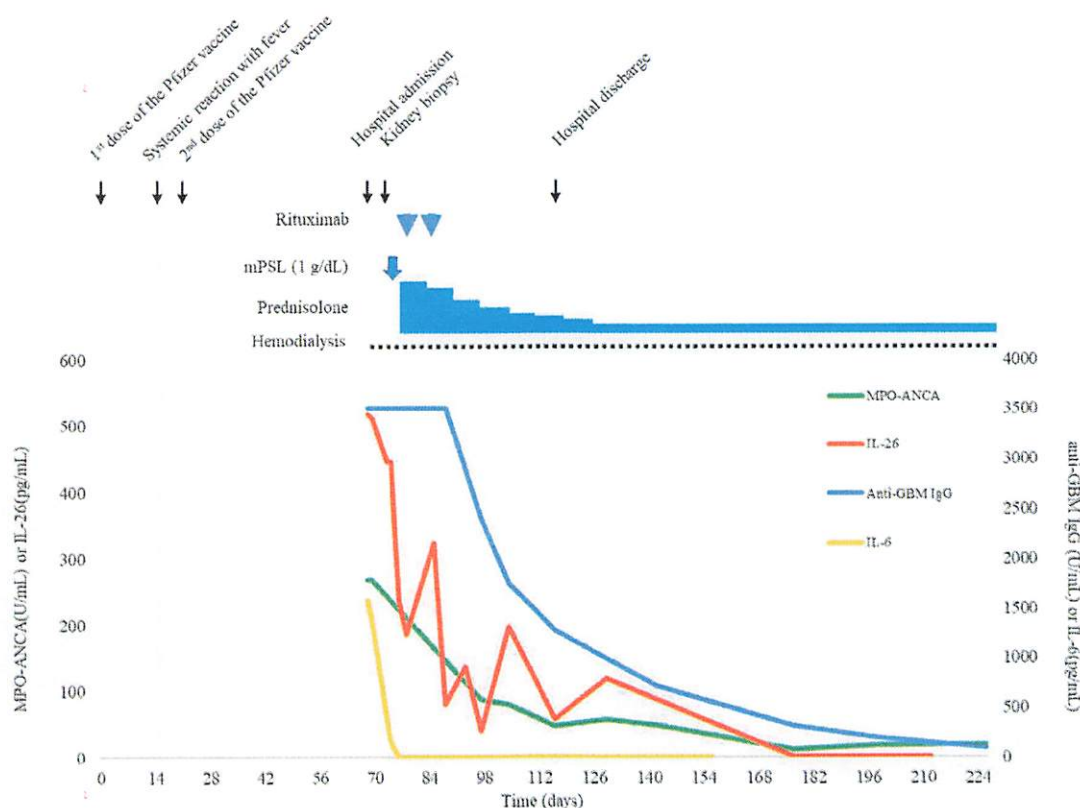


Figure 2. Timeline of clinical events and trends in the serum IgG antibody to GBM titer, MPO-ANCA titer, serum IL-26 concentration, and serum IL-6 concentration from the time of vaccination until the four-month follow-up after discharge.

tivity (16). The recent confirmation of spatial and temporal clustering of anti-GBM disease suggests that environmental factors, including certain infections, may trigger the disease in susceptible individuals (17, 18). We suspect that genetic susceptibility to anti-GBM disease and the history of pulmonary tuberculosis, followed by vaccination, may have triggered the secondary autoimmunity in our case.

Anti-GBM disease is a monophasic non-relapsing illness. However, this may not be so in patients with dual positivity for both ANCA and anti-GBM antibodies. The relapse of clinical features while anti-GBM antibodies are still present is common, and although relapses can also occur in double-positive cases, such instances are often in the context of co-existent ANCA positivity (19). In the present case, decreases in serum IL-26 levels were correlated to a decline in the serum levels of anti-GBM IgG and MPO-ANCA, with no relapses. IL-26 might be a specific biomarker of disease activity. Furthermore, we recently developed a humanized neutralizing anti-IL-26 monoclonal antibody (mAb) for therapeutic use (20). Humanized anti-IL-26 mAb might be a useful therapeutic agent for the treatment of AAV.

This case highlights the association between an aberrant immune response to a vaccine and development of anti-GBM disease concomitant with MPO-ANCA positivity through IL-26. A deeper analysis of the immune response through IL-26 may provide better insight into the mecha-

nism underlying the development of AAV and anti-GBM disease. However, at present, there is insufficient evidence to postulate causality, as it may have been coincidental that mRNA-based SARS-CoV-2 vaccine administration closely preceded the new-onset anti-GBM disease with ANCA positivity. Given the possibility of further usage of mRNA-based vaccines against viral infections, strict pharmacovigilance will be important to determine the true frequency and potential causality between these vaccines and small-vessel vasculitides.

The authors state that they have no Conflict of Interest (COI).

Patient Consent: The authors declare that they have obtained consent from the patient reported in this article for the publication of information about him that appears within this Case Report.

Funding statement: No specific funding was received from anyone in the public, commercial, or not-for-profit sectors to carry out the work described in this article.

Authors' contributions: SK was directly involved in the treatment of the patient, conceived the case report, collected and analyzed the data, and wrote the manuscript. RH and CM analyzed the data. All authors contributed to the article and ap-

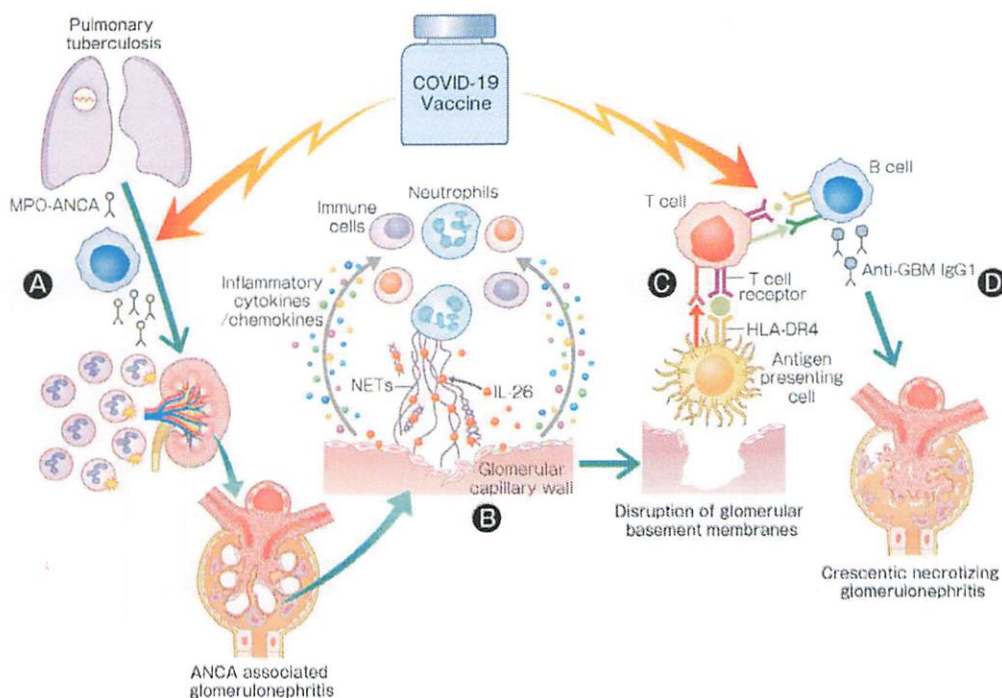


Figure 3. Hypothetical schematic illustration of the role of IL-26 and the mRNA-based COVID-19 vaccine in anti-GBM disease concomitant with MPO-ANCA following vaccination. (A) Latent MPO-ANCA, which might have developed following pulmonary tuberculosis, may have been enhanced following receipt of the SARS-CoV-2 mRNA vaccine, triggering ANCA-associated glomerulonephritis. (B) IL-26 potentiates recruitment of immune cells to necrotizing lesions through inflammatory cytokines and chemokines, leading to ANCA-associated glomerulonephritis. (C) The T-cell-mediated immune response to peptides derived from the ruptured GBM through HLA-DR4 from HLA DRB1*04:03 on antigen-presenting cells may have induced the development of anti-GBM antibodies. (D) The COVID-19 vaccine may have been responsible for triggering extremely high titers of anti-GBM IgG1 and the onset of anti-GBM disease.

proved the manuscript.

Data availability statement: The data are included in the current report.

References

- Johns Hopkins University Coronavirus Resource Center. COVID-19 dashboard by the Center for Systems Science and Engineering (CSSE) at Johns Hopkins University. September 1, 2022 [Internet]. Available from: <https://coronavirus.jhu.edu/map.html>
- Li NL, Coates PT, Rovin BH. COVID-19 vaccination followed by activation of glomerular diseases: does association equal causation? *Kidney Int* **100**: 959-965, 2021.
- Hellmark T, Segelmark M. Diagnosis and classification of Goodpasture's disease (anti-GBM). *J Autoimmun* **48-49**: 108-112, 2014.
- Jennette JC, Nachman PH. ANCA glomerulonephritis and vasculitis. *Clin J Am Soc Nephrol* **12**: 1680-1691, 2017.
- Shabgah AG, Abdelbasset WK, Rahman HS, et al. A comprehensive review of IL-26 to pave a new way for a profound understanding of the pathobiology of cancer, inflammatory diseases and infections. *Immunology* **165**: 44-60, 2022.
- Poli C, Augusto JF, Dauvé J, et al. IL-26 Confers Proinflammatory Properties to Extracellular DNA. *J Immunol* **198**: 3650-3661, 2017.
- Shakoor MT, Birkenbach MP, Lynch M. ANCA-associated vasculitis following the Pfizer-BioNTech COVID-19 vaccine. *Am J Kidney Dis* **78**: 611-613, 2021.
- Gupta RK, Ellis BK. Concurrent antiglomerular basement membrane nephritis and antineutrophil cytoplasmic autoantibody-mediated glomerulonephritis after second dose of SARS-CoV-2 mRNA vaccination. *Kidney Int Rep* **7**: 127-128, 2022.
- Irure-Ventura J, Belmar-Vega L, Fernández-Fresnedo G, et al. Increased induction of de novo serum ANCA and ANCA-associated vasculitis after mass vaccination against SARS-CoV-2. *iScience* **25**: 104847, 2022.
- Frangou E, Vassilopoulos D, Boletis J, Boumpas DT. An emerging role of neutrophils and NETosis in chronic inflammation and fibrosis in systemic lupus erythematosus (SLE) and ANCA-associated vasculitides (AAV): Implications for the pathogenesis and treatment. *Autoimmun Rev* **18**: 751-760, 2019.
- Flores-Suárez LF, Cabiedes J, Villa AR, van der Woude FJ, Alcocer-Varela J. Prevalence of antineutrophil cytoplasmic autoantibodies in patients with tuberculosis. *Rheumatology (Oxford)* **42**: 223-229, 2003.
- Elkayam O, Bendayan D, Segal R, et al. The effect of anti-tuberculosis treatment on levels of anti-phospholipid and antineutrophil cytoplasmic antibodies in patients with active tuberculosis. *Rheumatol Int* **33**: 949-953, 2013.
- Fisher M, Pusey CD, Vaughan RW, Rees AJ. Susceptibility to anti-glomerular basement membrane disease is strongly associated with HLA-DRB1 genes. *Kidney Int* **51**: 222-229, 1997.

14. Sahin U, Muik A, Derhovanessian E, et al. COVID-19 vaccine BNT162b1 elicits human antibody and TH1 T cell responses. *Nature* **586**: 594-599, 2020.
15. Levy JB, Hammad T, Coulthart A, Dougan T, Pusey CD. Clinical features and outcome of patients with both ANCA and anti-GBM antibodies. *Kidney Int* **66**: 1535-1540, 2004.
16. Alchi B, Griffiths M, Sivalingam M, Jayne D, Farrington K. Predictors of renal and patient outcomes in anti-GBM disease: clinicopathologic analysis of a two-centre cohort. *Nephrol Dial Transplant* **30**: 814-821, 2015.
17. Canney M, O'Hara PV, McEvoy CM, et al. Spatial and Temporal Clustering of Anti-Glomerular Basement Membrane Disease. *J Am Soc Nephrol* **11**: 1392-1399, 2016.
18. Predecki M, Candice Clarke C, Cairns T, et al. Anti-glomerular basement membrane disease during the COVID-19 pandemic. *Kidney Int* **98**: 780-781, 2020.
19. Levy JB, Lachmann RH, Pusey CD. Recurrent Goodpasture's disease. *Am J Kidney Dis* **27**: 573-578, 1996.
20. Hatano R, Itoh T, Otsuka H, et al. Humanized anti-IL-26 monoclonal antibody as a novel targeted therapy for chronic graft-versus-host disease. *Am J Transplant* 2022 Aug 23.

The Internal Medicine is an Open Access journal distributed under the Creative Commons Attribution-NonCommercial-NoDerivatives 4.0 International License. To view the details of this license, please visit (<https://creativecommons.org/licenses/by-nc-nd/4.0/>).

© The Japanese Society of Internal Medicine
Intern Med Advance Publication

Article

Anti-Human CD9 Fab Fragment Antibody Blocks the Extracellular Vesicle-Mediated Increase in Malignancy of Colon Cancer Cells

Mark F. Santos ¹, Germana Rappa ¹, Simona Fontana ², Jana Karbanová ³, Feryal Aalam ¹, Derek Tai ¹, Zhiyin Li ¹, Marzia Pucci ², Riccardo Alessandro ^{2,4}, Chikao Morimoto ⁵, Denis Corbeil ^{3,*}, and Aurelio Lorico ^{1,*}

¹ Department of Basic Sciences, Touro University College of Medicine, Henderson, NV 89014, USA

² Department of Biomedicine, Neurosciences and Advanced Diagnostics, University of Palermo, 90133 Palermo, Italy

³ Tissue Engineering Laboratories, Biotechnology Center (BIOTEC) and Center for Molecular and Cellular Bioengineering, Technische Universität Dresden, 01307 Dresden, Germany

⁴ Institute for Biomedical Research and Innovation (IRIB), National Research Council (CNR), 90146 Palermo, Italy

⁵ Department of Therapy Development and Innovation for Immune Disorders and Cancers, Graduate School of Medicine, Juntendo University, Tokyo 113-8421, Japan

* Correspondence: denis.corbeil@tu-dresden.de (D.C.); alorico@touro.edu (A.L.)



Citation: Santos, M.F.; Rappa, G.; Fontana, S.; Karbanová, J.; Aalam, F.; Tai, D.; Li, Z.; Pucci, M.; Alessandro, R.; Morimoto, C.; et al. Anti-Human CD9 Fab Fragment Antibody Blocks the Extracellular Vesicle-Mediated Increase in Malignancy of Colon Cancer Cells. *Cells* **2022**, *11*, 2474. <https://doi.org/10.3390/cells11162474>

Academic Editors: Wassim Abou-Kheir and Hisham Bahmad

Received: 8 July 2022

Accepted: 8 August 2022

Published: 10 August 2022

Publisher's Note: MDPI stays neutral with regard to jurisdictional claims in published maps and institutional affiliations.



Copyright: © 2022 by the authors. Licensee MDPI, Basel, Switzerland. This article is an open access article distributed under the terms and conditions of the Creative Commons Attribution (CC BY) license (<https://creativecommons.org/licenses/by/4.0/>).

Abstract: Intercellular communication between cancer cells themselves or with healthy cells in the tumor microenvironment and/or pre-metastatic sites plays an important role in cancer progression and metastasis. In addition to ligand–receptor signaling complexes, extracellular vesicles (EVs) are emerging as novel mediators of intercellular communication both in tissue homeostasis and in diseases such as cancer. EV-mediated transfer of molecular activities impacting morphological features and cell motility from highly metastatic SW620 cells to non-metastatic SW480 cells is a good in vitro example to illustrate the increased malignancy of colorectal cancer leading to its transformation and aggressive behavior. In an attempt to intercept the intercellular communication promoted by EVs, we recently developed a monovalent Fab fragment antibody directed against human CD9 tetraspanin and showed its effectiveness in blocking the internalization of melanoma cell-derived EVs and the nuclear transfer of their cargo proteins into recipient cells. Here, we employed the SW480/SW620 model to investigate the anti-cancer potential of the anti-CD9 Fab antibody. We first demonstrated that most EVs derived from SW620 cells contain CD9, making them potential targets. We then found that the anti-CD9 Fab antibody, but not the corresponding divalent antibody, prevented internalization of EVs from SW620 cells into SW480 cells, thereby inhibiting their phenotypic transformation, i.e., the change from a mesenchymal-like morphology to a rounded amoeboid-like shape with membrane blebbing, and thus preventing increased cell migration. Intercepting EV-mediated intercellular communication in the tumor niche with an anti-CD9 Fab antibody, combined with direct targeting of cancer cells, could lead to the development of new anti-cancer therapeutic strategies.

Keywords: cancer; CD9; Fab; cell morphology; migration; colon carcinoma; extracellular vesicle

1. Introduction

Intercellular communication between cancer and healthy cells is now recognized as an important aspect of tissue transformation that would promote the growth of cancer and the dissemination and seeding of cancer cells in pre-metastatic sites. Nanosized extracellular vesicles (EVs) appear to play a major role in these processes [1]. They carry biological information (e.g., membrane and soluble proteins, lipids, metabolites, and nucleic acids—notably messenger RNA, microRNA, and long non-coding RNA) that reflect, at

least in part, the characteristics of donor cells [2,3]. These bioactive molecules could act as mediators in the regulation of neighboring and distant host/recipient cells. EVs are released either by a membrane budding process occurring at the plasma membrane or by fusion of late endosomal multivesicular bodies (LE/MVBs) with the plasma membrane, resulting in the release of their intraluminal vesicles [4–6]. EVs are then referred to as microvesicles/ectosomes and exosomes according to the first and second mode of release, respectively. Once discharged into the extracellular medium, such as a biological fluid, in addition to their potential degradation, EVs may be trapped in the extracellular matrix and/or taken up by surrounding cells [7]. The direct interaction between EVs and cells has become the basis of a short- or long-distance intercellular communication mechanism where EVs can trigger a cellular response in host cells. Thus, EVs can reprogram their fate, by promoting their proliferation or differentiation, as well as stimulate their migration among various cellular processes [8–10].

The fusion of EVs and cell membranes and/or various mechanisms of endocytosis are described to explain the transfer of EV cargoes [11–14]. Direct binding of EVs to cells, similar to ligand–receptor interaction, could also occur and promote cell signaling. EVs as mediators of intercellular communication mechanisms are of general interest in various fields, as the molecular transfer of active biomolecules is involved in development, enables homeostasis, and is often dysregulated in various diseases, including cancers [15]. In the latter case, the increased release of cancer cell-derived EVs may not only promote cancer growth but also metastasis [16–18] (reviewed in Ref. [19]). In such a context, the interception of EV-mediated communication could find an application in oncology.

Inhibition of the biogenesis and release of EVs from donor cells could be a possibility to counteract their effect in cancer. For instance, proteins involved in exosome formation and/or secretion, such as neutral sphingomyelinase 2 and Rab27a, could be targeted, resulting in a reduction of certain exosome subpopulations [20–23]. Similarly, the intracellular calcium (Ca^{2+}) pool may also be altered, resulting in a defect in EV release from cancer cells [24,25]. Other regulators and potent drugs of exosome secretion have also been identified [26] (reviewed in Ref. [27]). Alternatively, it is possible to impede EV uptake into receptor/target cells by interfering with certain modes of endocytosis, such as clathrin-dependent or independent mechanisms, e.g., the lipid raft/caveolin-mediated pathways using chemical drugs. The uptake of EVs by phagocytosis or micropinocytosis can also be intercepted when these mechanisms occur. For a list of inhibitors and their molecular targets/pathways, readers are referred to the following review [13]. However, the general use of these inhibitors is limited because several mechanisms of EV internalization may be involved concurrently, and systemic application of these drugs, which often act on various cellular pathways, could result in toxic side effects.

Other therapeutic strategies to remove or neutralize cancer cell-derived EVs from circulation have been suggested (reviewed in Ref. [28]). For example, Nishida-Aoki and colleagues proposed to capture circulating EVs derived from cancer cells using specific antibodies (Abs) against EV-associated proteins [29]. Treatment of mice with anti-CD9 (see below) or anti-CD63 Abs stimulated EV clearance by macrophages. Although this treatment had no effect on the primary tumor, tumor metastasis was significantly reduced. Thus, elimination of cancer-derived EVs may be a novel therapy strategy for cancer metastasis. Targeting EV surface proteins may also impede their distribution to distant anatomical sites [29,30], as evidenced by the correlation between expression of specific integrins on the surface of EVs and metastatic tropism [7].

In such a context, one of the EV-associated proteins has attracted attention in the literature, namely CD9 (also known as tetraspanin-29, motility-related protein). CD9 is a member of the tetraspanin superfamily that, by interacting with various protein partners, has various cellular functions, such as cell–cell contact, cell–extracellular matrix interaction, integrin-dependent cell migration, and membrane fusion, among others (reviewed in Refs [31–33]). In addition to localizing at the cell surface, where it orchestrates membrane organization, CD9 is associated with EVs including exosomes [34,35]. Of note, a nuclear

pool of CD9 was also reported [36]. It has been shown that the presence of CD9 on the surface of EVs and/or on the plasma membrane of recipient breast cancer cells is essential for the uptake of EVs, as its silencing by RNA interference prevents internalization [37]. CD9 is also important for sperm–egg fusion as CD9-deficient oocytes do not fuse properly with sperm during fertilization, thus reduced female fertility is consequently observed in CD9 knockout mice [38,39]. Interestingly, sperm fusion properties are conferred by the CD9⁺ EVs released from eggs [40], and Abs directed against the extracellular domains of CD9 inhibited sperm–egg interaction and fusion [41]. Anti-CD9 Abs can also block the transfer of molecules between CD9⁺ EVs in the epididymal fluid and maturing spermatozoa [42]. Caution should be applied when divalent anti-CD9 Abs are proposed for clinical application. Being the major platelet surface protein [43], CD9, together with the fibrinogen receptor $\alpha 2b\beta 3$, can trigger platelet activation, aggregation, or lysis, depending on the Ab subclass used [44]. Therefore, the clinical development of such biological tools should exclude the occurrence of potential toxic events, including severe thrombocytopenia and/or thrombocyte aggregation [45–48] (reviewed in Ref. [33]).

Recently, we designed a CD9-based strategy to block EV transfer between cells using fragment antigen-binding fragments (Fab fragments; hereafter Fab) generated from 5H9 Ab (CD9 Ab) directed to human CD9 [49,50]. We showed that monovalent CD9 Fab impedes the internalization of melanoma cell-derived EVs and nuclear transfer of their cargo proteins in recipient cells [50]. Here, we investigated whether this approach could have therapeutic utility for intercepting the EV-mediated transformation of colon carcinoma. To this aim, we used the established isogenic cell line model of non-metastatic SW480 cells and highly metastatic SW620 cells, where EVs derived from the latter can transform the former and impact their malignant properties, including their motility [10,51]. These cell lines were derived from primary (i.e., SW480 cells) and secondary (SW620 cells) tumors from a single patient [52–54]. Our data reveal that monovalent CD9 Fab, but not divalent CD9 Ab, blocks the EV-mediated increase in malignancy of colorectal cancer cells.

2. Materials and Methods

2.1. Cell Culture

Human SW480 (CCL-228TM) and SW620 cells (CCL-227TM) were obtained from the American Type Culture Collection (ATCC, Manassas, VA, USA). They were cultured in RPMI-1640 medium (catalog number (#) 10-041-CV, Corning Inc., Corning, NY, USA) supplemented with 10% fetal bovine serum (FBS, #26140079), 2 mM L-glutamine (#25030081), 100 U/mL penicillin, and 100 μ g/mL streptomycin (#15140122), all from Thermo Fisher Scientific (Waltham, MA, USA), and incubated at 37 °C in a 5% CO₂ humidified incubator. Both cell lines were regularly tested for mycoplasma contamination by polymerase chain reaction using the MycoSEQTM Mycoplasma Detection Kit (#4460626, Thermo Fisher Scientific) according to the manufacturer's protocol, or upon staining with 4',6-diamidino-2-phenylindole (DAPI; #D9542, Sigma-Aldrich, St. Louis, MO, USA) and visualization under an Eclipse TE2000-U inverted fluorescence microscope (Nikon, Melville, NY, USA).

2.2. Lentiviral Infection

To inhibit the expression of human CD9 (NCBI protein accession number: P21926), transduction-ready CD9 short hairpin (sh) RNA lentiviral particles (#sc-35032-V, Santa Cruz Biotechnology, Dallas, TX, USA) were employed. Viruses were loaded on non-tissue culture treated 24-well plates (#15705-060, VWR International, Radnor, PA, USA) coated with 50 μ g/mL of RetroNectin[®] recombinant human fibronectin fragment (#T100B, Takara Bio USA, San Jose, CA, USA), then centrifuged at 960 \times g for 30 min at 4 °C. The supernatant was removed and plates were washed with PBS before addition of SW480 cells. CD9-deficient (shCD9) SW480 cells were then selected by introducing 2 μ g/mL of puromycin into the culture medium for a week. The antibiotic was removed three days before the start of the experiments.

2.3. Plasmid and Transfection

SW620 cells were transfected with pCMV6-AC-GFP plasmid encoding for CD9 with a GFP tag at its C-terminus under the control of the cytomegalovirus promoter (#RG202000; OriGene Technologies, Rockville, MD, USA) using Lipofectamine 3000 (#L3000008, Thermo Fisher Scientific) in a 1:2 DNA/lipid ratio. Cells expressing the neomycin resistance gene were selected by introducing 400 µg/mL of G418 Sulfate (Geneticin™ Selective Antibiotic, #10131035, Thermo Fisher Scientific) into the culture medium. After selection, at least 98% of the cells expressed CD9-GFP fusion protein, assessed by fluorescence microscopy. The antibiotic was removed three days before the start of the experiments.

2.4. Isolation and Characterization of EVs

EVs released from SW480, SW620, or CD9-GFP⁺ SW620 cells (250,000 cells) cultured in a serum-free medium supplemented with 2% B-27 supplement (#17504044, Thermo Fisher Scientific) on a 6-well plate coated with 20 µg/mL of poly(2-hydroxyethyl methacrylate) (#P3932, Sigma-Aldrich) were enriched by differential centrifugation from the conditioned media after 72 h of incubation. Briefly, after low-speed centrifugations (300 and 1200 × *g*) of the conditioned medium, the supernatant was centrifuged at 10,000 × *g* for 30 min. The resulting supernatant was centrifuged at 200,000 × *g* for 60 min. All centrifugation steps were performed at 4 °C. The 200,000 *g*-pellet was resuspended in 200 µL PBS and stored at −80 °C in small aliquots. The concentration and size of EVs were evaluated by nanoparticle tracking analysis (NTA). We used the light-scattering characteristics of 488 nm laser light on EV preparations injected into the sample chamber of the ZetaView unit (software v8.05.10, Particle Metrix GmbH, Meerbusch, Germany). The calculated EV concentration and size were an average of 11 positions across the analysis window, each recorded in 2 s videos (30 frames per second). Camera gain and minimum trace length were set to 10 and 15, respectively. The concentrations for SW480, SW620, and CD9-GFP⁺ SW620 EVs were 7.3×10^{10} , 6.9×10^{10} , and 7.6×10^{10} particles/mL, respectively.

EVs were characterized either by immunoblotting for the presence of tetraspanin proteins CD9, CD63, CD81, and ALG-2-interacting protein X (ALIX) or the absence of endoplasmic reticulum (ER)-associated calnexin according to the guidelines of the International Society of Extracellular Vesicles (MISEV2018) [55] or by high-resolution direct stochastic optical reconstruction microscopy (dSTORM) (see below). All relevant data concerning our EV characterization were submitted to the EV-TRACT knowledgebase (EV-TRACK, <https://evtrack.org>, ID: EV220040, accessed on 13 January 2022) [56].

2.5. CD9 Antibody Fab Fragment

The culture of 5H9 hybridoma cells [49] and the production of mouse monoclonal CD9 Ab were recently described [50]. The corresponding CD9 Fab was generated using the Pierce Fab Purification kit (#44985, Thermo Fisher Scientific). Herein, CD9 Ab (500 µg) was incubated with papain immobilized on agarose resin for 3 h at 37 °C. The digested Abs were collected by centrifugation (5000 × *g*, 1 min) using a spin column, and the flow through containing the Abs was placed in a new tube. The fragment crystalline (Fc) fragment was removed from digested Ab samples by centrifugation (1000 × *g*, 10 min) using the NAb Protein A Plus Spin Column, and the flow through containing the purified Fab fraction was collected. The column was then washed twice with PBS and each wash fraction was combined with the Fab fraction. Using the Microsep Advance Centrifugal Device (10K molecular weight cut-off) purchased from Pall Corporation (#MCP010C46, Westborough, MA, USA), the Fab fraction was concentrated by spinning at 3000 × *g* for 25 min at 4 °C. Concentration was then measured by absorbance at 280 nm (final yield of 0.4–0.8 mg/mL). CD9 Fab preparation was assessed by sodium dodecyl sulfate-polyacrylamide gel electrophoresis (SDS-PAGE) and Coomassie blue staining as described in [50].

2.6. Immunoblotting

Cells were lysed in cold buffer containing 1% Triton X-100 (#X100, Sigma-Aldrich), 100 mM NaCl, and 50 mM Tris-HCl with a pH of 7.5 and supplemented with Protease Inhibitor Cocktail Set III (#539134, Sigma-Aldrich), followed by incubation on ice for 30 min. Samples were then centrifuged at $12,000\times g$ for 10 min at 4 °C. Detergent lysate was collected and Laemmli sample buffer (#1610747, Bio-Rad, Hercules, CA, USA) containing β -mercaptoethanol (#444203, Sigma-Aldrich) was added. The reducing agent was omitted for CD9, CD63, and CD81 immunoblots. For the analysis of EVs, the Laemmli buffer was added directly to the enriched EVs. All samples were heated at 95 °C for 5 min. Proteins were separated by SDS-PAGE using a 4–20% Mini-PROTEAN TGX precast gel (#4561096, Bio-Rad) along with the Trident pre-stained protein molecular weight ladder (#GTX50875, GeneTex, Irvine, CA, USA) and were then transferred to a nitrocellulose membrane (#88018, Thermo Fisher Scientific) overnight at 4 °C. Membranes were incubated in the blocking buffer (PBS containing 1% bovine serum albumin (BSA, #001-000-161, Jackson ImmunoResearch Laboratories Inc., West Grove, PA, USA)) for 60 min at room temperature (RT) and then probed with primary Abs (see below) for 60 min at RT. After 3 washing steps of 10 min each with PBS containing 0.1% Tween 20, membranes were incubated with fluorescein (FITC)-conjugated donkey anti-mouse IgG (1:100, #715-095-150, Jackson ImmunoResearch Laboratories) for 30 min at RT. Finally, membranes were washed thrice (10 min each) in PBS containing 0.1% Tween 20, rinsed in deionized H₂O, and antigen-Ab complexes were visualized in the iBright FL1000 system (Thermo Fisher Scientific).

Blots were probed with mouse monoclonal anti-CD9 (clone 5H9, 1:500, see above) [49] or anti-CD63 (clone Ts63, 1:500), anti-CD81 (clone 1.3.3.22, 1:500), and anti-Calnexin Abs (clone AF18, 1:500), all purchased from Thermo Fisher Scientific (#10628D, MA5-13548, and MA3-027, respectively), or with anti-Alix Ab (clone 3A9, 1:500, #2171, Cell Signaling Technology, Danvers, MA, USA) and anti- β -actin Ab (clone C-2, 1:1000, #sc-8432, Santa Cruz Biotechnology).

2.7. Cell–EV Incubation

SW480 cells or shCD9 SW480 cells (1×10^5) seeded in 1 mL cell medium on poly-D-lysine-coated 35 mm dishes containing #1.5 glass coverslips (#P35GC-1.5-14-C, MatTek Corporation, Ashland, MA, USA) were pre-incubated with various concentrations (6.25, 12.5, and 25 $\mu\text{g}/\text{mL}$) of CD9 Fab or divalent CD9 Ab for 30 min at 37 °C. Concurrently, EVs (1×10^9 particles, equivalent volume of $\approx 15 \mu\text{L}$) derived from SW620 or CD9-GFP⁺ SW620 cells were pre-incubated with the same concentrations of Abs for 30 min at 4 °C. Afterward, EVs were added to the cells and co-incubated for 5 (or 16) h in the presence of Abs. The final EV concentration is 1×10^9 particles/mL or 27 μg protein/mL. These conditions will be referred as protocol #1 (*Cells and EVs*). As control, Abs were omitted. In some experiments, EVs (1×10^9 particles) alone were pre-incubated with CD9 Fab or divalent CD9 Ab as above and then added to cells (protocol #2, *EVs*). Conversely, cells were pre-incubated with CD9 Fab or divalent CD9 Ab as above and EVs (1×10^9 particles), which were not incubated with Abs, were then added and both cells and EVs were incubated together for 5 h (protocol #3, *Cells*). Note that in all conditions, Abs were not removed prior to co-incubation of cells and EVs, resulting in different Ab concentrations during the 5 h co-incubation, especially for protocol #1 (or #3) compared to protocol #2. Alternatively, the Abs were removed from cells after the 30 min pre-incubation and before the addition of EVs which were not pre-incubated with Abs (protocol #3', *Cells*). These distinct protocols are summarized in Supplementary Figure S1. In other experiments, cells were pre-treated with or without 10 μM PRR851, a drug synthesized in one of our laboratories (for detail, see Ref. [57]), in the presence or absence of CD9 Fab (25 $\mu\text{g}/\text{mL}$) for 30 min at 37 °C. CD9-GFP⁺ EVs were then added for 5 h. DMSO alone was used as vehicle control. Cells were then fixed and prepared for immunocytochemistry.

2.8. Confocal Laser Scanning Microscopy

Cells grown on poly-D-lysine-coated dishes, as described above, were fixed in 4% paraformaldehyde (PFA) in PBS for 15 min, washed twice with PBS, and permeabilized with 0.2% Tween 20 in PBS (permeabilization buffer, PB) for 15 min. They were first blocked with 1% BSA diluted in PB for 30 min and then immunolabeled, using either rabbit antiserum directed against the SUN domain-containing protein 2 (SUN2) (1:50, #PA5-51539, Thermo Fisher Scientific), which labels the inner nuclear membrane (INM), or mouse monoclonal CD9 Ab (clone 5H9, see above), to label the cell membrane for 60 min. In some experiments, cells were not permeabilized. All steps were performed at RT. Afterward, cells were washed twice with PBS and incubated with Alexa Fluor[®]647-conjugated goat anti-rabbit IgG (1:1000, #A-21246) or Alexa Fluor[®]488-conjugated goat anti-mouse IgG (1:1000, #A11017), both from Thermo Fisher Scientific, for 30 min. The washing step was repeated prior to observation. Primary and secondary Abs were diluted either in PB containing 1% BSA or, in the case of non-permeabilized immunolabeling, in PBS with 1% BSA. To assess membrane rounding and blebbing, PFA-fixed cells were instead stained with Alexa Fluor488[®]-conjugated Phalloidin (#A12379, Thermo Fisher Scientific) for 40 min to label actin. Nuclei were counterstained with DAPI. Images were acquired by confocal laser scanning microscopy (CLSM) using the Nanoimager S Mark II system (Oxford Nanoimaging (ONI), Oxford, UK) with 100× oil-immersion objective under constant microscope settings. A total of 20 x-y optical sections of 0.45 μm thickness were acquired for each cell of interest. Raw images were processed using Fiji. To measure GFP fluorescence derived from endocytosed CD9-GFP⁺ SW620 cell-derived EVs in the cytoplasm, regions of interest (ROIs), excluding the DAPI-stained nucleus, were drawn around the plasma membrane using corresponding bright-field images (not shown) as a guide. Total cell fluorescence was then determined using the “measure” function in Fiji across all optical sections. To count nuclear fluorescent materials, each optical section through the cell was assessed individually by drawing ROIs around the SUN2-labeled nuclear membrane. An auto threshold was then applied and, using the “analyze particle” function in Fiji, signals showing greater than 8 pixel counts were considered as positive and the results from all sections were combined.

2.9. Stochastic Optical Reconstruction Microscopy

Direct stochastic optical reconstruction microscopy (dSTORM) was applied on EVs derived from SW480, SW620, and CD9-GFP⁺ SW620 cells. EVs were immunolabeled and imaged using the EasyVisi Single-Extracellular Vesicle Characterization kit from ONI (beta v1.0, Oxford Nanoimaging, UK) as described previously [57]. Briefly, EVs (3.5×10^7 particles) were incubated overnight at 4 °C with the fluorescently labeled Abs: CD9-Atto488, CD63-Cy3B, and CD81-AlexaFluor[®]647. Labeled EVs were then immobilized on microfluidic chips coated with PEG-Biotin. All preparations were performed on a Roboflow automated system platform (ONI). Freshly prepared BCubed STORM-imaging buffer was added prior to image acquisition. Labeled proteins were imaged sequentially at 45%, 50%, and 50% power for the 647, 561, and 488 nm lasers, respectively, at 2000 frames per channel with the angle of illumination set to 52.5°. Prior to the start of the imaging session, channel mapping was calibrated using 0.1 μm TetraSpeck beads (#T7279, Thermo Fisher Scientific). Data were processed on NimOS software (v1.18, ONI, Oxford, UK). Note that under these conditions, GFP fluorescence is not detected (data not shown). To identify subpopulations of EVs that express one, two, or three markers, images were analyzed using ONI’s online platform called CODI (<https://alto.codi.bio/>, release versions 0.20 to 0.24; July to October 2021, accessed on 21 September 2021). Density-based clustering analysis with drift correction was then performed to evaluate each vesicle.

2.10. Flow Cytometry

To determine the number of cell surface CD9 molecules, the Quantum[™] Simply Cellular[®] (QSC) anti-mouse IgG kit (#815, Bangs Laboratories Inc., Fishers, IN, USA) was

utilized. SW480 and SW620 cells (1×10^5) and 4 microsphere populations containing increasing levels of Fc-specific capture Ab were incubated with FITC-conjugated anti-CD9 Ab (clone eBioSN4, 1:20, #11-0098-42, Thermo Fisher Scientific) in PBS containing 0.5% BSA for 30 min on ice. Both cells and microspheres were then analyzed by the CytoFlex flow cytometer (Beckman Coulter, Indianapolis, IN, USA) using the same detector gain for all samples. A standard curve was generated using the median channel values of the microspheres, and the amount of CD9 molecules per cell was determined from this curve. All calculations were performed using the QuickCal[®] program (v2.3, www.bangslabs.com, accessed on 13 October 2021).

2.11. Cell Migration

Scratch wound healing assay—Cell migration was evaluated by a scratch wound healing assay. Briefly, SW480 cells were seeded at a concentration of 2×10^5 cells/well in 12-well standard cell culture plates (#83.3921, Sarstedt Inc., Nümbrecht, Germany) and, after reaching 100% confluence, a scratch was introduced on the cell monolayer with a sterile pipet tip. The detached cells were washed with PBS. Cells and/or SW620 cell-derived EVs were then pre-incubated for 30 min with CD9 Fab or divalent CD9 Ab at various concentrations (6.25, 12.5, and 25 $\mu\text{g}/\text{mL}$) according to protocols #1 to #3. Afterward, cells and EVs were co-incubated for 5 h. In all conditions, Abs were not removed during cell–EV incubation. As positive control, cells were exposed to EVs without incubation with Ab. Images of scratch wounds were captured using an inverted Olympus IX70 microscope (Olympus Italia S.r.l, Segrate, Italy) before (0 h) and after (5 h) the addition of EVs. Wound areas were measured by ImageJ software [58]. The wound area at 0 h was considered as baseline (100%). The wound healing assays were performed at least five times for each condition.

Transwell filter assay—SW480 or SW620 cells were grown to 80% confluency then serum starved for 24 h in DMEM-F12 cell medium (#12634010, Thermo Fisher Scientific) supplemented with 0.5% FBS at 37 °C. The migration assay was performed using 8 μm pore size 24-well Transwell plates (#3464, Corning Inc.). Briefly, the lower chamber was filled with 800 μL of cell medium as described above, followed by the addition of starved 1×10^5 cells in 200 μL medium to the upper chamber. For SW480 cells, they were allowed to attach for 3 h prior to incubation with 25 $\mu\text{g}/\text{mL}$ CD9 Fab or divalent CD9 Ab for 30 min at 37 °C. Concurrently, SW620-derived EVs (1×10^9 particles) were incubated with the same concentration of Abs for 30 min at 4 °C according to protocol #1, then co-incubated with the cells for 24 h at 37 °C. As controls, either EVs or Abs were omitted or cell medium contained 10% FBS (data not shown). In experiments involving SW620 cells, the same procedure was performed as above without the addition of EVs. After the 24 h incubation, the number of migrated cells was evaluated as previously described with minor modifications [59]. Briefly, cells on the upper chamber were carefully removed using cotton swabs, and the migrated cells adhered to the bottom side of the microporous membrane, as well as those in the lower chamber, were detached by trypsinization. Cells were collected, pelleted by centrifugation, and resuspended in the residual medium. The number of invasive cells was determined by automated counting using the TC20 automated cell counter (Bio-Rad).

2.12. Statistical Analysis

All experiments were performed at least in triplicate. Data are presented as the mean \pm standard deviation (S.D.). Statistical analysis was determined using a two-tailed Student's *t*-test, and *p* values < 0.05 were considered significant. All graphs were created using GraphPad Prism 8 (v8.4.3, Dotmatics, Boston, MA, USA).

3. Results

To investigate whether a monovalent Fab generated from mouse monoclonal CD9 Ab (clone 5H9) directed to human CD9 [49,50] impedes EV-mediated morphological transformation of colon cancer cells, we used the established model of non-metastatic SW480 and

highly metastatic SW620 cells [52,53]. One of our laboratories has previously shown that morphological traits of SW620 cells can be transferred to SW480 cells via EVs [10,52,53]. Labeling of these cells with CD9 Ab confirmed their distinct morphologies; SW480 cells are flat with a spread mesenchymal-like shape and tend to form multicellular clusters, whereas SW620 cells are rounded and have numerous membrane blebs reminiscent of an amoeboid phenotype (Figure 1A). In both cell lines, CD9 antigen is present on the cell surface and in the cytoplasmic compartment (Figure 1A). The number of cell surface CD9 molecules per cell was quantified by flow cytometry after labeling with fluorochrome-conjugated anti-CD9 Ab (clone eBioSN4, see Section 2), while the total amount of CD9 was quantified by immunoblotting (Figure 1B,C). Both approaches revealed that CD9 protein is significantly more expressed in SW480 compared to SW620 cells. These observations are in agreement with the previously reported CD9 transcript level for these cells [60]. These data suggest, albeit indirectly, that CD9 per se is not responsible for the morphological difference between SW480 and SW620 cells, although some level of its expression may regulate the function of its interacting partners [10,52,53].

To monitor EV-mediated cell transformation, we engineered SW620 cells to express the CD9-GFP protein that would produce fluorescent EVs (Figure 1D,E). As observed by GFP fluorescence, CD9 overexpression did not alter the morphology of SW620 cells, with their rounded appearance and membrane blebs remaining present (Figure 1D).

3.1. Characterization of EVs Released by SW620 Cells

Next, for comparison, we characterized the EVs released by SW620 cells as well as those produced by CD9-GFP⁺ SW620 and SW480 cells. The EVs were enriched from the conditioned media by differential ultracentrifugation (for technical detail, see Section 2). First, we measured their size by NTA. The EVs derived from the SW620, CD9-GFP⁺ SW620, and SW480 cell lines showed a similar diameter of 148 ± 1.9 , 157 ± 9.4 , and 144 ± 2.5 nm (mean \pm S.D., $n = 3$ independent measurements), respectively (Figure 2A, pink area). Interestingly, large EVs with a size of 350–500 nm were preferentially observed in those produced by SW480 cells (Figure 2A, grey area). Second, the expression of bona fide EV markers was determined by immunoblotting in EVs released by SW620 cells. The tetraspanin membrane proteins CD9, CD63, CD81, and cytoplasmic ALIX were detected therein (Figure 2B). Alix was demonstrated to be involved in the sorting of tetraspanins to exosomes [61]. As expected, the ER-associated calnexin was absent (Figure 2B). These data are in agreement with our previous studies, as well as studies by others [57,62–64]. The overexpression of CD9-GFP did not influence the presence or absence of these proteins in SW620 cell-derived EVs (Figure 2C). Third, the distribution of tetraspanins among the EVs was determined at super-resolution using dSTORM (Figure 2D). Analysis of small EVs (<200 nm in diameter) revealed the heterogeneity of the EV population with a variable distribution of single, double, and triple positives (Figure 2E and Supplementary Figure S2A), in agreement with previous studies [57,65]. Triple-positive EVs (CD9, CD63, and CD81) constituted the major population (>70%) of EVs. They could correspond to exosomes arising from LE/MVB fusion with the plasma membrane [34]. Single-positive EVs represented minor or negligible fractions among the EV subpopulation, irrespective of the CD marker. Of note, overexpression of CD9-GFP in SW620 cells slightly reduced the amount of CD63⁺CD81⁺ EVs with a concomitant increase in triple-positives. In SW620 cells, CD63⁺CD81⁺ EVs constituted about $17 \pm 10\%$ of total EVs. These EVs cannot be targeted by anti-CD9 Ab. In contrast, single CD9⁺ EVs are highly enriched in large EVs (350–500 nm in diameter) and represent the major fraction (>80%) (Supplementary Figure S2B,C). They could correspond to microvesicles/ectosomes derived directly from the plasma membrane. Double- or single-positive CD63 and CD81 were not detected. Thus, all large EVs contain CD9. Overall, the complexity of EV subtypes (exosomes versus microvesicles) and their subpopulations, as monitored at an individual level, indicates that CD9⁺ EVs account for the majority of EVs.

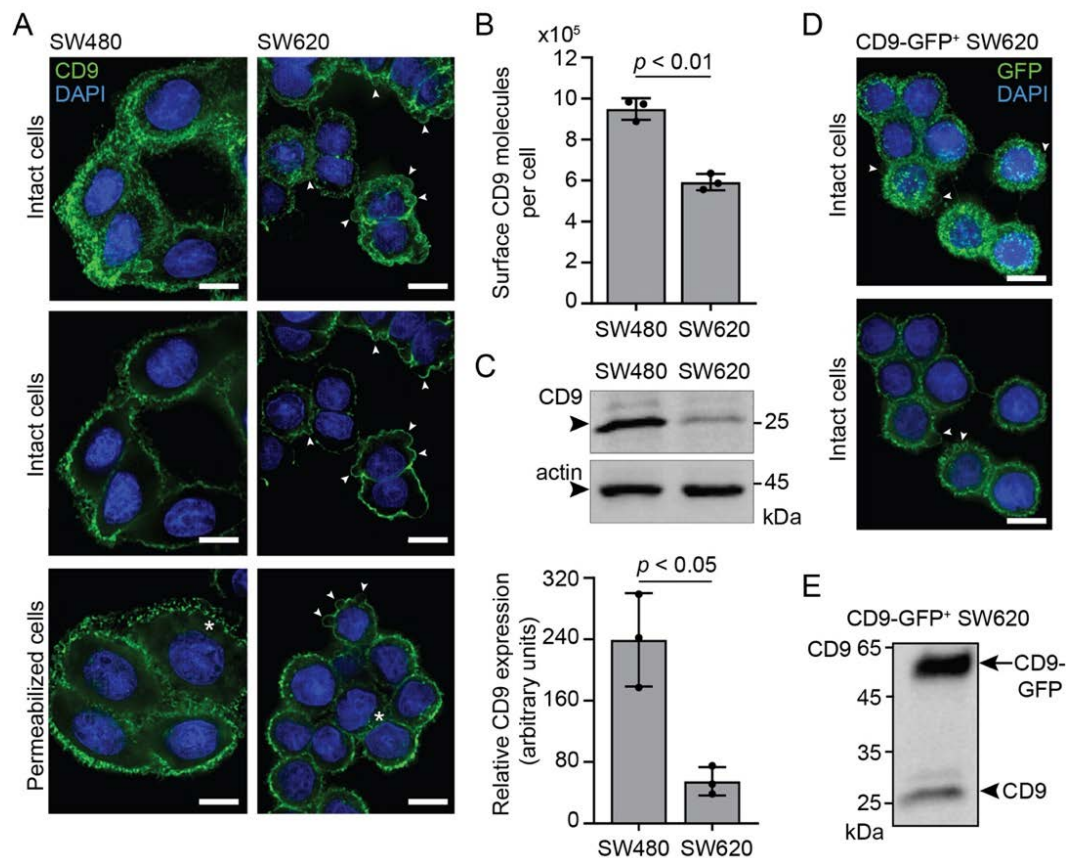


Figure 1. CD9 expression in SW480 and SW620 cells. **(A)** CD9 expression was investigated by indirect immunofluorescence labeling using anti-CD9 5H9 Abs on either intact or permeabilized SW480 and SW620 cells cultured on poly-D-lysine-coated dishes. Nuclei were stained with DAPI and samples were observed by CLSM. Composite images (top panels) or single x-y sections (middle and bottom panels) are shown. Arrowheads indicate membrane blebs, while asterisks mark cytoplasmic CD9 immunoreactivity. **(B)** The amount of surface CD9 antigens per cell detected with FITC-conjugated eBioSN4 Abs was estimated using a flow cytometer calibrated with fluorescent microparticles. **(C)** Total CD9 antigens were analyzed by immunoblotting (top panel) using 5H9 Abs and quantified (bottom panel). The samples were normalized to β -actin. Molecular mass markers (kDa) are indicated. Arrowhead indicates the protein of interest. **(D,E)** SW620 cells stably transfected with CD9-GFP were analyzed either by fluorescence microscopy without permeabilization **(D)** or immunoblotting **(E)**. For the microscopy, nuclei were stained with DAPI and samples were observed by CLSM. A composite image (top panel) or a single x-y section (bottom panel) is displayed. Arrowheads indicate membrane blebs. For immunoblotting, the membrane was probed with 5H9 Abs. The arrow and arrowhead indicate the CD9-GFP fusion protein and the endogenous CD9, respectively. Means \pm S.D. and individual values for each experiment are shown ($n = 3$). p values are indicated. Scale bars, 10 μ m.

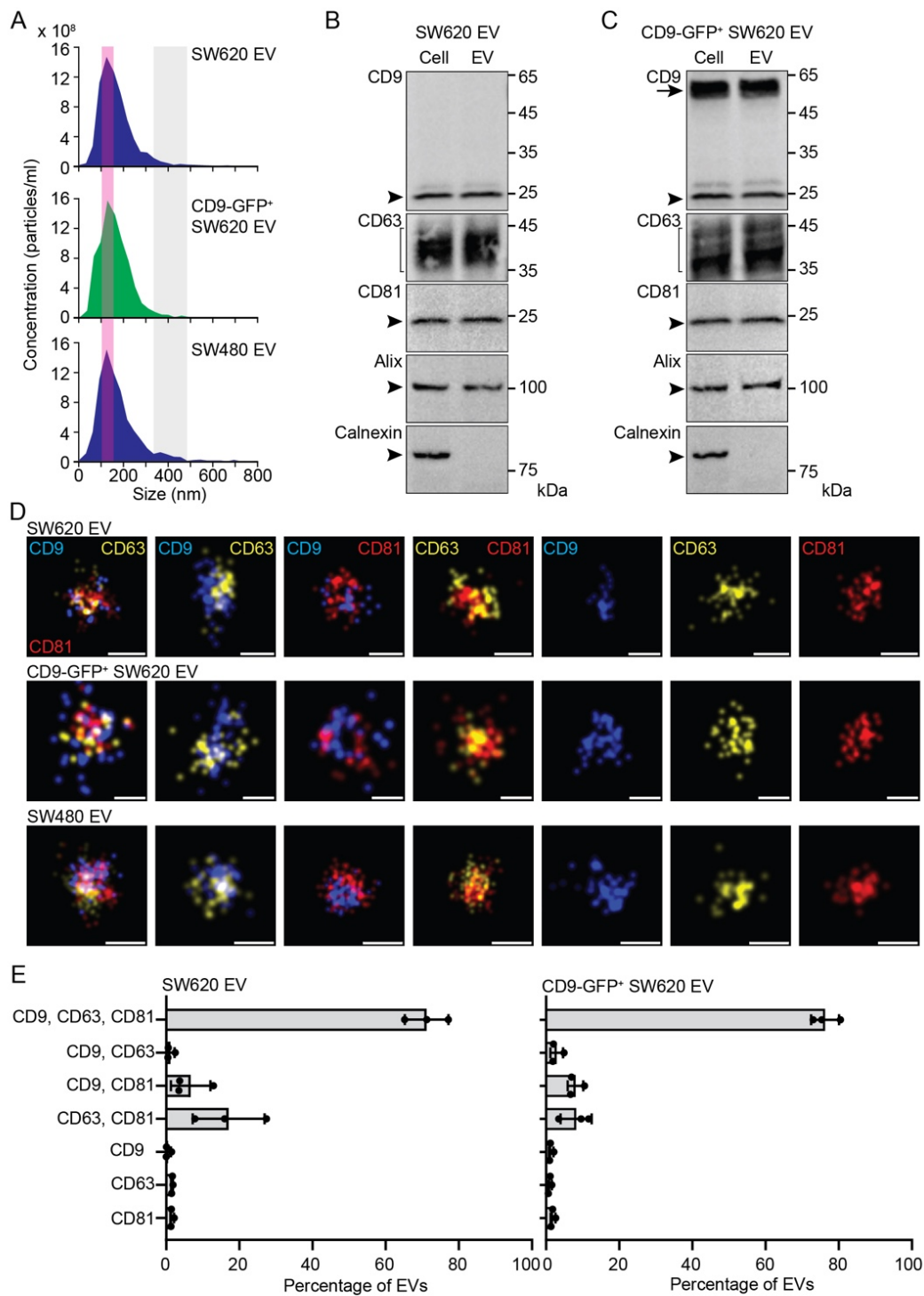


Figure 2. Characterization of EVs released by SW620, CD9-GFP+ SW620, and SW480 cells. (A–E) EVs were recovered from the conditioned media of SW620, CD9-GFP+ SW620, and SW480 cells by differential centrifugation, and the resulting $200,000\times g$ pellets were analyzed by the ZetaView particle analyzer (A), immunoblotting (B,C), and dSTORM (D,E). The concentration and size of EVs derived from the indicated cells are shown (A). Note the presence of a common population of small particles (<200 nm) with a peak at 100–150 nm (pink area), and larger ones (350–500 nm, gray areas) enriched in SW480 samples. EVs, and for comparison the cells from which they were derived, were probed by immunoblotting for CD9, CD63, CD81, Alix, and Calnexin (B,C). Arrowheads and brackets indicate the endogenous proteins of interest, while the arrow points to the CD9-GFP fusion protein. Molecular

mass markers (kDa) are indicated. EVs were imaged after immunolabeling of three tetraspanins using dSTORM (D). The proteins of interest (CD9, CD63, and CD81) were pseudo-colored as indicated. Small single-, double-, and triple-positive EVs were shown (D) and quantified (E). Means \pm S.D. and individual values for the three experiments are shown ($n > 5000$ EVs per experiment). Note that small and large EVs derived from SW480 cells were also quantified (Supplementary Figure S2). Scale bars, 50 nm.

3.2. Internalization of SW620 Cell-Derived CD9-GFP⁺ EVs into SW480 Cells: Impact of CD9 Ab

By applying fluorescent EVs released by CD9-GFP⁺ SW620 cells to recipient SW480 cells for a period of 5 h, we observed, after cell fixation and DAPI staining, the internalization of CD9-GFP, as detected by green fluorescence in the cytoplasmic compartment (Figure 3A, control). To assess the impact of anti-CD9 Abs on EV internalization, we pre-incubated both cells and EVs with either monovalent CD9 Fab or divalent Ab (25 μ g/mL) for 30 min and then co-incubated them for 5 h in the presence of Abs. This is the first of three protocols (#1-3) used in this study, which are summarized in Supplementary Figure S1 (see below and Section 2). Interestingly, application of CD9 Fab, but not CD9 Ab, reduced the amount of GFP in the cytoplasmic compartment as observed by CLSM (Figure 3A, CD9 Fab). Through a series of x-y optical sections covering the entire cell of interest, quantification revealed a significant decrease in cytoplasmic GFP fluorescence in CD9 Fab-treated cells, whereas an increase occurred in those incubated with CD9 Ab (Figure 3B). The effect of CD9 Fab depends on the concentration used (Figure 3B).

We recently demonstrated that EV-associated CD9 can reach the nucleus after EV internalization and their endocytic transport, where EV-containing late endosomes enter the type II nuclear envelope invaginations of the nucleoplasmic reticulum [37] (reviewed in Ref. [14]). The latter process involved a protein complex (named VOR) formed by vesicle-associated membrane protein (VAMP)-associated protein A (VAP-A), which is localized at the outer nuclear membrane, oxysterol-binding protein (OSBP)-related protein-3 (ORP3), and endosomal Rab7 [66]. Their interactions can be inhibited by a novel chemical drug, PRR851, which blocks Rab7 binding to VAP-A-ORP3 and thereby prevents nuclear transfer of the EV-associated protein [57]. To visualize the nuclear transfer of the EV cargo and the impact of CD9 Abs on it, upon 5 h incubation with CD9-GFP⁺ EVs, SW480 cells were fixed, immunolabelled for SUN2 to highlight the inner nuclear membrane, and analyzed by CLSM. In each x-y optical section, the nuclear CD9-GFP appeared as discrete punctate signals (Figure 3C), in which we set a threshold level above eight pixels to exclude (auto)fluorescent signals (see Section 2, Supplementary Figure S3A). Analysis of the 20 sections covering the entire nuclear compartment revealed a reduction in nuclear CD9-GFP in cells and EVs treated with CD9 Fab (Figure 3C and Supplementary Figure S3B). This effect did not seem to occur with those incubated with CD9 Ab. Quantification of these cells confirmed these observations (Figure 3D). Although significant, the CD9 Fab-mediated reduction in nuclear transfer of CD9-GFP appeared moderate compared to EV internalization (compare Figure 3B versus Figure 3D, CD9 Fab). Indeed, fold change analysis indicates that CD9 Fab had more impact on the initial internalization of CD9-GFP than on its nuclear transfer (Supplementary Figure S3C). In contrast, the addition of PRR851, alone or in combination with CD9 Fab, abolished the nuclear transfer of CD9-GFP (Supplementary Figure S3D). This observation suggests that intracellular transport of EV-associated proteins from the plasma membrane to the nucleoplasm of recipient cells via the endocytic compartment is highly efficient (see Section 4).

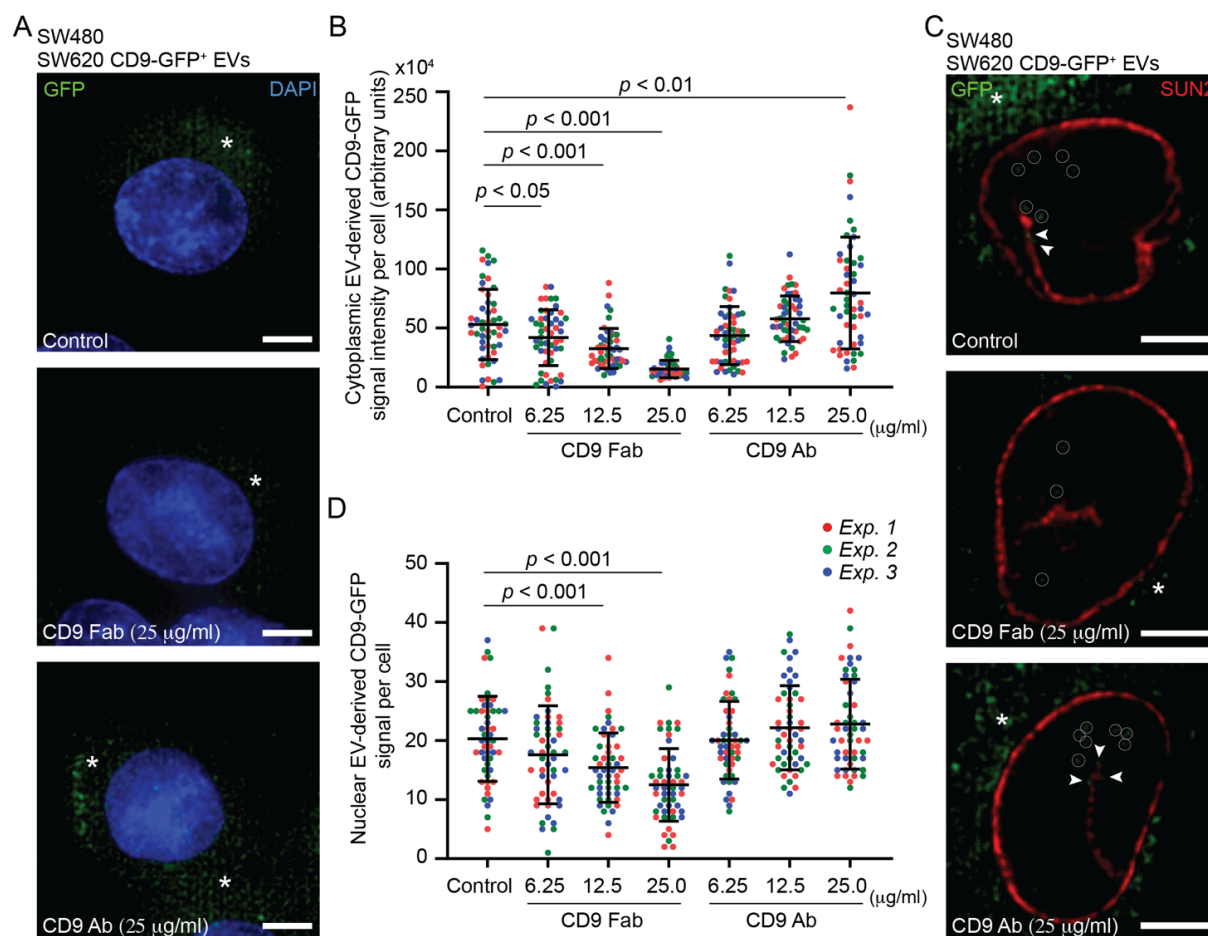


Figure 3. Effects of CD9 Fab and divalent Abs on the internalization of SW620 cell-derived CD9-GFP⁺ EVs into SW480 cells. (A–D) SW480 cells and fluorescent EVs derived from CD9-GFP⁺ SW620 cells (1×10^9 particles) were individually pre-incubated for 30 min without (control) or with different concentrations of anti-CD9 Fab or divalent Ab as indicated before their co-incubation for 5 h in the absence or presence of Abs (protocol #1). Fixed cells were either stained with DAPI (A,B) or immunolabeled for SUN2 (C,D) before observation by CLSM. Note the presence of discrete punctate GFP signals in the cytoplasmic (A,C) or nucleoplasmic (C) compartments (asterisk and circle, respectively). Their intensity (B) or amount (D) was quantified using serial optical sections through a cell (see Supplementary Figure S3). Means \pm S.D. of individual signals from three independent experiments, as indicated by color coding, are shown ($n > 15$ cells per experiment). p values are indicated. Arrowheads indicate CD9-GFP signals in the nuclear envelope invagination (C). Scale bars, 5 µm.

3.3. Pro-Metastatic Morphological Alterations of SW480 Cells by SW620 Cell-Derived EVs Are Blocked by CD9 Fab

To assess whether CD9 Fab negatively interfered with the pro-metastatic morphological alterations of SW480 cells induced by SW620 cell-derived EVs, we co-incubated them in the presence or absence of Abs using three distinct protocols (Supplementary Figure S1) and then determined their phenotypic modification, i.e., cell rounding and induction of membrane blebs. In the first set of experiments, following protocol #1, both cells and EVs were pre-incubated with either monovalent CD9 Fab or divalent Ab (25 µg/mL) for 30 min. Cells and EVs were then co-incubated for a period of 5 h. SW480 cell morphology was determined by fixing and staining them with fluorochrome-conjugated phalloidin and DAPI to label actin filaments [67] and nuclei, respectively, prior to CLSM analysis. As negative and positive controls, we used SW480 cells and those incubated with SW620 cell-derived

EVs, respectively. In the latter, we observed cellular transformation with the appearance of rounded cells and membrane blebbing (Figure 4A). Quantification revealed that both phenotypes were infrequently detected in those not incubated with EVs (Figure 4B,C, respectively). The addition of CD9 Fab (25 µg/mL) significantly reduced EV-mediated cell transformation, a phenomenon also observed at lower concentrations (Figure 4A–C). In contrast, the divalent CD9 Ab did not interfere with such processes (Figure 4A–C). Similar results were obtained when co-incubation of cells and EVs was increased to 16 h (Supplementary Figure S4).

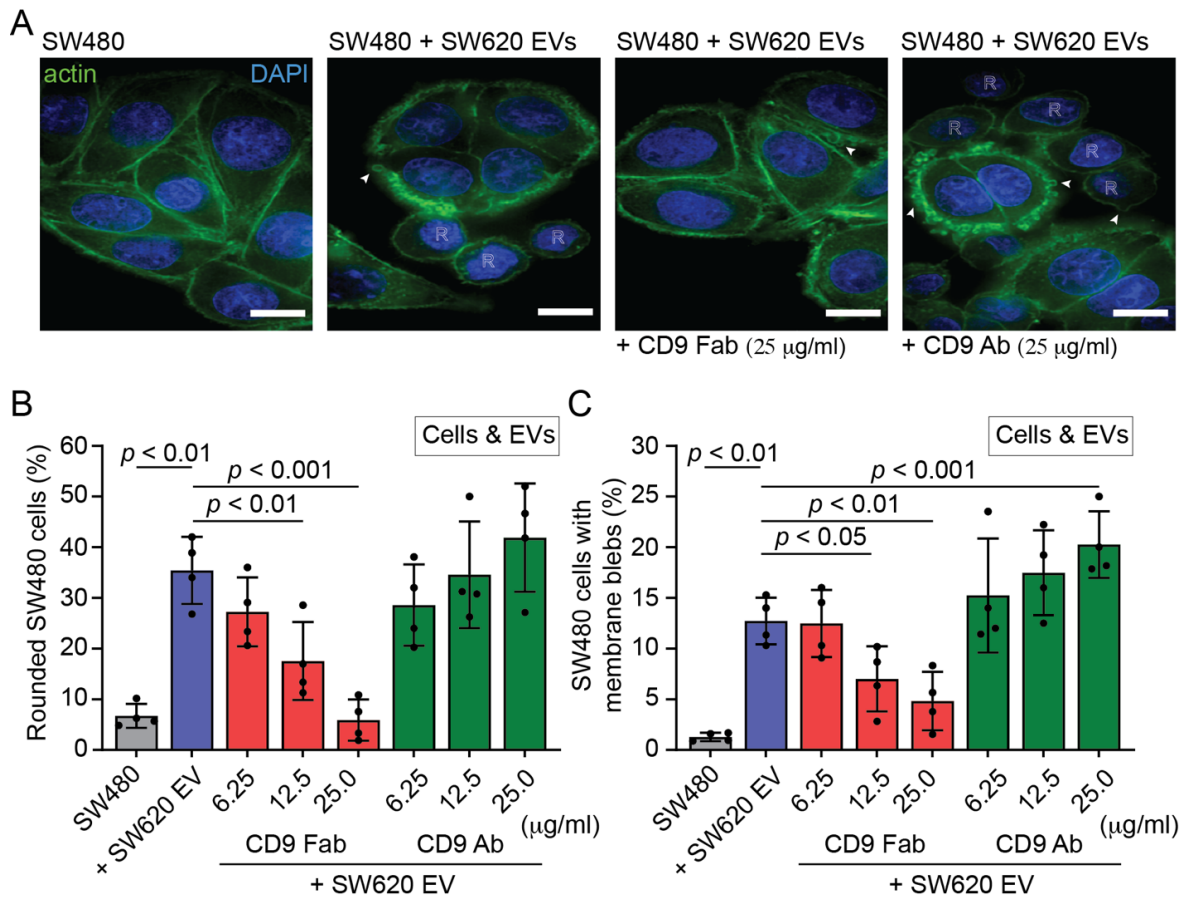


Figure 4. Effects of CD9 Fab and divalent Ab on the pro-metastatic morphological alterations of SW480 cells exposed to SW620 cell-derived EVs. (A–C) SW480 cells and SW620 cell-derived EVs (1×10^9 particles) were individually pre-incubated for 30 min with different concentrations of anti-CD9 Fab (red) or divalent Ab (green) as indicated before their co-incubation for 5 h in the presence of Abs, as described for protocol #1. As negative and positive controls, cells were not exposed (SW480, grey) or were exposed to EVs in the absence of Ab (+ SW620 EV, blue), respectively. Afterward, fixed cells were stained with DAPI and fluorochrome-conjugated phalloidin to label nuclei and actin filaments, respectively, before observation by CLSM (A). Single sections are presented. Rounded cell morphology and membrane blebs induced by EVs are indicated by the letter R and the arrowheads, respectively. The percentage of cells with rounded morphology (B) or membrane blebs (C) was quantified. Means \pm S.D. and individual values for each experiment are shown ($n = 4$). At least 100 cells were evaluated for each experiment. p values are indicated. Similar experiments were performed by pre-incubating only EVs or cells with Abs (Supplementary Figure S5). Scale bars, 10 µm.

In the second set of experiments, following protocol #2 (Supplementary Figure S1B), only EVs were pre-incubated with monovalent CD9 Fab or divalent Ab for 30 min, then added to cells and co-incubated for 5 h. Again, cell rounding and membrane detachment were both

inhibited by the addition of CD9 Fab but not CD9 Ab (Supplementary Figure S5A), suggesting that saturation of EV-associated CD9 interferes with these EV-mediated processes. Finally, similar data were obtained when only cells were pre-incubated with either monovalent or divalent CD9 Abs, according to protocol #3 (Supplementary Figure S1C), prior to their 5 h co-incubation (Supplementary Figure S5B). Note the presence of CD9 Abs during cell–EV incubation, especially in protocol #3, where free Abs would bind to EVs and could therefore have an impact on the result. To evaluate this, we performed a variant of protocol #3 (#3') where unbound CD9 Abs were removed from the cells after the 30 min pre-incubation and before the addition of EVs (Supplementary Figure S1C). Interestingly, under these conditions, the pre-metastasis morphological alterations of SW480 cells were not significantly impacted by the addition of CD9 Fab (Supplementary Figure S5C), suggesting that the saturation of CD9 present in EVs is essential to interfere with their action.

3.4. SW620 Cell-Derived EV-Induced Migration of SW480 Cells Is Impeded by CD9 Fab

SW620 cells have a more rounded shape and strong plasma membrane blebbing activity (see above Figure 1A,D), which is associated with amoeboid motility [68]. Since these morphological traits can be transferred to SW480 cells via EVs derived from SW620 cells and influence their motility [8–10,51], we evaluated their migration and the impact of CD9 Abs. For this purpose, we used two classical methods: the linear wound healing assay and the Transwell filter assay (see Section 2). First, the wound healing assay, performed for 5 h, revealed that SW620 cell-derived EVs stimulated the motility of SW480 cells (Figure 5A), which is in agreement with our previous study [57]. Interestingly, exposure of cells and EVs or only EVs to CD9 Fab according to protocol #1 or #2, respectively, before their co-incubation for 5 h had a highly negative effect on their migration (Figure 5A,B). In contrast, divalent CD9 Ab either did not prevent this migration or stimulated it, which is consistent with the data regarding morphological alterations (Figure 4 and Supplementary Figure S5A). Pre-incubation of cells with CD9 Fab or CD9 Ab, as described in protocol #3, did not block cell migration (Figure 5C). The latter data contrast with those observed for the impact of CD9 Fab on morphological alterations (protocol #3, Supplementary Figure S5B) but are consistent with those observed when CD9 Abs were removed prior to the addition of EVs (protocol #3', Supplementary Figure S5C), again emphasizing the importance of intercepting EVs with CD9 Fab. In protocol #3, we could not exclude that a fraction of EVs reaches some recipient cells before being neutralized by CD9 Fab, and thus stimulates the cellular transformation impacting their migrations.

Second, we used a Transwell membrane filter with 8 μm pores allowing migration of cells from the upper to the lower chamber (Figure 5D). After attachment of the cells to the membrane, we added SW620 cell-derived EVs and co-incubated them for 24 h. The trans-membrane migrated cells recovered in the lower chamber revealed the stimulation of motility for SW480 cells primed by EVs (Figure 5E). The experiment was then repeated by pre-incubating the cells and EVs with CD9 Fab or CD9 Ab (25 $\mu\text{g}/\text{mL}$) for 30 min before their co-incubation (Figure 5D). In agreement with EV-mediated morphological transformation, addition of CD9 Fab reduced the number of migrating cells, whereas divalent Ab increased it, although not to a statistically significant extent (Figure 5E).

Finally, caution should be considered with these assays, as horizontal CD9 binding to adhesion and/or integrin molecules, as well as certain lipids, can suppress or promote cell–cell and cell–extracellular matrix interactions (and consequently cell motility), as these processes potentially being dependent on the cellular system [69–72] (reviewed in Ref. [33]). This prompted us to evaluate the impact of CD9 Abs on SW620 cell migration. As evaluated with the Transwell filter assay, highly metastatic SW620 cells are migrating more than SW480 cells under the same culture conditions (Figure 5F), as recently reported in [73,74]. Indirectly, these data indicated that CD9 expression levels in SW480 and SW620 cells inversely correlate with migration behavior, suggesting a negative impact of CD9 on cell migration in such SW480/620 cell systems. Interestingly, addition of CD9 Fab to SW620 cells prevented their migration, similar to EV-primed SW480 cells, whereas, unlike the

latter whose migration was partly stimulated by divalent CD9 Ab, this Ab further inhibited SW620 cell migration (Figure 5F). The differential response to divalent CD9 Ab suggests that EV uptake and subsequent cellular transformation of SW480 cells is the primary cause of their migration. Further research is needed to determine whether a certain CD9 threshold impacts SW480/620 cell migration (and their morphology, see above), which is beyond the scope of this study.

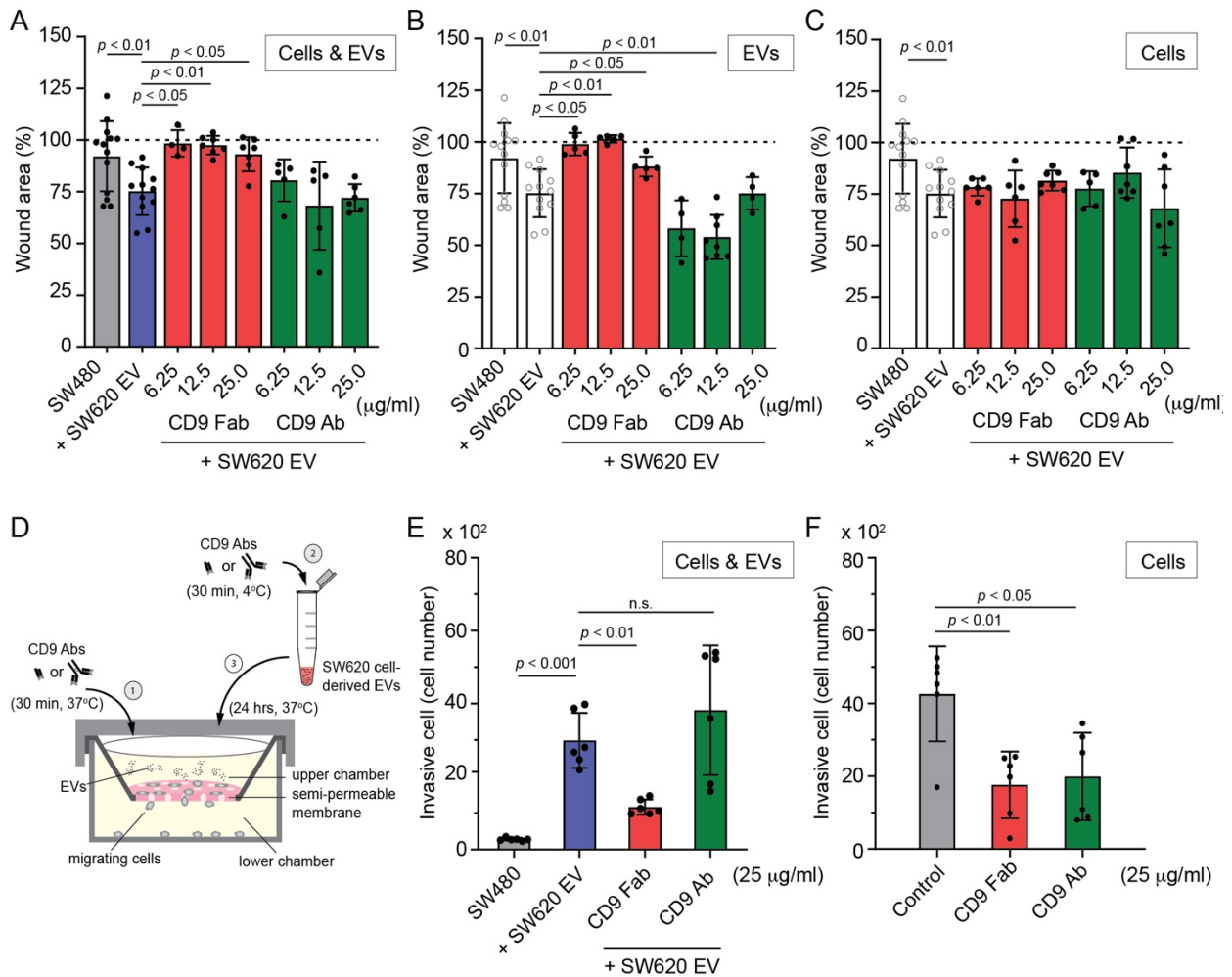


Figure 5. Effects of CD9 Fab and divalent Ab on the migration of SW480 cells exposed to SW620 cell-derived EVs. (A) The migration–wound healing assay was performed by introducing a scratch on confluent SW480 cell monolayers cultured on 12-well standard cell culture plates and incubating them for 5 h in the absence (negative control, grey) or presence (positive control, blue) of SW620 cell-derived EVs (1×10^9 particles/mL). Alternatively, after introducing a scratch on the cell monolayer, cells and EVs were individually pre-incubated for 30 min with different concentrations of anti-CD9 Fab (red) or divalent Ab (green) as indicated before their 5 h co-incubation in the presence of Abs (A). The percentage of remaining wound areas after 5 h was quantified. Baseline (100%, dashed line) refers to wound area at 0 h. (B,C) Solely EVs (B) or cells (C) were pre-incubated for 30 min with Abs prior to co-incubation with cells or EVs for 5 h. Wound area was quantified. Controls (white) are shown for comparison. Means \pm S.D. from multiple scratches are shown ($n = 4$ –13). (D–F) The migration–Transwell filter assay was performed using a Transwell chamber as illustrated (D), where SW480 (E) or SW620 (F) cells were added to the upper chamber. Cells and EVs were pre-treated, as described in panel A, using 25 μ g/mL CD9 Fab or divalent Ab ((D), steps 1 and 2) before 24 h of co-incubation ((D), step 3). In the case of SW620 cells, they were not incubated with EVs (F). The amount of migrating cells recovered in the lower chamber was then quantified. Each individual value is shown. p values are indicated. n.s., not significant.

3.5. CD9 Is Essential for Pro-Metastatic Morphological Alterations of SW480 Cells Mediated by SW620 Cell-Derived EVs

All data described so far suggest that CD9 Fab blocks EV-mediated transfer of morphological traits from SW620 to SW480 cells. However, we do not know whether CD9 per se is involved in this process, particularly in the initial binding of EVs to the surface of SW480 cells. To address this issue, we silenced its expression in SW480 cells using shRNA technology. As shown by immunoblotting (Figure 6A), approximately $91 \pm 2.7\%$ ($n = 3$) of CD9 is reduced in shCD9 cells compared to parental cells. CD9 knockdown did not affect the overall mesenchymal-like spreading morphology of SW480 cells (data not shown), suggesting that CD9 is not the only player involved in this phenotype (see Discussion). We then co-incubated them with SW620 cell-derived EVs for 5 h and determined their morphological alterations. Interestingly, EV-induced rounded morphology and membrane blebbing were prevented in shCD9 cells (Figure 6B,C, respectively), suggesting that cell-associated CD9 is involved in the initial binding of CD9 EVs and/or their internalization and upstream events.

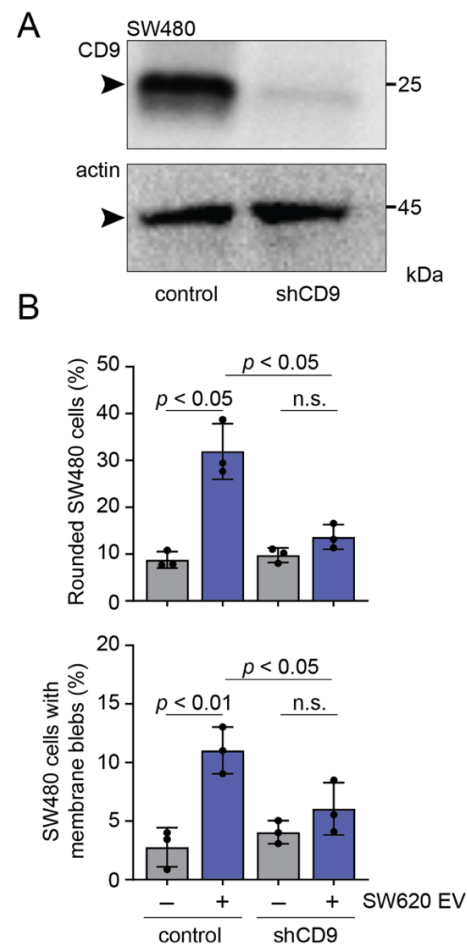


Figure 6. The lack of CD9 in SW480 cells impedes pro-metastatic morphological alterations produced by SW620 cell-derived EVs. **(A)** Parental (control) or CD9-knockdown (shCD9) SW480 cells were analyzed by immunoblotting for CD9 and β -actin. Molecular mass markers (kDa) are indicated. Arrowhead indicates the protein of interest. **(B)** SW480 cells as indicated were incubated with (+) SW620 cell-derived EVs (1×10^9 particles) or without (-) for 5 h. Afterward, fixed cells were stained with DAPI and fluorochrome-conjugated phalloidin to label nuclei and actin filaments, respectively, before observation by CLSM. The percentage of cells with rounded morphology (top panel) or membrane blebs (bottom panel) was quantified. Means \pm S.D. and individual values for each experiment are shown ($n = 3$). At least 100 cells were evaluated for each experiment. p values are indicated. n.s., not significant.

4. Discussion

It is now well recognized that the growth of cancer and its metastases at distinct sites involve not only intrinsic factors, but also extrinsic ones in which EVs secreted either by the cancer cells themselves or by surrounding resident cells, such as mesenchymal stromal cells and fibroblasts, play a role [7,35,75]. This bidirectional intercellular crosstalk contributed to the establishment of tumor microenvironmental niches that favor cancer cells over resident cells. Therefore, the development of therapies that target the intercellular communication and metastasis process may find clinical application (reviewed in Refs [76,77]). In this context, we have recently developed a novel approach, based on human CD9 protein, where a monovalent anti-CD9 Fab intercepts the internalization of CD9⁺ EVs by recipient cells such as mesenchymal stromal cells [50].

Here, we report that CD9 Fab can intercept the internalization of CD9⁺ EVs derived from highly metastatic SW620 colon cells to non-metastatic SW480 cells, thereby blocking their cellular transformation. The presence of CD9 at the surface of recipient cells is also important for promoting EV uptake. Among the pro-metastatic properties transferred by SW620 cell-derived EVs are general alterations in cell structure, e.g., a shift from a mesenchymal-like spreading morphology to an amoeboid shape, which promotes conversion of migration from a mesenchymal to amoeboid mode [10,78]. This change is called the mesenchymal–amoeboid transition, which responds to a change in the cellular microenvironment [79]. As shown by the linear wound healing assay and Transwell filter assay, CD9 Fab prevented increased cell motility of EV-primed SW480 cells or impeded SW620 cell migration. In this context, one of our laboratories has previously shown that EVs derived from SW620 cells are enriched in cytoskeleton-associated proteins as well as RhoA interactors that activate the RhoA/ROCK pathway, which is known to induce amoeboid cell migration [10]. This pathway and possibly others, including those that involve the nuclear transfer of EV content (see below) [57], could explain the morphological transformation of SW480 cells. The Akt/mTOR pathway could also be involved [51].

As demonstrated using CD9-GFP, not only the internalization of EV-derived cargo proteins is blocked by CD9 Fab, but also the fraction of them that is transferred into the nucleoplasm of recipient cells. Nuclear transfer of EV cargo could play a role in the reprogramming of host cells, leading to their transformation. For example, nuclear translocation of epidermal growth factor receptor (EGFR) or androgen receptor (AR) associated with EVs released from prostate cancer cells and taken up by indolent receptor cells (i.e., cells without EGFR/AR) activated distinct signaling pathways in the latter [80]. Similarly, we have shown that the transcriptome of mesenchymal stromal cells is altered after their exposure to EVs derived from melanoma cells [37]. Among the genes whose expression is modified are those involved in the inflammation process. More recently, it has been shown that RNA cargoes of EVs released by *Plasmodium falciparum* reach the nucleoli of recipient cells, i.e., monocytes, revealing new aspects of communication, and perhaps function, between pathogen-derived EVs and their host cells [81]. We showed that the nuclear transfer of EV-associated proteins and nucleic acids involved the VOR protein complex [66], which brings together Rab7⁺ late endosomes containing endocytosed EVs and the outer nuclear membrane, with the former entering and/or stimulating the formation of type II nuclear envelope invaginations [37]. Nuclear transfer can be inhibited by a chemical drug, PRR851, which blocks the formation of the VOR complex, i.e., the binding of VAP-A-ORP3 to Rab7, and thus prevents nuclear transfer of the EV-associated protein [57]. Application of PRR851 to SW480 cells before and during their incubation with SW620 cell-derived CD9-GFP⁺ EVs severely impaired the nuclear localization of the fusion protein to a greater extent than that of CD9 Fab alone. Given that PRR851 also blocked the SW620 cell-derived EVs mediated transformation of SW480 cells [57] without impacting the internalization of EVs [57] (this study), the modest reduction in the nuclear transfer of EV cargoes observed with CD9 Fab nevertheless contributed, along with perhaps other factors mentioned above, to the membrane rounding and blebbing phenotypes. This partial inhibition of the nuclear translocation of EV cargoes by Fab CD9 is also interesting despite the significant inhibition

of EV internalization at the plasma membrane, suggesting that endocytic transport of the minute fraction of internalized EVs is highly efficient. Loading of late endosomes with EV cargo could facilitate their transport to perinuclear areas and translocation into nuclear envelope invaginations. More investigations are needed to further dissect the mechanisms underlying the transport of EV-loaded endosomes en route to nuclear compartment. By reducing the amount of internalized EVs, CD9 Fab may facilitate such studies.

How does CD9 stimulate cellular internalization of EVs? Although the lateral interactions of CD9 with itself, other tetraspanins, or other membrane proteins forming tetraspanin-enriched microdomains are well described [82], little is known about its potential trans-interaction, i.e., involving CD9 molecules in opposite membranes. However, it has been described that CD9 promotes the clustering of adhesive proteins at the plasma membrane of T cells, antigen-presenting cells, or endothelial cells, e.g., integrin lymphocyte function-associated antigen 1 (LFA-1) and its ligands (intercellular adhesion molecule 1 (ICAM-1) and ICAM-3), and that these regulate cellular interactions at the level of immune synapses [83] or firm adhesion and transendothelial migration of leukocytes [84,85] (reviewed in Ref. [31]). Similarly, CD9 increases cell adhesion mediated by the activated leukocyte cell adhesion molecule (ALCAM, CD166) [86]. In such a context, CD9 Fab could interfere with CD9-mediated clustering of adhesive proteins. It remains to be determined whether CD9–CD9 trans-interaction occurs, as suggested but not proven by divalent CD9 Ab and the impact of CD9 Fab on it. Silencing CD9 in recipient SW480 cells highlighted the implication of this tetraspanin in the cellular internalization of EVs and upstream cellular transformation events. In our previous study, using melanoma or breast cancer cells, we showed that CD9 depletion in EVs also interfered with their cellular uptake [37], indicating that CD9 in both recipient cells and EVs is involved in this process. The lack of major morpho-phenotypic change in SW480 cells depleted of CD9 will deserve additional investigation as upregulation of other tetraspanin proteins might contribute to the overall organization of the plasma membrane, as well as cellular adhesion, allowing the maintenance of their mesenchymal-like morphology in the absence of CD9. In a similar context, an upregulation of CD81 was observed in breast cancer cells upon silencing CD9 [87]. Likewise, the CD9 overexpression, as shown with CD9-GFP in SW620 cells, revealed that other players are essential in establishing a mesenchymal-like morphology. Further studies to examine the impact of CD9 Fab on cell invasion using three-dimensional cultures and/or mouse xenograft models are also needed in the future. This is particularly true for assessing the amount of monovalent Abs and the frequency of injection that would block intercellular communication mediated by cancer cell-derived EVs. In vivo, CD9⁺ EVs released by other cell types, albeit to a lesser extent, can technically neutralize CD9 Fab.

Caution should be taken when targeting CD9 as it may also play a tumor suppressor role in certain cancers and blocking its activity may stimulate cancer progression [88–91] (reviewed in Ref. [33]). For instance, the examination of surgical tumor samples from patients with colon carcinoma indicated that CD9 was strongly expressed at the primary cells compared to those at metastatic sites in colon carcinoma [60]. This differential expression of CD9 correlated with their invasive properties, in which the divalent CD9 Ab interfered. In our cell system and assays, the situation was more complex when divalent CD9 Ab was used because it either stimulated (although not significantly) or reduced migration as observed for EV-primed SW480 and SW620 cells, respectively, and did not block EV uptake by SW480 cells, but rather enhanced it. This last observation reinforces the principle of not using divalent CD9 Ab for therapeutic purposes (see Section 1). By interacting with various partners, the negative or positive effects of CD9 on cancer cells could depend not only on its own expression level, but also on its binding proteins. In addition, we must consider that CD9 may be involved simultaneously or sequentially in various cellular events (e.g., EV uptake, membrane organization, migration). Thus, interfering with or stimulating its sequestration may favor one function over another. Additional studies are needed to dissect the complete CD9 interactome and determine how the threshold of CD9 (or other tetraspanins and interacting partner proteins) influences cellular transformation and migration processes.

Collectively, we demonstrated that CD9 associated with EVs derived from donor colon cancer cells and present in recipient cells is involved in EV uptake leading to morphological transformation of recipient cells, including the acquisition of aggressive migratory behavior, and that a monovalent Ab directed against this tetraspanin protein can impede its function. Intercepting EV-mediated intercellular communication in the tumor niches (i.e., primary and secondary sites) with an anti-CD9 Fab, combined with direct targeting of cancer cells, could lead to the development of new anti-cancer therapeutic strategies.

5. Patents

The United Kingdom patent application GB1814065.7 and United States provisional patents US62724183/US17271690 as well as PTC/EPO applications IB2019/057294/EP19783649.7 are pending. The authors declare no other competing interests.

Supplementary Materials: The following supporting information can be downloaded at: <https://www.mdpi.com/article/10.3390/cells11162474/s1>, Figure S1. Schematic representation of the three main protocols used to study the impact of SW620 cell-derived on SW480 cells; Figure S2. Characterization of small and large EVs released by SW480 cells; Figure S3. Quantification of EV-derived CD9-GFP signals in the nucleoplasm of recipient SW480 cells; Figure S4. Effects of CD9 Fab and divalent Ab on the pro-metastatic morphological alterations of SW480 cells exposed to SW620 cell-derived EVs; Figure S5. Effects of different concentrations of CD9 Fab and divalent Ab on the pro-metastatic morphological alterations of SW480 cells exposed to SW620 cell-derived EVs.

Author Contributions: Investigation, M.F.S., S.F., F.A., D.T., Z.L. and M.P.; data analysis and curation, M.F.S., G.R., S.F., J.K., F.A., D.C. and A.L.; resources, R.A., C.M. and A.L.; conceptualization, D.C. and A.L.; writing—original draft preparation, D.C. and A.L.; project administration; funding acquisition, A.L. and G.R. All authors have read and agreed to the published version of the manuscript.

Funding: This research was funded by NIH grant R15CA252990 to A.L. and G.R.

Institutional Review Board Statement: Not applicable.

Informed Consent Statement: Not applicable.

Data Availability Statement: The raw data supporting the conclusions of this article will be made available by the authors, without undue reservation.

Acknowledgments: The authors thank Emmett Findlay, Wolfgang Gilliar, and Andrew Priest for their constant support and encouragement. We thank the two anonymous reviewers for their comments and suggestions.

Conflicts of Interest: The authors declare no conflict of interest. The funders had no role in the design of the study; in the collection, analyses, or interpretation of data; in the writing of the manuscript; or in the decision to publish the results.

References

1. Zhao, K.; Wang, Z.; Hackert, T.; Pitzer, C.; Zöller, M. Tspan8 and Tspan8/CD151 knockout mice unravel the contribution of tumor and host exosomes to tumor progression. *J. Exp. Clin. Cancer Res.* **2018**, *37*, 312. [[CrossRef](#)] [[PubMed](#)]
2. Raposo, G.; Stoorvogel, W. Extracellular vesicles: Exosomes, microvesicles, and friends. *J. Cell Biol.* **2013**, *200*, 373–383. [[CrossRef](#)] [[PubMed](#)]
3. van Niel, G.; D'Angelo, G.; Raposo, G. Shedding light on the cell biology of extracellular vesicles. *Nat. Rev. Mol. Cell Biol.* **2018**, *19*, 213–228. [[CrossRef](#)] [[PubMed](#)]
4. Cocucci, E.; Racchetti, G.; Meldolesi, J. Shedding microvesicles: Artefacts no more. *Trends Cell Biol.* **2009**, *19*, 43–51. [[CrossRef](#)]
5. Bobrie, A.; Colombo, M.; Raposo, G.; Théry, C. Exosome secretion: Molecular mechanisms and roles in immune responses. *Traffic* **2011**, *12*, 1659–1668. [[CrossRef](#)]
6. Piper, R.C.; Katzmann, D.J. Biogenesis and function of multivesicular bodies. *Annu. Rev. Cell Dev. Biol.* **2007**, *23*, 519–547. [[CrossRef](#)] [[PubMed](#)]
7. Hoshino, A.; Costa-Silva, B.; Shen, T.L.; Rodrigues, G.; Hashimoto, A.; Tesic Mark, M.; Molina, H.; Kohsaka, S.; Di Giannatale, A.; Ceder, S.; et al. Tumour exosome integrins determine organotropic metastasis. *Nature* **2015**, *527*, 329–335. [[CrossRef](#)]
8. Ratajczak, J.; Wysoczynski, M.; Hayek, F.; Janowska-Wieczorek, A.; Ratajczak, M.Z. Membrane-derived microvesicles: Important and underappreciated mediators of cell-to-cell communication. *Leukemia* **2006**, *20*, 1487–1495. [[CrossRef](#)]

9. Valadi, H.; Ekström, K.; Bossios, A.; Sjöstrand, M.; Lee, J.J.; Lötval, J.O. Exosome-mediated transfer of mRNAs and microRNAs is a novel mechanism of genetic exchange between cells. *Nat. Cell Biol.* **2007**, *9*, 654–659. [[CrossRef](#)]
10. Schillaci, O.; Fontana, S.; Monteleone, F.; Taverna, S.; Di Bella, M.A.; Di Vizio, D.; Alessandro, R. Exosomes from metastatic cancer cells transfer amoeboid phenotype to non-metastatic cells and increase endothelial permeability: Their emerging role in tumor heterogeneity. *Sci. Rep.* **2017**, *7*, 4711. [[CrossRef](#)]
11. Théry, C.; Ostrowski, M.; Segura, E. Membrane vesicles as conveyors of immune responses. *Nat. Rev. Immunol.* **2009**, *9*, 581–593. [[CrossRef](#)] [[PubMed](#)]
12. Montecalvo, A.; Larregina, A.T.; Shufesky, W.J.; Stolz, D.B.; Sullivan, M.L.; Karlsson, J.M.; Baty, C.J.; Gibson, G.A.; Erdos, G.; Wang, Z.; et al. Mechanism of transfer of functional microRNAs between mouse dendritic cells via exosomes. *Blood* **2012**, *119*, 756–766. [[CrossRef](#)] [[PubMed](#)]
13. Mulcahy, L.A.; Pink, R.C.; Carter, D.R. Routes and mechanisms of extracellular vesicle uptake. *J. Extracell. Vesicles* **2014**, *3*, 24641. [[CrossRef](#)]
14. Corbeil, D.; Santos, M.F.; Karbanová, J.; Kurth, T.; Rappa, G.; Lorico, A. Uptake and Fate of Extracellular Membrane Vesicles: Nucleoplasmic Reticulum-Associated Late Endosomes as a New Gate to Intercellular Communication. *Cells* **2020**, *9*, 1931. [[CrossRef](#)]
15. Becker, A.; Thakur, B.K.; Weiss, J.M.; Kim, H.S.; Peinado, H.; Lyden, D. Extracellular Vesicles in Cancer: Cell-to-Cell Mediators of Metastasis. *Cancer Cell* **2016**, *30*, 836–848. [[CrossRef](#)] [[PubMed](#)]
16. Osti, D.; Del Bene, M.; Rappa, G.; Santos, M.; Matafora, V.; Richichi, C.; Faletti, S.; Beznoussenko, G.V.; Mironov, A.; Bachi, A.; et al. Clinical Significance of Extracellular Vesicles in Plasma from Glioblastoma Patients. *Clin. Cancer Res.* **2019**, *25*, 266–276. [[CrossRef](#)]
17. Peinado, H.; Alečković, M.; Lavotshkin, S.; Matei, I.; Costa-Silva, B.; Moreno-Bueno, G.; Hergueta-Redondo, M.; Williams, C.; García-Santos, G.; Ghajar, C.; et al. Melanoma exosomes educate bone marrow progenitor cells toward a pro-metastatic phenotype through MET. *Nat. Med.* **2012**, *18*, 883–891. [[CrossRef](#)]
18. Melo, S.A.; Luecke, L.B.; Kahlert, C.; Fernandez, A.F.; Gammon, S.T.; Kaye, J.; LeBleu, V.S.; Mittendorf, E.A.; Weitz, J.; Rahbari, N.; et al. Glypican-1 identifies cancer exosomes and detects early pancreatic cancer. *Nature* **2015**, *523*, 177–182. [[CrossRef](#)]
19. Wortzel, I.; Dror, S.; Kenific, C.M.; Lyden, D. Exosome-Mediated Metastasis: Communication from a Distance. *Dev. Cell* **2019**, *49*, 347–360. [[CrossRef](#)]
20. Fabbri, M.; Paone, A.; Calore, F.; Galli, R.; Gaudio, E.; Santhanam, R.; Lovat, F.; Fadda, P.; Mao, C.; Nuovo, G.J.; et al. MicroRNAs bind to Toll-like receptors to induce prometastatic inflammatory response. *Proc. Natl. Acad. Sci. USA* **2012**, *109*, E2110–E2116. [[CrossRef](#)]
21. Kosaka, N.; Iguchi, H.; Hagiwara, K.; Yoshioka, Y.; Takeshita, F.; Ochiya, T. Neutral sphingomyelinase 2 (nSMase2)-dependent exosomal transfer of angiogenic microRNAs regulate cancer cell metastasis. *J. Biol. Chem.* **2013**, *288*, 10849–10859. [[CrossRef](#)] [[PubMed](#)]
22. Bobrie, A.; Krumeich, S.; Rey, F.; Recchi, C.; Moita, L.F.; Seabra, M.C.; Ostrowski, M.; Théry, C. Rab27a supports exosome-dependent and -independent mechanisms that modify the tumor microenvironment and can promote tumor progression. *Cancer Res.* **2012**, *72*, 4920–4930. [[CrossRef](#)]
23. Bobrie, A.; Colombo, M.; Krumeich, S.; Raposo, G.; Théry, C. Diverse subpopulations of vesicles secreted by different intracellular mechanisms are present in exosome preparations obtained by differential ultracentrifugation. *J. Extracell. Vesicles* **2012**, *1*, 18397. [[CrossRef](#)] [[PubMed](#)]
24. Savina, A.; Furlan, M.; Vidal, M.; Colombo, M.I. Exosome release is regulated by a calcium-dependent mechanism in K562 cells. *J. Biol. Chem.* **2003**, *278*, 20083–20090. [[CrossRef](#)] [[PubMed](#)]
25. Chalmin, F.; Ladoire, S.; Mignot, G.; Vincent, J.; Bruchard, M.; Remy-Martin, J.P.; Boireau, W.; Rouleau, A.; Simon, B.; Lanneau, D.; et al. Membrane-associated Hsp72 from tumor-derived exosomes mediates STAT3-dependent immunosuppressive function of mouse and human myeloid-derived suppressor cells. *J. Clin. Investig.* **2010**, *120*, 457–471. [[CrossRef](#)] [[PubMed](#)]
26. Datta, A.; Kim, H.; McGee, L.; Johnson, A.E.; Talwar, S.; Marugan, J.; Southall, N.; Hu, X.; Lal, M.; Mondal, D.; et al. High-throughput screening identified selective inhibitors of exosome biogenesis and secretion: A drug repurposing strategy for advanced cancer. *Sci. Rep.* **2018**, *8*, 8161. [[CrossRef](#)]
27. McAndrews, K.M.; Kalluri, R. Mechanisms associated with biogenesis of exosomes in cancer. *Mol. Cancer* **2019**, *18*, 52. [[CrossRef](#)]
28. Kogure, A.; Yoshioka, Y.; Ochiya, T. Extracellular Vesicles in Cancer Metastasis: Potential as Therapeutic Targets and Materials. *Int. J. Mol. Sci.* **2020**, *21*, 4463. [[CrossRef](#)]
29. Nishida-Aoki, N.; Tominaga, N.; Takeshita, F.; Sonoda, H.; Yoshioka, Y.; Ochiya, T. Disruption of Circulating Extracellular Vesicles as a Novel Therapeutic Strategy against Cancer Metastasis. *Mol. Ther.* **2017**, *25*, 181–191. [[CrossRef](#)]
30. Yoshioka, Y.; Konishi, Y.; Kosaka, N.; Katsuda, T.; Kato, T.; Ochiya, T. Comparative marker analysis of extracellular vesicles in different human cancer types. *J. Extracell. Vesicles* **2013**, *2*, 20424. [[CrossRef](#)]
31. Reyes, R.; Cardenes, B.; Machado-Pineda, Y.; Cabañas, C. Tetraspanin CD9: A Key Regulator of Cell Adhesion in the Immune System. *Front. Immunol.* **2018**, *9*, 863. [[CrossRef](#)] [[PubMed](#)]
32. Brosseau, C.; Colas, L.; Magnan, A.; Brouard, S. CD9 Tetraspanin: A New Pathway for the Regulation of Inflammation? *Front. Immunol.* **2018**, *9*, 2316. [[CrossRef](#)] [[PubMed](#)]
33. Lorico, A.; Lorico-Rappa, M.; Karbanová, J.; Corbeil, D.; Pizzorno, G. CD9, a tetraspanin target for cancer therapy? *Exp. Biol. Med. (Maywood)* **2021**, *9*, 1121–1138. [[CrossRef](#)] [[PubMed](#)]

34. Kowal, J.; Arras, G.; Colombo, M.; Jouve, M.; Morath, J.P.; Primdal-Bengtson, B.; Dingli, F.; Loew, D.; Tkach, M.; Théry, C. Proteomic comparison defines novel markers to characterize heterogeneous populations of extracellular vesicle subtypes. *Proc. Natl. Acad. Sci. USA* **2016**, *113*, E968–E977. [[CrossRef](#)]
35. Miki, Y.; Yashiro, M.; Okuno, T.; Kitayama, K.; Masuda, G.; Hirakawa, K.; Ohira, M. CD9-positive exosomes from cancer-associated fibroblasts stimulate the migration ability of scirrhous-type gastric cancer cells. *Br. J. Cancer* **2018**, *118*, 867–877. [[CrossRef](#)]
36. Rappa, G.; Green, T.M.; Lorico, A. The nuclear pool of tetraspanin CD9 contributes to mitotic processes in human breast carcinoma. *Mol. Cancer Res.* **2014**, *12*, 1840–1850. [[CrossRef](#)]
37. Rappa, G.; Santos, M.F.; Green, T.M.; Karbanová, J.; Hassler, J.; Bai, Y.; Barsky, S.H.; Corbeil, D.; Lorico, A. Nuclear transport of cancer extracellular vesicle-derived biomaterials through nuclear envelope invagination-associated late endosomes. *Oncotarget* **2017**, *8*, 14443–14461. [[CrossRef](#)]
38. Le Naour, F.; Rubinstein, E.; Jasmin, C.; Prenant, M.; Boucheix, C. Severely reduced female fertility in CD9-deficient mice. *Science* **2000**, *287*, 319–321. [[CrossRef](#)]
39. Miyado, K.; Yamada, G.; Yamada, S.; Hasuwa, H.; Nakamura, Y.; Ryu, F.; Suzuki, K.; Kosai, K.; Inoue, K.; Ogura, A.; et al. Requirement of CD9 on the egg plasma membrane for fertilization. *Science* **2000**, *287*, 321–324. [[CrossRef](#)]
40. Miyado, K.; Yoshida, K.; Yamagata, K.; Sakakibara, K.; Okabe, M.; Wang, X.; Miyamoto, K.; Akutsu, H.; Kondo, T.; Takahashi, Y.; et al. The fusing ability of sperm is bestowed by CD9-containing vesicles released from eggs in mice. *Proc. Natl. Acad. Sci. USA* **2008**, *105*, 12921–12926. [[CrossRef](#)]
41. Chen, M.S.; Tung, K.S.; Coonrod, S.A.; Takahashi, Y.; Bigler, D.; Chang, A.; Yamashita, Y.; Kincade, P.W.; Herr, J.C.; White, J.M. Role of the integrin-associated protein CD9 in binding between sperm ADAM 2 and the egg integrin alpha6beta1: Implications for murine fertilization. *Proc. Natl. Acad. Sci. USA* **1999**, *96*, 11830–11835. [[CrossRef](#)] [[PubMed](#)]
42. Caballero, J.N.; Frenette, G.; Belleannée, C.; Sullivan, R. CD9-positive microvesicles mediate the transfer of molecules to Bovine Spermatozoa during epididymal maturation. *PLoS ONE* **2013**, *8*, e65364. [[CrossRef](#)] [[PubMed](#)]
43. Kaprielian, Z.; Cho, K.O.; Hadjiargyrou, M.; Patterson, P.H. CD9, a major platelet cell surface glycoprotein, is a ROCA antigen and is expressed in the nervous system. *J. Neurosci.* **1995**, *15*, 562–573. [[CrossRef](#)] [[PubMed](#)]
44. Carroll, R.C.; Rubinstein, E.; Worthington, R.E.; Boucheix, C. Extensive C1q-complement initiated lysis of human platelets by IgG subclass murine monoclonal antibodies to the CD9 antigen. *Thromb. Res.* **1990**, *59*, 831–839. [[CrossRef](#)]
45. Hato, T.; Ikeda, K.; Yasukawa, M.; Watanabe, A.; Kobayashi, Y. Exposure of platelet fibrinogen receptors by a monoclonal antibody to CD9 antigen. *Blood* **1988**, *72*, 224–229. [[CrossRef](#)]
46. Worthington, R.E.; Carroll, R.C.; Boucheix, C. Platelet activation by CD9 monoclonal antibodies is mediated by the Fc gamma II receptor. *Br. J. Haematol.* **1990**, *74*, 216–222. [[CrossRef](#)]
47. Jennings, L.K.; Fox, C.F.; Kouns, W.C.; McKay, C.P.; Ballou, L.R.; Schultz, H.E. The activation of human platelets mediated by anti-human platelet p24/CD9 monoclonal antibodies. *J. Biol. Chem.* **1990**, *265*, 3815–3822. [[CrossRef](#)]
48. Kawakatsu, T.; Suzuki, M.; Kido, H.; Sakane, H.; Hada, S.; Yamaguchi, K.; Fukuroi, T.; Yanabu, M.; Nagata, H.; Nomura, S.; et al. Antithrombotic effect of an anti-glycoprotein IIB/IIIA antibody in primate lethal thrombosis. *Thromb. Res.* **1993**, *70*, 245–254. [[CrossRef](#)]
49. Kobayashi, H.; Hosono, O.; Iwata, S.; Kawasaki, H.; Kuwana, M.; Tanaka, H.; Dang, N.H.; Morimoto, C. The tetraspanin CD9 is preferentially expressed on the human CD4(+)CD45RA+ naive T cell population and is involved in T cell activation. *Clin. Exp. Immunol.* **2004**, *137*, 101–108. [[CrossRef](#)]
50. Santos, M.F.; Rappa, G.; Karbanová, J.; Vanier, C.; Morimoto, C.; Corbeil, D.; Lorico, A. Anti-human CD9 antibody Fab fragment impairs the internalization of extracellular vesicles and the nuclear transfer of their cargo proteins. *J. Cell Mol. Med.* **2019**, *23*, 4408–4421. [[CrossRef](#)]
51. Pang, H.; Liu, L.; Sun, X.; Xi, W.; Bao, Y.; Wu, L.; Shan, J.; Wang, Z.; Guo, Y.; Zhao, C. Exosomes derived from colon cancer cells and plasma of colon cancer patients promote migration of SW480 cells through Akt/mTOR pathway. *Pathol. Res. Pract.* **2021**, *222*, 153454. [[CrossRef](#)] [[PubMed](#)]
52. Leibovitz, A.; Stinson, J.C.; McCombs, W.B., 3rd; McCoy, C.E.; Mazur, K.C.; Mabry, N.D. Classification of human colorectal adenocarcinoma cell lines. *Cancer Res.* **1976**, *36*, 4562–4569. [[PubMed](#)]
53. Hewitt, R.E.; McMarlin, A.; Kleiner, D.; Wersto, R.; Martin, P.; Tsokos, M.; Stamp, G.W.; Stetler-Stevenson, W.G. Validation of a model of colon cancer progression. *J. Pathol.* **2000**, *192*, 446–454. [[CrossRef](#)]
54. Melcher, R.; Steinlein, C.; Feichtinger, W.; Müller, C.R.; Menzel, T.; Lührs, H.; Scheppach, W.; Schmid, M. Spectral karyotyping of the human colon cancer cell lines SW480 and SW620. *Cytogenet. Genome Res.* **2000**, *88*, 145–152. [[CrossRef](#)]
55. Théry, C.; Witwer, K.W.; Aikawa, E.; Alcaraz, M.J.; Anderson, J.D.; Andriantsitohaina, R.; Antoniou, A.; Arab, T.; Archer, F.; Atkin-Smith, G.K.; et al. Minimal information for studies of extracellular vesicles 2018 (MISEV2018): A position statement of the International Society for Extracellular Vesicles and update of the MISEV2014 guidelines. *J. Extracell. Vesicles* **2018**, *7*, 1535750. [[CrossRef](#)]
56. EV-TRACT Consortium; Van Deun, J.; Mestdagh, P.; Agostinis, P.; Akay, O.; Anand, S.; Anckaert, J.; Martinez, Z.A.; Baetens, T.; Beghein, E.; et al. EV-TRACK: Transparent reporting and centralizing knowledge in extracellular vesicle research. *Nat. Methods* **2017**, *14*, 228–232.

57. Santos, M.F.; Rappa, G.; Karbanová, J.; Fontana, S.; Di Bella, M.A.; Pope, M.R.; Parrino, B.; Cascioferro, S.M.; Vistoli, G.; Diana, P.; et al. Itraconazole inhibits nuclear delivery of extracellular vesicle cargo by disrupting the entry of late endosomes into the nucleoplasmic reticulum. *J. Extracell. Vesicles* **2021**, *10*, e12132. [[CrossRef](#)]
58. Schindelin, J.; Arganda-Carreras, I.; Frise, E.; Kaynig, V.; Longair, M.; Pietzsch, T.; Preibisch, S.; Rueden, C.; Saalfeld, S.; Schmid, B.; et al. Fiji: An open-source platform for biological-image analysis. *Nat. Methods* **2012**, *9*, 676–682. [[CrossRef](#)]
59. Qian, F.; Li, Y.P.; Sheng, X.; Zhang, Z.C.; Song, R.; Dong, W.; Cao, S.X.; Hua, Z.C.; Xu, Q. PRL-3 siRNA inhibits the metastasis of B16-BL6 mouse melanoma cells in vitro and in vivo. *Mol. Med.* **2007**, *13*, 151–159. [[CrossRef](#)]
60. Cajot, J.F.; Sordat, I.; Silvestre, T.; Sordat, B. Differential display cloning identifies motility-related protein (MRP1/CD9) as highly expressed in primary compared to metastatic human colon carcinoma cells. *Cancer Res.* **1997**, *57*, 2593–2597.
61. Larios, J.; Mercier, V.; Roux, A.; Gruenberg, J. ALIX- and ESCRT-III-dependent sorting of tetraspanins to exosomes. *J. Cell Biol.* **2020**, *219*, e201904113. [[CrossRef](#)] [[PubMed](#)]
62. Suwakulsiri, W.; Rai, A.; Xu, R.; Chen, M.; Greening, D.W.; Simpson, R.J. Proteomic profiling reveals key cancer progression modulators in shed microvesicles released from isogenic human primary and metastatic colorectal cancer cell lines. *Biochim. Biophys. Acta Proteins Proteom.* **2019**, *1867*, 140171. [[CrossRef](#)] [[PubMed](#)]
63. Popēna, I.; Ābols, A.; Saulīte, L.; Pleiko, K.; Zandberga, E.; Jēkabsons, K.; Endzeliņš, E.; Llorente, A.; Linē, A.; Riekstina, U. Effect of colorectal cancer-derived extracellular vesicles on the immunophenotype and cytokine secretion profile of monocytes and macrophages. *Cell Commun. Signal.* **2018**, *16*, 17. [[CrossRef](#)]
64. Depciuch, J.; Klebowski, B.; Stec, M.; Szatanek, R.; Weglarczyk, K.; Baj-Krzyworzeka, M.; Parlinska-Wojtan, M.; Baran, J. Similarities in the General Chemical Composition of Colon Cancer Cells and Their Microvesicles Investigated by Spectroscopic Methods-Potential Clinical Relevance. *Int. J. Mol. Sci.* **2020**, *21*, 1826. [[CrossRef](#)]
65. Han, C.; Kang, H.; Yi, J.; Kang, M.; Lee, H.; Kwon, Y.; Jung, J.; Lee, J.; Park, J. Single-vesicle imaging and co-localization analysis for tetraspanin profiling of individual extracellular vesicles. *J. Extracell. Vesicles* **2021**, *10*, e12047. [[CrossRef](#)]
66. Santos, M.F.; Rappa, G.; Karbanová, J.; Kurth, T.; Corbeil, D.; Lorico, A. VAMP-associated protein-A and oxysterol-binding protein-related protein 3 promote the entry of late endosomes into the nucleoplasmic reticulum. *J. Biol. Chem.* **2018**, *293*, 13834–13848. [[CrossRef](#)] [[PubMed](#)]
67. Fackler, O.T.; Grosse, R. Cell motility through plasma membrane blebbing. *J. Cell Biol.* **2008**, *181*, 879–884. [[CrossRef](#)]
68. de Toledo, M.; Anguille, C.; Roger, L.; Roux, P.; Gadea, G. Cooperative anti-invasive effect of Cdc42/Rac1 activation and ROCK inhibition in SW620 colorectal cancer cells with elevated blebbing activity. *PLoS ONE* **2012**, *7*, e48344. [[CrossRef](#)]
69. Ono, M.; Handa, K.; Sonnino, S.; Withers, D.A.; Nagai, H.; Hakomori, S. GM3 ganglioside inhibits CD9-facilitated haptotactic cell motility: Coexpression of GM3 and CD9 is essential in the downregulation of tumor cell motility and malignancy. *Biochemistry* **2001**, *40*, 6414–6421. [[CrossRef](#)]
70. Ovalle, S.; Gutiérrez-López, M.D.; Olmo, N.; Turnay, J.; Lizarbe, M.A.; Majano, P.; Molina-Jimenez, F.; López-Cabrera, M.; Yáñez-Mó, M.; Sánchez-Madrid, F.; et al. The tetraspanin CD9 inhibits the proliferation and tumorigenicity of human colon carcinoma cells. *Int. J. Cancer* **2007**, *121*, 2140–2152. [[CrossRef](#)]
71. Zöllner, M. Tetraspanins: Push and pull in suppressing and promoting metastasis. *Nat. Rev. Cancer* **2009**, *9*, 40–55. [[CrossRef](#)] [[PubMed](#)]
72. Orchard-Webb, D.J.; Lee, T.C.; Cook, G.P.; Blair, G.E. CUB domain containing protein 1 (CDCP1) modulates adhesion and motility in colon cancer cells. *BMC Cancer* **2014**, *14*, 754. [[CrossRef](#)] [[PubMed](#)]
73. Chen, Z.; Zhong, T.; Zhong, J.; Tang, Y.; Ling, B.; Wang, L. MicroRNA129 inhibits colorectal cancer cell proliferation, invasion and epithelial to mesenchymal transition by targeting SOX4. *Oncol. Rep.* **2021**, *45*, 61. [[CrossRef](#)] [[PubMed](#)]
74. Huang, G.; Ma, L.; Shen, L.; Lei, Y.; Guo, L.; Deng, Y.; Ding, Y. MIF/SCL3A2 depletion inhibits the proliferation and metastasis of colorectal cancer cells via the AKT/GSK-3 β pathway and cell iron death. *J. Cell Mol. Med.* **2022**, *26*, 3410–3422. [[CrossRef](#)] [[PubMed](#)]
75. Ji, R.; Zhang, B.; Zhang, X.; Xue, J.; Yuan, X.; Yan, Y.; Wang, M.; Zhu, W.; Qian, H.; Xu, W. Exosomes derived from human mesenchymal stem cells confer drug resistance in gastric cancer. *Cell Cycle* **2015**, *14*, 2473–2483. [[CrossRef](#)] [[PubMed](#)]
76. Steeg, P.S. Targeting metastasis. *Nat. Rev. Cancer* **2016**, *16*, 201–218. [[CrossRef](#)]
77. Beans, C. News Feature: Targeting metastasis to halt cancer’s spread. *Proc. Natl. Acad. Sci. USA* **2018**, *115*, 12539–12543. [[CrossRef](#)]
78. Shafqat-Abbasi, H.; Kowalewski, J.M.; Kiss, A.; Gong, X.; Hernandez-Varas, P.; Berge, U.; Jafari-Mamaghani, M.; Lock, J.G.; Stromblad, S. An analysis toolbox to explore mesenchymal migration heterogeneity reveals adaptive switching between distinct modes. *Elife* **2016**, *5*, e11384. [[CrossRef](#)] [[PubMed](#)]
79. Wolf, K.; Mazo, I.; Leung, H.; Engelke, K.; von Andrian, U.H.; Deryugina, E.I.; Strongin, A.Y.; Bocker, E.B.; Friedl, P. Compensation mechanism in tumor cell migration: Mesenchymal-amoeboid transition after blocking of pericellular proteolysis. *J. Cell Biol.* **2003**, *160*, 267–277. [[CrossRef](#)]
80. Read, J.; Ingram, A.; Al Saleh, H.A.; Platko, K.; Gabriel, K.; Kapoor, A.; Pinthus, J.; Majeed, F.; Qureshi, T.; Al-Nedawi, K. Nuclear transportation of exogenous epidermal growth factor receptor and androgen receptor via extracellular vesicles. *Eur. J. Cancer* **2017**, *70*, 62–74. [[CrossRef](#)]
81. Alfandari, D.; Ben Ami Pilo, H.; Abou Karam, P.; Dagan, O.; Joubran, C.; Rotkopf, R.; Regev-Rudzki, N.; Porat, Z. Monitoring Distribution Dynamics of EV RNA Cargo Within Recipient Monocytes and Macrophages. *Front. Cell. Infect. Microbiol.* **2021**, *11*, 739628. [[CrossRef](#)] [[PubMed](#)]

82. Kovalenko, O.V.; Yang, X.; Kolesnikova, T.V.; Hemler, M.E. Evidence for specific tetraspanin homodimers: Inhibition of palmitoylation makes cysteine residues available for cross-linking. *Biochem. J.* **2004**, *377*, 407–417. [[CrossRef](#)] [[PubMed](#)]
83. Reyes, R.; Monjas, A.; Yáñez-Mó, M.; Cardeñes, B.; Morlino, G.; Gilsanz, A.; Machado-Pineda, Y.; Lafuente, E.; Monk, P.; Sánchez-Madrid, F.; et al. Different states of integrin LFA-1 aggregation are controlled through its association with tetraspanin CD9. *Biochim. Biophys. Acta* **2015**, *1853*, 2464–2480. [[CrossRef](#)] [[PubMed](#)]
84. Barreiro, O.; Yáñez-Mó, M.; Sala-Valdés, M.; Gutiérrez-Lopez, M.D.; Ovalle, S.; Higginbottom, A.; Monk, P.N.; Cabañas, C.; Sánchez-Madrid, F. Endothelial tetraspanin microdomains regulate leukocyte firm adhesion during extravasation. *Blood* **2005**, *105*, 2852–2861. [[CrossRef](#)] [[PubMed](#)]
85. Barreiro, O.; Zamai, M.; Yáñez-Mó, M.; Tejera, E.; López-Romero, P.; Monk, P.N.; Gratton, E.; Caiolfa, V.R.; Sánchez-Madrid, F. Endothelial adhesion receptors are recruited to adherent leukocytes by inclusion in preformed tetraspanin nanoplateforms. *J. Cell Biol.* **2008**, *183*, 527–542. [[CrossRef](#)]
86. Gilsanz, A.; Sánchez-Martín, L.; Gutiérrez-López, M.D.; Ovalle, S.; Machado-Pineda, Y.; Reyes, R.; Swart, G.W.; Figdor, C.G.; Lafuente, E.M.; Cabañas, C. ALCAM/CD166 adhesive function is regulated by the tetraspanin CD9. *Cell Mol. Life Sci.* **2013**, *70*, 475–493. [[CrossRef](#)]
87. Rappa, G.; Green, T.M.; Karbanová, J.; Corbeil, D.; Lorico, A. Tetraspanin CD9 Determines Invasiveness and Tumorigenicity of Human Breast Cancer Cells. *Oncotarget* **2015**, *6*, 7970–7991. [[CrossRef](#)]
88. Mori, M.; Mimori, K.; Shiraishi, T.; Haraguchi, M.; Ueo, H.; Barnard, G.F.; Akiyoshi, T. Motility related protein 1 (MRP1/CD9) expression in colon cancer. *Clin. Cancer Res.* **1998**, *4*, 1507–1510.
89. Kim, K.J.; Kwon, H.J.; Kim, M.C.; Bae, Y.K. CD9 Expression in Colorectal Carcinomas and Its Prognostic Significance. *J. Pathol. Transl. Med.* **2016**, *50*, 459–468. [[CrossRef](#)]
90. Hashida, H.; Takabayashi, A.; Tokuhara, T.; Hattori, N.; Taki, T.; Hasegawa, H.; Satoh, S.; Kobayashi, N.; Yamaoka, Y.; Miyake, M. Clinical significance of transmembrane 4 superfamily in colon cancer. *Br. J. Cancer* **2003**, *89*, 158–167. [[CrossRef](#)]
91. Zeng, H.; Bain, L.J.; Belinsky, M.G.; Kruh, G.D. Expression of multidrug resistance protein-3 (multispecific organic anion transporter-D) in human embryonic kidney 293 cells confers resistance to anticancer agents. *Cancer Res.* **1999**, *59*, 5964–5967. [[PubMed](#)]

ORIGINAL ARTICLE

Humanized anti-IL-26 monoclonal antibody as a novel targeted therapy for chronic graft-versus-host disease

Ryo Hatano¹  | Takumi Itoh^{1,2} | Haruna Otsuka¹ | Harumi Saeki³ | Ayako Yamamoto¹ | Dan Song¹ | Yuki Shirakawa¹ | Satoshi Iyama⁴ | Tsutomu Sato⁵ | Noriaki Iwao⁶ | Norihiro Harada⁷  | Thomas M. Aune⁸ | Nam H. Dang⁹ | Yutaro Kaneko¹⁰ | Taketo Yamada^{11,12} | Chikao Morimoto¹ | Kei Ohnuma¹

¹Department of Therapy Development and Innovation for Immune Disorders and Cancers, Graduate School of Medicine, Juntendo University, Tokyo, Japan

²Atopy (Allergy) Research Center, Graduate School of Medicine, Juntendo University, Tokyo, Japan

³Department of Human Pathology, Graduate School of Medicine, Juntendo University, Tokyo, Japan

⁴Department of Hematology, Sapporo Medical University School of Medicine, Hokkaido, Japan

⁵Department of Hematology, Toyama University Hospital, Toyama, Japan

⁶Department of Hematology, Juntendo University Shizuoka Hospital, Shizuoka, Japan

⁷Department of Respiratory Medicine, Juntendo University Faculty of Medicine and Graduate School of Medicine, Tokyo, Japan

⁸Department of Medicine, Vanderbilt University School of Medicine, Vanderbilt University Medical Center, Nashville, Tennessee, USA

⁹Division of Hematology/Oncology, University of Florida, Gainesville, Florida, USA

¹⁰Y's AC Co., Ltd., Tokyo, Japan

¹¹Department of Pathology, Saitama Medical University, Saitama, Japan

¹²Department of Pathology, Keio University School of Medicine, Tokyo, Japan

Correspondence

Ryo Hatano, Department of Therapy Development and Innovation for Immune Disorders and Cancers, Graduate School of Medicine, Juntendo University, 2-1-1, Hongo, Bunkyo-ku, Tokyo 113-8421, Japan.

Email: rhatano@juntendo.ac.jp

Funding information

President's Grant for Educational Excellence, Juntendo University, Grant/Award Number: GP21-04; Japan Research Institute of Industrial Science; Japanese Society of Hematology; JSPS KAKENHI, Grant/Award Number: JP18H02782, JP20H03471, JP20K07683 and JP20K07683; Ministry of Health, Labour, and Welfare, Japan, Grant/Award Number: 180101-01 and 210901-02

IL-26 is a Th17 cytokine, with its gene being absent in rodents. To characterize the in vivo immunological effects of IL-26 in chronic systemic inflammation, we used human *IL26* transgenic (hIL-26Tg) mice and human umbilical cord blood mononuclear cells (hCBMC) in mouse allogeneic-graft-versus-host disease (GVHD) and chronic xenogeneic-GVHD model, respectively. Transfer of bone marrow and spleen T cells from hIL-26Tg mice into B10.BR mice resulted in GVHD progression, with clinical signs of tissue damage in multiple organs. IL-26 markedly increased neutrophil levels both in the GVHD-target tissues and peripheral blood. Expression levels of Th17 cytokines in hIL-26Tg mice-derived donor CD4 T cells were significantly increased, whereas IL-26 did not affect cytotoxic function of donor CD8 T cells. In addition, granulocyte-colony stimulating factor, IL-1 β , and IL-6 levels were particularly enhanced in hIL-26Tg mice. We also developed a humanized neutralizing anti-IL-26 monoclonal antibody (mAb) for therapeutic use, and its administration after onset of chronic xenogeneic-GVHD mitigated weight loss and prolonged survival, with preservation of graft-versus-leukemia effect. Taken together, our data elucidate the in vivo immunological effects

Abbreviations: A20-luc, firefly luciferase-transfected A20; allo-GVHD, allogeneic-GVHD; allo-HSCT, allogeneic hematopoietic stem cell transplantation; BAC, bacterial artificial chromosome; BM, bone marrow; CNS, conserved noncoding sequence; G-CSF, granulocyte-colony stimulating factor; GVHD, graft-versus-host disease; GVL, graft-versus-leukemia; hCBMC, human umbilical cord blood mononuclear cells; hIL-26Tg, human *IL26* transgenic; mAb, monoclonal antibody; NETs, neutrophil extracellular traps; NOG, NOD/Shi-scidIL2r^{null}; TCD-BM, T-cell-depleted bone marrow; xeno-GVHD, xenogeneic GVHD.

© 2022 The American Society of Transplantation and the American Society of Transplant Surgeons.

of IL-26 in chronic GVHD models and suggest that a humanized anti-IL-26 mAb may be a potential therapeutic agent for the treatment of chronic GVHD.

KEYWORDS

graft-versus-host disease, humanized monoclonal antibody, interleukin-26, neutrophils, T helper 17 cells

1 | INTRODUCTION

Allogeneic hematopoietic stem cell transplantation (allo-HSCT) is a well-established procedure for hematological malignancies or bone marrow (BM) failure syndromes,¹⁻³ with acute and chronic graft-versus-host disease (GVHD) due to an immunological attack on target recipient organs by donor allogeneic T cells being significant complications. While suppression of donor allogeneic T cells is highly effective for preventing GVHD, complications such as loss of graft-versus-leukemia (GVL) effect or increased opportunistic infections can occur.⁴ In-depth understanding of the molecular mechanisms involved in human GVHD will improve allo-HSCT clinical outcome.

IL-26 belonging to the IL-10 cytokine family,^{5,6} is conserved in several vertebrate species but not found in mice and rats.⁷ IL-26 is known as a Th17 cytokine, while NK cells, macrophages, bronchial epithelial cells, and synoviocytes have capacity to produce IL-26.⁸⁻¹¹ IL-20RA/IL-10RB heterodimer is an IL-26 receptor, and IL-26 binding to IL-20RA/IL-10RB results in functional activation via STAT3 phosphorylation.¹² However, IL-26 can activate human monocytes and NK cells,^{8,13} despite the lack of IL-20RA expression on these cell types.¹⁴ IL-26 also acts on vascular endothelial cells to stimulate angiogenesis and activates EGFR-tyrosine kinase inhibitor-associated bypass pathway to promote drug resistance in triple-negative breast cancer cells despite a lack of IL-20RA expression.^{11,15} These findings strongly suggest the existence of an unidentified IL-26 receptor besides IL-20RA/IL-10RB. Furthermore, IL-26 is a cationic and amphipathic cytokine with characteristics of an antimicrobial peptide,^{16,17} capable of binding to DNA/RNA released from bacteria or dying cells or neutrophil extracellular traps (NETs), triggering inflammatory cytokine production from plasmacytoid dendritic cells, monocytes, and neutrophils in a TLR9 or STING- and inflammasome-dependent manner,^{16,18} indicating the diverse mechanism of action of IL-26.

Without accessible animal models due partly to the absence of the *IL26* gene in mice, IL-26 role in inflammatory disorders is not clearly characterized. Utilizing human *IL26* bacterial artificial chromosome (BAC) transgenic (hIL-26Tg) mice,^{19,20} we recently investigated the in vivo effects of IL-26 in acute local inflammation models and showed that vascularization and immune cell infiltration were enhanced in the skin of imiquimod-applied hIL-26Tg mice.^{15,21} These findings strongly suggest that IL-26 may represent a novel therapeutic target for inflammatory disorders, although IL-26 role in chronic inflammation still needs clarification. In the murine models utilizing

hIL-26Tg mice, human IL-26 is not expressed constitutively but is induced only when the cells capable of expressing IL-26 are activated, which resembles the human condition. However, a potential drawback of the hIL-26 BAC Tg mouse model is that the expression level of human IL-26 in murine CD4 T cells is quite low as compared with the activated human CD4 T cells,²⁰ resulting in suboptimal biological effects of human IL-26 in the inflammation models involving hIL-26Tg mice. For these reasons, inflammation models utilizing human T cells are essential to investigate the inherent functions of human IL-26.

Due to the reasons above, in the present study, we examined mouse allogeneic (allo)-GVHD model utilizing hIL-26Tg mice and chronic xenogeneic (xeno)-GVHD model utilizing human umbilical cord blood mononuclear cells (hCBMC) to evaluate the in vivo immunological effects of IL-26 in the pathology of chronic systemic inflammation, and created a humanized neutralizing anti-IL-26 monoclonal antibody (mAb) based on our recently developed murine mAb²² as a potential treatment for chronic GVHD.

2 | METHODS

2.1 | Human samples

Serum samples were obtained from nine mild acute skin GVHD patients (6 males and 3 females, 2 grade I and 7 grade II, age 47.56 ± 9.62) and six moderate/severe chronic lung GVHD patients (4 males and 2 females, 2 severe, and 4 moderate, age 48.33 ± 15.04). Serum was collected from patients following GVHD diagnosis at Sapporo Medical University. Serum was collected from 12 healthy volunteers (8 males and 4 females, age 46.83 ± 11.47) at Juntendo University. All serum samples were stored at -80°C . Mononuclear cells isolated from human cord blood with Ficoll density gradation method were purchased from RIKEN BioResource Center.

2.2 | Mice

Female B10.BR (H-2^k) and NOD/Shi-*scid*IL2 γ ^{null} (NOG) (H-2^d) mice were purchased from Sankyo Labo-Service and In-Vivo Science, respectively. C57BL/6 (H-2^b) mice carrying a 190-kb BAC transgene with human *IFNG* and *IL26* gene (hIL-26Tg) and a BAC Tg-deleting conserved noncoding sequence (CNS) positioned at 77 kb upstream

FIGURE 1 Severe manifestations of allo-GVHD in B10.BR recipients receiving TCD-BM and splenic T cells from hIL-26Tg donors. (A) Kaplan–Meier survival curves for B10.BR recipients receiving T cell-depleted bone marrow (TCD-BM) alone from Δ CNS-77Tg donors (light orange line, $n = 6$), TCD-BM with splenic T cells from Δ CNS-77Tg donors (orange line, $n = 12$), TCD-BM alone from human *IL26* transgenic (hIL-26Tg) donors (light blue line, $n = 6$), or TCD-BM with splenic T cells from hIL-26Tg donors (blue line, $n = 12$) ($p = .0215$ vs. TCD-BM with splenic T cells from Δ CNS-77Tg group). (B) Average body weight (mean percentage \pm S.D. of initial) for mice surviving on a given day for different groups of mice as shown in (A). (C) Time-course changes of average percentage (\pm S.D.) of donor cells (H-2D^b+H-2D^k) in total leukocytes, percentage of granulocytes fraction (SSC^{hi}), CD4 T cells (CD4⁺CD8a⁺), or CD8 T cells (CD4⁺CD8a⁺) in donor cells (gated for H-2D^b+H-2D^k) in peripheral blood of B10.BR recipients were analyzed by flow cytometry. (D) Pathological GVHD scores for lung (range 0 to 9), liver (range 0 to 8), colon (range 0 to 8), or skin (range 0 to 10) from normal B10.BR mice ($n = 3$) or B10.BR recipients 4–5 weeks post-transplantation (TCD-BM alone from Δ CNS-77Tg or hIL-26Tg group $n = 3$ each, TCD-BM with splenic T cells from Δ CNS-77Tg or hIL-26Tg group $n = 5$ each). (E) H&E staining of lung, liver, colon, or skin from each group as shown in (D). Original magnification lung $\times 100$, liver, colon, skin $\times 200$. (F) Azan-Mallory staining of liver from each group as shown in (D). Original magnification $\times 400$. (E, F) Representative images are shown with similar results. Lower magnification images are shown in Figure S3. (A–F) Data represent the combined results of three (A–C) or two (D–F) independent experiments. (C, D) Data are shown as mean \pm S.D. of each group, comparing values in TCD-BM with splenic T cells from hIL-26Tg group to TCD-BM with splenic T cells from Δ CNS-77Tg group ($*p < .05$).

of the *IFNG* transcription start site (Δ CNS-77Tg) were developed in Dr. Aune's laboratory.^{19,20} Human IL-26 expression was completely abrogated in Δ CNS-77Tg mice.²⁰ Although both hIL-26Tg mice and Δ CNS-77Tg mice-derived CD4 T cells were capable of producing human IFN- γ , it has been reported that human IFN- γ does not transduce intracellular signals through murine IFNGR nor exhibit biological activity.²³ All mice used in this study were housed in a specific pathogen-free facility in micro-isolator cages, and used at 10–12 weeks of age.

All other information is detailed in [Supplementary methods](#).

3 | RESULTS

3.1 | Exacerbation of systemic manifestations of allo-GVHD by IL-26

We first used hIL-26Tg mice for a complete MHC-mismatched allo-GVHD model, having previously demonstrated that human IL-26 can act on both murine and human cells.^{11,15,24} Δ CNS-77Tg mice lacking human IL-26 transcription were used as controls. The basic characteristics of spleen T cells in hIL-26Tg mice were generally similar as those in control mice (Figure S1). Transplantation of T cell-depleted bone marrow (TCD-BM) alone hardly affected survival and weight of B10.BR recipients (Figure 1A,B). In contrast, acute weight loss occurred until one-week post-transplant of donor BM plus splenic T cells, followed by a slight body weight recovery and then a gradual decrease due to allo-GVHD. B10.BR mice receiving hIL-26Tg mice-derived BM and splenic T cells (hIL-26Tg-B10.BR mice) exhibited significantly decreased overall survival ($p = .0215$) and body weight, compared to recipients transplanted with Δ CNS-77Tg mice-derived BM and splenic T cells (Δ CNS-77Tg-B10.BR mice) (Figure 1A,B). Blood leukocytes of recipient mice were mostly from donor-derived H-2D^b+H-2D^k cells (Figure 1C). Although there was no difference in donor CD4 and CD8 T cell expansion between allo-GVHD groups, donor granulocyte levels were apparently increased in hIL-26Tg-B10.BR mice compared to Δ CNS-77Tg-B10.BR mice (Figures 1C, Figure S2).

GVHD manifestations were hardly observed in B10.BR mice receiving TCD-BM alone (Figure 1D,E). In contrast, histiocytes in pulmonary alveoli, portal inflammatory cell infiltration around portal vein, and severe colitis with ulceration were observed in hIL-26Tg-B10.BR mice, with significantly higher pathological scores of these organs compared to those of control mice, whereas skin GVHD manifestations were moderate in this model (Figures 1D,E, Figure S3). Moreover, collagen deposition was clearly observed in the portal area of the liver of hIL-26Tg-B10.BR mice (Figure 1F). Considering the survival period of recipient mice after transplantation, the manifestation of colon and liver GVHD and lung inflammation, and the fibroproliferation in the liver, this allo-GVHD model appears to display the characteristics of both acute and chronic GVHD. Taken together, our data indicate that IL-26 further exacerbates systemic GVHD progression and severity.

3.2 | IL-26-mediated enhancement of neutrophil levels and augmentation of Th17 response

Our next studies examined the mechanisms involved in IL-26-mediated allo-GVHD. CD45⁺ leukocytes were localized in the lung of normal B10.BR or B10.BR recipients receiving TCD-BM alone while being at low levels in the liver. Both allo-GVHD groups demonstrated increased levels of donor leukocytes in the lung and particularly in the liver (Figure 2A). There was a higher percentage of CD4 T cells than CD8 T cells in donor leukocytes in B10.BR mice receiving TCD-BM alone, with the ratio reversed in the allo-GVHD mice (Figure 2B). The percentage of donor CD4 and CD8 T cells in hIL-26Tg-B10.BR and Δ CNS-77Tg-B10.BR mice were similar, whereas neutrophil levels were markedly increased in lung, liver, spleen, and colon of hIL-26Tg-B10.BR mice, as well as a trend toward an enhanced level of donor monocytes and macrophages (Figure 2B, Figures S4 and S5). Meanwhile, B cell percentage was prominently decreased in the allo-GVHD mice as compared with recipients receiving TCD-BM alone (Figure 2B, Figure S6). We next evaluated the effect of anti-mouse Ly6G mAb to determine whether the increased neutrophil levels in the GVHD-target organs from hIL-26Tg-B10.BR mice were associated with GVHD

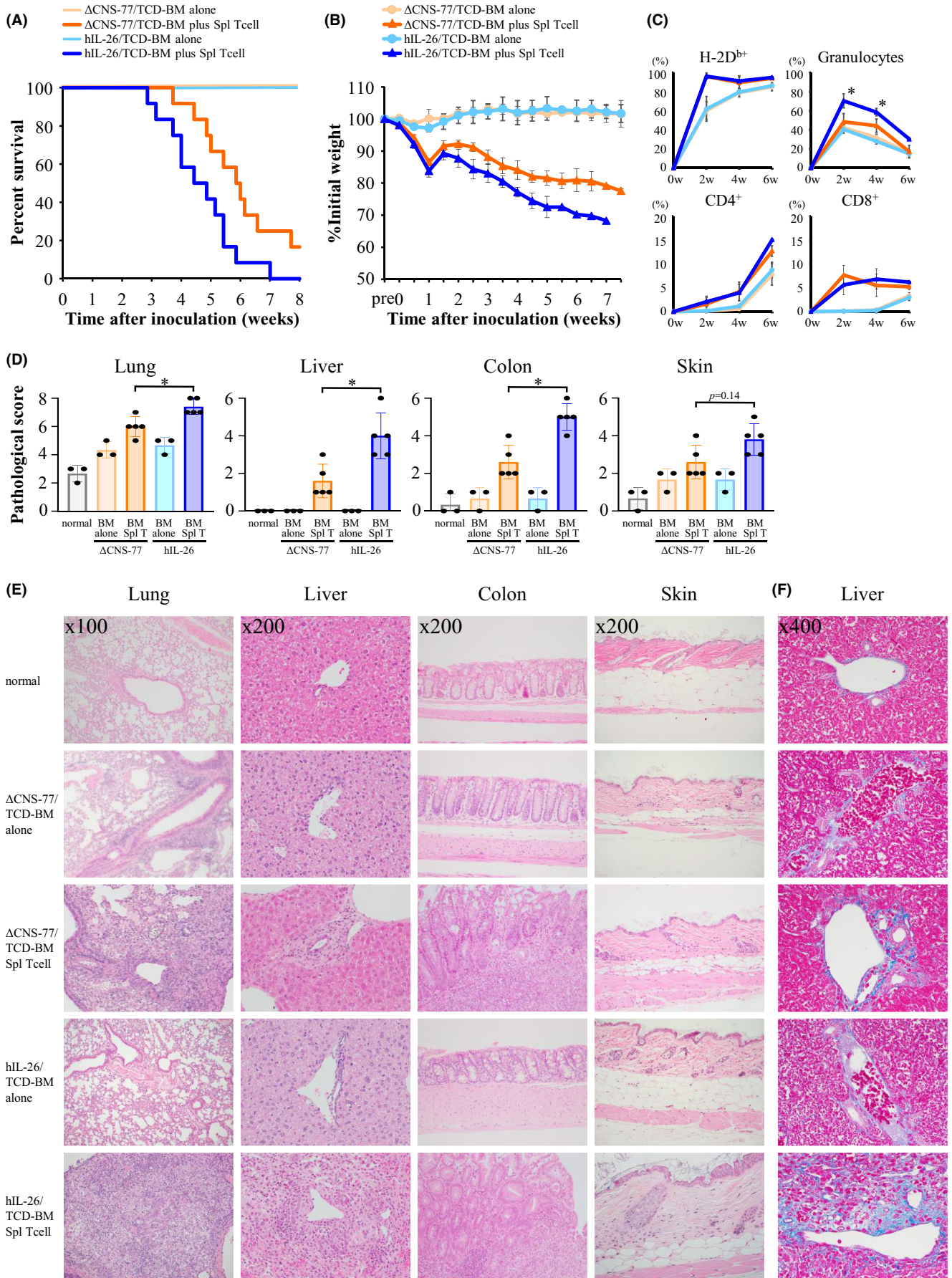


FIGURE 2 Enhanced neutrophil cell number and Th17 cytokine expression in donor CD4 T cells in B10.BR recipients receiving TCD-BM and splenic T cells from hIL-26Tg donors. (A–F, I) Spleen, lung, liver, or colon was harvested from normal B10.BR mice ($n = 3$) or B10.BR recipients 4–5 weeks post-transplantation (T cell-depleted bone marrow [TCD-BM] alone from Δ CNS-77Tg or human *IL26* transgenic [hIL-26Tg] group $n = 3$ each, TCD-BM with splenic T cells from Δ CNS-77Tg or hIL-26Tg group $n = 5$ each). (A) The number of donor leukocytes (mean \pm S.D.) in the lung or liver of B10.BR mice were determined by cell counting and the percentage of donor (H-2D^b+H-2D^k) CD45⁺ cells were analyzed by flow cytometry. NS denotes “not significant.” (B) Average percentage (\pm S.D.) of CD4 T cells (TCR β ⁺CD4⁺CD8a⁻), CD8 T cells (TCR β ⁺CD4⁻CD8a⁺), B cells (CD19⁺), neutrophils (CD11b⁺Ly-6G⁺), or monocytes/macrophages (CD11b⁺CD14⁺ plus CD11b⁺F4/80⁺) in donor leukocytes (gated for H-2D^b+H-2D^kCD45⁺) in spleen, lung, or liver of B10.BR recipients were analyzed by flow cytometry. (C, E) Average percentage (\pm S.D.) of PD-1⁺ in donor CD4 T cells (C) (gated for H-2D^b+H-2D^kCD45⁺TCR β ⁺CD4⁺CD8a⁻) or CD8 T cells (E) (gated for H-2D^b+H-2D^kCD45⁺TCR β ⁺CD4⁻CD8a⁺) in spleen, lung, or liver of B10.BR recipients were analyzed by flow cytometry. (D, F) Donor CD4 T cells (D) or CD8 T cells (F) in the liver of recipient mice were purified by cell sorting (gated for H-2D^b+H-2D^kCD45⁺TCR β ⁺CD4⁺CD8a⁻ or CD4⁻CD8a⁺, respectively). mRNA expression levels of indicated genes in these cells were quantified by real-time RT-PCR. ND denotes undetectable. (G, H) Plasma was collected from B10.BR recipients at the indicated time points (for each, $n = 3$ in TCD-BM alone from Δ CNS-77Tg or hIL-26Tg group, $n = 8$ at 4w, $n = 8$ at 6w and $n = 4$ at 8w in TCD-BM with splenic T cells from Δ CNS-77Tg group, $n = 8$ at 4w, $n = 6$ at 6w and $n = 3$ at 8w in TCD-BM with splenic T cells from hIL-26Tg group). (G) Plasma levels of human IL-26 and mouse IL-17A were quantified by ELISA. The dashed line indicates the detection limit. ND denotes undetectable. (H) Plasma levels of 23 mouse cytokines were quantified utilizing multiplex assay kit, as described in [Supplemental Materials and Methods](#). Representative results among 23 cytokines were shown. (I) mRNA expression levels of indicated mouse genes in the homogenates of lung, liver, or colon tissue of B10.BR recipients were quantified by real-time RT-PCR. (A–I) Data represent the combined results of two (A–F, I) or three (G, H) independent experiments. Data are shown as mean \pm S.D. of each group, comparing values in TCD-BM with splenic T cells from hIL-26Tg group to TCD-BM with splenic T cells from Δ CNS-77Tg group ($*p < .05$). (D, F, I) Each expression was normalized to mouse hypoxanthine phosphoribosyltransferase (*Hprt*). [Color figure can be viewed at [wileyonlinelibrary.com](#)]

exacerbation. Although anti-Ly6G mAb administration did not result in complete neutrophil depletion, levels of neutrophil infiltration in the lung and liver of hIL-26Tg-B10.BR mice were decreased, concurrent with a trend toward reduced allo-GVHD-associated lethality ($p = .1546$) and weight loss (Figure S7). These results suggest that the increased neutrophil levels in the GVHD-target organs are at least partially responsible for GVHD exacerbation.

In contrast with mice receiving TCD-BM alone, most of the donor CD4 and CD8 T cells in the allo-GVHD mice expressed PD-1, suggesting a TCR-stimulated phenotype (Figure 2C,E). Human *IL26* mRNA expression was observed only in donor CD4 T cells transplanted from hIL-26Tg but not Δ CNS-77Tg mice (Figure 2D). Expression levels of all the genes examined in donor CD4 and CD8 T cells purified from allo-GVHD mice were higher than from mice receiving TCD-BM alone. Mouse *Il17a* and *Il21* levels in donor CD4 T cells in the liver of hIL-26Tg-B10.BR mice were significantly higher than those from Δ CNS-77Tg-B10.BR mice, with similar levels of effector molecules in donor CD8 T cells from hIL-26Tg-B10.BR mice and control recipients (Figure 2D,F). Higher expression level of mouse IL-17A in donor CD4 T cells in the liver of hIL-26Tg-B10.BR mice was also confirmed by flow cytometry (Figure S8). Similar results were observed for lung and spleen donor T cells (data not shown). Plasma levels of human IL-26 and mouse IL-17A were similar to those shown in Figure 2D,G.

Inflammatory factors highly associated with human IL-26 expression were identified by multiplex assays. Among 23 cytokines and chemokines evaluated, plasma levels of mouse RANTES, IL-1 α , IL-1 β , IL-6, and granulocyte-colony stimulating factor (G-CSF) in hIL-26Tg-B10.BR mice were significantly higher than those in Δ CNS-77Tg-B10.BR mice (Figure 2H). Furthermore, quantitative RT-PCR analyses confirmed the enhanced mRNA expression of these genes, particularly *Il1b*, *Il6*, and *Csf3*, in the GVHD-target organs of hIL-26Tg-B10.BR mice (Figure 2I). Our data hence indicate that IL-26 markedly increases neutrophil levels in GVHD-target tissues and

peripheral blood, and augments Th17 response associated with enhanced levels of G-CSF, IL-1 β , and IL-6.

3.3 | IL-26-mediated augmentation of Th17 response and G-CSF production

Since IL-26 and DNA have synergistic effect on IL-1 β and IL-6 production,¹⁸ we next analyzed *Il1b* and *Il6* expression in mouse myeloid cells. Human IL-26 plus mouse genomic DNA stimulated both *Il1b* and *Il6* mRNA expression and IL-1 β and IL-6 production from primary mouse splenic CD11b⁺ cells (Figure 3A,B), but not *Il12b* and *Il23a* expression (data not shown). Similar results were observed for the mouse macrophage cell line RAW264.7 (Figure S9).

Other cytokines besides TGF- β and IL-6 are involved in the functional maturation and maintenance of Th17 cells.^{25–28} Since we demonstrated that IL-26 exposure was associated with enhanced IL-1 β and IL-6 expression, we next examined IL-1 β and IL-6 effect on Th17 polarization and activation. Exogenous mouse IL-1 β and IL-6 augmented mouse *Il17a* and human *IL26* expression, respectively, in hIL-26Tg mice-derived splenic CD4⁺ T cells co-stimulated via CD3 and CD28 in the presence of mouse TGF- β 1, IL-1 β , and IL-6 (Figure 3C). In contrast, stimulation with TGF- β 1 and IL-6 but not IL-1 β was essential to induce CD4⁺ T cell *Rorc* expression, the master transcription factor driving Th17 cell differentiation (Figure 3C), while *Il21* expression was regulated by IL-6 alone (Figure 3C). TGF- β 1 and IL-6 stimulation suppressed *Ifng* expression while slightly enhanced *Il4* expression (Figure 3C). Mouse cytokine and *Rorc* levels were similar in Δ CNS-77Tg mice-derived and hIL-26Tg mice-derived splenic CD4⁺ T cells, while human *IL26* expression was never observed in Δ CNS-77Tg mice-derived CD4⁺ T cells in all stimulatory conditions (data not

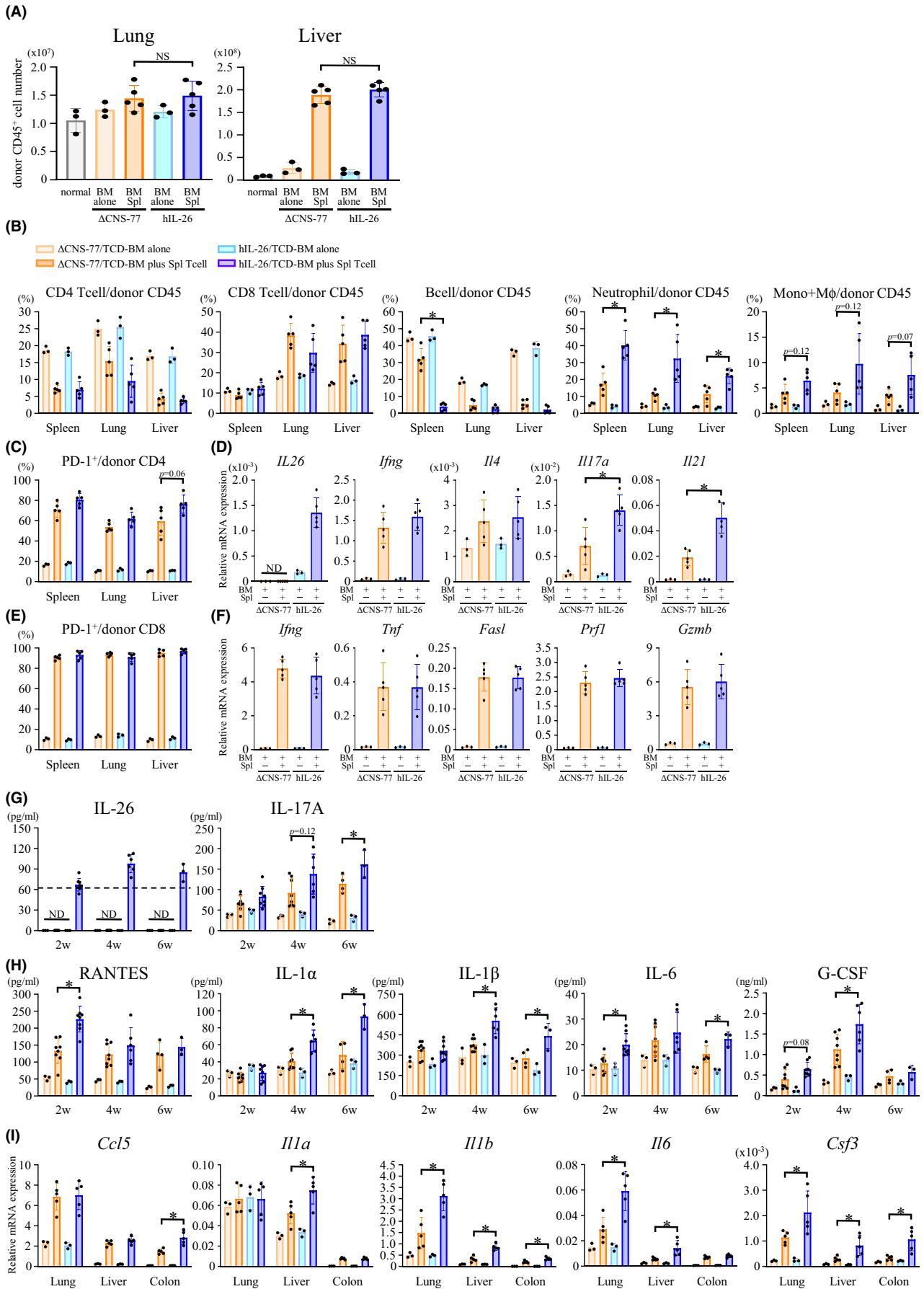


FIGURE 3 IL-1 β and IL-6 enhanced by IL-26 and nucleic acid stimulation augments Th17 response, resulting in increased G-CSF production. (A, B) Freshly purified splenic CD11b⁺ myeloid cells obtained from C57BL/6 mice were stimulated with recombinant human IL-26 (50 ng/mL) and/or mouse genomic DNA (1, 5 μ g/mL), or lipopolysaccharide (LPS) (100 ng/mL) for 4 h (A) or 24 h (B). (A) mRNA expression of mouse IL-1 β (*Il1b*) and IL-6 (*Il6*) was quantified by real-time RT-PCR. (B) Concentrations of mouse IL-1 β and IL-6 in culture supernatants were examined by ELISA. (C) Freshly purified splenic CD4⁺ T cells obtained from hIL-26Tg mice were stimulated with anti-CD3 ϵ (10 μ g/mL) plus anti-CD28 (2 μ g/mL) mAbs in the presence of mouse cytokines at the indicated concentrations for 24 h. mRNA expression of mouse IL-4 (*Il4*), IL-17A (*Il17a*), IL-21 (*Il21*), IFN- γ (*Ifng*), RORC (*Rorc*), and human IL-26 (*IL26*) was quantified by real-time RT-PCR. (D, E) RAW264.7 cells (D) or NIH3T3 cells (E) were stimulated with recombinant mouse IL-1 β (20 ng/mL), IL-6 (20 ng/mL), IL-17A (20 ng/mL), human IL-26 (50 ng/mL), and/or mouse genomic DNA (5 μ g/mL) for 24 h. Concentrations of mouse G-CSF in culture supernatants were examined by ELISA. (A–E) Representative data of three independent experiments are shown as mean \pm S.D. of triplicate samples, comparing values in each stimulatory condition (* p < .01), and similar results were obtained in each experiment. (A, C) Each expression was normalized to mouse hypoxanthine phosphoribosyltransferase (*Hprt*). [Color figure can be viewed at wileyonlinelibrary.com]

shown). These results indicate that both IL-1 β and IL-6 are essential for the marked increase in mouse IL-17A and human IL-26 expression in CD4⁺ T cells of hIL-26Tg mice.

We also examined the association between IL-26-mediated positive-feedback and G-CSF expression, a critical factor for granulopoiesis.²⁹ Stimulation with mouse IL-1 β dramatically induced G-CSF production from RAW264.7 cells, with additional enhancement by mouse IL-17A, genomic DNA, and human IL-26 (Figure 3D). Meanwhile, mouse IL-1 β and IL-17A synergistically enhanced G-CSF production from NIH3T3 cells, with minimal effect by mouse IL-6, genomic DNA, and human IL-26 (Figure 3E).

3.4 | Development of novel humanized anti-IL-26 mAb

To develop a novel IL-26-targeted therapy, we have succeeded in developing humanized mAb h69-10 with strong binding affinity and neutralizing activity against IL-26 as compared with the original murine mAb m69-10 (Figure S10).

3.5 | Suppression of xeno-GVHD progression by anti-IL-26 mAb treatment

Acute GVHD is caused by T cells within the original stem cell transplant, whereas chronic GVHD is theoretically caused by allo- (auto-) reactive T cells that have matured through the host thymus. We previously established a chronic xeno-GVHD model,²⁴ which has two inherent advantages that allow us to investigate the therapeutic effect of anti-IL-26 mAb. One is human IL-26 expression level in human CD4 T cells is much higher than hIL-26Tg mice-derived CD4 T cells, and the other is disease progression is moderate as compared with the hIL-26Tg-B10.BR allo-GVHD model. m69-10 or h69-10 treatment following the appearance of GVHD clinical symptoms on day +28 markedly increased overall survival of hCBMC-NOG mice (Figure 4A), with stable body weight for up to 7 weeks post-transplantation (Figure 4B). In this model, recipient-derived hematopoietic stem cells were not destroyed completely by sublethal irradiation, resulting in the development of chimeric mice. Human leukocytes were mainly composed of T cells, whereas mouse

leukocytes were mostly granulocytes and monocytes/macrophages. Although anti-IL-26 mAb administration did not affect donor CD4 and CD8 T cell expansion, there was a trend toward a decrease in the percentage of mouse granulocytes in hCBMC-NOG mice receiving m69-10 or h69-10 (Figure 4C).

Although consolidation in lung, regenerative change in bile duct epithelium, cholestasis in hepatocytes, and acanthosis, follicular dropout, sclerosis of reticular dermis, and fat loss in skin were often observed in hCBMC-NOG mice receiving control IgG, progression of these systemic GVHD symptoms were prominently suppressed in m69-10 or h69-10-administered hCBMC-NOG mice, with hardly any GVHD manifestation observed in colon tissues of all mice (Figure 4D,E, Figure S11). Furthermore, significant decrease in resistance and elastance, and increase in compliance were observed in pulmonary functions of hCBMC-NOG mice receiving anti-IL-26 mAb (Figure 4F). Serum alanine transaminase activity was also elevated in mice treated with control IgG compared to anti-IL-26 mAb (Figure 4G). These data indicate that both h69-10 and m69-10 treatment significantly impeded chronic GVHD development.

3.6 | Anti-IL-26 mAb-mediated suppression of T cell and neutrophil infiltration, Th17 response, and fibroproliferation

Administration of h69-10 or m69-10 markedly reduced the total number of donor leukocytes in both lung and liver of hCBMC-NOG mice, while the percentage of CD4 and CD8 T cells in donor leukocytes of mice receiving anti-IL-26 mAb was nearly identical to that of mice receiving control IgG, indicating that anti-IL-26 mAb treatment decreased the absolute number of donor CD4 and CD8 T cells in the GVHD-target organs (Figure 5A–C). Anti-IL-26 mAb administration also significantly reduced the total number of recipient leukocytes in lung and the percentage of neutrophils in recipient leukocytes in the spleen, lung, or liver of hCBMC-NOG mice, indicating that anti-IL-26 mAb treatment reduced neutrophils systemically, but particularly in lung of hCBMC-NOG mice (Figure 5A–C, Figure S12).

Most of donor CD4 and CD8 T cells in hCBMC-NOG recipients expressed PD-1, suggesting a TCR-stimulated phenotype (Figure 5D). In addition, anti-IL-26 mAb treatment markedly decreased human *IL26*, *IL17A*, and *IL21* but not *IFNG* and *IL4* expression

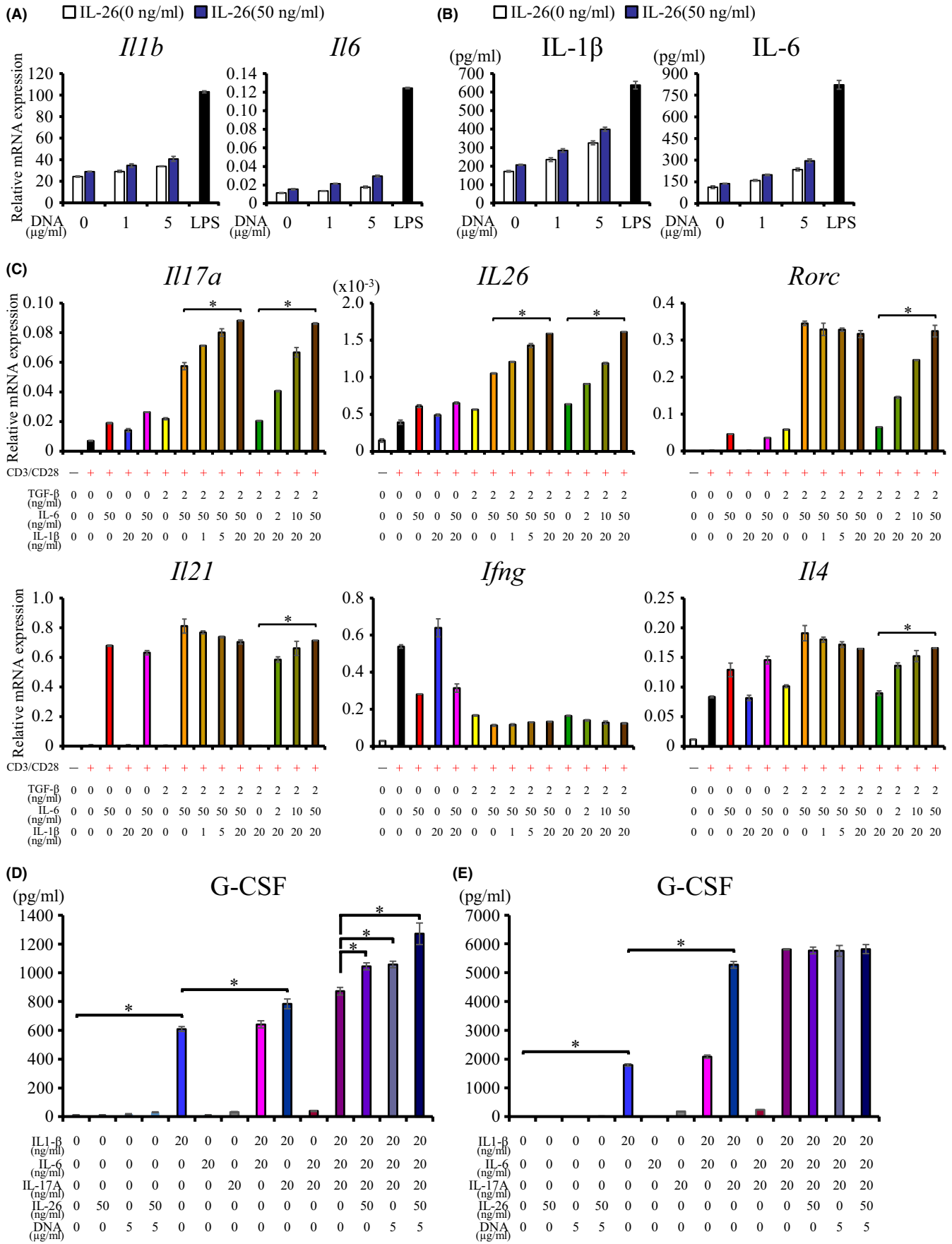


FIGURE 4 Reduced xeno-GVHD-associated lethality and weight loss in hCBMC-NOG mice by anti-IL-26 mAb treatment. Human umbilical cord blood mononuclear cells (hCBMC)-NOG mice were injected intraperitoneally with control mouse IgG (isotype), mouse anti-human IL-26 mAb (m69-10), or humanized anti-IL-26 mAb (h69-10) at 100 μ g per dose twice weekly from day +28 until the end of experiments. (A) Kaplan–Meier survival curves for NOG mice receiving hCBMC plus control IgG (blue line, $n = 10$), m69-10 (orange line, $n = 10$) ($p < .0001$ vs. control IgG group), or h69-10 (red line, $n = 5$) ($p = .0028$ vs. control IgG group). (B) Average body weight (mean percentage \pm S.D. of initial) for mice surviving on a given day for different groups of mice as shown in (A). (C) Time-course changes of average percentage (\pm S.D.) of donor cells (hCD45⁺H-2K^d) or mouse granulocytes fraction (hCD45⁺H-2K^d+SSC^{hi}) in total leukocytes, percentage of human CD4 T cells (hCD4⁺hCD8a⁻) or CD8 T cells (hCD4⁺hCD8a⁺) in donor cells (gated for hCD45⁺H-2K^d) in peripheral blood of NOG recipients were analyzed by flow cytometry. (D) Pathological GVHD scores for lung (range 0 to 9), liver (range 0 to 8), colon (range 0 to 8), or skin (range 0 to 10) from normal NOG mice ($n = 3$) or NOG recipients 8 weeks post-transplantation of hCBMC (control IgG group $n = 6$, m69-10 group $n = 6$, h69-10 group $n = 5$). NS denotes “not significant.” (E) H&E staining of lung, liver, colon, or skin from each group as shown in (D). Representative images are shown with similar results. Original magnification lung $\times 100$, liver, colon, skin $\times 200$. Lower magnification images are shown in Figure S11. (F) Pulmonary function of normal NOG mice ($n = 3$) or NOG recipients 8 weeks post-transplantation of hCBMC (control IgG, m69-10, or h69-10 group $n = 5$ each) was analyzed by the flexiVent system. (G) Serum alanine transaminase (ALT) activity of normal NOG mice ($n = 3$) or NOG recipients 8 weeks post-transplantation of hCBMC (control IgG group $n = 8$, m69-10 group $n = 8$, h69-10 group $n = 5$). (A–G) Data represent the combined results of three (A–C, G) or two (D–F) independent experiments. (C, D, F, G) Data are shown as mean \pm S.D. of each group, comparing values in control IgG group to m69-10 group or h69-10 group ($*p < .05$).

levels in human CD4 T cells (Figure 5E, Figure S13), plasma levels of human IL-26 and IL-17A (Figure 5F), and mRNA expression levels of mouse *Ccl3*, *Ccl5*, *Cxcl1*, *Cxcl2*, *Il1b*, *Il6*, and *Csf3* in lung or liver of hCBMC-NOG recipients (Figure 5G).

While the lung of hCBMC-NOG mice receiving control IgG manifested significant peribronchiolar and perivascular collagen deposition and enhanced α -smooth muscle actin-positive myofibroblast level as compared with normal NOG mice (Figure, 5H,I, Figure S14), levels of collagen deposition, myofibroblasts as well as IL-26⁺ cells were prominently decreased in the lung of anti-IL-26 mAb-treated hCBMC-NOG mice (Figure 5H,I). Taken together, our data indicate that anti-IL-26 mAb treatment significantly suppresses T cell and neutrophil infiltration into GVHD-target organs, Th17 response, and fibroproliferation.

3.7 | Maintenance of GVL effect in hCBMC-NOG mice receiving anti-IL-26 mAb treatment

Since GVHD and GVL are highly linked immune reactions,³⁰ our next studies evaluated the potential influence of anti-IL-26 mAb on GVL effect. To stably develop tumor-disseminated recipient mice, firefly luciferase-transfected A20 (A20-luc) cells were inoculated on day +28 after hCBMC transplantation, followed by anti-IL-26 mAb treatment (Figure 6A). NOG mice inoculated with A20-luc alone displayed prominent tumor proliferation (Figure 6B,C), succumbing to high tumor burden within 3 weeks post-tumor inoculation. hCBMC-NOG recipients receiving control IgG exhibited clinical symptoms of GVHD such as weight loss and alopecia, although tumor progression was clearly suppressed, possibly by human T cells. In contrast, anti-IL-26 mAb treatment suppressed both tumor progression and GVHD manifestations (Figure 6B,C).

Meanwhile, mRNA expression levels of *IFNG*, *TNF*, *FASLG*, and protein expression levels of perforin and granzyme B as effector molecules in human CD8 T cells isolated from the spleen of hCBMC-NOG recipients following 3 weeks of anti-IL-26 mAb were

comparable to mice treated with control IgG (Figure 6D,E). Taken together, our data indicate that effective GVL function is preserved in IL-26 mAb-treated recipients, possibly due to the maintenance of donor CD8 T cell cytotoxic functions.

3.8 | Elevated serum IL-26 level in GVHD patients

Extending our findings to the clinical setting, we found that two of nine patients with mild acute skin GVHD (829.1 and 723.1 pg/mL) and three of six chronic lung GVHD patients (1913.8, 1683.4, and 851.9 pg/mL) exhibited markedly high IL-26 levels, and the mean value of chronic lung GVHD patients (919.7 ± 739.5 pg/mL, $n = 6$) was significantly higher as compared with acute skin GVHD patients (219.9 ± 320.9 pg/mL, $n = 9$) and healthy controls (85.6 ± 80.8 pg/mL, $n = 12$; Figure 7A). Time-course analysis was conducted for one patient with severe chronic lung GVHD manifested by pneumothorax and pneumomediastinum at 137 days post-transplantation. Along with increased levels of neutrophils and several inflammatory cytokines, IL-26 serum level was markedly increased by day +143 with the onset of chronic GVHD, with a significant decrease by day +160 following 3 weeks of prednisolone treatment (from 1913.8 to 198.6 pg/mL), associated with improved clinical symptoms (Figure 7B). In contrast, serum IL-26 level in another patient with moderate chronic lung GVHD was hardly affected by 3 weeks of prednisolone treatment (from 624.1 to 578.3 pg/mL; Figure 7C). Our data indicate that serum IL-26 level is elevated at least in some chronic GVHD patients.

Based on our findings, Figure 8 depicts a schematic of the immunological effects of IL-26 in the pathophysiology of chronic systemic inflammation.

4 | DISCUSSION

Although IL-26 is known as a Th17 cytokine, its precise role in inflammatory disorders is not fully understood due to the deficiency

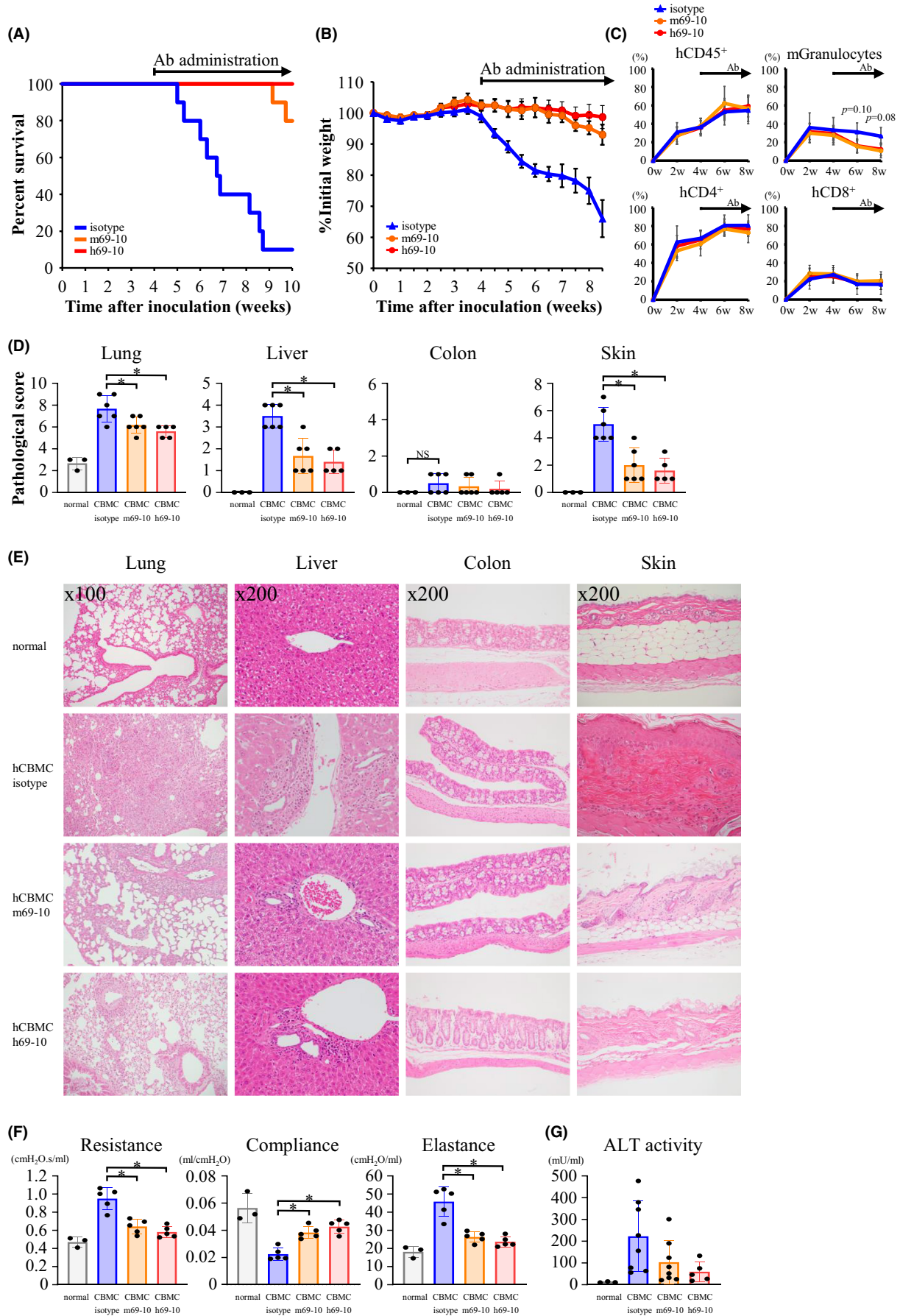


FIGURE 5 Anti-IL-26 mAb-mediated reduction of inflammatory cell infiltration into GVHD-target tissues and suppression of proinflammatory cytokine/chemokine expression and collagen deposition in lung of hCBMC-NOG mice. Transplantation and mAb treatment were performed as described in Figure 4. (A–E, G–I) Spleen, lung, or liver was harvested from normal NOG mice ($n = 3$) or NOG recipients 8 weeks post-transplantation of human umbilical cord blood mononuclear cells (hCBMC) (control mouse IgG [isotype] group $n = 6$, mouse anti-human IL-26 mAb [m69-10] group $n = 6$, humanized anti-IL-26 mAb [h69-10] group $n = 5$). (A, B) The number of donor and recipient leukocytes (mean \pm S.D.) in the lung (A) or liver (B) of NOG mice was determined by cell counting and the percentage of donor cells (hCD45⁺mCD45⁻) and recipient cells (hCD45⁻mCD45⁺) was analyzed by flow cytometry. NS denotes “not significant.” (C) Average percentage (\pm S.D.) of human CD4 T cells (hCD3⁺hCD4⁺hCD8a⁻) or CD8 T cells (hCD3⁺hCD4⁻hCD8a⁺) in donor leukocytes (gated for hCD45⁺mCD45⁻), or mouse neutrophils (mCD11b⁺mLy-6G⁺) in recipient leukocytes (gated for hCD45⁻mCD45⁺) in spleen, lung, or liver of NOG recipients were analyzed by flow cytometry. (D) Average percentage (\pm S.D.) of PD-1⁺ in donor CD4 T cells (gated for hCD45⁺mCD45⁻hCD3⁺hCD4⁺hCD8a⁻) or CD8 T cells (gated for hCD45⁺mCD45⁻hCD3⁺hCD4⁻hCD8a⁺) in spleen, lung, or liver of NOG recipients were analyzed by flow cytometry. (E) Donor CD4 T cells in the spleen, lung, or liver of hCBMC-NOG mice were purified by cell sorting (gated for hCD45⁺H-2K^dhCD3⁺hCD4⁺hCD8a⁻). mRNA expression levels of indicated human genes in those cells were quantified by real-time RT-PCR. (F) Plasma was collected from hCBMC-NOG mice at the indicated time points (for each, $n = 8$ in control mouse IgG or m69-10 group). Plasma levels of human IL-26 and human IL-17A were quantified by ELISA. The dashed line indicates the detection limit. (G) mRNA expression levels of indicated mouse genes in the homogenates of lung or liver tissue of hCBMC-NOG mice were quantified by real-time RT-PCR. (H) Representative images of Azan-Mallory staining or immunohistochemical staining with α -smooth muscle actin (α -SMA) and human IL-26 of lung from each group are shown with similar results. Original magnification $\times 80$ (Azan-Mallory staining, α -SMA), $\times 200$ (human IL-26). Insets, higher magnification images of the boxed regions. Red arrows indicate IL-26-positive lymphocytes. Lower magnification images are shown in Figure S14. (I) Staining intensity was analyzed using Image-J software. For quantification, five images were taken per mouse, and each dot indicates the mean %positive area. The dashed line indicates the percentage of non-specific staining (background intensity). (A–I) Data represent the combined results of two (A–E, G–I) or five (F) independent experiments. (A–G, I) Data are shown as mean \pm S.D. of each group, comparing values in control IgG group to m69-10 group or h69-10 group ($*p < .05$). (E, G) Each expression was normalized to human hypoxanthine phosphoribosyltransferase 1 (HPRT1) (E) or mouse *Hprt* (G).

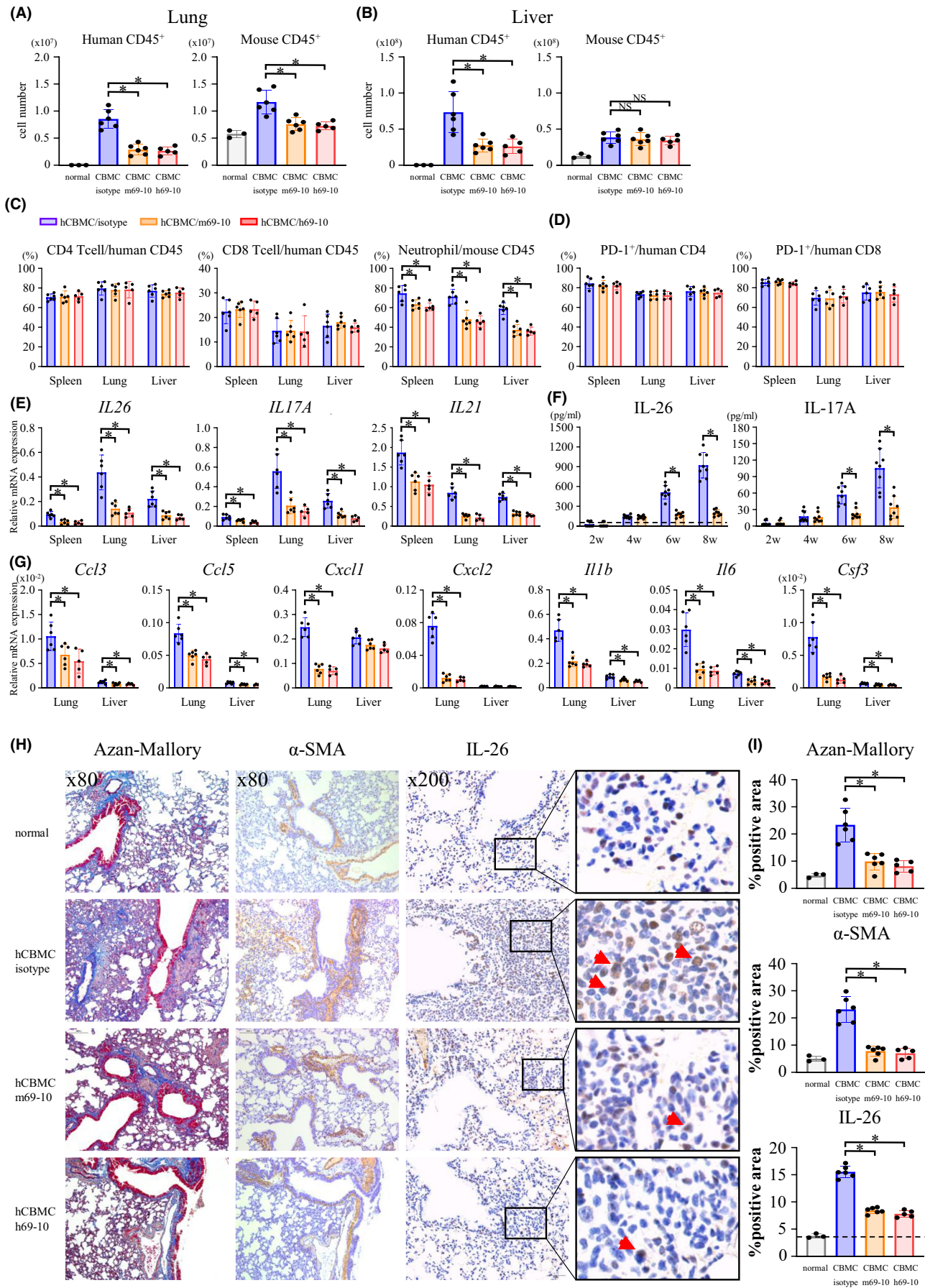
of IL26 in mice. Our group has previously shown that CD26 is a key costimulatory molecule for inducing IL-26 production from human CD4 T cells, and IL-26 is strongly associated with lung fibrosis in a chronic xeno-GVHD model.²⁴ In this present paper, we evaluate the in vivo immunological effects of IL-26 on the level and composition of immune cells, T cell phenotypes, and inflammatory cytokine/chemokine expression utilizing hIL-26Tg mice and hCBMC. Furthermore, we demonstrate that humanized neutralizing anti-IL-26 mAb significantly impedes the development of chronic xeno-GVHD with preservation of GVL effect.

The xeno-GVHD model has several artificial characteristics. For example, almost all the human leukocytes engrafted in the recipient NOG mice are T cells and B cells, while neither human NK cells, antigen-presenting cells nor granulocytes have normal maturation and differentiation in this model. In addition, as human IFN- γ has been reported not to transduce signals through murine IFN- γ receptor,²³ it is possible that several human effector molecules may not regulate murine cell functions as compared with human cells. In human, IL-26 can be produced not only from CD4 T cells but also from other cell types,^{8–11} while the cellular mechanisms involved in regulating IL-26 transcription have not been fully elucidated, including detailed characterization of IL-26-associated transcription factors or promoter regions. For these reasons, we utilized BAC Tg mice carrying a 190-kb that includes sequences upstream and downstream of the human IL-26 transcription region. In this murine model, human IL-26 is induced only when the cells capable of expressing IL-26 are activated, although the expression level of human IL-26 in murine cells is quite low as compared with activated human CD4 T cells. For these reasons, inflammation models utilizing human T cells are essential to investigate the inherent functions of human IL-26.

Cross-species models have imperfections that need to be addressed, but we also believe that they can be used to improve our knowledge of human immunology, particularly for detailed analysis of genes that are deficient in mice or have different functions between human and mice. Of note, in the present study, we investigated the in vivo immunological effects of IL-26 utilizing both allo- and xeno-GVHD models and found that IL-26 markedly increases neutrophil levels and augments Th17 response associated with enhanced levels of G-CSF, IL-1 β , and IL-6 in both models.

In fact, several differences were found between the allo- and xeno-GVHD models. The number of donor T cells infiltrated in GVHD-target organs were not affected by IL-26 in the allo-GVHD model (Figure 2A), whereas administration of anti-IL-26 mAb significantly reduced donor T cell infiltration in the xeno-GVHD model (Figure 5A,B). In addition, IL-26-induced enhancement of mouse *Ccl3*, *Cxcl1*, and *Cxcl2* expression and lung fibroproliferation was prominently observed only in the xeno-GVHD model but not the allo-GVHD model (Figure 5G,H). These observed differences may be partially due to the higher expression levels of IL-26 in donor human CD4 T cells as compared with hIL-26Tg mouse-derived donor CD4 T cells (Figures 2D,G and 5E,F), and may be reflected in the survival curves shown for these two models (Figures 1A and 4A).

Our in vivo models indicate that IL-26 has the capacity to augment Th17 response (Figures 2D and 5E). Involvement of Th17 cells in the pathology of various autoimmune diseases has been reported.³¹ Regarding GVHD, transfer of in vitro polarized Th17 cells resulted in extensive pathologic cutaneous and pulmonary lesions in murine GVHD models.³² Our in vitro data suggest that the potential synergistic effect of IL-26 and nucleic acids (Figure 3A,B), or other inflammatory cytokines may lead to enhanced IL-1 β and IL-6



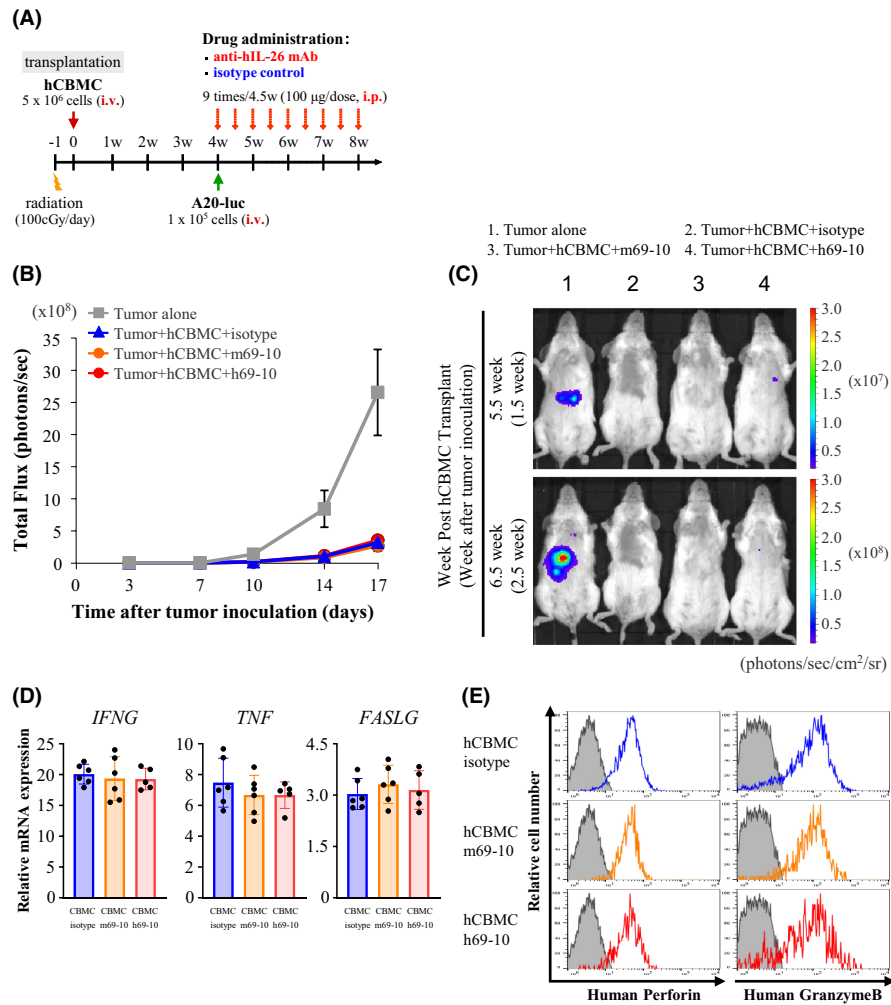


FIGURE 6 Retention of GVL effect following anti-IL-26 mAb treatment. (A) Schematic showing a schedule of GVL experiments. Firefly luciferase-transfected A20 (A20-luc) cells (1×10^5) were inoculated intravenously on day +28 post-transplantation of human umbilical cord blood mononuclear cells (hCBMC). hCBMC/A20-luc-NOG mice were injected intraperitoneally with control mouse IgG (isotype $n = 6$), mouse anti-human IL-26 mAb (m69-10 $n = 6$), or humanized anti-IL-26 mAb (h69-10 $n = 5$) at 100 µg per dose twice weekly from day +28 until the end of experiments. (B) Tumor dissemination was monitored twice weekly using in vivo bioluminescence imaging. NOG mice inoculated with A20-luc without transplantation of hCBMC were used as a control (Tumor alone $n = 5$). Data are shown as mean \pm S.D. of each group. (C) Representative in vivo bioluminescence images from each group 1.5 week or 2.5 week after A20-luc inoculation are shown with similar results. (D) Donor CD8 T cells in the spleen of hCBMC/A20-luc-NOG mice 7 weeks post-transplantation of hCBMC were purified by cell sorting (gated for $hCD45^+H-2K^d^-hCD3^+hCD4^-hCD8a^+$). mRNA expression levels of indicated human genes in those cells were quantified by real-time RT-PCR. Each expression was normalized to human hypoxanthine phosphoribosyltransferase 1 (*HPRT1*). Data are shown as mean \pm S.D. of each group. (E) Data are shown as histogram of human perforin and granzyme B in donor CD8 T cells as described in (D) (gated for $hCD45^+H-2K^d^-hCD3^+hCD4^-hCD8a^+$). The gray areas in each histogram show the data of isotype controls. Representative results from each group are shown with similar results. (B, D) Data represent the combined results of three independent experiments.

expression in the GVHD-target organs (Figures 2I and 5G), resulting in a positive-feedback loop which further augmented Th17-cytokine production including IL-26, IL-17A, and IL-21 (Figure 8).

In the current study, we analyzed donor immune cell numbers and composition. In addition to the immune cells shown in Figure 2B, we also analyzed the percentage of NK cells, NKT cells, $\gamma\delta$ T cells, plasma cells, basophils, eosinophils, mast cells, conventional, and plasmacytoid dendritic cells (data not shown). Among them, IL-26 appeared to be involved in the marked increase in

neutrophil levels (Figures 1C and 2B). While neutrophils have a well-known role in host defense against pathogens, recent studies have described various effector functions of neutrophils.³³ Although the role of neutrophils in the pathology of GVHD is not fully understood, production of reactive oxygen species and antigen presentation by neutrophils affected the severity of intestinal acute GVHD.^{34,35} Moreover, release of NETs caused epitheliopathy and delayed epithelial wound healing in ocular chronic GVHD.³⁶ In a human CD4 T cell-induced cutaneous xeno-GVHD model,

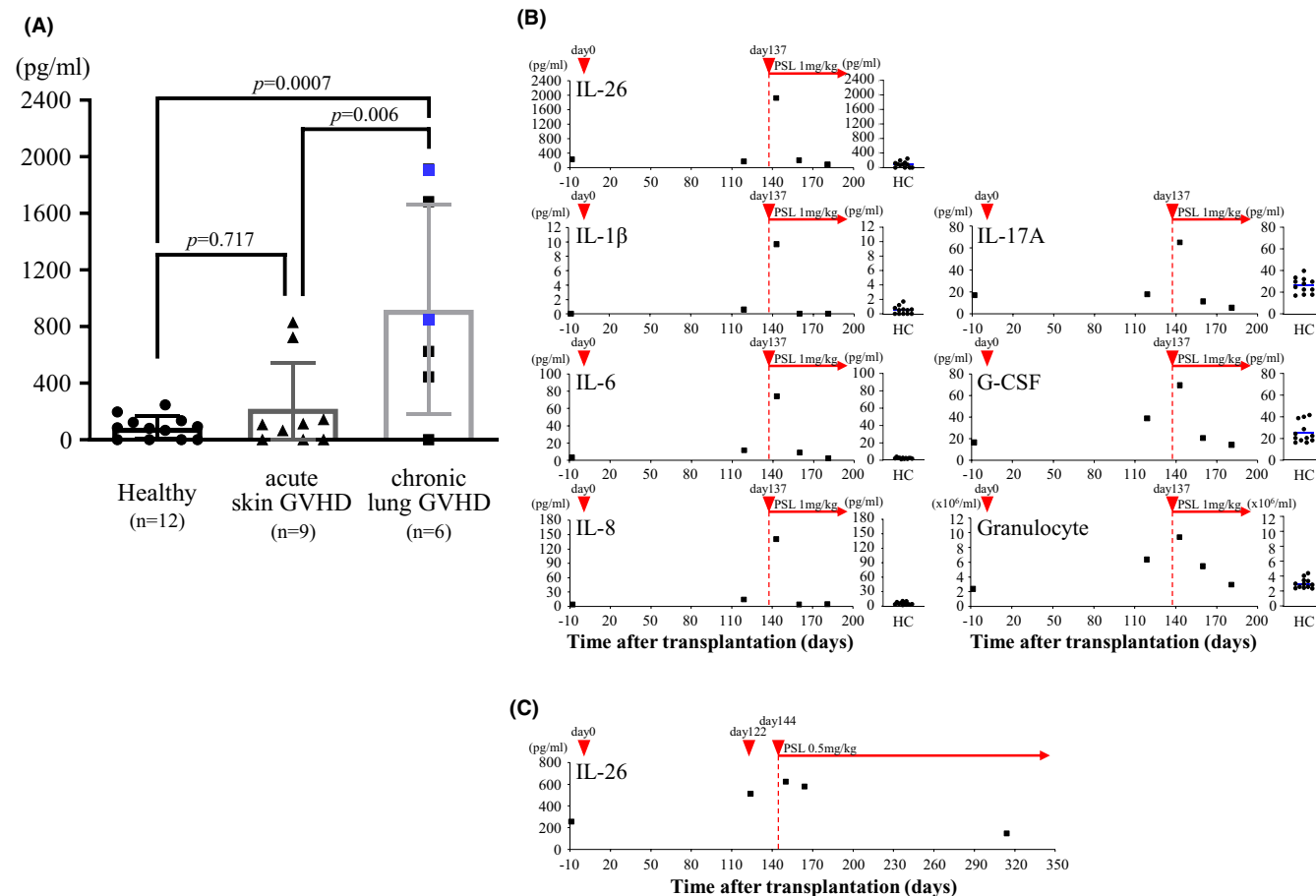


FIGURE 7 IL-26 concentrations in the serum of acute skin GVHD and chronic lung GVHD patients. (A) IL-26 concentrations in the serum of 12 healthy controls, nine mild acute skin GVHD patients (two grade I and seven grade II), or six moderate/severe chronic lung GVHD patients (two severe and four moderate) were quantified by ELISA. Serum was collected after the onset of GVHD. Two blue squares in the chronic lung GVHD group indicate the values of severe GVHD patients. Data are shown as mean \pm S.D. of each group, comparing values in each group, respectively. (B) Time-course analysis of the serum of one severe chronic lung GVHD patient is shown in (A). Serum was collected on day -8 (before transplantation), day +119 (before onset of chronic GVHD), day +143, +160, and +181 (after receiving prednisolone [PSL] treatment [1 mg/kg/day]). Transplantation was performed on day 0. The patient was diagnosed with severe chronic lung GVHD on day +137 and started receiving PSL treatment on day +137. Serum levels of IL-26 were quantified by ELISA, and serum levels of 17 human cytokines were quantified utilizing multiplex assay kit, as described in [Supplementary Materials and Methods](#). Representative results among 17 cytokines are shown, along with the number of neutrophils in the peripheral blood. Serum levels of each cytokine in 12 healthy controls (HC) were measured as control. Each dot indicates individual value, and blue horizontal bars indicate mean value. (C) Time-course analysis in the serum of one moderate chronic lung GVHD patient is shown in (A). Serum was collected on day -9 (before transplantation), day +124 (immediately after diagnosis of chronic GVHD), day +150, +164, and +314 (after receiving PSL treatment [0.5 mg/kg/day]). Transplantation was performed on day 0. The patient was diagnosed with moderate chronic lung GVHD on day +122 and started receiving PSL treatment on day +144. Serum levels of IL-26 were quantified by ELISA. [Color figure can be viewed at [wileyonlinelibrary.com](#)]

murine neutrophils appeared to be involved in the onset of alopecia.³⁷ Neutrophils are able to acquire different functions depending on the microenvironment and their differentiation/activation status.³⁸ Our current work shows that IL-26 exposure was associated with elevated IL-6 and G-CSF expression (Figures 2I and 5G). Stimulation of human neutrophils with G-CSF enhanced antibody-dependent cellular cytotoxicity and cytokine production.³⁹ Others reported that costimulation of mouse neutrophils with IL-6 and G-CSF increased matrix metalloproteinase-9.⁴⁰ Therefore, in-depth analyses of the effector functions of neutrophils that accumulated in the GVHD-target organs in the presence of IL-26, as

well as their involvement in the pathology of GVHD in our models, are needed in future studies.

G-CSF can be produced from diverse cell types such as monocytes/macrophages, epithelial cells, endothelial cells, and fibroblasts in response to various stimuli including IL-1 β , IL-6, TNF- α , IL-17A, and lipopolysaccharide,⁴¹⁻⁴⁴ suggesting that the overall IL-26-mediated positive-feedback loop is possibly associated with enhanced G-CSF expression. Likewise, although TGF- β 1 plays a central role in fibrosis, diverse factors such as IL-17A, IL-11, IL-13, IL-1 β , TNF- α , PDGF- α , CTGF also participate in the complex cellular mechanisms involved in fibrosis.⁴⁵⁻⁴⁷ Our group previously

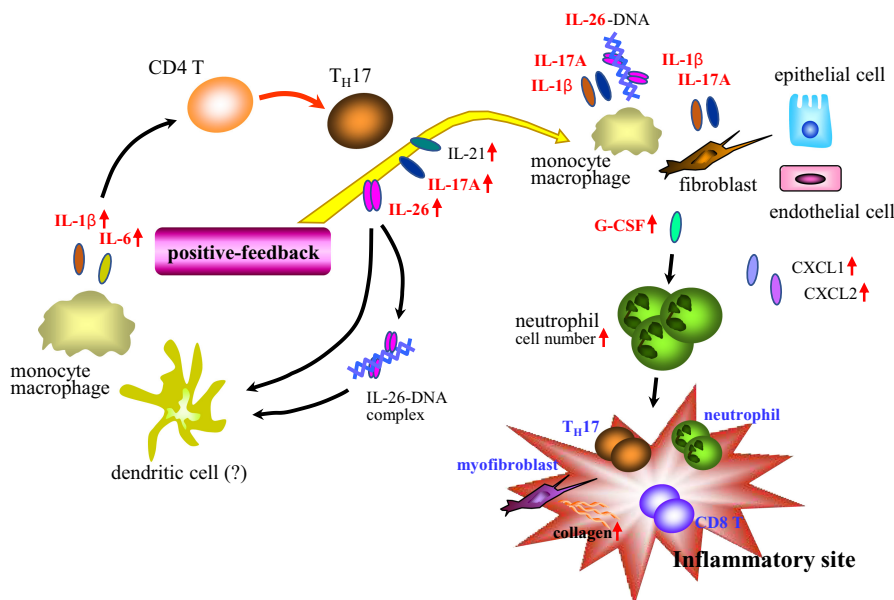


FIGURE 8 Hypothetical schema of immunological effects of IL-26 in the pathology of chronic systemic inflammation. IL-26 solely or the combination of IL-26 and nucleic acids cooperatively activates antigen-presenting cells (myeloid cells) to enhance the production of IL-1 β and IL-6, resulting in the differentiation and activation of Th17 cells to augment Th17-cytokine production such as IL-26, IL-17A, and IL-21. Granulocyte-colony stimulating factor (G-CSF), a key factor for the differentiation and proliferation of neutrophils, can be produced by various cell types such as monocytes/macrophages, fibroblasts, epithelial cells, and endothelial cells. Since IL-1 β and IL-17A have the capacity to markedly enhance G-CSF production from these cells, IL-26-mediated positive-feedback loop described above greatly augments G-CSF production, resulting in increased neutrophil cell number not only at the inflammatory sites but also in the whole body (both in the blood and spleen). In addition, high levels of IL-26 may enhance production of CXCL1 and CXCL2 as neutrophil chemo-attractants, and recruitment of both CD4 T cells and CD8 T cells at the inflammatory sites. Furthermore, IL-26 enhances myofibroblast level and collagen deposition, particularly in the lung and skin.

showed that IL-26 directly acted on fibroblasts to enhance collagen production,²⁴ while alteration in the immune cell infiltration process and cytokine milieu by IL-26 is likely associated with the IL-26-mediated fibrosis. The mechanisms involved in IL-26 regulation of myofibroblast biology and collagen production will be evaluated in future studies.

In summary, our current work indicates that anti-IL-26 mAb treatment significantly suppressed the progression of GVHD via multiple mechanisms of action. We plan to analyze the serum concentration of IL-26 in GVHD patients and investigate the relationship between serum IL-26 levels and clinical outcomes for patients such as the severity or disease types of GVHD, types of hematological malignancies, and effects of steroid or other immunosuppressive agents. These basic findings will provide the necessary foundation for the use of humanized anti-IL-26 mAb for the treatment of chronic GVHD.

ACKNOWLEDGMENTS

This study was supported in part by a grant of the Ministry of Health, Labour, and Welfare, Japan (Grant Number 180101-01 (C.M.) and 210901-02 (C.M.)), JSPS KAKENHI Grant Numbers JP20K07683 (R.H.), JP21K16389 (T.I.), JP20H03471 (C.M.), and JP18H02782 (K.O.). This work was also supported by a research grant from the Japanese Society of Hematology (R.H.), a research grant from the Japan

Research Institute of Industrial Science (R.H.), and President's Grant for Educational Excellence, Juntendo University Grant Number GP21-04 (K.O.). The authors thank Dr. Naoko Arano and Dr. Hitoshi Sasano for their excellent assistance with pulmonary function tests (Department of Respiratory Medicine, Juntendo University, Japan). The authors also thank members of the Atopy (Allergy) Research Center (Juntendo University Graduate School of Medicine, Japan) and members of the Laboratory of Morphology and Image Analysis, the Laboratory of Cell Biology, the Laboratory of Proteomics and Biomolecular Science, and the Laboratory of Molecular and Biochemical Research (Biomedical Research Core Facilities, Juntendo University Graduate School of Medicine, Japan) for their technical assistance and for the use of the experimental apparatus.

DISCLOSURE

The authors of this manuscript have conflicts of interest to disclose as described by the *American Journal of Transplantation*. Ryo Hatano, Takumi Itoh, Yutaro Kaneko, Chikao Morimoto, and Kei Ohnuma are the inventors and patent holders of murine and humanized anti-human IL-26 mAbs. Yutaro Kaneko is the chief executive officer of Y's AC Co., Ltd, and Chikao Morimoto, Kei Ohnuma, Nam H. Dang, and Taketo Yamada are stockholders of Y's AC Co., Ltd. Other authors declare no competing financial interests associated with this manuscript.

DATA AVAILABILITY STATEMENT

The data that support the findings of this study are available in the supporting information files of this article.

ORCID

Ryo Hatano  <https://orcid.org/0000-0002-2727-7275>

Norihiro Harada  <https://orcid.org/0000-0002-0962-5731>

REFERENCES

1. Beura LK, Rosato PC, Masopust D. Implications of resident memory T cells for transplantation. *Am J Transplant.* 2017;17(5):1167-1175.
2. Copelan EA. Hematopoietic stem-cell transplantation. *N Engl J Med.* 2006;354(17):1813-1826.
3. Anasetti C, Logan BR, Lee SJ, et al. Peripheral-blood stem cells versus bone marrow from unrelated donors. *N Engl J Med.* 2012;367(16):1487-1496.
4. Chang YJ, Zhao XY, Huang XJ. Strategies for enhancing and preserving anti-leukemia effects without aggravating graft-versus-host disease. *Front Immunol.* 2018;9:3041.
5. Kotenko SV. The family of IL-10-related cytokines and their receptors: related, but to what extent? *Cytokine Growth Factor Rev.* 2002;13(3):223-240.
6. Donnelly RP, Sheikh F, Dickensheets H, Savan R, Young HA, Walter MR. Interleukin-26: an IL-10-related cytokine produced by Th17 cells. *Cytokine Growth Factor Rev.* 2010;21(5):393-401.
7. Schoenborn JR, Dorschner MO, Sekimata M, et al. Comprehensive epigenetic profiling identifies multiple distal regulatory elements directing transcription of the gene encoding interferon-gamma. *Nat Immunol.* 2007;8(7):732-742.
8. Corvaisier M, Delneste Y, Jeanvoine H, et al. IL-26 is overexpressed in rheumatoid arthritis and induces proinflammatory cytokine production and Th17 cell generation. *PLoS Biol.* 2012;10(9):e1001395.
9. Che KF, Tengvall S, Levanen B, et al. Interleukin-26 in antibacterial host defense of human lungs. Effects on neutrophil mobilization. *Am J Respir Crit Care Med.* 2014;190(9):1022-1031.
10. Che KF, Kaarteenaho R, Lappi-Blanco E, et al. Interleukin-26 production in human primary bronchial epithelial cells in response to viral stimulation: modulation by Th17 cytokines. *Mol Med.* 2017;23:247-257.
11. Itoh T, Hatano R, Horimoto Y, et al. IL-26 mediates epidermal growth factor receptor-tyrosine kinase inhibitor resistance through endoplasmic reticulum stress signaling pathway in triple-negative breast cancer cells. *Cell Death Dis.* 2021;12(6):520.
12. Hor S, Pirzer H, Dumoutier L, et al. The T-cell lymphokine interleukin-26 targets epithelial cells through the interleukin-20 receptor 1 and interleukin-10 receptor 2 chains. *J Biol Chem.* 2004;279(32):33343-33351.
13. Miot C, Beaumont E, Duluc D, et al. IL-26 is overexpressed in chronically HCV-infected patients and enhances TRAIL-mediated cytotoxicity and interferon production by human NK cells. *Gut.* 2015;64(9):1466-1475.
14. Wolk K, Kunz S, Asadullah K, Sabat R. Cutting edge: immune cells as sources and targets of the IL-10 family members? *J Immunol.* 2002;168(11):5397-5402.
15. Itoh T, Hatano R, Komiya E, et al. Biological effects of IL-26 on T cell-mediated skin inflammation, including psoriasis. *J Invest Dermatol.* 2019;139(4):878-889.
16. Meller S, Di Domizio J, Voo KS, et al. T(H)17 cells promote microbial killing and innate immune sensing of DNA via interleukin 26. *Nat Immunol.* 2015;16(9):970-979.
17. Dang AT, Teles RM, Weiss DI, et al. IL-26 contributes to host defense against intracellular bacteria. *J Clin Invest.* 2019;129(5):1926-1939.
18. Poli C, Augusto JF, Dauve J, et al. IL-26 confers proinflammatory properties to extracellular DNA. *J Immunol.* 2017;198(9):3650-3661.
19. Collins PL, Chang S, Henderson M, et al. Distal regions of the human IFNG locus direct cell type-specific expression. *J Immunol.* 2010;185(3):1492-1501.
20. Collins PL, Henderson MA, Aune TM. Lineage-specific adjacent IFNG and IL26 genes share a common distal enhancer element. *Genes Immun.* 2012;13(6):481-488.
21. Corridoni D, Antanaviciute A, Gupta T, et al. Single-cell atlas of colonic CD8(+) T cells in ulcerative colitis. *Nat Med.* 2020;26(9):1480-1490.
22. Hatano R, Itoh T, Otsuka H, et al. Characterization of novel anti-IL-26 neutralizing monoclonal antibodies for the treatment of inflammatory diseases including psoriasis. *MAbs.* 2019;11(8):1428-1442.
23. Gibbs VC, Williams SR, Gray PW, et al. The extracellular domain of the human interferon gamma receptor interacts with a species-specific signal transducer. *Mol Cell Biol.* 1991;11(12):5860-5866.
24. Ohnuma K, Hatano R, Aune TM, et al. Regulation of pulmonary graft-versus-host disease by IL-26+CD26+CD4 T lymphocytes. *J Immunol.* 2015;194(8):3697-3712.
25. Bettelli E, Carrier Y, Gao W, et al. Reciprocal developmental pathways for the generation of pathogenic effector TH17 and regulatory T cells. *Nature.* 2006;441(7090):235-238.
26. Chung Y, Chang SH, Martinez GJ, et al. Critical regulation of early Th17 cell differentiation by interleukin-1 signaling. *Immunity.* 2009;30(4):576-587.
27. McGeachy MJ, Chen Y, Tato CM, et al. The interleukin 23 receptor is essential for the terminal differentiation of interleukin 17-producing effector T helper cells in vivo. *Nat Immunol.* 2009;10(3):314-324.
28. Korn T, Bettelli E, Gao W, et al. IL-21 initiates an alternative pathway to induce proinflammatory T(H)17 cells. *Nature.* 2007;448(7152):484-487.
29. Lieschke GJ, Grail D, Hodgson G, et al. Mice lacking granulocyte colony-stimulating factor have chronic neutropenia, granulocyte and macrophage progenitor cell deficiency, and impaired neutrophil mobilization. *Blood.* 1994;84(6):1737-1746.
30. Wu CJ, Ritz J. Revealing tumor immunity after hematopoietic stem cell transplantation. *Clin Cancer Res.* 2009;15(14):4515-4517.
31. Kuwabara T, Ishikawa F, Kondo M, Kakiuchi T. The role of IL-17 and related cytokines in inflammatory autoimmune diseases. *Mediators Inflamm.* 2017;2017:3908061.
32. Carlson MJ, West ML, Coghill JM, Panoskaltis-Mortari A, Blazar BR, Serody JS. In vitro-differentiated TH17 cells mediate lethal acute graft-versus-host disease with severe cutaneous and pulmonary pathologic manifestations. *Blood.* 2009;113(6):1365-1374.
33. Tecchio C, Cassatella MA. Uncovering the multifaceted roles played by neutrophils in allogeneic hematopoietic stem cell transplantation. *Cell Mol Immunol.* 2021;18(4):905-918.
34. Schwab L, Goroncy L, Palaniyandi S, et al. Neutrophil granulocytes recruited upon translocation of intestinal bacteria enhance graft-versus-host disease via tissue damage. *Nat Med.* 2014;20(6):648-654.
35. Hulsdunker J, Ottmuller KJ, Neeff HP, et al. Neutrophils provide cellular communication between ileum and mesenteric lymph nodes at graft-versus-host disease onset. *Blood.* 2018;131(16):1858-1869.
36. An S, Raju I, Surenkhuu B, et al. Neutrophil extracellular traps (NETs) contribute to pathological changes of ocular graft-vs.-host disease (oGVHD) dry eye: implications for novel biomarkers and therapeutic strategies. *Ocul Surf.* 2019;17(3):589-614.
37. Ito R, Katano I, Kawai K, et al. A novel xenogeneic graft-versus-host disease model for investigating the pathological role of human CD4(+) or CD8(+) T cells using immunodeficient NOG mice. *Am J Transplant.* 2017;17(5):1216-1228.
38. Scapini P, Marini O, Tecchio C, Cassatella MA. Human neutrophils in the saga of cellular heterogeneity: insights and open questions. *Immunol Rev.* 2016;273(1):48-60.

39. Carulli G. Effects of recombinant human granulocyte colony-stimulating factor administration on neutrophil phenotype and functions. *Haematologica*. 1997;82(5):606-616.
40. Yan B, Wei JJ, Yuan Y, et al. IL-6 cooperates with G-CSF to induce pro-tumor function of neutrophils in bone marrow by enhancing STAT3 activation. *J Immunol*. 2013;190(11):5882-5893.
41. Fossiez F, Djossou O, Chomarat P, et al. T cell interleukin-17 induces stromal cells to produce proinflammatory and hematopoietic cytokines. *J Exp Med*. 1996;183(6):2593-2603.
42. Roberts AW. G-CSF: a key regulator of neutrophil production, but that's not all! *Growth Factors*. 2005;23(1):33-41.
43. Numasaki M, Takahashi H, Tomioka Y, Sasaki H. Regulatory roles of IL-17 and IL-17F in G-CSF production by lung microvascular endothelial cells stimulated with IL-1beta and/or TNF-alpha. *Immunol Lett*. 2004;95(1):97-104.
44. Wolk K, Brembach TC, Simaite D, et al. Activity and components of the granulocyte colony-stimulating factor pathway in hidradenitis suppurativa. *Br J Dermatol*. 2021;185(1):164-176.
45. Wynn TA, Ramalingam TR. Mechanisms of fibrosis: therapeutic translation for fibrotic disease. *Nat Med*. 2012;18(7):1028-1040.
46. Chanda D, Otoupalova E, Smith SR, Volckaert T, De Langhe SP, Thannickal VJ. Developmental pathways in the pathogenesis of lung fibrosis. *Mol Aspects Med*. 2019;65:56-69.
47. Henderson NC, Rieder F, Wynn TA. Fibrosis: from mechanisms to medicines. *Nature*. 2020;587(7835):555-566.

SUPPORTING INFORMATION

Additional supporting information can be found online in the Supporting Information section at the end of this article.

How to cite this article: Hatano R, Itoh T, Otsuka H, et al. Humanized anti-IL-26 monoclonal antibody as a novel targeted therapy for chronic graft-versus-host disease. *Am J Transplant*. 2022;22:2804-2820. doi: [10.1111/ajt.17178](https://doi.org/10.1111/ajt.17178)

Peripheral endomorphins drive mechanical allodynia under the enzymatic control of CD26/DPPIV



Eriko Komiya, PhD,^a Mitsutoshi Tominaga, PhD,^{a,b} Ryo Hatano, PhD,^c Yuji Kamikubo, PhD,^d Sumika Toyama, PhD,^a Hakushun Sakairi, MD, PhD,^d Kotaro Honda, PhD,^a Takumi Itoh, PhD,^{c,e} Yayoi Kamata, PhD,^{a,b} Munehiro Tsurumachi, MD,^{a,f} Ryoma Kishi, MD,^{a,f} Kei Ohnuma, MD, PhD,^c Takashi Sakurai, MD, PhD,^d Chikao Morimoto, MD, PhD,^c and Kenji Takamori, MD, PhD^{a,b,f} *Chiba and Tokyo, Japan*

Background: Mechanical allodynia (or innocuous mechanical stimuli-evoked itch) often occurs in dry skin-based disorders such as atopic dermatitis and psoriasis. However, the molecular and cellular mechanisms underlying mechanical allodynia remain unclear. We recently reported the involvement of CD26 in the regulation of psoriatic itch. This molecule exhibits dipeptidyl peptidase IV (DPPIV) enzyme activity and exerts its biologic effects by processing various substances, including neuropeptides. **Objective:** The aim of the present study was to investigate the peripheral mechanisms of mechanical allodynia by using CD26/DPPIV knockout (CD26KO) mice.

Methods: We applied innocuous mechanical stimuli to CD26KO or wild-type mice. The total number of scratching responses was counted as the allodynia score. Immunohistochemical and behavioral pharmacologic analyses were then performed to examine the physiologic activities of CD26/DPPIV or endomorphins (EMs), endogenous agonists of μ -opioid receptors.

Results: Mechanical allodynia was more frequent in CD26KO mice than in wild-type mice. The allodynia score in CD26KO mice was significantly reduced by the intradermal

administration of recombinant DPPIV or naloxone methiodide, a peripheral μ -opioid receptor antagonist, but not by that of mutant DPPIV without enzyme activity. EMs (EM-1 and EM-2), selective ligands for μ -opioid receptors, are substrates for DPPIV. Immunohistochemically, EMs were located in keratinocytes, fibroblasts, and peripheral sensory nerves. Behavioral analyses revealed that EMs preferentially provoked mechanical allodynia over chemical itch. DPPIV-digested forms of EMs did not induce mechanical allodynia.

Conclusion: The present results suggest that EMs induce mechanical allodynia at the periphery under the enzymatic control of CD26/DPPIV. (J Allergy Clin Immunol 2022;149:1085-96.)

Key words: CD26, dipeptidyl peptidase IV enzyme, endomorphin, mechanical allodynia, mechanical itch, peripheral μ -opioid receptor, skin

From ^athe Juntendo Itch Research Center, Institute for Environmental and Gender-Specific Medicine, and ^bthe Anti-Aging Skin Research Laboratory, Graduate School of Medicine, Juntendo University, Chiba; ^cthe Department of Therapy Development and Innovation for Immune Disorders and Cancers and ^dthe Atopy (Allergy) Research Center, Graduate School of Medicine, Juntendo University, Tokyo; ^ethe Department of Pharmacology, Juntendo University School of Medicine, Tokyo; and ^fthe Department of Dermatology, Juntendo University Urayasu Hospital, Chiba.

Supported by a grant-in-aid from the Foundation of Strategic Research Projects in Private Universities from the Ministry of Education, Culture, Sports, Science, and Technology, Japan (grant S1311011 [to K.T.]); Japanese Society for the Promotion of Science Grants-in-Aid for Scientific Research Program (grants 17K16353 [to E.K.], 20K08680 [to E.K.], 18H02783 [to K.O.], 18K07396 [to M.T.], 16H05345 [to C.M.], 16K08997 [to K.T.], and 20H03568 [to K.T.]); the Ministry of Health, Labour, and Welfare, Japan (grants 150401-01 [to C.M.] and 180101-01 [to C.M.]); and a grant from the Lydia O'Leary Memorial Pias Dermatological Foundation (2021 [to M.T.]).

Disclosure of potential conflicts of interest: The authors declare that they have no relevant conflicts of interest.

Received for publication July 22, 2020; revised June 29, 2021; accepted for publication August 2, 2021.

Available online August 17, 2021.

Corresponding author: Kenji Takamori MD, PhD, Juntendo University Graduate School of Medicine, 2-1-1 Tomioka, Urayasu, Chiba 279-0021, Japan. E-mail: ktakamor@juntendo.ac.jp.

The CrossMark symbol notifies online readers when updates have been made to the article such as errata or minor corrections

0091-6749

© 2021 The Authors. Published by Elsevier Inc. on behalf of the American Academy of Allergy, Asthma & Immunology. This is an open access article under the CC BY-NC-ND license (<http://creativecommons.org/licenses/by-nc-nd/4.0/>).

<https://doi.org/10.1016/j.jaci.2021.08.003>

In many skin disorders with chronic itch, including xerosis, atopic dermatitis (AD), and psoriasis, there often occurs a vicious itch-scratch cycle in which scratching behaviors themselves aggravate the itch sensation by exacerbating skin lesions.¹⁻³ These skin conditions often concomitantly display itch hypersensitivity, in which the threshold for itch is lower than in healthy controls and sensitivity to pruritogens is increased.³⁻⁵

The phenomenon of itch hypersensitivity, which is caused by normally innocuous mechanical stimuli, is referred to as mechanical allodynia and has been reported in various mouse models and patients with dry skin-based skin diseases such as AD.⁶⁻¹⁰ Accumulating evidence indicates that innocuous mechanical stimuli-evoked itch (mechanical allodynia) is mediated by neural pathways distinct from those of chemical itch, which is caused by chemical mediators, including histamine or proteases, released from cutaneous cells or exogenous sources.⁹⁻¹²

Chemical itch is transmitted to the spinal cord by various chemical mediators through C-pruriceptors expressing Mas-related GPR A3 (MrgprA3), natriuretic peptide B (Nppb), and gastrin-releasing peptide (GRP) at the peripheral level.¹³⁻¹⁵ At the spinal cord level, a subpopulation of excitatory interneurons (INs) expressing the GRP receptor (GRPR) or natriuretic peptide receptor A (Npra) convey chemical itch signals,^{14,16,17} whereas inhibitory INs expressing the transcription factor BHLHB5 negatively regulate these signals.¹⁸⁻²⁰ Regarding the innocuous mechanical stimuli-evoked itch pathway at the spinal cord, a subpopulation of inhibitory neuropeptide Y-expressing (NPY⁺) INs was found to negatively modulate this sensation without affecting chemical itch.¹² Moreover, NPY 1 receptor (Y1)-expressing neurons and

Abbreviations used

AD:	Atopic dermatitis
CD26KO:	CD26/DPPIV knockout
CGRP:	Calcitonin gene-related peptide
DPPIV:	Dipeptidyl peptidase IV
EM:	Endomorphin
GRP:	Gastrin-releasing peptide
GRPR:	Gastrin-releasing peptide receptor
IN:	Interneuron
MOR:	μ -Opioid receptor
Mrgpr:	Mas-related gastrin-releasing peptide
NF200:	Neurofilament 200
NK1R:	Neurokinin 1 receptor
Nppb:	Natriuretic peptide B
Npra:	Natriuretic peptide receptor A
NPY:	Neuropeptide Y
sDPPIV:	Soluble intact CD26/DPPIV ⁺
smDPPIV:	Soluble mutant CD26/DPPIV ⁻
SP:	Substance P
TrkB:	Tropomyosin-related tyrosine kinase B
Ucn3:	Urocortin 3
WT:	Wild-type
Y1:	NPY 1 receptor

urocortin 3-expressing (Ucn3⁺) neurons were identified as excitatory neurons gated by NPY⁺ INs.^{21,22} Although evidence obtained from patients with AD suggests involvement of both the central and peripheral nervous systems,^{7,8,23,24} the cellular and molecular mechanisms underlying innocuous mechanical stimuli-evoked itch at the periphery remain unknown, except for Merkel cells in the touch dome being important for negative regulation.²⁵

CD26 is a 110-kDa multifunctional glycoprotein that is expressed on various cell types, including T cells, epithelial cells, endothelial cells, fibroblasts, and various tumor cells. CD26 exhibits dipeptidyl peptidase IV activity (DPPIV [EC 3.4.14.5]) in its extracellular domain and is capable of cleaving the N-terminus of peptides with L-proline or L-alanine at the penultimate position.²⁶⁻²⁸ This enzyme is involved in the activation and inactivation of a number of cytokines, chemokines, and neuropeptides.²⁹ We recently reported that DPPIV is associated with psoriatic itch by regulating the cleavage of substance P (SP).³⁰ However, the involvement of the CD26 molecule or DPPIV in mechanical allodynia remains unclear.

In the present study, we investigated the role of CD26/DPPIV in the regulation of mechanical allodynia at the periphery by using CD26 knockout (CD26KO) mice. We focused on substrates for DPPIV, namely, the endomorphins (EMs) EM-1 and EM-2, which are selective ligands for μ -opioid receptors (MORs), and we identified them as pruritogens that preferentially provoke mechanical allodynia over chemical itch. Herein, we have demonstrated that EM-MOR signaling and its degradation pathway by DPPIV play a pivotal role in the peripheral mechanisms of mechanical allodynia.

METHODS**Animals**

C57BL/6 mice were purchased from CLEA Japan (Tokyo, Japan) or Oriental BioService (Kyoto, Japan). CD26KO (CD26^{-/-}) mice developed from C57BL/6 mice were kindly gifted from the laboratory of Dr Takeshi Watanabe at Kyusyu University (Fukuoka, Japan).³¹ These mice were bred in-house and

used at 8 to 16 weeks of age. They were kept under controlled temperature (23°C–25°C) and light (exposure to light from 8:00 AM to 8:00 PM) conditions. Food and water were freely available to the mice. All experiments on animals were approved by the animal ethics committee at Juntendo University (authorization nos. 280038, 290132, 300024, 310029, 2020063, and 2021079).

Recombinant proteins, antibodies, and reagents

Recombinant EMs (EM-1 and EM-2) were purchased from the Peptide Institute (Osaka, Japan). Truncated peptides of EMs (YP [common N-terminal side dipeptides], WF-NH₂ [C-terminal side amidated dipeptides of EM-1], and FF-NH₂ [C-terminal side amidated dipeptides of EM-2]) were purchased from BEX Co, Ltd (Tokyo, Japan). All peptides were dissolved in 2.5% dimethyl sulfoxide physiologic saline to make a stock solution. Recombinant soluble CD26/DPPIV (sDPPIV) and sDPPIV lacking DPPIV enzyme activity mutated at catalytic site (Ser630 was replaced by Ala) (soluble mutant DPPIV [smDPPIV]) were produced according to a previously described method.³² The primary antibodies used in the present study were as follows: goat anti-mouse CD26/DPPIV (1:1000; R&D Systems, Minneapolis, Minn), rabbit anti-EM-1 (1:200; Phoenix Pharmaceuticals, Inc, Burlingame, Calif), rabbit anti-EM-2 (1:200; Phoenix Pharmaceuticals, Inc), guinea pig anti-cytokeratin 10 (anti-CK10, 1:200; Progen Biotechnic GmbH, Heidelberg, Germany), guinea pig anti-CK14 (1:200; Progen Biotechnic GmbH), and chicken anti-vimentin (1:200, Abcam, Cambridge, United Kingdom). A cyanine 3-conjugated rabbit polyclonal anti- β -III tubulin antibody was purchased from Merck Millipore (Temecula, Calif) and used at a dilution of 1:500 to 1:800. A secondary rabbit antibody conjugated with Alexa 488 was obtained from Thermo Fisher Scientific (Rockford, Ill). Other secondary antibodies conjugated with Alexa 488 or Alexa 594 were purchased from Jackson ImmunoResearch Laboratories, Inc (West Grove, Pa). All secondary antibodies were used at a 1:300 dilution. The peripheral MOR antagonist naloxone methiodide was purchased from Merck (Darmstadt, Germany) and dissolved, stocked, and used in saline.

Mechanical allodynia assay

Mechanical allodynia assays were performed by using a previously described method with some modifications.^{9,22,25} The rostral back of each mouse was shaved at least 2 days before the test. On the day of the test, each mouse was placed in a new cage and habituated for at least 1 hour. Mechanical stimuli were delivered with von Frey filaments (Bioseb, Chaville, France) with bending forces ranging between 0.008 and 1.4 g. Unless otherwise noted, von Frey filaments with bending forces of 0.07 and 0.16 g were used for the test, and data obtained with a force of 0.16 g were shown. Each mouse received 3 innocuous mechanical stimuli on the rostral back by using this filament with longer than 5-second intervals (average 20 seconds). Within a 3-minute interval, this sequence was repeated 10 times (30 stimulations in total). Mechanical allodynia scores were calculated as the total number of scratching responses. To test the effects of reagents or peptides on mice, CD26KO or control wild-type (WT) mice received a 50- μ L intradermal injection of recombinant sDPPIV, smDPPIV, or naloxone methiodide into the center of the shaved area through use of a 29G Myjector syringe (Thermo, Tokyo, Japan). Mechanical allodynia assays were then immediately conducted. To test EM-evoked mechanical allodynia, WT mice received an intradermal injection of EM (EM-1, EM-2, or their fragments) with or without naloxone methiodide under the same conditions as used for the CD26KO mouse test, and to prevent scratching behavior caused by spontaneous itch affecting mechanical allodynia scores, mechanical allodynia assays were performed 30 minutes after the intradermal injection. Each experiment was performed with 6 or more mice in all groups.

Scratching bout counting assay

The rostral part of the back was shaved at least 2 days before the test. Before behavioral recording, the mice (4 animals per observation) were placed in an acrylic cage (19.5 \times 24 \times 35 cm) for at least 1 hour for acclimation. The frequency of scratching bouts of the rostral back was analyzed by using the

SCLABA-Real system (NOVERTEC, Kobe, Japan) for the indicated time intervals, with observers being kept out of the experimental room. To test EM-evoked scratching bouts, each mouse received an intradermal injection under the same conditions as used for the EM-evoked mechanical alloknesis assay. After the injection, the mice were immediately placed back in the acrylic cage, and behavioral recording using the SCLABA-Real system was started. “One-time” scratching behavior by mice was defined as scratching occurring from the initiation of scratching with the hind limb to cessation thereof. Each experiment was performed with 6 or more mice in all groups.

Evaluation of skin conditions

Transepidermal water loss and stratum corneum hydration were evaluated in each mouse by using the Tewameter TM300 and Corneometer CM825 (Courage and Khazawa, Cologne, Germany), respectively (at a room temperature of $25.1^{\circ}\text{C} \pm 0.6^{\circ}\text{C}$ and relative humidity of $43.4\% \pm 1.3\%$). At the time of both measurements, each measuring device was placed on the surface of murine back skin for approximately 20 to 30 seconds after the achievement of isoflurane anesthesia. Each experiment was performed with 7 WT mice and 8 CD26KO mice.

Immunohistochemistry

Frozen blocks were prepared by embedding the unfixed upper back skin of the mice in optimal cutting temperature (OCT) compound (Sakura Finetechnical Co, Ltd, Tokyo, Japan). Next, 10- μm -thick cryosections were made by cutting the blocks using a CM1850 cryostat (Leica, Wetzlar, Germany). Skin sections were air-dried and fixed with ice-cold acetone for 10 minutes. After rehydration with PBS solution, the sections were blocked with blocking buffer (PBS solution with 5% normal donkey serum, 2% BSA, and 0.2% Triton X-100) at room temperature for 2 hours and then incubated with each primary antibody at 4°C overnight. After washing with wash buffer (PBS solution with 2% BSA and 0.05% Tween 20), secondary antibodies were added to the sections and incubated at room temperature for 2 hours with shading. As negative control experiments, the primary antibodies were either omitted or replaced with normal IgG. After washing with wash buffer with shading, VECTOSHIELD Mounting Medium with 4',6-diamidino-2-phenylindole (Vector Labs, Burlingame, Calif) was added, the sections were covered with coverslips, and images were taken by using a Keyence BZ-X800 microscope (Osaka, Japan). Even in cases without statistical processing, 2 or more mice were examined and 3 to 9 visual fields per sample were photographed.

Semiquantification of β -III tubulin-immunoreactive fibers

There were 8 mice in each group; 3 skin specimens from each mouse were incubated with an anti- β -III tubulin antibody. A BZ-X800 all-in-one fluorescence microscope was used to scan 10- μm -thick sections at a thickness of 1.0 μm in the z-axis of the stained samples, and images were reconstructed in 3 dimensions by using the BZ-X800 viewer (Keyence). The entire fluorescence intensity on the field and its nerve fiber-positive areas (superficial measure) were assessed in 9 fields of view for each mouse by using the BZ-X800 analyzer (Keyence). By dividing the intensity of fluorescence in the whole field by the nerve fiber-positive areas in the field, the fluorescence intensity of each neuronal marker per unit area was calculated. All values are reported as means plus or minus SEMs.

Statistical analysis

Data were expressed as mean values plus or minus SEMs and analyzed by the 2-tailed Student *t*-test for 2 group comparisons or by ANOVA for multiple comparisons followed by the Tukey-Kramer *post hoc* test. *P* values of .05 or less were considered significant. Calculations were performed and graphed by using GraphPad Prism 6 (GraphPad Software Inc, La Jolla, Calif).

RESULTS

CD26KO mice display mechanical alloknesis

We initially conducted mechanical alloknesis assays to clarify susceptibility to innocuous mechanical stimuli in CD26KO mice

(Fig 1, A). The frequency of hind limb scratching evoked by von Frey filaments (mechanical alloknesis score) with a low bending force (0.04-0.6 g) was significantly higher in CD26KO mice than in WT mice (Fig 1, B). Only slight differences were observed between these mice at each of the other forces tested (Fig 1, B). In contrast, spontaneous scratching with no mechanical stimuli was similar between CD26KO and WT mice (Fig 1, C).

Characterization of mechanical alloknesis in CD26KO mice

We examined the skin condition of CD26KO mice, including barrier function and innervation. No significant differences in the degree of transepidermal water loss (Fig 2, A) or stratum corneum hydration (Fig 2, B) were observed between the WT and CD26KO mice. To assess innervation, the fluorescence intensity of the neuronal marker β -III tubulin per area in the skin was evaluated immunohistochemically. No significant differences were noted in the fluorescence intensity of β -III tubulin between the WT and CD26KO mice (Fig 2, C and D).

Immunohistochemically, CD26 was expressed in the skin of the WT mice but not in the skin of the CD26KO mice, and it was more strongly expressed in the dermis (Fig 2, E) than in nerve fibers (see Fig E1 in this article's Online Repository at www.jacionline.org). The expression of CD26 was markedly weaker in the spinal cord, except for the meninges, than in the skin (see Fig E2 in this article's Online Repository at www.jacionline.org).

We then investigated whether a CD26 deficiency in skin was responsible for the induction of mechanical alloknesis. CD26KO mice were injected intradermally with 0.2 nmol soluble intact CD26/DPPIV⁺ (sDPPIV), and mechanical alloknesis assays were performed. Mechanical alloknesis scores were significantly lower in sDPPIV-injected CD26KO mice than in vehicle-injected CD26KO mice. In contrast, the smCD26/DPPIV soluble form (0.2 nmol) did not affect the mechanical alloknesis scores of CD26KO mice (Fig 2, F). Moreover, mechanical alloknesis in CD26KO mice was almost completely abrogated by the intradermal injection of 30 μg naloxone methiodide (Fig 2, G). These results strongly suggest that DPPIV enzyme activity in the dermal layer of mouse skin negatively regulates MOR-mediated mechanical alloknesis.

EMs are distributed in mouse keratinocytes, nerve fibers, and fibroblasts

EM-1 and EM-2 are selective ligands for MOR and substrates for DPPIV.^{33,34} Because these ligands evoke scratching behavior in mice following their intracisternal injection,³⁵ we focused on whether these EMs are significant pruritogens that are regulated by DPPIV enzyme activity in the skin. Although previous studies reported that these MOR ligands are both expressed in the central nervous system, such as in the brain and spinal cord,^{36,37} there is currently no information on whether these ligands are expressed in mouse skin. Therefore, we immunohistochemically examined the expression and distribution patterns of the EM-1 and EM-2 proteins in mouse skin (Fig 3). In murine skin, both EMs were strongly detected in the epidermis, both in the squamous cell layer (Fig 3, A and B) and basal layer (Fig 3, C and D) of keratinocytes. In addition to distinct expression in some cutaneous nerve fibers (Fig 3, E and F), these EMs were also detectable in dermal fibroblasts (Fig 3, G and H).

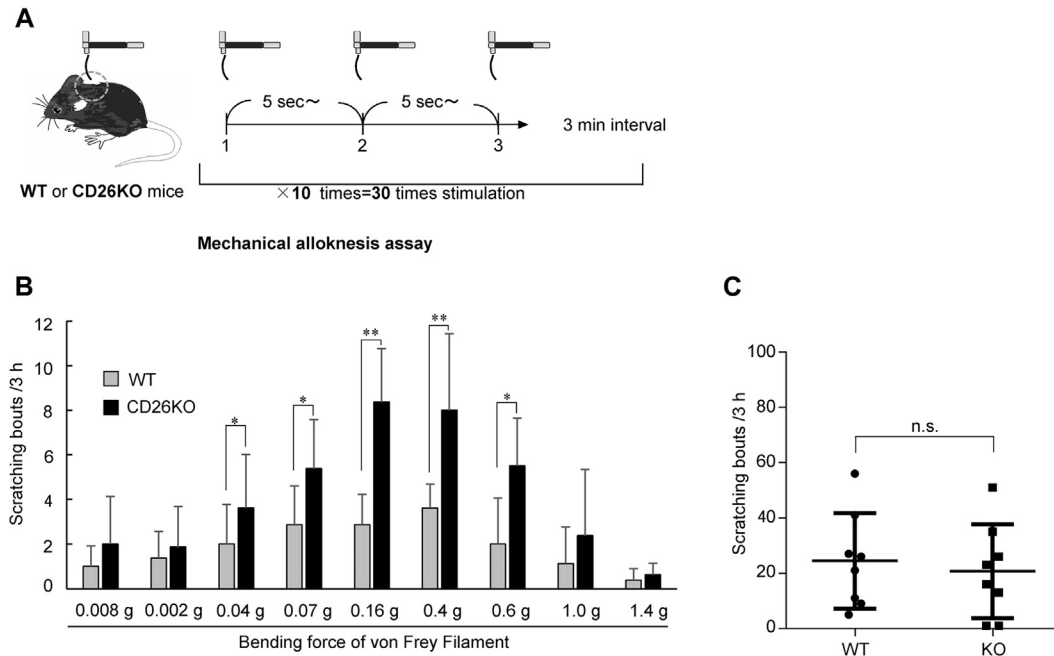


FIG 1. CD26KO mice display mechanical allodynia. **A**, Schematic showing a mechanical allodynia assay. **B**, Frequency of scratching bouts induced by von Frey filaments (mechanical allodynia score) with various bending forces (0.008–1.4 g) in WT or CD26KO mice. **C**, Frequency of scratching bouts during 3 hours with no mechanical stimulation in WT or CD26KO mice. * $P < .05$; ** $P < .01$. *n.s.*, Not significant.

To further identify subpopulations of EM-containing sensory nerve fibers, costaining and triple staining of mouse skin were conducted by using each EM antibody, C- and A-fiber markers (for costaining and triple staining), and peptidergic neuron and A β -fiber markers (for triple staining), respectively.^{38,39} The results of costaining revealed EMs in both C- and A-fibers (see Fig E3, A–D in this article's Online Repository at www.jacionline.org). Triple staining showed that EM-1 and EM-2 were mainly expressed in peptidergic C- and A β -fibers and weakly expressed in A δ -fibers (see Fig E4, A–F in this article's Online Repository at www.jacionline.org).

EM preferentially induce mechanical allodynia over chemical itch

To clarify whether EM-1 or EM-2 induces innocuous mechanical stimulus-evoked itch, we used WT mice and conducted mechanical allodynia assays following the intradermal injection of EM-1 or EM-2 at various concentrations (Fig 4, A). To exclude the effects of EM-derived spontaneous itch (nonmechanical itch) from mechanical allodynia scores, we also performed scratching bout counting assays under the same administration conditions (Fig 4, A). The results obtained showed that only high concentrations of each EM (eg, 100 or 200 nmol per mouse) evoked scratching bouts compared with when the control vehicle was used under nonmechanical conditions (Fig 4, B and C); however, the frequency of scratching bouts under these conditions peaked approximately 0 to 20 minutes after administration and then converged to the level of the vehicle within 30 to 40 minutes (see Fig E5, A and B in this article's Online Repository at www.jacionline.org). Therefore, we performed mechanical allodynia assays 30 minutes after the subsidence of EM-evoked itch. We found that intradermal injection of EM at a concentration of 25 to 200

nmol caused mechanical allodynia in a dose-dependent manner (Fig 4, D and E). Mechanical allodynia was induced in the presence of mechanical stimuli (Fig 4, D and E) even at low concentrations at which scratching behaviors hardly occurred in the absence of mechanical stimuli (eg, 25 and 50 nmol) (Fig 4, B and C).

EM-induced mechanical allodynia is mediated by MOR and also regulated by DPPIV

To confirm whether EMs evoke mechanical allodynia via peripheral MORs, mice were coadministered 100 nmol of each EM (EM-1 or EM-2) with 30 μ g of naloxone methiodide, after which mechanical allodynia scores were assessed (Fig 5, A). Pharmacologically, naloxone methiodide inhibited EM-evoked mechanical allodynia to a level similar to that observed with the vehicle (Fig 5, B and C). We investigated the effects of DPPIV enzyme activity on this allodynia. Because both EMs comprise 4 amino acids and have a DPPIV cleavage site at the penultimate position, we synthesized 3 types of dipeptides as estimated forms of EM-1 and EM-2 cleaved by the enzyme DPPIV (ie, YP, WF-NH₂, and FF-NH₂ [Fig 6, A]). Using a mouse MOR-expressing cell line, we confirmed that the cleaved forms of these peptides did not bind to MOR, whereas full-length EMs did (on the basis of the functional changes that occurred when EM bound to MOR [see Figs E6 and E7 in this article's Online Repository at www.jacionline.org]). We coadministered 100 nmol of these peptides (mixtures of YP and WF-NH₂ or YP and FF-NH₂, as components that make up full-length EM-1 or EM-2, respectively) to WT mice (Fig 6, B). None of the combinations of truncated EM peptides induced mechanical allodynia compared with its intact full-length EM (100 nmol), respectively (Fig 6, C and D).

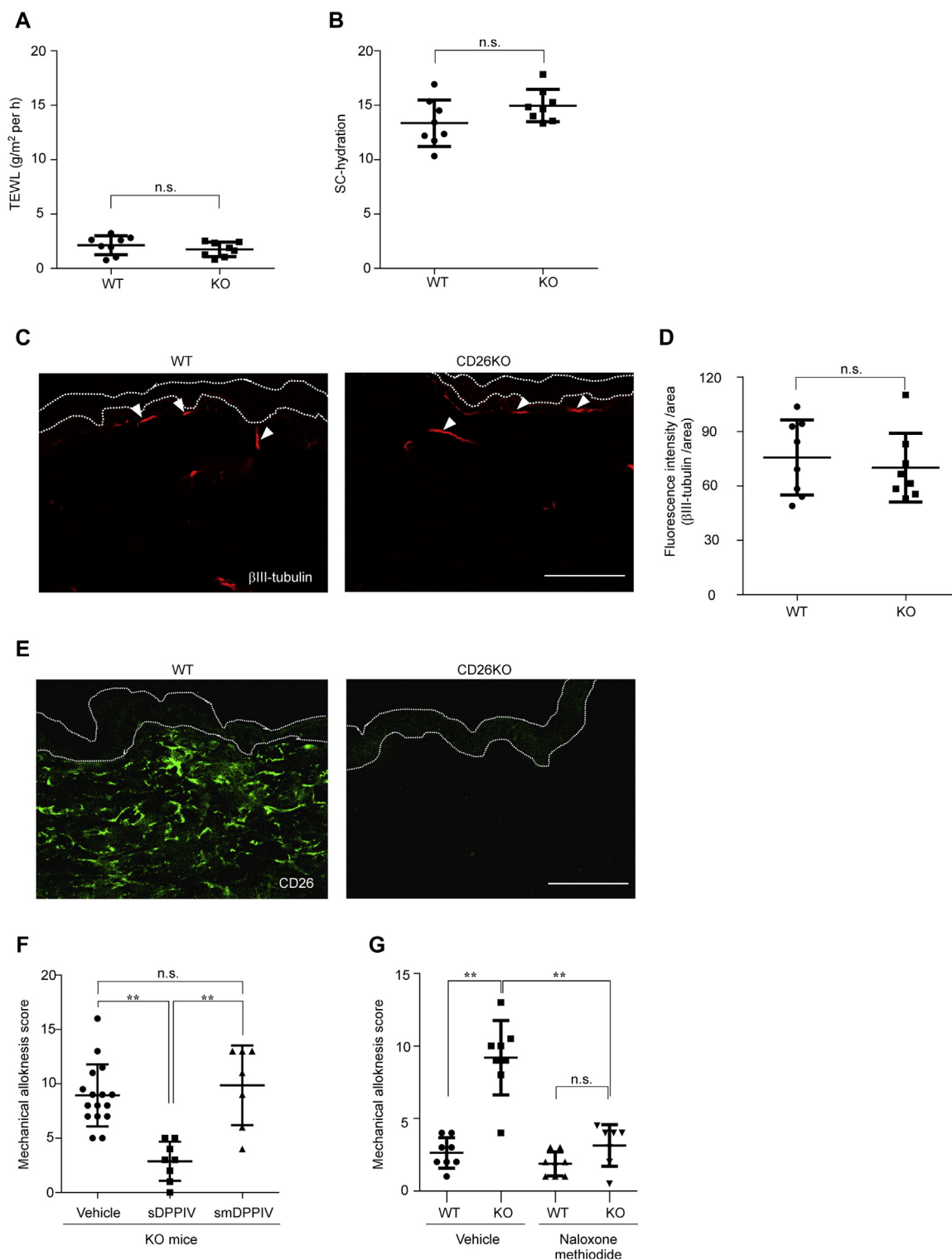


FIG 2. Characterization of mechanical allodynia in CD26KO mice. **A** and **B**, Transepidermal water loss (TEWL) (**A**) and stratum corneum (SC) hydration (**B**) were evaluated in the skin of WT and CD26KO mice. **C**, Representative immunofluorescence image of the back skin from a WT or CD26KO mouse using a cyanine 3-labeled β -III tubulin antibody (red indicates a neuronal marker). Arrowheads indicate β -III tubulin-immunoreactive fibers. Each image between the dotted lines indicates the epidermis. Scale bar = 100 μ m. **D**, The fluorescence intensity per unit area of the β -III tubulin antibody was measured for WT or CD26KO mice by using Keyence software (BZ-X800). **E**, Representative immunofluorescence images of the back skin of WT and CD26KO mice obtained by using the anti-CD26 antibody (green). Each image between the dotted lines indicates the epidermis. Scale bar = 100 μ m. **F**, Effects of sDPPIV and smDPPIV on mechanical allodynia in CD26KO mice. Mechanical allodynia in CD26KO mice was inhibited by an intradermal injection of sDPPIV but not smDPPIV. **G**, Naloxone methiodide (a peripheral MOR antagonist) inhibited mechanical allodynia in CD26KO mice. ****** $P < .01$. *n.s.*, Not significant.

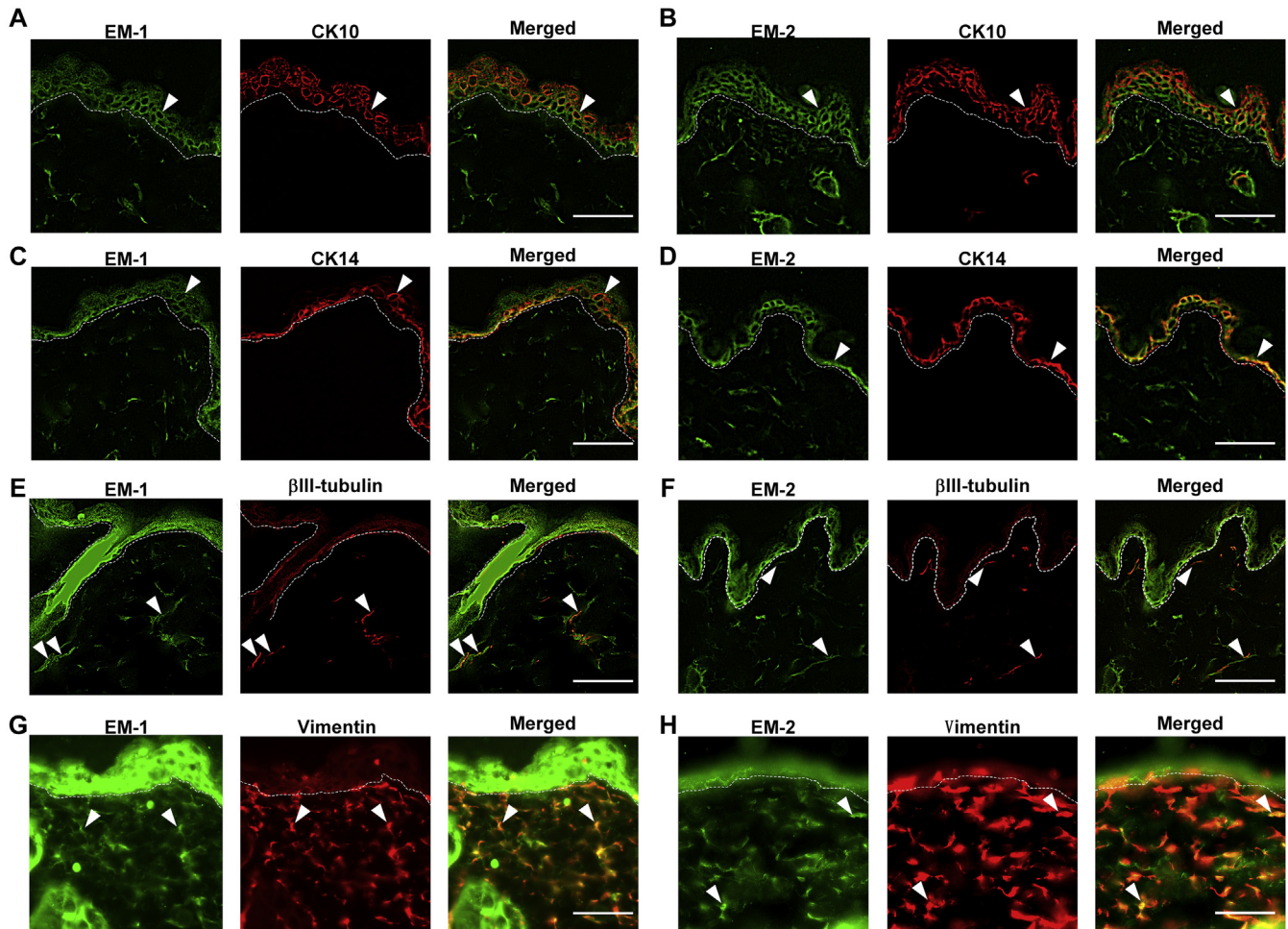


FIG 3. Distribution pattern of EMs in mouse skin. Double immunofluorescence staining with antibodies against EM (EM-1 or EM-2) and marker proteins for epidermal keratinocytes, nerve fibers, or fibroblasts in the skin of WT mice (**A-G**). Representative images of double staining with anti-EM-1 (**A**) or anti-EM-2 (**B**) (EM in green) and anti-cytokeratin 10 (anti-CK10) (squamous epithelial marker in red). Representative images of double staining with anti-EM-1 (**C**) or anti-EM-2 (**D**) (EM in green) and anti-CK14 (basal epithelial marker in red). Representative images of double staining with anti-EM-1 (**E**) or anti-EM-2 (**F**) (EM in green) and anti- β -III tubulin (neuronal marker in red). Representative images of double staining with anti-EM-1 (**G**) or anti-EM-2 (**H**) (EM in green) and anti-vimentin (fibroblast marker in red). Arrowheads indicate double-positive signals (yellow in the merged panel). The white dotted line in each panel indicates the border between the epidermis and dermis. Scale bar = 50 μ m.

To clarify whether the mechanisms underlying EM-induced itch differ between mechanical and nonmechanical conditions, we also conducted scratching bout counting assays under nonmechanical conditions by using the same administration protocol as that used for the mechanical allodynia assays. Similar to what we observed in the case of mechanical conditions, neither naloxone methiodide (see Fig E5, C and D) nor the mixture of each truncated EM peptide (see Fig E5, E and F) induced more frequent scratching bouts than did intact full-length EM alone. Furthermore, when WT or CD26KO mice were intradermally administered 100 nmol of EM-1 or EM-2, the frequency of scratching bouts within 1 hour was significantly higher in CD26KO mice than in WT mice (see Fig E5, G and H).

DISCUSSION

The present results suggest that a peripheral EM (EM-1 or EM-2)-MOR system mediates mechanical-induced itch (mechanical

allodynia) and that this pathway is modulated by CD26/DPPIV in mouse skin (Fig 7). Our immunohistochemical analyses showed that EM-1 and EM-2 were both expressed in nerve fibers, keratinocytes, and fibroblasts (Fig 3). Therefore, sensory nerve fibers and cutaneous cells, such as keratinocytes and fibroblasts, are considered to be sources of EMs. We also found that an intradermal injection of EM induced mechanical allodynia in a dose-dependent manner (Fig 4) and that CD26KO mice exhibited mechanical allodynia, which was rescued by an intradermal injection of the active form of soluble intact CD26/DPPIV⁺ (sDPPIV) (Fig 2, F). Mechanical allodynia was significantly inhibited by the peripheral MOR antagonist naloxone methiodide (Figs 2, G and 5, B and C). Thus, although further analyses of molecular and cellular mechanisms are needed to obtain a more detailed understanding of mechanical allodynia, cutaneous EM-MOR may play a pivotal role in its induction under the enzymatic control of DPPIV. This concept may also be supported by the present results showing that cleaved EMs (YP + WF-NH₂

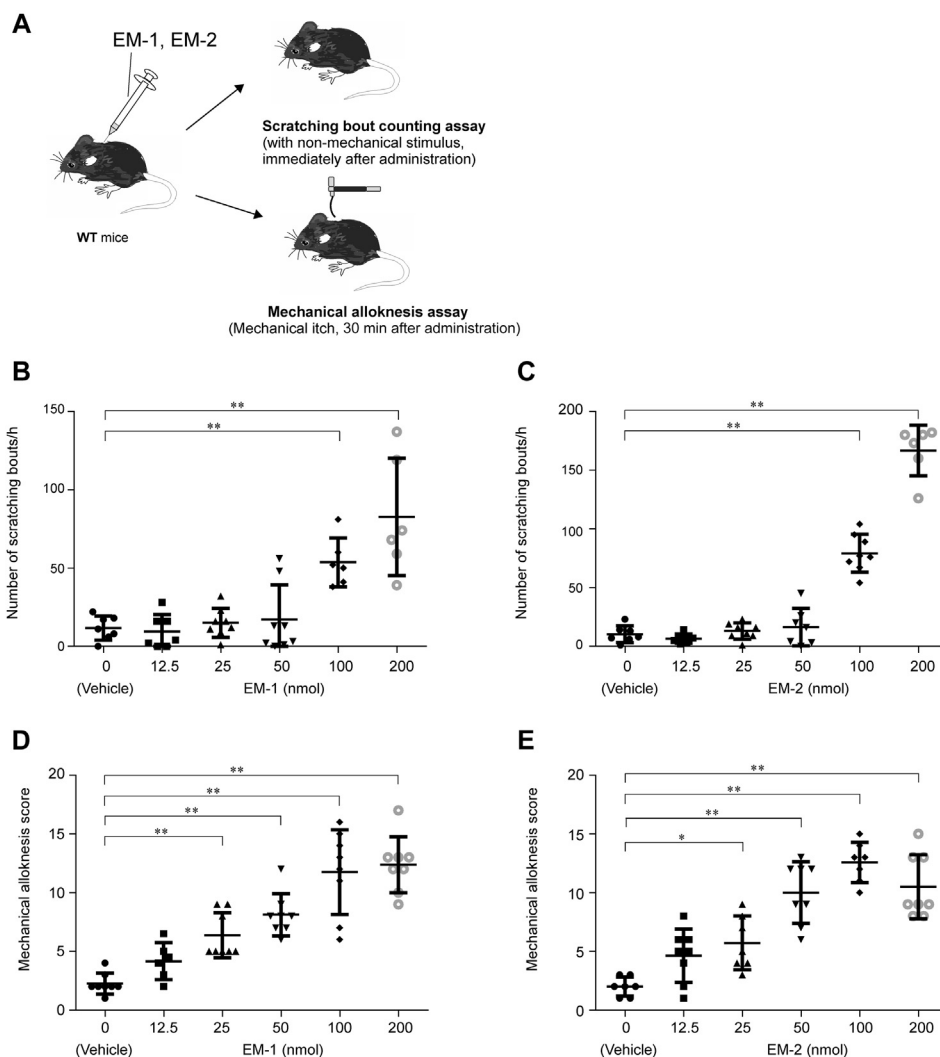


FIG 4. Effects of different concentrations of EMs on scratching bouts and mechanical allodynia. **A**, Schematic procedure of experiments to assess the sensitivity of EMs (EM-1 and EM-2) at various concentrations in scratching bouts and mechanical allodynia. A scratching bout counting assay was performed immediately after the intradermal administration of EM, and mechanical allodynia assays were performed 30 minutes later. **B** and **C**, The frequency of scratching bouts following the intradermal injection of EM-1 (**B**) or EM-2 (**C**) at various concentrations. **D** and **E**, Mechanical allodynia scores following the intradermal injection of EM-1 (**D**) or EM-2 (**E**) at various concentrations. * $P < .05$; ** $P < .01$.

and YP + FF-NH₂) did not induce mechanical allodynia (Fig 6, C and D).

CD26 was expressed in the dermal layer of WT mouse skin but not in the dermal layer of CD26KO mouse skin (Fig 2, E). Mechanical allodynia in CD26KO mice was almost completely abrogated by the intradermal injection of sDPPIV but not by the enzymatic mutant (Fig 2, F). Thus, although we cannot exclude the possibility of other degradation systems for EM, such as aminopeptidase M⁴⁰ or dipeptidyl peptidase III,⁴¹ in CD26KO mice, these results suggest that DPPIV enzyme activity in the dermal layer is at least partially responsible for the negative regulation of mechanical allodynia in normal mouse skin.

We also found that intradermal injection of EM caused mechanical allodynia in WT mice in a dose-dependent manner (Fig 4, D and E). This phenomenon occurred even at low EM concentrations at which scratching behaviors hardly occurred in the

absence of mechanical stimuli (Fig 4, B and C). This may explain why CD26KO mice exhibited only mechanical allodynia (Fig 1, B and C).

A previous study also reported that CD26KO mice displayed high susceptibility to nociceptive stimuli, which was restored by a substance P (SP) receptor (NK-1R) antagonist.⁴² We recently reported that DPPIV exaggerated itch in psoriasis by cleaving SP.³⁰ Mechanical allodynia in CD26KO mice was markedly inhibited (to a level that was not significantly different from that in WT) by the peripheral MOR inhibitor naloxone methiodide (Fig 2, G). In contrast, when we examined the effects of SP on mechanical allodynia induced in CD26KO mice by an intradermal injection of the SP receptor antagonist QWF (Boc-Gln-D-Trp(Formyl)-Phe benzyl ester trifluoroacetate salt, which is an inhibitor of the SP receptors NK1R, the enzyme DPPIV MrgprA1, and MrgprB2),⁴³ the mechanical allodynia score was partially

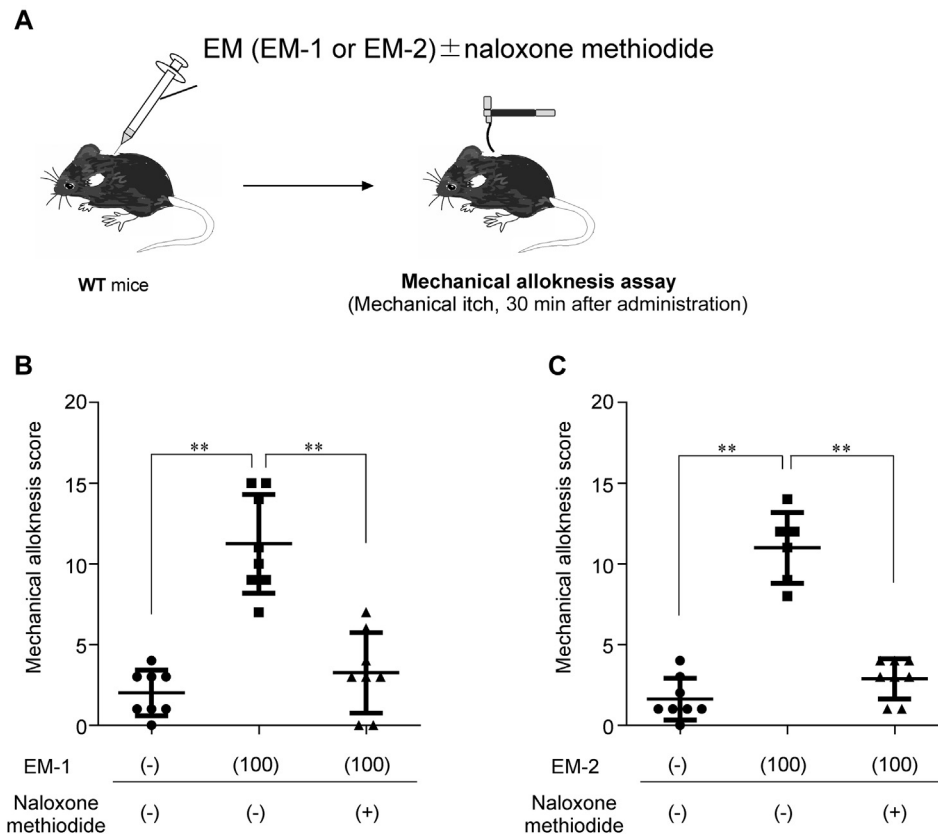


FIG 5. Effects of a peripheral MOR antagonist on EM-induced mechanical alloknesis. **A**, Schematic procedure for the mechanical alloknesis assay under a peripheral MOR antagonist (naloxone methiodide). WT mice were intradermally administered EM-1 or EM-2 with or without naloxone methiodide, and after 30 minutes the measurement of mechanical alloknesis scores in each mouse was started. **B** and **C**, Effects of naloxone methiodide on mechanical alloknesis induced by EM-1 (**B**) or EM-2 (**C**).

attenuated by the highest dose of QWF (see Fig E8 in this article's Online Repository at www.jacionline.org). Although previous findings showed that SP is an important itch mediator and also a substrate for DPPIV in a psoriasis model,³⁰ SP and its receptors did not appear to make a significant contribution to the present results. The reason for this may be differences in skin SP levels between previous psoriasis model mice and the CD26KO mice in the present study. In the psoriasis model, SP levels were systemically elevated.³⁰ Serum SP levels of nontreated CD26KO were significantly lower than those in the WT psoriasis model (unpublished observation, 2017). We speculate that the effects of cutaneous SP were weaker in CD26KO mice than in the WT psoriasis model. Furthermore, SP was shown to play a role in mechanical itch at the spinal level.² However, because DPPIV levels in the spinal cord were markedly lower than those in the skin (see Fig E2), the effects of DPPIV on SP in the spinal cord were considered to be limited. Therefore, these results suggest that MOR ligands, rather than SP, play a central role in the regulatory mechanisms of DPPIV-associated mechanical alloknesis at the periphery, and also that the SP-NK1R system may be one of the important signaling pathways for mechanical alloknesis at the spinal level.^{10,44}

EM-1 and EM-2 are endogenous opioid peptides that have high affinity and selectivity for MOR.⁴⁵ Although EM-1 and EM-2 expression patterns differ in different brain regions, both are strongly expressed in the central nervous system, in which

MOR is concentrated.^{36,37} Furthermore, an intracisternal injection of both EMs elicited scratching behavior that was inhibited by an MOR antagonist.³⁵ In the present study, we showed that an intradermal injection of EM elicited mechanical alloknesis, and that this was inhibited by a peripheral MOR antagonist (Fig 5, B and C). Our histologic analyses revealed that EM-1 and EM-2 were expressed in some sensory nerve fibers (Fig 3, E and F), which is consistent with previous findings on EM-2 expression in rat skin.⁴⁶ We also provided the first evidence for EMs in keratinocytes (Fig 3, A-D) and fibroblasts (Fig 3, G and H). Because general peripheral itch sensations are transmitted and induced through sensory nerve fibers, it appears to be important for EM to act on nerves. EM-1 and/or EM-2 located in nerve fibers may be digested by DPPIV around nerves and involved in the induction of itch and mechanical alloknesis. However, in addition to the nerve fibers themselves potentially secreting these EMs, we were unable to exclude the possibility that EM-1 and/or EM-2 located at nerves are secreted by keratinocytes, which are their most potent expressors in the skin, or fibroblasts localized around nerves in the present study. Similarly, previous findings showing that MORs are located in nerve endings^{38,47} and keratinocytes^{48,49} imply that EM mediated the induction of mechanical alloknesis via MORs expressed in sensory nerves; however, we cannot completely exclude the possibility of an indirect pathway via MOR-expressing keratinocytes. This concept appears to be supported by the present results showing that

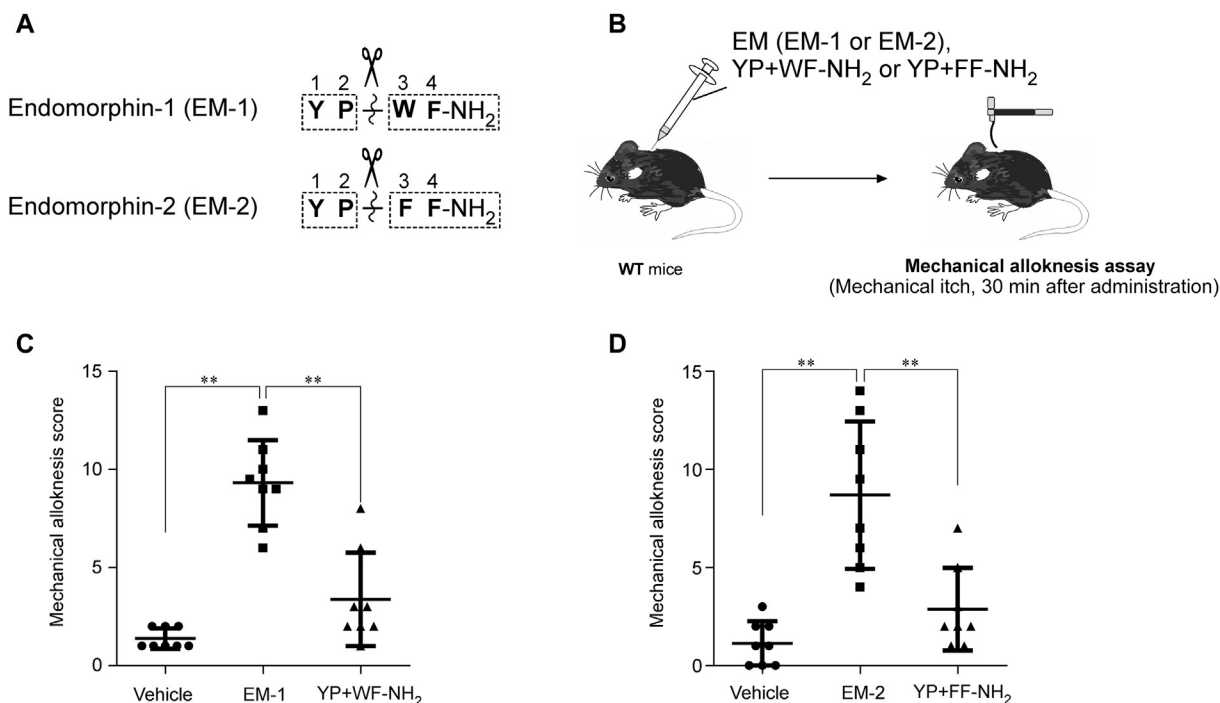


FIG 6. Effect of cleavage by DPPIV on EM-induced mechanical allodynia. **A**, Schematic diagram of the peptide sequences of EM-1 and EM-2 and their DPPIV cleavage sites. Scissors represent DPPIV, and the short wavy lines represent cleavage sites. **B**, Schematic procedure for the mechanical allodynia assay for characterization of estimated DPPIV cleaved form mixture of EMs. WT mice were intradermally administered an intact or cleaved form mixture of EM-1 or EM-2. After 30 minutes, measurement of mechanical allodynia scores in each mouse was started. **C** and **D**, Effects of the DPPIV cleaved form mixture of EM-1 (**C**) or EM-2 (**D**) on mechanical allodynia. ** $P < .01$.

mechanical allodynia was strongly affected by DPPIV in the dermal layer, which closely surrounds nerve fibers (Fig 2, E and F and see Fig E1).

In addition to mechanical allodynia, chemical itch began to appear in normal mice at high concentrations of EMs (>100 nmol) (Fig 4, B and C and see also Fig E5, A and B). Our pharmacologic analyses showed that chemical itch was also mediated via MORs and controlled by DPPIV (see Fig E5, C-H). Currently, the mechanisms by which MOR agonists induce chemical itch remain unclear. MOR generally suppresses nerve activation by stimulating the heterotrimeric Gi/o protein.⁵⁰ Whole-cell patch recordings revealed that EM-1 and EM-2 acted on spinal neurons and attenuated excitatory and inhibitory synaptic currents via MORs.⁵¹ Wang et al recently reported that itch induced by the intrathecal administration of MOR agonists was caused by the suppression of vesicular γ -aminobutyric acid transporter (Vgat)⁺ inhibitory neurons in the spinal cord.⁵² Furthermore, Liu et al demonstrated that one of the isoforms of MOR, MOR-1D, activated nerves by forming a heterodimer with the GRPR.⁵³

Accumulating evidence recently showed that similar to the involvement of C-fibers in chemical itch, A β -fibers play a pivotal role in mechanical itch.^{22,25} Multiple staining of mouse skin with neuronal fiber markers revealed the presence of both EMs in A β -fibers (neurofilament 200 [NF200⁺]/TrkB⁺) and peptidergic C-fibers (Peripherin⁺/CGRP⁺), and to a lesser extent, in A δ -fibers (NF200⁺/CGRP⁺) (see Fig E4); however, their expression profiles in other subpopulations remain unknown. Therefore, we performed a functional silencing experiment on A β - and

C-fibers^{22,54} and found that the functional silencing of A β -fibers suppressed EM-evoked allodynia, whereas silencing of C-fibers did not (unpublished observation, 2020). Moreover, the functional silencing of A β -fibers did not attenuate spontaneous scratching behavior (unpublished observation, 2020). Although further studies are needed, these results indicate that EM-1 and EM-2 evoke chemical itch by suppressing the activation of C-fiber neurons innervating inhibitory spinal neurons or activating those innervating excitatory spinal neurons (eg, subpopulation of peptidergic neurons) through a heterodimer of MOR with other G protein-coupled receptors, such as a MOR1D-GRPR heterodimer in the spinal cord,^{53,55-57} whereas EM-evoked allodynia is due to the suppression of A β -fiber neurons innervating inhibitory spinal neurons. Because Merkel cells are mechanoreceptors with A β -fibers that suppress mechanical itch,²⁵ they are promising targets for EM-1 and/or EM-2. Although we did not obtain such data in this study, EM-1 and EM-2 may have also been expressed in these cells, because it has been reported that various neuropeptides and opioid receptors are expressed in Merkel cells.⁵⁸

On the basis of the finding showing that many opioids cause mast cell degranulation,⁵⁹ in addition to the direct pathway via nerve fibers, a mast cell-mediated pathway is also conceivable as a chemical itch- and/or mechanical itch-inducing pathway. The results of the toluidine blue staining experiment revealed that the mast cell degranulation ratio was significantly higher in CD26KO mice than in WT mice, whereas the number of mast cells in the skin was very low and similar to that in WT

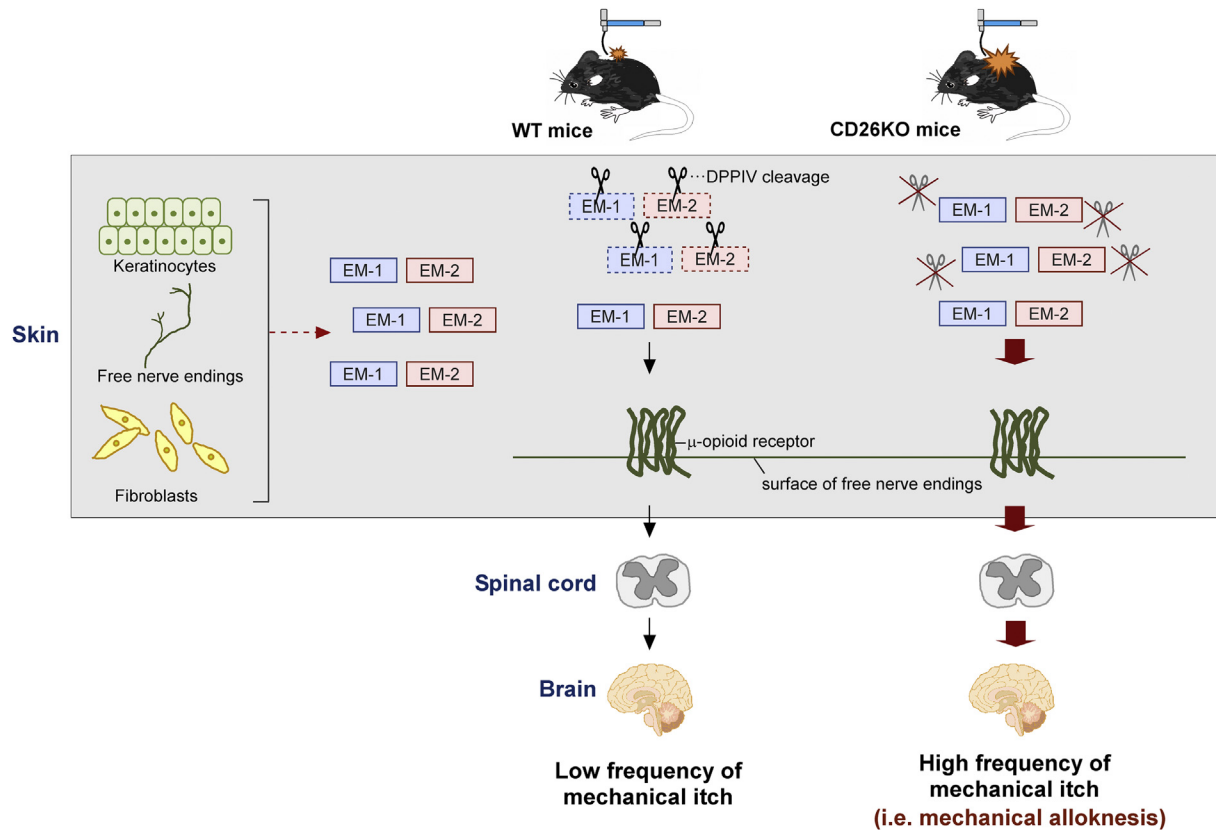


FIG 7. A model for the regulation of EM-induced mechanical allodynia in WT or CD26KO mice. EMs are produced from keratinocytes, parts of nerve endings, and fibroblasts in the skin, and EM may preferentially evoke mechanical allodynia in a dose-dependent manner over nonmechanical scratching bouts. In WT mice, mechanical allodynia induced by EM was normally controlled because EM in the skin may have been degraded by DPPIV (one of the functions of CD26). Because EM may not be degraded by DPPIV in CD26KO mice, the sensitivity of innocuous mechanical stimuli-evoked itch (ie, mechanical allodynia) may be increased via the MOR expressed in skin components, such as sensory nerve fibers.

mice (see Fig E9, A-D in this article's Online Repository at www.jacionline.org). Furthermore, our β -hexosaminidase assay on mouse bone marrow-derived mast cells revealed that the highest dose (such as 1 mM) of full-length EM-1 or EM-2, but not the mixture of dipeptides, significantly induced mast cell degranulation (see Fig E10, B and C in this article's Online Repository at www.jacionline.org). However, in contrast to the results regarding EM-evoked chemical and/or mechanical itch, this degranulation was not inhibited by naloxone (see Fig E10, D). Therefore, the contribution of mast cell degranulation to EM-induced chemical and/or mechanical itch is estimated to be small.

We investigated the expression of CD26, EM-1, and EM-2 in the skin of patients with several diseases and in mouse models for which allodynia has been reported.^{6-10,25} Although allodynia in AD has been reported both in human and mice models, the expression of CD26 was not reduced in human AD skin.^{7,8} CD26 expression was also unchanged in human psoriatic skin, mouse dry skin model nor aged mouse skin, which all have been reported to have allodynia in mouse models^{6,9,25} (see Figs E11, A and B and E12 in this article's Online Repository at www.jacionline.org). According to these data, because the expression of EM-1 and EM-2 was significantly increased in some cases even in the absence of reductions in CD26, DPPIV does not appear to be the sole contributor to the degradation of EM-1 and/or EM-2.^{40,41} In

addition, no significant differences were observed in skin EM-1 and/or EM-2 levels between WT and CD26KO mice (see Fig E13 in this article's Online Repository at www.jacionline.org). These results may highlight the difficulties associated with using immunohistochemistry to detect alterations in EM-1 and EM-2 levels in skin with allodynia induced by EM-1 or EM-2. This may also be due to transient or local increases in EM level in skin around the site that received the mechanical stimulus or the low concentration of EM that induced mechanical itch (Fig 4). In contrast to these data, although the number of samples was small, in cutaneous T-cell lymphoma skin, a disease associated with severe itch, the expression of CD26 decreased whereas that of EM-1 and/or EM-2 increased in cancer cells and fibroblasts (see Fig E11, D). These data indicate that there are definitely cases of itchy diseases in which there is a significant increase in the expression of EM-1 and EM-2 with the decreased activity of DPPIV. In addition, increased expression of EM-2 was also observed in patients with bullous pemphigoid (a well-known skin disease characterized by itching, in which DPPIV inhibitors, first-line drugs for diabetes,⁶⁰ are suspected to be among the causes of its development) who are taking a DPPIV inhibitor (bullous pemphigoid + DPPIV inhibitor [see Fig E11, C]).⁶¹ Although as far as we know there are no reports that DPPIV inhibitors directly induce itch or allodynia, our preliminary results

showing scratching bouts under nonmechanical conditions in WT mice after an intradermal injection of sitagliptin provide support for this concept (Komiya et al, unpublished observations, 2016). These results indicate that in at least some clinical cases, DPPIV enzyme regulates spontaneous itch, and possibly allodynia, through the degradation of EMs.

In conclusion, the present study showed that EM-1 and EM-2 in the skin preferentially induced mechanical allodynia over chemical itch and that CD26/DPPIV is the regulatory enzyme for mechanical allodynia at the periphery. These results at least partly support the role of the peripheral nervous system in the allodynia-inducing mechanism that has been demonstrated in clinical studies on skin diseases,^{7,8} and they also suggest that in addition to being effective in studies of the central nervous system, peripheral approaches are effective for diseases associated with itch hypersensitivity.

We thank Ms H. Otsuka, Dr N. Takahashi, Dr C. S. Moniaga, Dr M. Kurosawa, Mr R. Kosuge, Mrs M. Fujishiro, Mr R. Kosaka, Dr M. Sato, Ms Y. Narita, Ms S. Okamoto, Dr H. Yamazaki, and Dr N. Iwao for their technical support.

Key messages

- EM-MOR signaling provoked mechanical allodynia at the periphery under the enzymatic control of CD26/DPPIV.
- Topically applied MOR antagonists and CD26/DPPIV are promising treatments for mechanical allodynia.

REFERENCES

1. Mack MR, Kim BS. The itch-scratch cycle: a neuroimmune perspective. *Trends Immunol* 2018;39:980-91.
2. Matsumoto A, Murota H, Terao M, Katayama I. Attenuated activation of homeostatic glucocorticoid in keratinocytes induces allodynia via aberrant artemin production. *J Invest Dermatol* 2018;138:1491-500.
3. Moniaga CS, Tominaga M, Takamori K. Mechanisms and management of itch in dry skin. *Acta Derm Venereol* 2020;100:adv00024.
4. Tominaga M, Takamori K. An update on peripheral mechanisms and treatments of itch. *Biol Pharm Bull* 2013;36:1241-7.
5. Tominaga M, Takamori K. Itch and nerve fibers with special reference to atopic dermatitis: therapeutic implications. *J Dermatol* 2014;41:205-12.
6. Sakai K, Sanders KM, Youssef MR, Yanushkevski KM, Jensen L, Yosipovitch G, et al. Mouse model of imiquimod-induced psoriatic itch. *Pain* 2016;157:2536-43.
7. Ikoma A, Fartasch M, Heyer G, Miyachi Y, Handwerker H, Schmelz M. Painful stimuli evoke itch in patients with chronic pruritus: central sensitization for itch. *Neurology* 2004;62:212-7.
8. Andersen HH, Elberling J, Sølvsten H, Yosipovitch G, Arendt-Nielsen L. Nonhistaminergic and mechanical itch sensitization in atopic dermatitis. *Pain* 2017;158:1780-91.
9. Akiyama T, Carstens MI, Ikoma A, Cevikbas F, Steinhoff M, Carstens E. Mouse model of touch-evoked itch (allodynia). *J Invest Dermatol* 2012;132:1886-91.
10. Akiyama T, Nguyen T, Curtis E, Nishida K, Devireddy J, Delahanty J, et al. A central role for spinal dorsal horn neurons that express neurokinin-1 receptors in chronic itch. *Pain* 2015;156:1240-6.
11. Fukuoka M, Miyachi Y, Ikoma A. Mechanically evoked itch in humans. *Pain* 2013;154:897-904.
12. Bourane S, Duan B, Koch SC, Dalet A, Britz O, Garcia-Campmany L, et al. NPY Cre Science 2015 Gate control of mechanical itch by a subpopulation of spinal cord interneurons. *Science* 2015;350:550-4.
13. Han L, Ma C, Liu Q, Weng HJ, Cui Y, Tang Z, et al. A subpopulation of nociceptors specifically linked to itch. *Nat Neurosci* 2013;16:174-82.
14. Mishra SK, Hoon MA. The cells and circuitry for itch responses in mice. *Science* 2013;340:968-71.
15. Barry DM, Liu XT, Liu B, Liu XY, Gao F, Zeng X, et al. Exploration of sensory and spinal neurons expressing gastrin-releasing peptide in itch and pain related behaviors. *Nat Commun* 2020;11:1397.
16. Sun YG, Chen ZF. A gastrin-releasing peptide receptor mediates the itch sensation in the spinal cord. *Nature* 2007;448:700-3.
17. Sun YG, Zhao ZQ, Meng XL, Yin J, Liu XY, Chen ZF. Cellular basis of itch sensation. *Science* 2009;325:1531-4.
18. Ross SE, Mardinly AR, McCord AE, Zurawski J, Cohen S, Jung C, et al. Loss of inhibitory interneurons in the dorsal spinal cord and elevated itch in Bhlhb5 mutant mice. *Neuron* 2010;65:886-98.
19. Kardon AP, Polgár E, Hachisuka J, Snyder LM, Cameron D, Savage S, et al. Dynorphin acts as a neuromodulator to inhibit itch in the dorsal horn of the spinal cord. *Neuron* 2014;82:573-86.
20. Huang J, Polgár E, Solinski HJ, Mishra SK, Tseng PY, Iwagaki N, et al. Circuit dissection of the role of somatostatin in itch and pain. *Nat Neurosci* 2018;21:707-16.
21. Acton D, Ren X, Di Costanzo S, Dalet A, Bourane S, Bertocchi I, et al. Spinal neuropeptide Y1 receptor-expressing neurons form an essential excitatory pathway for mechanical itch. *Cell Rep* 2019;28:625-39.e6.
22. Pan H, Fatima M, Li A, Lee H, Cai W, Horwitz L, et al. Identification of a spinal circuit for mechanical and persistent spontaneous itch. *Neuron* 2019;103:1135-49.e6.
23. Ikoma A, Handwerker H, Miyachi Y, Schmelz M. Electrically evoked itch in humans. *Pain* 2005;113:148-54.
24. Andersen HH, Akiyama T, Nattkemper LA, van Laarhoven A, Elberling J, Yosipovitch G, et al. Allodynia and hyperknesis-mechanisms, assessment methodology, and clinical implications of itch sensitization. *Pain* 2018;159:1185-97.
25. Feng J, Luo J, Yang P, Du J, Kim BS, Hu H. Piezo2 channel-Merkel cell signaling modulates the conversion of touch to itch. *Science* 2018;360:530-3.
26. Morimoto C, Schlossman SF. The structure and function of CD26 in the T-cell immune response. *Immunol Rev* 1998;161:55-70.
27. Ohnuma K, Dang NH, Morimoto C. Revisiting an old acquaintance: CD26 and its molecular mechanisms in T cell function. *Trends Immunol* 2008;29:295-301.
28. Ohnuma K, Hatano R, Komiya E, Otsuka H, Itoh T, Iwao N, et al. A novel role for CD26/dipeptidyl peptidase IV as a therapeutic target. *Front Biosci (Landmark Ed)* 2018;23:1754-79.
29. Ohnuma K, Hosono O, Dang NH, Morimoto C. Dipeptidyl peptidase in autoimmune pathophysiology. *Adv Clin Chem* 2011;53:51-84.
30. Komiya E, Hatano R, Otsuka H, Itoh T, Yamazaki H, Yamada T, et al. A possible role for CD26/DPPIV enzyme activity in the regulation of psoriatic pruritus. *J Dermatol Sci* 2017;86:212-21.
31. Marguet D, Baggio L, Kobayashi T, Bernard AM, Pierres M, Nielsen PF, et al. Enhanced insulin secretion and improved glucose tolerance in mice lacking CD26. *Proc Natl Acad Sci U S A* 2000;97:6874-9.
32. Tanaka T, Kameoka J, Yaron A, Schlossman SF, Morimoto C. The costimulatory activity of the CD26 antigen requires dipeptidyl peptidase IV enzymatic activity. *Proc Natl Acad Sci U S A* 1993;90:4586-90.
33. Shane R, Wilk S, Bodnar RJ. Modulation of endomorphin-2-induced analgesia by dipeptidyl peptidase IV. *Brain Res* 1999;815:278-86.
34. Sakurada C, Sakurada S, Hayashi T, Katsuyama S, Tan-No K, Sakurada T. Degradation of endomorphin-2 at the supraspinal level in mice is initiated by dipeptidyl peptidase IV: an in vitro and in vivo study. *Biochem Pharmacol* 2003;66:653-61.
35. Yamaguchi T, Kitagawa K, Kuraishi Y. Itch-associated response and antinociception induced by intracisternal endomorphins in mice. *Jpn J Pharmacol* 1998;78:337-43.
36. Martin-Schild S, Gerall AA, Kastin AJ, Zadina JE. Differential distribution of endomorphin 1- and endomorphin 2-like immunoreactivities in the CNS of the rodent. *J Comp Neurol* 1999;405:450-71.
37. Schreff M, Schulz S, Wiborny D, Höllt V. Immunofluorescent identification of endomorphin-2-containing nerve fibers and terminals in the rat brain and spinal cord. *Neuroreport* 1998;9:1031-4.
38. Bardoni R, Tawfik VL, Wang D, François A, Solorzano C, Shuster SA, et al. Delta opioid receptors presynaptically regulate cutaneous mechanosensory neuron input to the spinal cord dorsal horn. *Neuron* 2014;81:1312-27.
39. Usoskin D, Furlan A, Islam S, Abdo H, Lönnberg P, Lou D, et al. Unbiased classification of sensory neuron types by large-scale single-cell RNA sequencing. *Nat Neurosci* 2015;18:145-53.
40. Tomboly C, Peter A, Toth G. In vitro quantitative study of the degradation of endomorphins. *Peptides* 2002;23:1573-80.
41. Barsun M, Jajcanin N, Vukelić B, Spoljarić J, Abramić M. Human dipeptidyl peptidase III acts as a post-proline-cleaving enzyme on endomorphins. *Biol Chem* 2007;388:343-8.

42. Guieu R, Fenouillet E, Devaux C, Fajloun Z, Carrega L, Sabatier JM, et al. CD26 modulates nociception in mice via its dipeptidyl-peptidase IV activity. *Behav Brain Res* 2006;166:230-5.
43. Azimi E, Reddy VB, Shade KC, Anthony RM, Talbot S, Pereira PJS, et al. Dual action of neurokinin-1 antagonists on Mas-related GPCRs. *JCI Insight* 2016;1:e89362.
44. Carstens E, Follansbee T, Iodi Carstens M. The challenge of basic itch research. *Acta Derm Venereol* 2020;100:adv00023.
45. Zadina JE, Hackler L, Ge LJ, Kastin AJ. A potent and selective endogenous agonist for the mu-opiate receptor. *Nature* 1997;386:499-502.
46. Barr GA, Zadina JE. Maturation of endomorphin-2 in the dorsal horn of the medulla and spinal cord of the rat. *Neuroreport* 1999;10:3857-60.
47. Ständer S, Gunzer M, Metzke D, Luger T, Steinhoff M. Localization of mu-opioid receptor 1A on sensory nerve fibers in human skin. *Regul Pept* 2002;110:75-83.
48. Bigliardi PL, Bigliardi-Qi M, Buechner S, Ruffli T. Expression of mu-opiate receptor in human epidermis and keratinocytes. *J Invest Dermatol* 1998;111:297-301.
49. Takahashi N, Tominaga M, Kosaka R, Kamata Y, Umehara Y, Matsuda H, et al. Involvement of μ -opioid Receptors and κ -opioid receptors in itch-related scratching behaviour of imiquimod-induced psoriasis-like dermatitis in mice. *Acta Derm Venereol* 2017;97:928-33.
50. Zhang L, Zhang JT, Hang L, Liu T. Mu opioid receptor heterodimers emerge as novel therapeutic targets: recent progress and future perspective. *Front Pharmacol* 2020;11:1078.
51. Wu SY, Ohtubo Y, Brailoiu GC, Dun NJ. Effects of endomorphin on substantia gelatinosa neurons in rat spinal cord slices. *Br J Pharmacol* 2003;140:1088-96.
52. Wang Z, Jiang C, Yao H, Chen O, Rahman S, Gu Y, et al. Central opioid receptors mediate morphine-induced itch and chronic itch via disinhibition. *Brain* 2021;144:665-81.
53. Liu XY, Liu ZC, Sun YG, Ross M, Kim S, Tsai FF, et al. Unidirectional cross-activation of GRPR by MOR1D uncouples itch and analgesia induced by opioids. *Cell* 2011;147:447-58.
54. Binshtok AM, Bean BP, Woolf CJ. Inhibition of nociceptors by TRPV1-mediated entry of impermeant sodium channel blockers. *Nature* 2007;449:607-10.
55. Borroto-Escuela DO, Romero-Fernandez W, Rivera A, Van Craenenbroeck K, Tarakanov AO, Agnati LF, et al. On the g-protein-coupled receptor heteromers and their allosteric receptor-receptor interactions in the central nervous system: focus on their role in pain modulation. *Evid Based Complement Alternat Med* 2013;2013:563716.
56. Akgün E, Javed MI, Lunzer MM, Powers MD, Sham YY, Watanabe Y, et al. Inhibition of inflammatory and neuropathic pain by targeting a mu opioid receptor/chemokine receptor5 heteromer (MOR-CCR5). *J Med Chem* 2015;58:8647-57.
57. Smeester BA, Lunzer MM, Akgün E, Beitz AJ, Portoghese PS. Targeting putative mu opioid/metabotropic glutamate receptor-5 heteromers produces potent antinociception in a chronic murine bone cancer model. *Eur J Pharmacol* 2014;743:48-52.
58. Tachibana T, Nawa T. Immunohistochemical reactions of receptors to met-enkephalin, VIP, substance P, and CGRP located on Merkel cells in the rat sinus hair follicle. *Arch Histol Cytol* 2005;68:383-91.
59. Lansu K, Karpiak J, Liu J, Huang XP, McCorvy JD, Kroeze WK, et al. In silico design of novel probes for the atypical opioid receptor MRGPRX2. *Nat Chem Biol* 2017;13:529-36.
60. Cahn A, Cernea S, Raz I. An update on DPP-4 inhibitors in the management of type 2 diabetes. *Expert Opin Emerg Drugs* 2016;21:409-19.
61. Béné J, Moulis G, Bennani I, Auffret M, Coupe P, Babai S, et al. Bullous pemphigoid and dipeptidyl peptidase IV inhibitors: a case-noncase study in the French Pharmacovigilance Database. *Br J Dermatol* 2016;175:296-301.

Phase I Study of Tremelimumab Monotherapy or in Combination With Durvalumab in Japanese Patients With Advanced Solid Tumors or Malignant Mesothelioma

Yutaka Fujiwara^{1,*}, Yasuo Takahashi², Morihito Okada³, Takumi Kishimoto⁴, Shunsuke Kondo⁵, Koshi Fujikawa², Manabu Hayama⁶, Masatoshi Sugeno⁶, Shinya Ueda⁶, Keiko Komuro⁶, Mark Lanasa⁷, Takashi Nakano⁸

¹National Cancer Center Hospital, Tokyo, Japan and Aichi Cancer Center, Nagoya, Japan

²National Hospital Organization Hokkaido Cancer Centre, Sapporo, Japan

³Hiroshima University Hospital, Hiroshima, Japan

⁴Okayama Rosai Hospital, Okayama, Japan

⁵National Cancer Center Hospital, Tokyo, Japan

⁶AstraZeneca, Osaka, Japan

⁷AstraZeneca, Gaithersburg, MD, USA

⁸Hyogo College of Medicine Hospital, Hyogo, Japan and Otemae Hospital, Osaka, Japan

*Corresponding author: Yutaka Fujiwara, MD, Department of Thoracic Oncology, Aichi Cancer Center, 1-1 Kanokoden, Chikusa-ku, Nagoya 464-0021, Japan.

Tel: +81 52 762 6111; Email: fu_ji_@yahoo.co.jp

[†]Principal investigator: Yutaka Fujiwara

Abstract

Background: The primary objective of this phase I, open-label trial was to assess safety and tolerability of tremelimumab monotherapy and combination therapy with durvalumab in Japanese patients with advanced cancer. Tremelimumab is a fully human monoclonal antibody against CTLA-4 in clinical trials; durvalumab is a monoclonal antibody against PD-L1 for the treatment of bladder and lung cancer.

Methods: In part 1, tremelimumab 3 or 10 mg/kg was given every 4 weeks (Q4W) for 6 doses, and thereafter every 12 weeks until discontinuation ($n = 8$); subsequently tremelimumab 10 mg/kg Q4W for 6 doses/Q12W and thereafter until discontinuation was administered in 41 patients with malignant pleural or peritoneal mesothelioma (MPM). In part 2, tremelimumab 10 mg/kg (Q4W for 6 doses followed by Q12W for 3 doses) was given in combination with durvalumab 15 mg/kg (Q4W for 13 doses) in cohort 1 ($n = 4$). In cohort 2 ($n = 6$), tremelimumab 1 mg/kg (Q4W for 4 doses) was given in combination with durvalumab 20 mg/kg (Q4W for 4 doses followed by 10 mg/kg Q2W for 22 doses), while in cohort 3 ($n = 6$), fixed-dose tremelimumab 75 mg Q4W for 4 doses plus durvalumab 1500 mg Q4W for 13 doses was given.

Results: In part 1, no dose-limiting toxicities (DLTs) for tremelimumab 3 or 10 mg/kg (Q4W for 6 doses/Q12W thereafter until discontinuation) were observed. Six (75%) patients reported treatment-related adverse events (trAEs). In the MPM dose-expansion cohort, 38 (92.7%) patients reported trAEs. In part 2, one DLT (Grade 4 myasthenia gravis) was reported for tremelimumab 10 mg/kg (Q4W for 6 doses/Q12W for 3 doses) plus durvalumab 15 mg/kg (Q4W for 13 doses). One DLT (Grade 4 hyperglycemia) was reported for tremelimumab 75 mg (Q4W for 4 doses) plus durvalumab 1500 mg (Q4W for 13 doses). Fourteen (87.5%) patients reported trAEs. Tremelimumab demonstrated low immunogenicity; 1 (16.7%) patient developed antidrug antibodies.

Conclusion: Tremelimumab 10 mg/kg (Q4W/Q12W), tremelimumab 1 mg/kg (Q4W) plus durvalumab 20 mg/kg (Q4W/10 mg/kg Q2W), and fixed-dose tremelimumab 75 mg (Q4W) plus durvalumab 1500 mg (Q4W) were safe and tolerable.

ClinicalTrials.gov Identifier: NCT02141347 (<https://clinicaltrials.gov/ct2/show/NCT02141347>)

Key words: durvalumab; immunotherapy; Japanese; malignant mesothelioma; tremelimumab.

Lessons Learned

- This phase I trial was the first evaluation of tremelimumab as monotherapy and in combination with durvalumab in Japanese patients with advanced solid malignancies.
- Tremelimumab 10 mg/kg monotherapy (Q4W for 6 doses/Q12W thereafter until discontinuation), tremelimumab 1 mg/kg (Q4W for 4 doses) plus durvalumab 20 mg/kg (Q4W for 4 doses followed by 10 mg/kg Q2W for up to 22 doses), and fixed-dose tremelimumab 75 mg (Q4W for 4 doses) plus durvalumab 1500 mg (Q4W for 13 doses) were generally safe and tolerable.

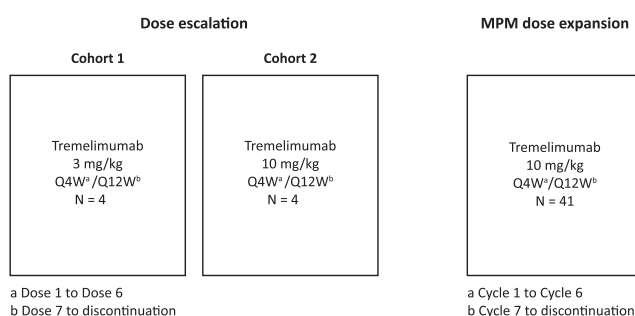
Discussion

In 2014 when the current study was initiated, an international phase IIb trial (DETERMINE) evaluated tremelimumab use in relapsed malignant pleural/peritoneal mesothelioma (MPM).¹ DETERMINE was not conducted in Japan. It was necessary to provide tremelimumab safety and efficacy data in the Japanese population, ahead of planned phase III programs. The primary and secondary objectives of this open-label, multicenter, phase I trial (NCT02141347) were to assess the safety and tolerability, and antitumor activity, of tremelimumab monotherapy and in combination therapy with durvalumab in Japanese patients with advanced cancer. The trial comprised tremelimumab monotherapy dose escalation and MPM dose expansion, and tremelimumab plus durvalumab combination dosing (including a fixed-dose cohort [tremelimumab 75 mg Q4W/durvalumab 1500 mg Q4W], which had not been previously studied) (Fig. 1).

During part 1 dose escalation, no dose-limiting toxicities (DLTs) were reported. Six (75.0%) patients reported treatment-related adverse events (trAEs); 2 (25.0%) reported grade ≥ 3 trAEs, and 5 (62.5%) reported treatment-related AEs of special interest (AESIs). For dose expansion, 38 (92.7%) patients reported any-grade AE and trAEs; 16 (39.0%) reported grade ≥ 3 trAEs, and 35 (85.4%) reported treatment-related AESIs. Adverse event rates were similar to previous investigations.¹⁻³ One (2.4%) patient had a partial response. Similar to DETERMINE results,¹ tremelimumab 10 mg/kg showed limited clinical activity in previously treated MPM patients. The recommended tremelimumab dose was 10 mg/kg.

During part 2 combination dosing, 1 patient receiving tremelimumab 10 mg/kg (Q4W for 6 doses/Q12W for 3 doses) plus durvalumab 15 mg/kg (Q4W for 13 doses) experienced a DLT (grade 4 myasthenia gravis); recruitment to this cohort was subsequently stopped. One DLT (grade 3 hyperglycemia) was reported by a patient receiving tremelimumab 75 mg (Q4W for 4 doses) plus durvalumab 1500 mg (Q4W for 13 doses). The severity grade was increased to grade 4 on day 19 and subsequently downgraded to grade 1 on day 37; the patient was permanently discontinued from the study treatment. Fourteen (87.5%)

Part 1 - Tremelimumab monotherapy



Part 2 - Tremelimumab + durvalumab combination multiple dosing

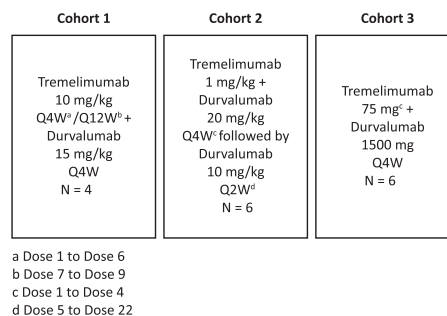


Figure 1. Study design.

patients reported any-grade AEs related to tremelimumab and durvalumab, respectively; 7 (43.8%) each reported grade ≥ 3 tremelimumab- and durvalumab-related AEs, and 9 (56.3%) reported treatment-related AESIs. No unexpected AEs were observed.⁴⁻⁶ The rate of any-grade trAEs (87.5%) aligned with the 88% incidence rate from a systematic review and meta-analysis.⁷ Antitumor activity with combination therapy was reported previously^{4-6,8-13}; however, it was limited in the current study.

Tremelimumab 10 mg/kg (Q4W/Q12W), tremelimumab 1 mg/kg (Q4W)/durvalumab 20 mg/kg (Q4W/10 mg/kg Q2W), and fixed-dose tremelimumab 75 mg (Q4W)/durvalumab 1500 mg (Q4W) were safe and tolerable in this phase I trial of Japanese patients with advanced cancer.

TRIAL INFORMATION

Disease	Advanced cancer/solid tumor only, mesothelioma
Stage of disease/treatment	Metastatic/advanced
Prior therapy	More than 2 prior regimens
Type of study	Phase I
Primary endpoints	Tolerability, safety, maximum tolerated dose
Secondary endpoints	Pharmacokinetics, immunogenicity, anti-tumor activity, efficacy
Investigator's analysis	Active and should be pursued further.

Additional details of endpoints of study design

Study design: [Fig. 1](#)

Primary endpoints:

Part 1: Dose escalation phase: To investigate the safety and tolerability of tremelimumab when given to Japanese patients with advanced solid malignancies and define the dose(s) for further clinical evaluation.

Part 1: MPM dose expansion: to investigate the safety and tolerability of tremelimumab when given to Japanese patients with unresectable pleural or peritoneal malignant mesothelioma.

Part 2: Tremelimumab plus durvalumab combination multiple dosing: to investigate the safety and tolerability of tremelimumab in combination with durvalumab when given to Japanese patients with advanced solid malignancies and to define the dose(s) for further clinical evaluation.

Secondary endpoints:

Part 1: Dose escalation phase: (1) to describe the PK of tremelimumab in Japanese patients with advanced solid tumors. (2) To determine the immunogenicity of tremelimumab in Japanese patients with advanced solid tumors. (3) To evaluate the anti-tumor activity of tremelimumab in Japanese patients with advanced solid tumors.

Part 1: MPM dose expansion: (1) To describe the PK of tremelimumab in Japanese patients with pleural or peritoneal malignant mesothelioma. (2) To evaluate the immunogenicity of tremelimumab in Japanese patients with pleural or peritoneal malignant mesothelioma. (3) To evaluate the efficacy of tremelimumab in Japanese patients with pleural or peritoneal malignant mesothelioma.

Part 2: Tremelimumab plus durvalumab combination multiple dosing: (1) To describe the PK of tremelimumab in combination with durvalumab in Japanese patients with advanced solid tumors. (2) To determine the immunogenicity of tremelimumab in combination with durvalumab in Japanese patients with advanced solid tumors. (3) To describe the PK of durvalumab in combination with tremelimumab in Japanese patients with advanced solid tumors. (4) To determine the immunogenicity of durvalumab in combination with tremelimumab in Japanese patients with advanced solid tumors. (5) To evaluate the anti-tumor activity of tremelimumab in combination with durvalumab in Japanese patients with advanced solid tumors.

DRUG INFORMATION: PART 1

Generic	Tremelimumab
Company name	AstraZeneca
Drug type	Antibody
Drug class	Immune therapy
Dose	See dose escalation table (part 1)
Route	i.v.
Schedule of administration	See dose escalation table (part 1)

DRUG INFORMATION: PART 2

Generic	Tremelimumab	Durvalumab
Company name	AstraZeneca	AstraZeneca
Drug type	Antibody	Antibody
Drug class	Immune therapy	Immune therapy
Dose	See dose escalation table (part 2)	See dose escalation table (part 2)
Route	i.v.	i.v.
Schedule of administration	See dose escalation table (part 2)	

DOSE ESCALATION TABLE

Dose level	Dose of drug: tremelimumab	Dose of drug: durvalumab	Number assigned	Number evaluable for treatment
Part 1 cohort 1	3 mg/kg Q4W for 6 doses/Q12W thereafter until discontinuation	n/a	4	4

Dose level	Dose of drug: tremelimumab	Dose of drug: durvalumab	Number assigned	Number evaluable for treatment
Part 1 cohort 2	10 mg/kg Q4W for 6 doses/Q12W thereafter until discontinuation	n/a	4	4
Part 1 MPM dose expansion	10 mg/kg Q4W for 6 doses/Q12W thereafter until discontinuation	n/a	41	41
Part 2 cohort 1	10 mg/kg Q4W for 6 doses/Q12W for 3 doses	15 mg/kg Q4W for 13 doses	4	4
Part 2 cohort 2	1 mg/kg Q4W for 4 doses	20 mg/kg Q4W for 4 doses followed by 10 mg/kg Q2W for up to 22 doses	6	6
Part 2 cohort 3	75 mg Q4W for 4 doses	1500 mg Q4W for 13 doses	6	6

PATIENT CHARACTERISTICS: PART 1 DOSE ESCALATION

Number of patients, male	5
Number of patients, female	3
Stage	Stage III (<i>n</i> = 1), stage IV (<i>n</i> = 7)
Age, years, median (range)	58.5 (40-72)
Number of prior systemic therapies	3 (<i>n</i> = 2); >3 (<i>n</i> = 6)
Performance status: ECOG	0, <i>n</i> = 6 (75%) 1, <i>n</i> = 2 (25%)

PATIENT CHARACTERISTICS: PART 1 MPM DOSE EXPANSION

Number of patients, male	36
Number of patients, female	5
Stage	Stage II (<i>n</i> = 7), stage III (<i>n</i> = 12), stage IV (<i>n</i> = 21), unknown (<i>n</i> = 1)
Age, years, median (range)	67.0 (40-79)
Number of prior systemic therapies	1 (<i>n</i> = 13); 2 (<i>n</i> = 16); 3 (<i>n</i> = 6); >3 (<i>n</i> = 6)
Performance Status: ECOG	0, <i>n</i> = 21 (51.2%) 1, <i>n</i> = 20 (48.8%)

PATIENT CHARACTERISTICS: PART 2

Number of patients, male	8
Number of patients, female	8
Stage	Stage III (<i>n</i> = 1), stage IV (<i>n</i> = 13), unknown (<i>n</i> = 2)
Age, years, median(range)	61.0 (34-74)
Number of prior systemic therapies	1 (<i>n</i> = 1); 2 (<i>n</i> = 1); 3 (<i>n</i> = 2); >3 (<i>n</i> = 12)
Performance Status: ECOG	0, <i>n</i> = 13 (81.3%) 1, <i>n</i> = 3 (18.8%)

Table 2 shows detailed baseline patient demographic and clinical characteristics.

PRIMARY ASSESSMENT METHOD: PART 1 DOSE ESCALATION

Number of patients assigned	8
Number of patients evaluable for toxicity	8
Number of patients evaluated for efficacy	8
Evaluation method	RECIST 1.1
Response assessment, SD	<i>n</i> = 1; 25.0% (1/4) in the tremelimumab 10 mg/kg (Q4W for 6 doses/Q12W thereafter until discontinuation) group
Response assessment, PD	<i>n</i> = 7; 100% (4/4) in the tremelimumab 3 mg/kg (Q4W for 6 doses/Q12W thereafter until discontinuation) group and 75.0% (3/4) in the tremelimumab 10 mg/kg (Q4W for 6 doses/Q12W thereafter until discontinuation) group
Duration of treatment	71.5 days

PRIMARY ASSESSMENT METHOD: PART 1 MPM DOSE EXPANSION

Number of patients assigned	41
Number of patients evaluable for toxicity	41
Number of patients evaluated for efficacy	41
Evaluation method	RECIST 1.1
Response assessment, PR	1 (2.4%)
Response assessment, SD	17 (41.5%)
Response assessment, PD	18 (43.9%)
Response assessment, other	5 (12.2%)
PFS	2.9 months (95% CI: 2.8-5.5)
OS	14.6 months (14.6-not calculable)
Duration of treatment	55.0 days
Outcome notes	RECIST v1.1 for peritoneal mesothelioma, modified RECIST v1.0 for pleural mesothelioma.

PRIMARY ASSESSMENT METHOD: PART 2

Number of patients assigned	16
Number of patients evaluable for toxicity	16
Number of patients evaluated for efficacy	16
Evaluation method	RECIST 1.1
Response assessment, CR	<i>n</i> = 1; 16.7% (1/6) in tremelimumab 1 mg/kg (Q4W for 4 doses) plus durvalumab 20 mg/kg (Q4W for 4 doses followed by 10 mg/kg Q2W for up to 22 doses) group
Response assessment, PR	<i>n</i> = 1; 16.7% (1/6) in tremelimumab 1 mg/kg (Q4W for 4 doses) plus durvalumab 20 mg/kg (Q4W for 4 doses followed by 10 mg/kg Q2W for up to 22 doses) group
Response assessment, SD	<i>n</i> = 2; 33.3% (2/6) in tremelimumab 75 mg (Q4W for 4 doses) plus durvalumab 1500 mg (Q4W for 13 doses) group
Response assessment, PD	<i>n</i> = 10; 75% (3/4) in tremelimumab 10 mg/kg (Q4W for 6 doses/Q12W for 3 doses) plus durvalumab 15 mg/kg group (Q4W for 13 doses); 66.7% (4/6) in tremelimumab 1 mg/kg (Q4W for 4 doses) plus durvalumab 20 mg/kg (Q4W for 4 doses followed by 10 mg/kg Q2W for up to 22 doses) group; 50% (3/6) in tremelimumab 75 mg (Q4W for 4 doses) plus durvalumab 1500 mg (Q4W for 13 doses) group
Response assessment, other	<i>n</i> = 2; 25% (1/4) in tremelimumab 10 mg/kg (Q4W for 6 doses/Q12W for 3 doses) plus durvalumab 15 mg/kg (Q4W for 13 doses) group; 16.7% (1/6) in tremelimumab 75 mg (Q4W for 4 doses) plus durvalumab 1500 mg (Q4W for 13 doses) group
Duration of treatment	44.0 days

DLT was not assessed for part 1 MPM dose expansion. See [Figs. 2 and 3](#) (Waterfall plots of best percentage change from baseline in tumor size), [Fig. 4](#) (Kaplan-Meier plots of progression-free survival and overall survival), and [Table 3](#) (Summary of antitumor activity).

DOSE-LIMITING TOXICITIES TABLE

Dose level	Dose of drug 1: Tremelimumab	Dose of drug 2: Durvalumab	No. enrolled	No. evaluable for treatment	No. with a dose-limiting toxicity	Dose-limiting toxicity information
Part 1 cohort 1	3 mg/kg Q4W for 6 doses/Q12W thereafter until discontinuation	n/a	4	4	0	None
Part 1 cohort 2	10 mg/kg Q4W for 6 doses/Q12W thereafter until discontinuation	n/a	4	4	0	None
Part 2 cohort 1	10 mg/kg Q4W for 6 doses/Q12W for 3 doses	15 mg/kg Q4W for 13 doses	4	4	1	Grade 4 myasthenia gravis
Part 2 cohort 2	1 mg/kg Q4W for 4 doses	20 mg/kg Q4W for 4 doses followed by 10 mg/kg Q2W for up to 22 doses	6	6	0	None
Part 2 cohort 3	75 mg Q4W for 4 doses	1500 mg Q4W for 13 doses	6	6	1	Grade 4 hyperglycemia

Pharmacokinetics and Pharmacodynamics

See Fig. 5 (Geometric mean serum concentration vs time) and Table 5 (Summary of PK characteristics).

Adverse Events

See Table 1 (Summary of AEs) and Table 4 (AEs of CTCAE grade ≥ 3 by system organ class and preferred term).

ASSESSMENT, ANALYSIS, AND DISCUSSION

Completion:

Study completed

Investigator's assessment:

Active and should be pursued further

The burden of cancer in Japan, including an estimated 1,017,200 incident cases in 2019,¹⁴ underscores the need for expanded and robust cancer treatment options for patients. Clinical trials have established the efficacy of monoclonal antibodies (mAbs), which block immune regulatory checkpoint receptors or their ligands (ie, programmed cell death-1 [PD-1]/programmed cell death ligand-1 [PD-L1] or cytotoxic T-lymphocyte-associated antigen-4 [CTLA-4]) in several tumor types.^{4-6,15-18} Durvalumab is a selective, high-affinity, engineered human immunoglobulin (Ig) G1 mAb that blocks PD-L1 binding to PD-1 and cluster of differentiation (CD) 80.¹⁹ Durvalumab, which demonstrates clinical activity and safety across multiple solid tumor types,^{4-6,20-22} is approved in Japan for consolidation therapy following definitive chemoradiation in patients with unresectable, locally advanced, non-small cell lung cancer.²³ In addition, it is also approved in Japan for treatment of patients with extensive-stage small cell lung cancer (ES-SCLC), in combination with etoposide plus a choice of platinum chemotherapy (either carboplatin or cisplatin).²⁴ Tremelimumab is a selective IgG2 mAb that promotes T-cell activity through CTLA-4 inhibition^{2,25} and has been investigated in a wide range of cancers.^{1,2,4,5,25,26}

The current study—an open-label, multicenter, phase I trial (NCT02141347)—assessed the safety and tolerability of tremelimumab monotherapy and combination therapy with durvalumab (including a fixed-dose cohort [tremelimumab 75 mg Q4W/durvalumab 1500 mg Q4W] (Fig. 1 and Table 1), which had not been previously studied) in Japanese patients with advanced cancer; secondary objectives included assessments of immunogenicity, antitumor activity, and pharmacokinetics (PK) after the first dose and at steady state. Previously, an international, double-blind, randomized, phase IIb trial (DETERMINE; NCT01843374) evaluated tremelimumab for second- and third-line treatment of patients with relapsed MPM.¹ The DETERMINE trial was not conducted in Japan, where MPM incidence is among the highest globally.^{27,28} The current study was conducted to address the need for safety and efficacy data for tremelimumab in the Japanese population prior to international phase III programs of tremelimumab monotherapy and combination therapy. The number of patients for the current study was informed by the need for adequate tolerability, safety, and PK data, while exposing as few patients as possible to the investigational product. Consequently, it was determined that 3-6 evaluable patients were needed for a dose group. For the MPM dose expansion, a sample size of 40 patients was considered sufficient for safety evaluations.

Previous studies have established the safety and tolerability of tremelimumab monotherapy in doses up to 15 mg/kg.^{2,3,29} The safety results from the dose-escalation period indicated

that 10 mg/kg was the recommended dose of tremelimumab for Japanese patients. Rates of adverse events (AEs) were similar to previous investigations of tremelimumab monotherapy in solid tumors and MPM.¹⁻³ No AE-related deaths, DLTs, or other safety concerns from the clinical laboratory assessments, electrocardiogram (ECG), vital signs, and physical findings were observed (see dose-limiting toxicities table). The immunogenicity of tremelimumab was low during both dose escalation and dose expansion. For dose escalation, the time to reach maximum serum concentration (t_{\max}) was similar after single- and multiple-dose tremelimumab 10 mg/kg (Q4W for 6 doses/Q12W thereafter until discontinuation; Table 5). No objective responses were observed with tremelimumab 3 or 10 mg/kg (Q4W for 6 doses/Q12W thereafter until discontinuation). Similar to the results of the DETERMINE trial,¹ tremelimumab 10 mg/kg (Q4W for 6 doses/Q12W thereafter until discontinuation) showed limited clinical activity in patients with previously treated MPM. The median overall survival in patients with previously treated MPM was longer than that reported in the DETERMINE trial (14.6 months vs. 7.7 months).¹ However, the current study was not primarily designed to evaluate the efficacy of tremelimumab monotherapy; conclusions can only be drawn with regard to study-specific dosing regimens and patients. In light of the results from Checkmate 743,³⁰ as well as the DREAM³¹ and PrE0505 trials,³² immune-oncology (IO) combinations or IO plus chemotherapy combinations demonstrate a greater degree of efficacy than cytotoxic T-lymphocyte-associated antigen 4 (CTLA-4) inhibitor monotherapy.

Tremelimumab 1 mg/kg (Q4W for 4 doses) plus durvalumab 20 mg/kg (Q4W for 4 doses followed by 10 mg/kg Q2W for up to 22 doses) and fixed-dose tremelimumab 75 mg (Q4W for 4 doses) plus durvalumab 1500 mg (Q4W for 13 doses) were found to be safe and tolerable (Tables 1 and 3), with no unexpected AEs based on the previous investigations of this combination.⁴⁻⁶ Across all study cohorts, the rate of any-grade treatment-related AEs (trAEs; 87.5%) was in accordance with the 88% incidence rate reported in a systematic review and meta-analysis of the safety and tolerability of anti-CTLA-4 plus anti-PD-1/PD-L1 combination therapy.⁷ Levels of antidrug antibodies were low (Table 6), and similar to previous investigations of tremelimumab and durvalumab combination therapy.⁴⁻⁶ The t_{\max} of tremelimumab plus durvalumab was similar across dose groups and when compared with the t_{\max} of cycle 1 (Table 5). Notably, PK linearity was observed in the area under the serum concentration-time curve within a dosing interval (AUC_{0-t}), minimum serum concentration (C_{\min}), and maximum serum concentration (C_{\max}) for tremelimumab and durvalumab in single and multiple doses. No PK interaction

was observed between tremelimumab and durvalumab. While promising antitumor activity with the tremelimumab plus durvalumab combination has been reported elsewhere for a variety of advanced cancers,^{4,6,8-13} evidence in the current study was limited. A notable exception was observed in 2 patients in the tremelimumab 1 mg/kg (Q4W for 4 doses) plus durvalumab 20 mg/kg cohort (Q4W for 4 doses followed by 10 mg/kg Q2W for up to 22 doses); 1 patient with lower bile duct cancer had a complete response and 1 patient with ampullary cancer had a partial response. Although these findings from a relatively small number of patients do not support conclusive statements, it suggests that biliary tract cancers may be sensitive to the tremelimumab 1 mg/kg (Q4W for 4 doses) plus durvalumab 20 mg/kg (Q4W for 4 doses followed by 10 mg/kg Q2W for up to 22 doses) combination regimen. Future studies are needed to evaluate how best to combine immune checkpoint inhibitors in Japanese patients with advanced solid tumors, along with the continued identification of biomarkers (eg estimated CD8+ T-cell abundance) that predict response to immunotherapy.³³⁻³⁶

In conclusion, tremelimumab 10 mg/kg monotherapy (Q4W for 6 doses/Q12W thereafter until discontinuations), tremelimumab 1 mg/kg (Q4W for 4 doses) plus durvalumab 20 mg/kg (Q4W for 4 doses followed by 10 mg/kg Q2W for up to 22 doses), and fixed-dose tremelimumab 75 mg (Q4W for 4 doses) plus durvalumab 1500 mg (Q4W for 13 doses) were found to be generally safe and tolerable in this Phase 1 trial of Japanese patients with advanced cancer and with a similar safety profile to that seen in other patient populations. Tremelimumab plus durvalumab combination doses were appropriate for future evaluation. Tremelimumab immunogenicity was observed to be low. Evidence of preliminary antitumor activity in this heavily pre-treated patient population was limited.

Acknowledgments

We thank Alicja Dabrowska Brown of AstraZeneca for reviewing early drafts of the manuscript. Medical writing support, which was in accordance with Good Publication Practice (GPP3) guidelines, was provided by Liam Gillies, Ph.D., C.M.P.P., of Cactus Life Sciences (part of Cactus Communications) and was funded by AstraZeneca.

Conflict of Interest

Yutaka Fujiwara: AstraZeneca, Daiichi-Sankyo, Otsuka, Ono Pharmaceutical (C/A), AstraZeneca, Bristol-Meyers Squibb, Novartis (H); Shunsuke Kondo: ASLAN Pharmaceuticals, AstraZeneca, Bayer, Eli Lilly, Merck Sharp & Dohme, Pfizer (RF); Manabu Hayama: AstraZeneca (E); Masatoshi Sugeno: AstraZeneca (E); Shinya Ueda: AstraZeneca (E, OI); Keiko Komuro: AstraZeneca (E); Mark Lanasa: AstraZeneca (E). The other authors indicated no financial relationships.

(C/A) Consulting/advisory relationship; (RF) Research funding; (E) Employment; (ET) Expert testimony; (H) Honoraria received; (OI) Ownership interests; (IP) Intellectual property rights/inventor/patent holder; (SAB) Scientific advisory board

Data Availability

The data underlying this article will be shared on reasonable request to the corresponding author.

References

1. Maio M, Scherpereel A, Calabrò L, et al. Tremelimumab as second-line or third-line treatment in relapsed malignant mesothelioma (DETERMINE): a multicentre, international, randomised, double blind, placebo-controlled phase 2b trial. *Lancet Oncol.* 2017;18(9):1261-1273. [https://doi.org/10.1016/S1470-2045\(17\)30446-1](https://doi.org/10.1016/S1470-2045(17)30446-1).
2. Comin-Anduix B, Escuin-Ordinas H, Ibarrrondo FJ. Tremelimumab: research and clinical development. *Onco Targets Ther.* 2016;9:1767-1776. <https://doi.org/10.2147/OTT.S65802>.
3. Calabrò L, Morra A, Fonsatti E, et al. Tremelimumab for patients with chemotherapy-resistant advanced malignant mesothelioma: an open-label, single-arm, phase 2 trial. *Lancet Oncol.* 2013;14(11):1104-1111. [https://doi.org/10.1016/S1470-2045\(13\)70381-4](https://doi.org/10.1016/S1470-2045(13)70381-4).
4. Antonia S, Goldberg SB, Balmanoukian A, et al. Safety and antitumor activity of durvalumab plus tremelimumab in non-small cell lung cancer: a multicentre, phase 1b study. *Lancet Oncol.* 2016;17(3):299-308. [https://doi.org/10.1016/S1470-2045\(15\)00544-6](https://doi.org/10.1016/S1470-2045(15)00544-6).
5. Calabrò L, Morra A, Giannarelli D, et al. Tremelimumab combined with durvalumab in patients with mesothelioma (NIBIT-MESO-1): an open-label, non-randomised, phase 2 study. *Lancet Respir Med.* 2018;6(6):451-460. [https://doi.org/10.1016/S2213-2600\(18\)30151-6](https://doi.org/10.1016/S2213-2600(18)30151-6).
6. Yang H, Shen K, Zhu C, et al. Safety and efficacy of durvalumab (MEDI4736) in various solid tumors. *Drug Des Devel Ther.* 2018;12:2085-2096. <https://doi.org/10.2147/DDDT.S162214>.
7. Gu L, Khadaroo PA, Su H, et al. The safety and tolerability of combined immune checkpoint inhibitors (anti-PD-1/PD-L1 plus anti-CTLA-4): a systematic review and meta-analysis. *BMC Cancer.* 2019;19:559. <https://doi.org/10.1186/s12885-019-5785-z>.
8. Kelley RK, Sangro B, Harris WP, et al. Efficacy, tolerability, and biologic activity of a novel regimen of tremelimumab (T) in combination with durvalumab (D) for patients (pts) with advanced hepatocellular carcinoma (aHCC). *J Clin Oncol.* 2020;38(SUPPL 15):4508.
9. Callahan MK, Odunsi K, Sznol M, et al. Phase 1 study to evaluate the safety and tolerability of MEDI4736 (durvalumab, DUR) + tremelimumab (TRE) in patients with advanced solid tumors. *J Clin Oncol.* 2017;35(suppl 15):3069.
10. Rizvi NA, Chul Cho B, Reinmuth N, et al. Abstract 496 - Durvalumab with or without tremelimumab vs platinum-based chemotherapy as first-line treatment for metastatic non-small cell lung cancer: MYSTIC. *Ann Oncol.* 2018;29(suppl 10):x39-x43.
11. Peters S, Chul Cho B, Reinmuth N, et al. Tumor mutational burden (TMB) as a biomarker of survival in metastatic non-small cell lung cancer (mNSCLC): blood and tissue TMB analysis from MYSTIC, a phase III study of first-line durvalumab ± tremelimumab vs chemotherapy. *Cancer Res.* 2019;79(suppl 13):CT074.
12. Siu LL, Even C, Mesía R, et al. Safety and efficacy of durvalumab with or without tremelimumab in patients with PD-L1-low/negative recurrent or metastatic HNSCC: the phase 2 CONDOR randomized clinical trial. *JAMA Oncol.* 2019;5(2):195-203. <https://doi.org/10.1001/jamaoncol.2018.4628>.
13. Chen EX, Jonker DJ, Kennecke HF, et al. CCTG CO.26 trial: A phase II randomized study of durvalumab (D) plus tremelimumab (T) and best supportive care (BSC) versus BSC alone in patients (pts) with advanced refractory colorectal carcinoma (rCRC). *J Clin Oncol.* 2019;37(suppl 4):481.
14. Cancer Registry and Statistics, Cancer Information Service, National Cancer Center. Cancer Statistics in Japan—2019. Avail-

- able at https://ganjoho.jp/data/reg_stat/statistics/brochure/2019/cancer_statistics_2019.pdf. Accessed December 22, 2020.
15. Dong H, Strome SE, Salomao DR, et al. Tumor associated B7-H1 promotes T-cell apoptosis: a potential mechanism of immune evasion. *Nat Med.* 2002;8(8):793-800. doi:10.1038/nm730.
 16. Rotte A. Combination of CTLA-4 and PD-1 blockers for treatment of cancer. *J Exp Clin Cancer Res.* 2019;38(1):255. doi:10.1186/s13046-019-1259-z.
 17. Postow MA, Callahan MK, Wolchok JD. Immune checkpoint blockade in cancer therapy. *J Clin Oncol.* 2015;33(17):1974-1982. doi:10.1200/JCO.2014.59.4358.
 18. Pardoll DM. The blockade of immune checkpoints in cancer immunotherapy. *Nat Rev Cancer.* 2012;12:252-264. doi:10.1038/nrc3239.
 19. Stewart R, Morrow M, Hammond SA, et al. Identification and characterization of MEDI4736, an antagonistic anti-PD-L1 monoclonal antibody. *Cancer Immunol Res.* 2015;3(9):1052-1062. doi:10.1158/2326-6066.CIR-14-0191.
 20. Antonia SJ, Villegas A, Daniel D, et al. PACIFIC investigators. Durvalumab after chemoradiotherapy in stage III non-small-cell lung cancer. *N Engl J Med.* 2017;377(20):1919-1929. doi:10.1056/NEJMoa1709937.
 21. Powles T, O'Donnell PH, Massard C, et al. Efficacy and safety of durvalumab in locally advanced or metastatic urothelial carcinoma: updated results from a phase 1/2 open-label study. *JAMA Oncol.* 2017;3(9):e172411. doi:10.1001/jamaoncol.2017.2411.
 22. Fujiwara Y, Iguchi H, Yamamoto N, et al. Tolerability and efficacy of durvalumab in Japanese patients with advanced solid tumors. *Cancer Sci.* 2019;110(5):1715-1723. doi:10.1111/cas.14003.
 23. AstraZeneca. Imfinzi approved in Japan for unresectable stage III non-small cell lung cancer. Available at <https://www.astrazeneca.com/media-centre/press-releases/2018/imfinzi-approved-in-japan-for-unresectable-stage-iii-non-small-cell-lung-cancer-02072018.html>. Accessed November 29, 2019.
 24. AstraZeneca. Imfinzi approved in Japan for the treatment of extensive-stage small cell lung cancer. Available at <https://www.astrazeneca.com/media-centre/press-releases/2020/imfinzi-approved-in-japan-for-sclc.html>. Accessed December 10, 2021.
 25. Tarhini AA. Tremelimumab: a review of development to date in solid tumors. *Immunotherapy.* 2013;5(3):215-229. doi:10.2217/imt.13.9.
 26. Narwal R, DiPietro A, Ibrahim R, et al. Tremelimumab, a fully human anti-CTLA-4 monoclonal antibody, optimal dosing regimen for patients with unresectable malignant mesothelioma (MM). *J Clin Oncol.* 2015;33(suppl 15):3042.
 27. Odgerel CO, Takahashi K, Sorahan T, et al. Estimation of the global burden of mesothelioma deaths from incomplete national mortality data. *Occup Environ Med.* 2017;74(12):851-858. doi:10.1136/oemed-2017-104298.
 28. Robinson BM. Malignant pleural mesothelioma: an epidemiological perspective. *Ann Cardiothorac Surg.* 2012;1(4):491-496. doi:10.3978/j.issn.2225-319X.2012.11.04.
 29. Ribas A, Camacho LH, Lopez-Berestein G, et al. Antitumor activity in melanoma and anti-self responses in a phase I trial with the anti-cytotoxic T lymphocyte-associated antigen 4 monoclonal antibody CP-675,206. *J Clin Oncol.* 2005;23(35):8968-8977. doi:10.1200/JCO.2005.01.109.
 30. Baas P, Scherpereel A, Nowak AK, et al. First-line nivolumab plus ipilimumab in unresectable malignant pleural mesothelioma (CheckMate 743): a multicentre, randomised, open-label, phase 3 trial. *Lancet.* 2021;397(10272):375-386. doi:10.1016/S0140-6736(20)32714-8.
 31. Nowak AK, Lesterhuis WJ, Koh P-S, et al. Durvalumab with first-line chemotherapy in previously untreated malignant pleural mesothelioma (DREAM): a multicentre, single-arm, phase 2 trial with a safety run-in. *Lancet Oncol.* 2020;21(9):1213-1223.
 32. Forde PM, Anagnostou V, Sun Z, et al. Durvalumab with platinum-pemetrexed for unresectable pleural mesothelioma: survival, genomic and immunologic analyses from the phase 2 PrE0505 trial. *Nat Med.* 2021;27(11):1910-1920. doi:10.1038/s41591-021-01541-0.
 33. Kvistborg P, Philips D, Kelderman S, et al. Anti-CTLA-4 therapy broadens the melanoma-reactive CD8+ T cell response. *Sci Transl Med.* 2014;6(254):254ra128. doi:10.1126/scitranslmed.3008918.
 34. Nixon NA, Blais N, Ernst S, et al. Current landscape of immunotherapy in the treatment of solid tumours, with future opportunities and challenges. *Curr Oncol.* 2018;25(5):e373-e384. doi:10.3747/co.25.3840.
 35. Li X, Song W, Shao C, et al. Emerging predictors of the response to the blockade of immune checkpoints in cancer therapy. *Cell Mol Immunol.* 2019;16(1):28-39. doi:10.1038/s41423-018-0086-z.
 36. Lee JS, Ruppin E. Multiomics prediction of response rates to therapies to inhibit programmed cell death 1 and programmed cell death 1 ligand 1. *JAMA Oncol.* 2019;5(11):1614-1618. doi:10.1001/jamaoncol.2019.2311.

FIGURES AND TABLES

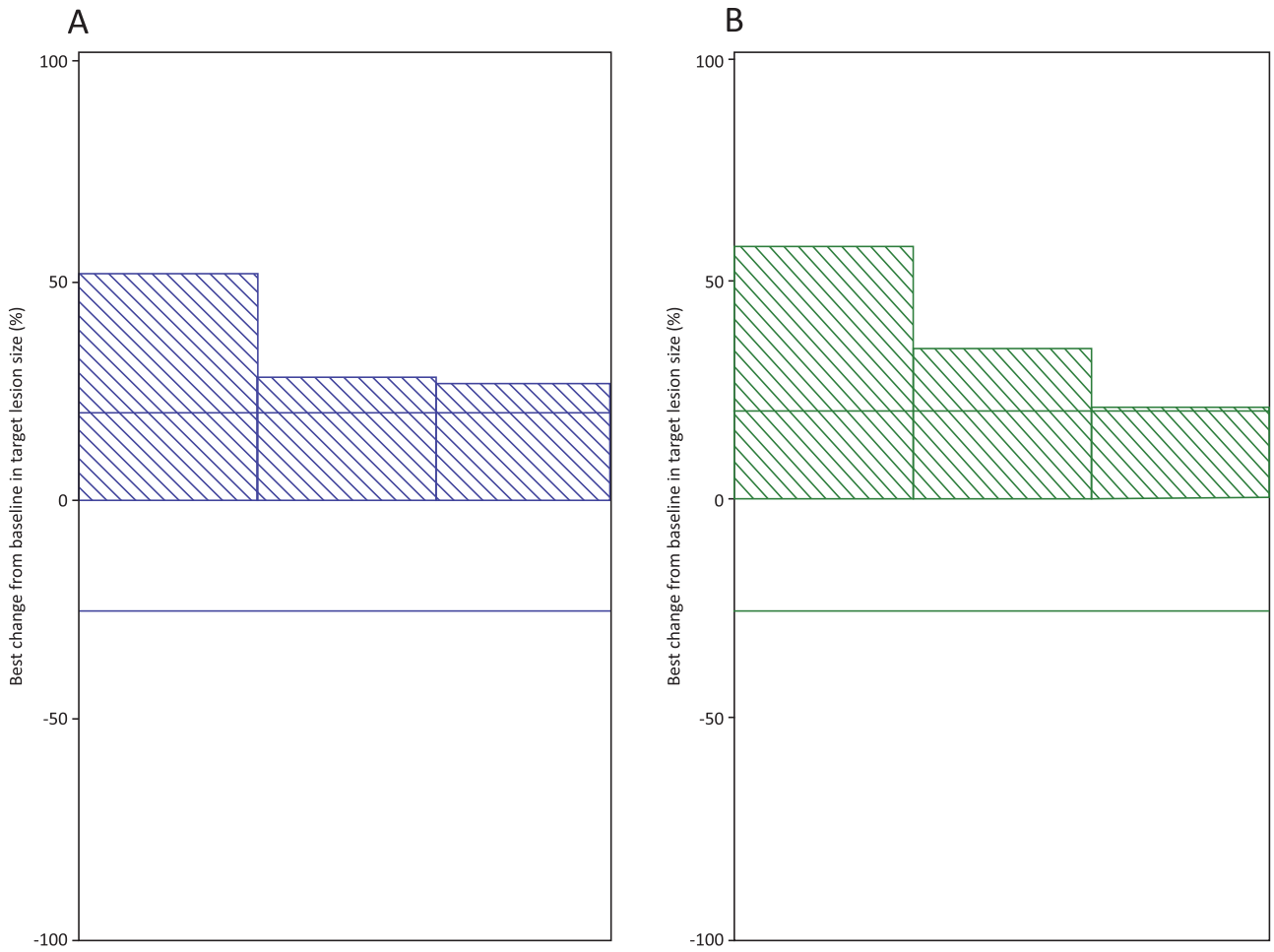


Figure 2. Waterfall plot of best percentage change from baseline in tumor size for (A) tremelimumab 3 mg/kg and (B) tremelimumab 10 mg/kg in dose escalation.

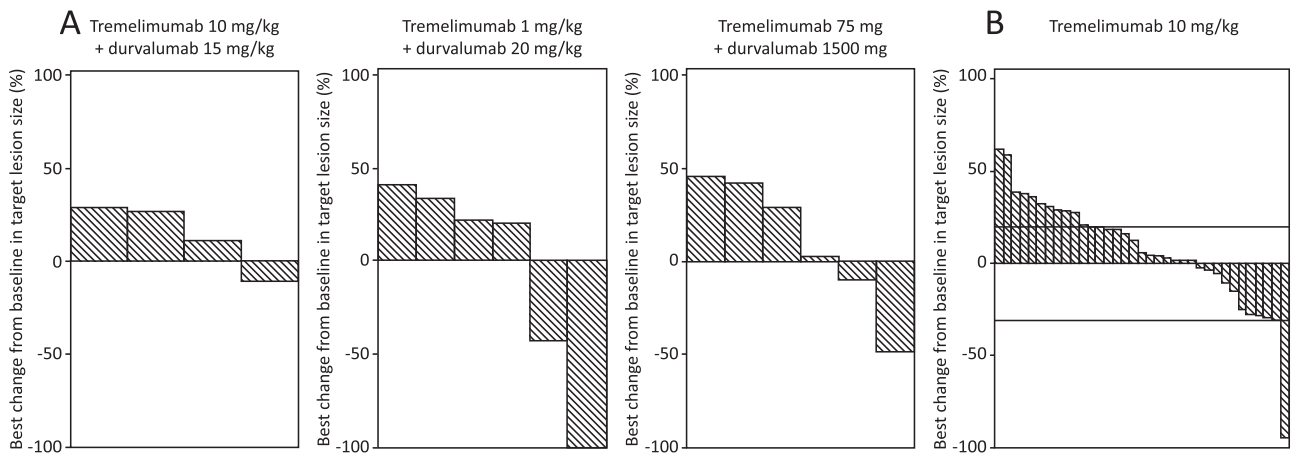


Figure 3. Waterfall plot of best percentage change from baseline in tumor size in (A) combination multiple dosing and (B) MPM dose expansion.

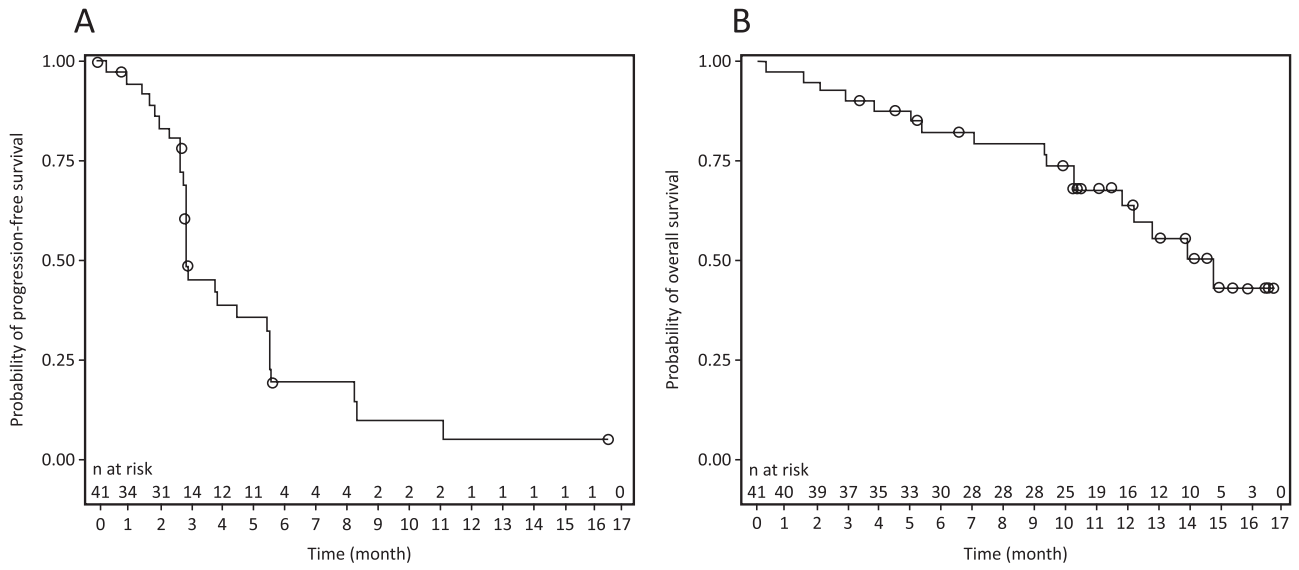


Figure 4. Kaplan-Meier plots of (A) progression-free survival and (B) overall survival in MPM dose expansion.

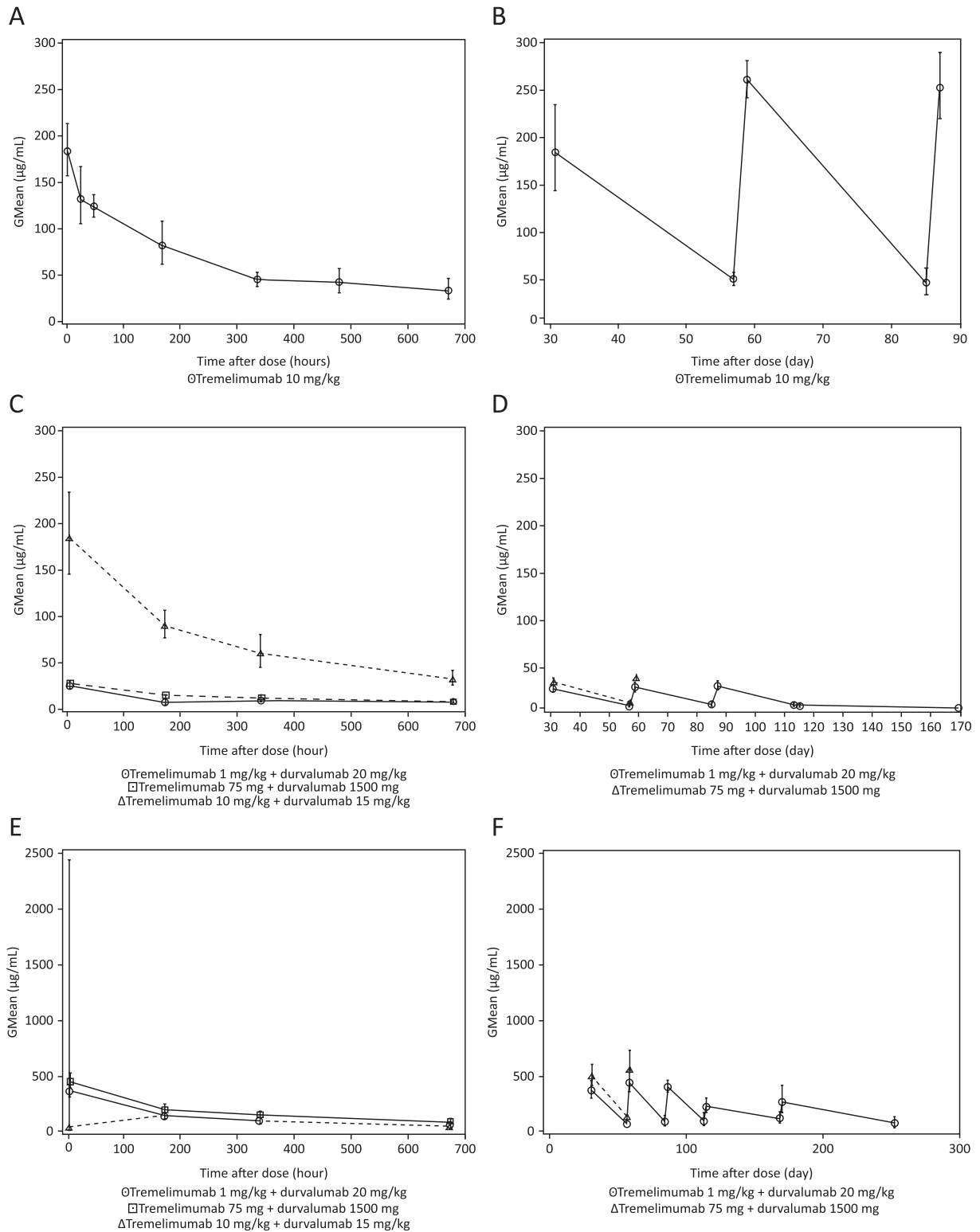


Figure 5. Geometric mean (±SD) serum concentration (µg/mL) versus time of (A) tremelimumab 10 mg/kg dose 1 in dose escalation; (B) tremelimumab 10 mg/kg dose 2 onward in dose escalation; (C) tremelimumab cycle 1-cycle 2 pre-dosing in combination multiple dosing; (D) tremelimumab cycle 2 onward in combination multiple dosing; (E) durvalumab cycle 1-cycle 2 pre-dosing in combination multiple dosing; and (F) durvalumab cycle 2 onward in combination multiple dosing.

Table 1. Summary of AEs.

AE category, n (%)	Part 1: dose escalation			Part 1: MPM dose expansion		Part 2: tremelimumab plus durvalumab combination multiple dosing			
	Tremelimumab 3 mg/kg (N = 4)	Tremelimumab 10 mg/kg (N = 4)	Total (N = 8)	Tremelimumab 10 mg/kg (N = 41)	Tremelimumab 10 mg/kg plus durvalumab 15 mg/kg (N = 4)	Tremelimumab 1 mg/kg plus durvalumab 20 mg/kg (N = 6)	Tremelimumab 75 mg plus durvalumab 1500 mg (N = 6)	Total (N = 16)	
Any AE	3 (75.0)	4 (100.0)	7 (87.5)	38 (92.7)	4 (100.0)	5 (83.3)	6 (100.0)	15 (93.8)	
Any AE related to tremelimumab	3 (75.0)	3 (75.0)	6 (75.0)	38 (92.7)	3 (75.0)	5 (83.3)	6 (100.0)	14 (87.5)	
Any AE related to durvalumab	—	—	—	—	3 (75.0)	5 (83.3)	6 (100.0)	14 (87.5)	
Any Grade ≥3 AE	1 (25.0)	3 (75.0)	4 (50.0)	20 (48.8)	2 (50.0)	3 (50.0)	3 (50.0)	8 (50.0)	
Any Grade ≥3 AE related to tremelimumab	1 (25.0)	1 (25.0)	2 (25.0)	16 (39.0)	2 (50.0)	2 (33.3)	3 (50.0)	7 (43.8)	
Any grade ≥3 AE related to durvalumab	—	—	—	—	2 (50.0)	2 (33.3)	3 (50.0)	7 (43.8)	
Any AE leading to death	0	0	0	0	0	0	0	0	
Any SAE	1 (25.0)	1 (25.0)	2 (25.0)	22 (53.7)	2 (50.0)	3 (50.0)	3 (50.0)	8 (50.0)	
Any SAE related to tremelimumab	1 (25.0)	1 (25.0)	2 (25.0)	20 (48.8)	2 (50.0)	1 (16.7)	3 (50.0)	6 (37.5)	
Any SAE related to durvalumab	—	—	—	—	2 (50.0)	1 (16.7)	3 (50.0)	6 (37.5)	
Any AE leading to discontinuation of study treatment	0	0	0	16 (39.0)	2 (50.0)	2 (33.3)	1 (16.7)	5 (31.3)	
Any AE leading to discontinuation of study treatment related to tremelimumab	0	0	0	15 (36.6)	2 (50.0)	2 (33.3)	1 (16.7)	5 (31.3)	
Any AE leading to discontinuation of study treatment related to durvalumab	—	—	—	—	2 (50.0)	2 (33.3)	1 (16.7)	5 (31.3)	
Any AEsI	3 (75.0)	3 (75.0)	6 (75.0)	36 (87.8)	3 (75.0)	5 (83.3)	3 (50.0)	11 (68.8)	
Treatment-related AEsI	3 (75.0)	2 (50.0)	5 (62.5)	35 (85.4)	3 (75.0)	3 (50.0)	3 (50.0)	9 (56.3)	
Any AEs by preferred term (≥10%)									
Fatigue	3 (75.0)	1 (25.0)	4 (50.0)	0	0	1 (16.7)	1 (16.7)	2 (12.5)	
Diarrhea	2 (50.0)	1 (25.0)	3 (37.5)	17 (41.5)	1 (25.0)	1 (16.7)	1 (16.7)	3 (18.8)	
Rash	0	2 (50.0)	2 (25.0)	17 (41.5)	2 (50.0)	2 (33.3)	0	4 (25.0)	
Decreased appetite	2 (50.0)	2 (50.0)	4 (50.0)	6 (14.6)	0	2 (33.3)	2 (33.3)	4 (25.0)	
Pruritus	2 (50.0)	1 (25.0)	3 (37.5)	7 (17.1)	2 (50.0)	1 (16.7)	2 (33.3)	5 (31.3)	
Constipation	0	0	0	7 (17.1)	0	1 (16.7)	0	1 (6.3)	
Hepatic function abnormal	0	0	0	5 (12.2)	0	0	0	0	
Insomnia	0	1 (25.0)	1 (12.5)	4 (9.8)	1 (25.0)	0	2 (33.3)	3 (18.8)	
Nausea	0	2 (50.0)	2 (25.0)	3 (7.3)	0	1 (16.7)	0	1 (6.3)	
Stomatitis	1 (25.0)	0	1 (12.5)	4 (9.8)	1 (25.0)	0	0	1 (6.3)	
Any other significant AEs	0	0	0	0	0	0	0	0	

Safety analysis set. Data are n (%).

Abbreviations: AE, adverse event; AEsI, adverse event of special interest; MPM, malignant pleural or peritoneal mesothelioma; SAE, serious adverse event.

Table 2. Baseline patient demographic and clinical characteristics.

Characteristic	Part 1: dose escalation		Part 1: MPM dose expansion		Part 2: tremelimumab plus durvalumab combination multiple dosing			
	Tremelimumab 3 mg/kg (N = 4)	Tremelimumab 10 mg/kg (N = 4)	Total (N = 8)	Tremelimumab 10 mg/kg (N = 41)	Tremelimumab 10 mg/kg plus durvalumab 15 mg/kg (N = 4)	Tremelimumab 1 mg/kg plus durvalumab 20 mg/kg (N = 6)	Tremelimumab 75 mg plus durvalumab 1500 mg (N = 6)	Total (N = 16)
Age (years)								
Median	64.0	51.0	58.5	67.0	52.5	66.0	61.0	61.0
Min	53	40	40	40	50	34	56	34
Max	72	62	72	79	64	74	73	74
Female	2 (50.0)	1 (25.0)	3 (37.5)	5 (12.2)	3 (75.0)	3 (50.0)	2 (33.3)	8 (50.0)
Race								
Asian	4 (100.0)	4 (100.0)	8 (100.0)	41 (100.0)	4 (100.0)	6 (100.0)	6 (100.0)	16 (100.0)
ECOG PS								
0	4 (100.0)	2 (50.0)	6 (75.0)	21 (51.2)	4 (100.0)	4 (66.7)	5 (83.3)	13 (81.3)
1	0	2 (50.0)	2 (25.0)	20 (48.8)	0	2 (33.3)	1 (16.7)	3 (18.8)
Tumor type								
Breast	0	0	0	0	0	0	2 (33.3)	2 (12.5)
Cervical	0	0	0	0	0	1 (16.7)	0	1 (6.3)
Colon	1 (25.0)	0	1 (12.5)	0	0	1 (16.7)	3 (50.0)	4 (25.0)
Gastric	0	0	0	0	1 (25.0)	0	0	1 (6.3)
NSCLC	0	0	0	0	0	1 (16.7)	0	1 (6.3)
Ovarian	0	0	0	0	1 (25.0)	0	0	1 (6.3)
Peritoneal mesothelioma	0	0	0	2 (4.9)	0	0	0	0
Pleural mesothelioma	0	0	0	39 (95.1)	0	0	0	0
Renal cell carcinoma	0	0	0	0	0	1 (16.7)	0	1 (6.3)
Other	3 (75.0)	4 (100.0)	7 (87.5)	0	2 (50.0)	2 (33.3)	1 (16.7)	5 (31.3)
Disease stage at study entry								
II	0	0	0	7 (17.1)	0	0	0	0
III	1 (25.0)	0	1 (12.5)	12 (29.3)	0	1 (16.7)	0	1 (6.3)
IV	3 (75.0)	4 (100.0)	7 (87.5)	21 (51.2)	4 (100.0)	4 (66.7)	5 (83.3)	13 (81.3)
Unknown	0	0	0	1 (2.4)	0	1 (16.7)	1 (16.7)	2 (12.5)

Safety analysis set. Data are n (%). Unless otherwise specified. Abbreviations: BMI, body mass index; ECOG PS, Eastern Cooperative Oncology Group performance status; Max, maximum; Min, minimum; MPM, malignant pleural or peritoneal mesothelioma; NSCLC, non-small cell lung cancer; SD, standard deviation.

Table 3. Summary of antitumor activity.

Antitumor activity	Part 1: dose escalation		Part 1: MPM dose expansion		Part 2: tremelimumab plus durvalumab combination multiple dosing		
	Tremelimumab 3 mg/kg (N = 4)	Tremelimumab 10 mg/kg (N = 4)	Tremelimumab 10 mg/kg (N = 4)	Tremelimumab 10 mg/kg plus durvalumab 15 mg/kg (N = 4)	Tremelimumab 1 mg/kg plus durvalumab 20 mg/kg (N = 6)	Tremelimumab 75 mg plus durvalumab 1500 mg (N = 6)	Tremelimumab
ORR, n (%) [95% CI]	0	0	1 (2.4) [0.1, 12.9]	0	2 (33.3) [4.3, 77.7]	0	0
DCR, n (%) [95% CI]	0	1 (25.0) [0.6, 80.6]	18 (43.9) [28.5, 60.3]	0	2 (33.3) [4.3, 77.7]	2 (33.3) [4.3, 77.7]	2 (33.3) [4.3, 77.7]
Durable DCR, n (%) [95% CI]	0	1 (25.0) [0.6, 80.6]	5 (12.2) [4.1, 26.2]	0	2 (33.3) [4.3, 77.7]	0	0
Response, n (%)							
Total	0	0	1 (2.4)	0	2 (33.3)	0	0
CR	0	0	0	0	1 (16.7)	0	0
PR	0	0	1 (2.4)	0	1 (16.7)	0	0
Nonresponse, n (%)							
Total	4 (100.0)	4 (100.0)	40 (97.6)	4 (100.0)	4 (66.7)	6 (100.0)	6 (100.0)
Stable disease ≥12 weeks	0	1 (25.0)	17 (41.5)	0	0	2 (33.3)	2 (33.3)
PD	4 (100.0)	3 (75.0)	18 (43.9)	3 (75.0)	4 (66.7)	3 (50.0)	3 (50.0)
Non-evaluable	0	0	5 (12.2)	1 (25.0)	0	1 (16.7)	1 (16.7)

Dose escalation and MPM dose expansion = safety analysis set. Combination = tumor response analysis set. Response data are n (%). ORR is defined as the proportion of patients with confirmed CR or PR. DCR is defined as the proportion of patients with stable disease of at least 12 weeks' (day 81) duration, PR, or CR. Durable DCR is defined as the proportion of patients with best response of CR, PR, or stable disease of ≥6 months' (day 165) duration measured from the date of the first dose. CR and PR required confirmation after 4 weeks. Abbreviations: CI, confidence interval; CR, complete response; DCR, disease control rate; MPM, malignant pleural or peritoneal mesothelioma; ORR, objective response rate; PD, progressive disease; PR, partial response.

Table 4. AEs of CTCAE grade ≥3 by system organ class and preferred term.

AE category, n (%)	Part 1: dose escalation		Part 1: MPM dose expansion		Part 2: tremelimumab plus durvalumab combination multiple dosing			
	Tremelimumab 3 mg/kg (N = 4)	Tremelimumab 10 mg/kg (N = 4)	Total (N = 8)	Tremelimumab 10 mg/kg (N = 41)	Tremelimumab 10 mg/kg plus durvalumab 1.5 mg/kg (N = 4)	Tremelimumab 1 mg/kg plus durvalumab 20 mg/kg (N = 6)	Tremelimumab 75 mg plus durvalumab 1500 mg (N = 6)	Total (N = 16)
	n (%)	n (%)	n (%)	n (%)	n (%)	n (%)	n (%)	n (%)
Patients with any AE of CTCAE grade 3 or higher	1 (25.0)	3 (75.0)	4 (50.0)	20 (48.8)	2 (50.0)	3 (50.0)	3 (50.0)	8 (50.0)
Infections and infestations	0	0	0	0	1 (25.0)	0	0	1 (6.3)
Pneumonia	0	0	0	0	1 (25.0)	0	0	1 (6.3)
Blood and lymphatic system disorders	0	1 (25.0)	1 (12.5)	1 (2.4)	0	1 (16.7)	0	1 (6.3)
Anemia	0	1 (25.0)	1 (12.5)	0	0	1 (16.7)	0	1 (6.3)
Normochromic normocytic anemia	0	0	0	1 (2.4)	0	0	0	0
Endocrine disorders	0	0	0	2 (4.9)	1 (25.0)	0	0	1 (6.3)
Hypophysitis	0	0	0	0	1 (25.0)	0	0	1 (6.3)
Hypopituitarism	0	0	0	2 (4.9)	0	0	0	0
Metabolism and nutrition disorders	1 (25.0)	1 (25.0)	2 (25.0)	1 (2.4)	1 (25.0)	1 (16.7)	1 (16.7)	3 (18.8)
Decreased appetite	1 (25.0)	0	1 (25.0)	1 (2.4)	0	0	0	0
Dehydration	0	1 (25.0)	1 (25.0)	0	0	0	0	0
Hyperglycemia	0	0	0	0	1 (25.0)	1 (16.7)	1 (16.7)	3 (18.8)
Hyponatremia	0	0	0	0	0	0	1 (16.7)	1 (6.3)
Nervous system disorders	0	0	0	0	1 (25.0)	0	0	1 (6.3)
Myasthenia gravis	0	0	0	0	1 (25.0)	0	0	1 (6.3)
Vascular disorders	0	0	0	0	0	0	1 (16.7)	1 (6.3)
Hypertension	0	0	0	0	0	0	1 (16.7)	1 (6.3)
Gastrointestinal disorders	0	0	0	10 (24.4)	0	1 (16.7)	0	1 (6.3)
Constipation	0	0	0	1 (2.4)	0	0	0	0
Diarrhea	0	0	0	3 (7.3)	0	0	0	0
Duodenal ulcer	0	0	0	0	0	1 (16.7)	0	1 (6.3)
Enteritis	0	0	0	1 (2.4)	0	0	0	0
Enterocolitis	0	0	0	1 (2.4)	0	0	0	0
Gastric ulcer	0	0	0	1 (2.4)	0	0	0	0
Intestinal perforation	0	0	0	1 (2.4)	0	0	0	0
Nausea	0	0	0	1 (2.4)	0	0	0	0
Pancreatitis acute	0	0	0	1 (2.4)	0	0	0	0

Table 4. Continued

AE category, n (%)	Part 1: dose escalation		Part 1: MPM dose expansion		Part 2: tremelimumab plus durvalumab combination multiple dosing			
	Tremelimumab 3 mg/kg (N = 4)	Tremelimumab 10 mg/kg (N = 4)	Total (N = 8)	Tremelimumab 10 mg/kg (N = 41)	Tremelimumab 10 mg/kg plus durvalumab 15 mg/kg (N = 4)	Tremelimumab 10 mg/kg plus durvalumab 20 mg/kg (N = 6)	Tremelimumab 1 mg/kg plus durvalumab 1500 mg (N = 6)	Tremelimumab 75 mg plus durvalumab 1500 mg (N = 16)
Hepatobiliary disorders	0	0	0	2 (4.9)	1 (25.0)	1 (16.7)	0	2 (12.5)
Cholangitis	0	0	0	0	0	1 (16.7)	0	1 (6.3)
Hepatic function abnormal	0	0	0	2 (4.9)	0	0	0	0
Hepatitis acute	0	0	0	0	1 (25.0)	0	0	1 (6.3)
Skin and subcutaneous tissue disorders	0	1 (25.0)	1 (12.5)	5 (12.2)	0	0	1 (16.7)	1 (6.3)
Rash	0	1 (25.0)	1 (12.5)	3 (7.3)	0	0	0	0
Rash maculo-papular	0	0	0	2 (4.9)	0	0	1 (16.7)	1 (6.3)
Musculoskeletal and connective tissue disorders	0	0	0	1 (2.4)	0	0	0	0
Muscular weakness	0	0	0	1 (2.4)	0	0	0	0
Investigations	0	0	0	4 (9.8)	1 (25.0)	3 (50.0)	1 (16.7)	5 (31.3)
Alanine aminotransferase increased	0	0	0	0	1 (25.0)	1 (16.7)	1 (16.7)	3 (18.8)
Amylase increased	0	0	0	2 (4.9)	0	1 (16.7)	0	1 (6.3)
Aspartate aminotransferase increased	0	0	0	0	1 (25.0)	1 (16.7)	0	2 (12.5)
Blood corticotrophin abnormal	0	0	0	0	0	1 (16.7)	0	1 (6.3)
Gamma-glutamyl transferase increased	0	0	0	0	0	0	1 (16.7)	1 (6.3)
Lipase increased	0	0	0	3 (7.3)	0	0	0	0
Lymphocyte percentage decreased	0	0	0	0	0	1 (16.7)	0	1 (6.3)
Neutrophil count decreased	0	0	0	1 (2.4)	0	0	0	0

Safety analysis set. Data are n (%).
Abbreviations: AE, adverse event; CTCAE = Common Terminology Criteria for Adverse Events; MPM, malignant pleural or peritoneal mesothelioma.

Table 5. Summary of PK characteristics.

Variable	N	GMean	Geometric CV (%)	Arithmetic mean	SD	Min	Median	Max
Dose escalation								
Part 1 Dose escalation (single-dose tremelimumab 3 mg/kg)								
AUC _{0-t} (day·µg/mL)	n/a	Not included in analysis						
C _{max} (µg/mL)	n/a	Not included in analysis						
C _{min} (µg/mL)	n/a	Not included in analysis						
t _{max} (day)	n/a	Not included in analysis						
Part 1 dose escalation (single-dose tremelimumab 10 mg/kg)								
AUC _{0-t} (day·µg/mL)	3	1850	3.12	1850	57.2	1780	1880	1890
C _{max} (µg/mL)	4	183	15.5	185	28.3	156	186	213
C _{min} (µg/mL)	3	33.0	35.2	34.3	11.3	23.2	33.9	45.8
t _{max} (day)	4	0.051	14	0.051	0.0072	0.045	0.051	0.058
Part 1 MPM dose expansion (multiple-dose tremelimumab 10 mg/kg)								
R _{AC} (C _{max})	3	1.34	10.2	1.34	0.132	1.19	1.41	1.42
R _{AC} (C _{min})	2	1.13	20.5	1.14	0.229	0.975	1.14	1.30
C _{ss,max} (µg/mL)	3	253	14.0	255	35.4	220	253	291
C _{ss,min} (µg/mL)	2	44.4	43.4	46.3	18.7	33.1	46.3	59.6
t _{ss,max} (day)	3	0.051	17	0.052	0.0084	0.042	0.056	0.057
Summary of tremelimumab concentration								
Week 1 (pre-infusion)	41 (Obs ≥ LOQ = 1)	NC	NC	NC	NC	NQ	NC	0.196
Week 1 (end of infusion)	41 (Obs ≥ LOQ = 41)	176	22.8	181	44.4	109	172	344
Week 5 (pre-infusion)	38 (Obs ≥ LOQ = 38)	26.5	27.5	27.3	6.3	12.4	28.5	38.4
Week 13 (pre-infusion)	17 (Obs ≥ LOQ = 17)	23.5	81.0	29.1	18.7	6.36	31.5	83.3
Week 25 (pre-infusion)	5 (Obs ≥ LOQ = 5)	36.2	28.6	37.2	9.23	23.0	41.7	45.1
Week 25 (end of infusion)	3 (Obs ≥ LOQ = 3)	172	2.87	172	4.94	167	171	177
Combination multiple dosing: tremelimumab PK								
Part 2 combination (single-dose tremelimumab 10 mg/kg plus durvalumab 15 mg/kg)								
AUC _{0-t} (day·µg/mL)	3	2010	24.5	2050	522	1710	1800	2650
C _{max} (µg/mL)	4	187	24.5	191	45.9	148	187	242
C _{min} (µg/mL)	3	28.8	28.1	29.6	8.55	23.2	26.2	39.3
t _{max} (day)	4	0.046	4.5	0.047	0.0021	0.044	0.047	0.049
Part 2 combination (single-dose tremelimumab 1 mg/kg plus durvalumab 20 mg/kg)								
AUC _{0-t} (day·µg/mL)	6	153	26.2	158	41.3	112	151	221
C _{max} (µg/mL)	6	20.5	12.9	20.6	2.74	17.5	20.2	25.4
C _{min} (µg/mL)	6	2.71	39.5	2.88	1.11	1.55	2.55	4.72
t _{max} (day)	6	0.046	3.6	0.046	0.0016	0.044	0.046	0.048

Table 5. Continued

Variable	N	GMean	Geometric CV (%)	Arithmetic mean	SD	Min	Median	Max
Part 2 combination (single-dose tremelimumab 75 mg plus durvalumab 1500 mg)								
AUC _{0-∞} (day·µg/mL)	6	239	15.9	242	38.4	202	240	296
C _{max} (µg/mL)	6	22.9	14.2	23.1	3.07	17.8	23.0	26.3
C _{min} (µg/mL)	6	3.35	40.7	3.57	1.39	2.16	3.30	5.50
t _{max} (day)	6	0.044	3.9	0.044	0.0017	0.042	0.044	0.047
Part 2 combination (multiple-dose tremelimumab 1 mg/kg plus durvalumab 20 mg/kg)								
R _{AC} (C _{max})	4	1.18	12.8	1.19	0.144	0.985	1.24	1.29
R _{AC} (C _{min})	4	1.44	13.5	1.45	0.188	1.20	1.48	1.64
C _{s,max} (µg/mL)	4	24.8	20.0	25.2	4.72	19.0	25.9	30.0
C _{s,min} (µg/mL)	4	4.14	45.5	4.41	1.58	2.22	4.88	5.66
t _{s,max} (day)	4	0.045	2.8	0.046	0.0013	0.044	0.046	0.047
Part 2 combination (multiple-dose tremelimumab 75 mg plus durvalumab 1500 mg)								
R _{AC} (C _{max})	2	1.39	12.1	1.40	0.167	1.28	1.40	1.51
R _{AC} (C _{min})	2	2.03	41.5	2.11	0.819	1.53	2.11	2.69
C _{s,max} (µg/mL)	2	36.4	12.9	36.5	4.67	33.2	36.5	39.8
C _{s,min} (µg/mL)	2	9.20	12.6	9.24	1.16	8.42	9.24	10.1
t _{s,max} (day)	2	0.045	4.7	0.046	0.0021	0.044	0.046	0.047
Combination multiple dosing: durvalumab PK								
Part 2 combination (single-dose tremelimumab 10 mg/kg plus durvalumab 15 mg/kg)								
AUC _{0-∞} (day·µg/mL)	3	2980	26.2	3050	812	2390	2790	3950
C _{max} (µg/mL)	3	278	24.1	283	62.9	212	307	331
C _{min} (µg/mL)	3	40.9	45.4	43.6	20.1	29.1	35.3	66.5
t _{max} (day)	3	0.12	85	0.14	0.075	0.050	0.18	0.18
Part 2 combination (single-dose tremelimumab 1 mg/kg plus durvalumab 20 mg/kg)								
AUC _{0-∞} (day·µg/mL)	6	3390	22.5	3460	812	2670	3160	4790
C _{max} (µg/mL)	6	353	16.5	357	59.6	284	339	450
C _{min} (µg/mL)	6	55.4	33.6	58.0	19.8	39.7	49.8	86.4
t _{max} (day)	6	0.055	11	0.056	0.0061	0.046	0.057	0.063
Part 2 combination (single-dose tremelimumab 75 mg plus durvalumab 1500 mg)								
AUC _{0-∞} (day·µg/mL)	6	4680	15.7	4730	718	3830	4920	5630
C _{max} (µg/mL)	6	439	15.8	443	75.0	378	422	585
C _{min} (µg/mL)	6	77.7	33.6	81.2	26.5	55.5	78.2	119
t _{max} (day)	6	0.052	21	0.053	0.012	0.044	0.048	0.076
Part 2 combination (multiple-dose tremelimumab 1 mg/kg plus durvalumab 20 mg/kg)								
R _{AC} (C _{max})	4	1.11	13.8	1.12	0.162	1.01	1.06	1.36
R _{AC} (C _{min})	4	1.49	31.2	1.53	0.416	0.960	1.61	1.95
C _{s,max} (µg/mL)	4	404	14.1	407	55.5	338	417	456
C _{s,min} (µg/mL)	4	94.6	63.9	106	50.2	42.1	114	154
t _{s,max} (day)	4	0.049	15	0.049	0.0072	0.042	0.049	0.057

Table 5. Continued

Variable	N	GMean	Geometric CV (%)	Arithmetic mean	SD	Min	Median	Max
Part 2 combination (multiple-dose/remelimumab 75 mg plus durvalumab 1500 mg)								
$R_{AC}(C_{max})$	2	2.01	0.932	2.01	0.0187	1.99	2.01	2.02
$R_{AC}(C_{min})$	2	1.91	26.1	1.94	0.492	1.59	1.94	2.29
$C_{ss,max}$ (µg/mL)	2	847	0.726	847	6.15	843	847	851
$C_{ss,min}$ (µg/mL)	2	200	7.55	200	15.1	189	200	211
$t_{ss,max}$ (day)	2	0.043	3.3	0.043	0.0014	0.042	0.043	0.044

PK analysis set; the multiple-dose PK data from combination cohort 1 were removed from the analyses.

Abbreviations: $AUC_{0-\infty}$ area under the serum concentration-time curve within a dosing interval; C_{max} maximum serum concentration; C_{min} minimum serum concentration; $C_{ss,max}$ maximum serum concentration at steady state; $C_{ss,min}$ minimum serum concentration at steady state; CV, coefficient of variation; GMean, geometric mean; Max, maximum; Min, minimum; n/a, not applicable; Obs \geq LOQ: observed above limit of quantification; PK, pharmacokinetic; SD, standard deviation; R_{AC} accumulation ratio on multiple dosing; t_{max} time to achieve C_{max} ; $t_{ss,max}$ time to achieve $C_{ss,max}$.

Table 6. Summary of antidrug antibody responses to tremelimumab.

	Part 1: dose escalation			Part 1: MPM dose expansion		Part 2: tremelimumab plus durvalumab combination multiple dosing			
	Tremelimumab	Tremelimumab	Tremelimumab	Tremelimumab	Tremelimumab, 10 mg/kg plus durvalumab	Tremelimumab, 10 mg/kg plus durvalumab	Tremelimumab, 1 mg/kg plus durvalumab	Tremelimumab, 20 mg/kg plus durvalumab	Tremelimumab, 75 mg plus durvalumab
	3 mg/kg (N = 4)	10 mg/kg (N = 4)	10 mg/kg (N = 4)	10 mg/kg (N = 41)	15 mg/kg (N = 4)	15 mg/kg (N = 4)	20 mg/kg (N = 6)	1500 mg (N = 6)	
Any ADA result	4 (100.0)	4 (100.0)	41 (100.0)	41 (100.0)	4 (100.0)	4 (100.0)	6 (100.0)	6 (100.0)	
Baseline ADA result	4 (100.0)	4 (100.0)	41 (100.0)	41 (100.0)	4 (100.0)	4 (100.0)	6 (100.0)	6 (100.0)	
ADA-positive at baseline	0	0	0	0	0	0	0	0	
ADA not detected postbaseline and positive at baseline	0	0	0	0	0	0	0	0	
Postbaseline ADA result	4 (100.0)	4 (100.0)	40 (97.6)	4 (100.0)	4 (100.0)	4 (100.0)	6 (100.0)	6 (100.0)	
ADA-positive postbaseline	1 (25.0)	0	4 (10.0)	4 (10.0)	0	0	0	1 (16.7)	
<i>n</i>	1	—	4	4	—	—	—	1	
Median of maximum titer ^a (min, max)	16.0 (16, 16)	—	32.0 (8, 64)	32.0 (8, 64)	—	—	—	8.0 (8, 8)	
ADA-positive postbaseline and positive at baseline	0	0	0	0	0	0	0	0	
ADA-positive postbaseline and not detected (or missing) at baseline	1 (25.0)	0	4 (10.0)	4 (10.0)	0	0	0	1 (16.7)	
<i>n</i>	1	—	4	4	—	—	—	1	
Median of maximum titer ^a (min, max)	16 (16, 16)	—	32.0 (8, 64)	32.0 (8, 64)	—	—	—	8.0 (8, 8)	
Persistent positive ^b	1 (25.0)	0	1 (2.5)	1 (2.5)	0	0	0	1 (16.7)	
<i>n</i>	1	—	1	1	—	—	—	1	
Median of maximum titer ^a (min, max)	16.0 (16, 16)	—	32.0 (32, 32)	32.0 (32, 32)	—	—	—	8.0 (8, 8)	
Transient positive ^c	0	0	3 (7.5)	3 (7.5)	0	0	0	0	
<i>n</i>	—	—	3	3	—	—	—	—	
Median of maximum titer ^a (min, max)	—	—	32.0 (8, 64)	32.0 (8, 64)	—	—	—	—	
ADA-positive postbaseline with nAb positive postbaseline	1 (25.0)	0	4 (10.0)	4 (10.0)	0	0	0	1 (16.7)	
<i>n</i>	1	—	4	4	—	—	—	1	
Median of maximum titer ^a (min, max)	16.0 (16, 16)	—	32.0 (8, 64)	32.0 (8, 64)	—	—	—	8.0 (8, 8)	

Data are *n* (%) unless specified.
^aAll postbaseline, ADA-positive assessments with reportable ADA titer results.
^bDefined as positive at postbaseline assessments with ≥16 weeks (112 days) between the first and the last positive or positive at last postbaseline assessment.
^cDefined as having at least one postbaseline ADA-positive assessment and not fulfilling the conditions of persistently positive.
Abbreviations: ADA, antidrug antibody; max, maximum; min, minimum; MPM, malignant pleural or peritoneal mesothelioma; nAb, neutralizing antibody.

A retrospective study on radiological findings of diffuse pleural thickening with benign asbestos pleural effusion in Japanese cases

Takumi KISHIMOTO^{1*}, Katsuya KATO², Kazuto ASHIZAWA³, Yasuyuki KURIHARA⁴, Takeshi TOKUYAMA⁵ and Fumikazu SAKAI⁶

¹Research and Training Center for Asbestos-Related Diseases Okayama, Japan

²Department of Radiology, Kawasaki General Medical Center, Japan

³Department of Clinical Oncology, Nagasaki University Hospital, Japan

⁴Department of Radiology, St. Luke's International Hospital, Japan

⁵Department of Internal Medicine, Saiseikai Chuwa Hospital, Japan

⁶Department of Diagnostic Radiology, Saitama Medical University, Japan

Received April 23, 2021 and accepted November 4, 2021

Published online in J-STAGE November 22, 2021

DOI <https://doi.org/10.2486/indhealth.2021-0099>

Abstract: The requirement for compensation for diffuse pleural thickening in benign asbestos pleural effusion include five computed tomography findings of organized pleural effusion: [1] heterogeneity in the pleural effusion, [2] declined chest capacity, [3] “crow’s feet” sign at the pleura, [4] immobilization of effusion volume, and [5] air in the effusion. Pleural effusion is diagnosed as organized, immobilized, and in the state of diffuse pleural thickening if at least three of these items are fulfilled, ([1] and [3] compulsory + one of the remaining items). This retrospective study investigated whether the requirement to confirm no organized pleural effusion changes after a follow-up of >3 months were available for cases fulfilling three of the five items; i.e., the confirmation of only [2] with [1] and [3]. Of 302 cases recognized by the Japanese laws, 105 cases with diffuse pleural thickening with organized effusion were enrolled. The number of subjects who fulfilled the diagnostic requirement for organized pleural effusion was confirmed. Eight subjects had a full score of 5 points, 82 subjects scored 4 points, and only 15 subjects scored 3 points. Furthermore, no changes were observed in the organized pleural effusion volume after a follow-up of >3 months.

Key words: Benign asbestos pleural effusion, Diffuse pleural thickening, Organized pleural effusion, Heterogeneity in the pleural effusion, Crow’s feet sign, Diagnostic criteria

Introduction

Diffuse pleural thickening is the pleural fibrosis (lesion

*To whom correspondence should be addressed.

E-mail address: nakisimt@okayamah.johas.go.jp

©2022 National Institute of Occupational Safety and Health

of the visceral pleura, resulting in adhesion to the parietal pleura) over a wide area involving at least one lung lobe. Unlike mesothelioma or pleural plaque, diffuse pleural thickening occurs secondarily to diseases other than asbestos exposure, such as rheumatism and tuberculous pleurisy. Thus, it is important to differentiate whether it is caused by asbestos exposure or other diseases¹⁾.

In Japan, it is a target disease of the Worker's Accident Compensation Law and the Act on Asbestos Health Damage Relief. The requirement for compensation and Asbestos Health Damage Relief are as follows:

- (1) Unilateral lesion with area $>1/2$ of the whole chest and bilateral lesion with area $>1/4$ of the whole chest
- (2) An occupational asbestos exposure history of >3 years
- (3) Complicated with a marked respiratory functional disorder

Benign asbestos pleural effusion (BAPE) is known as a factor of diffuse pleural thickening^{2, 3)}, but in many diffuse pleural thickening cases, BAPE has been reported to continue and organization remains³⁾. The Act on Asbestos Health Damage Relief of the Ministry of the Environment do not approve BAPE.

In 2017, the Act on Asbestos Health Damage Relief of the Ministry of the Environment set the requirement as chest computed tomography (CT) images for the development of diffuse pleural thickening in BAPE to determine diffuse pleural thickening. In other words, the five CT findings of organized pleural effusion, preventing lung re-expansion in diffuse pleural thickening, are as follows: [1] heterogeneity in the pleural effusion (high absorption of the pleural effusion), [2] declined chest capacity, [3] presence of the "crow's feet" sign in the pleural effusion site⁴⁾, [4] immobilization of the pleural effusion volume, and [5] presence of air in the pleural effusion. If at least three of the above items are fulfilled, with [1] and [3] being compulsory along with one of the remaining items, the pleural effusion can be diagnosed to be organized, immobilized, and in the state of diffuse pleural thickening. For approximately 3 months, we followed-up cases that fulfilled three of the five items, i.e., confirmation of [2] in addition to [1] and [3], and confirmed no changes in the state of organized pleural effusion.

In this study, of the previously approved cases, those whose clinical course could be examined using chest CT images were selected, and the availability of the requirement of three items of five chest CT finding was retrospectively evaluated.

Subjects and Methods

A total of 302 cases were recognized by the Worker's Accident Compensation Law and the Act on Asbestos Health Damage Relief (January 2020) in Japan with a history of occupational asbestos exposure of >3 years, pleural thickening of unilateral lesions that covered $>1/2$ of one

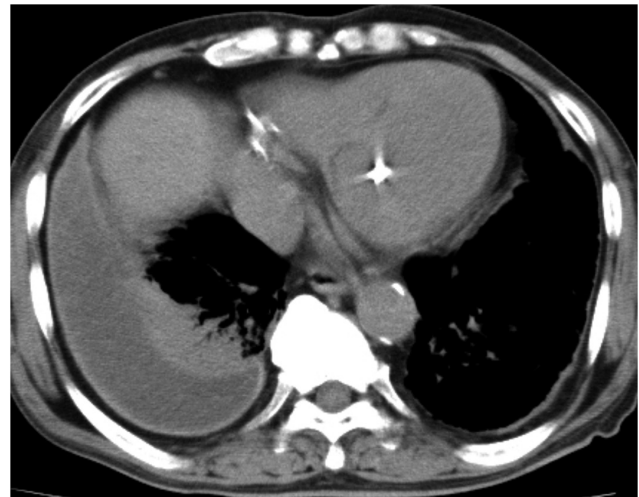


Fig. 1. A cross-sectional chest computed tomography (CT) image showing heterogeneity in the pleural effusion. The right pleural effusion has a high absorption value with heterogeneity. A small quantity of pleural effusion with heterogeneity was also observed in the left side.

side in the chest and bilateral lesions that covered $>1/4$ of two sides of the chest, and a marked respiratory functional disorder. Of these, 105 cases with organized pleural effusion who could be followed-up using chest CT images were included. Moreover, 57 cases without pleural effusion and 140 cases who could not be followed-up using chest CT images were excluded. Written informed consent was obtained from all patients in the study. This study was approved by the relevant center of our institute (Approval number #2) on May 14, 2020.

The chest X-ray and CT images that demonstrated the clinical course of these 105 patients were obtained. These images were interpreted by six specialists, including four chest radiologists and two pulmonologists.

The findings for organized pleural effusion in chest CT are as follows: [1] heterogeneity in the pleural effusion (high absorption of the pleural effusion) (Fig. 1), [2] declined chest capacity (Fig. 2), [3] presence of the "crow's feet" sign in the pleural effusion site⁴⁾ (Fig. 3), [4] immobilization of the pleural effusion volume, and [5] presence of air in the pleural effusion (Fig. 4). The availability of these findings for organized pleural effusion was evaluated with organization having a score of ≥ 3 points.

Furthermore, we examined the fluctuation in the pleural effusion of the subjects by evaluating their chest CT images at the onset of pleural effusion, organization of pleural effusion, immobilization with changes in the organized pleural effusion, and identifying their eligibility as per the diagnostic requirement following immobilization, diagnosis, and application.

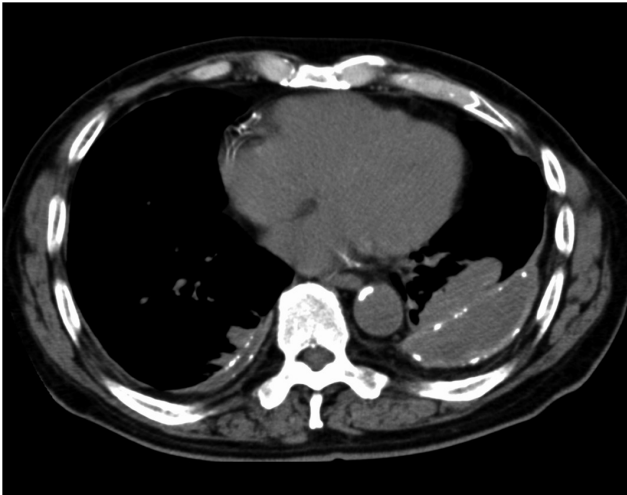


Fig. 2. A cross-sectional chest computed tomography (CT) image showing a decline in chest capacity. A slightly heterogeneous pleural effusion with the tendency to be encapsulated was observed in both sides, and the left chest is smaller than the right chest.

Results

In this study, 105 male subjects presented with diffuse pleural thickening and organized pleural effusion, aged 53–93 years at diagnosis with a mean age of 72.8 ± 6.2 years and median age of 73 years.

Based on the chest CT images, approximately the same number of subjects presented with unilateral diffuse pleural thickening and bilateral diffuse pleural thickening (51.6% and 48.4%, respectively). Among the subjects, 92.9% had pleural plaque and calcification was observed in 90.9% of them. Moreover, 32.6% of the subjects had pulmonary fibrosis as a complication; however, no typical asbestosis was observed (\geq type I) as stipulated by the pneumoconiosis law. On the other hand, round atelectasis showing fibrosis of the visceral pleura was observed in 69.5% of the subjects.

We calculated the number of subjects who met the five findings for organized pleural effusion. Eight subjects (7.6%) had a full score of 5 points, 82 subjects (78.1%) scored 4 points, and only 15 subjects (14.3%) scored 3 points (Table 1). The two findings of [1] heterogeneity in the pleural effusion and [3] the presence of the “crow’s feet” sign in the pleural effusion site were observed in all 105 subjects. [2] Declined chest capacity was observed in 93 subjects (88.6%). In addition, [4] immobilization of the pleural effusion volume was observed in 101 subjects (96.2%). The three subjects who did not show immobilization of the pleural effusion volume scored >3 points with [5] the presence of air in the pleural effusion.

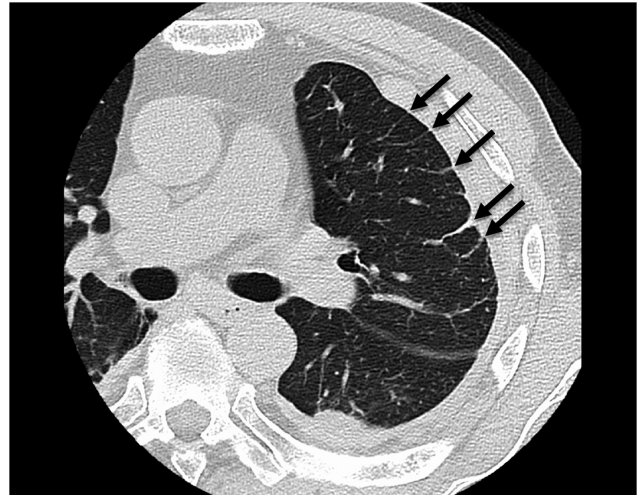


Fig. 3. A cross-sectional chest computed tomography (CT) image showing the presence of the “crow’s feet” sign in the pleural effusion site.

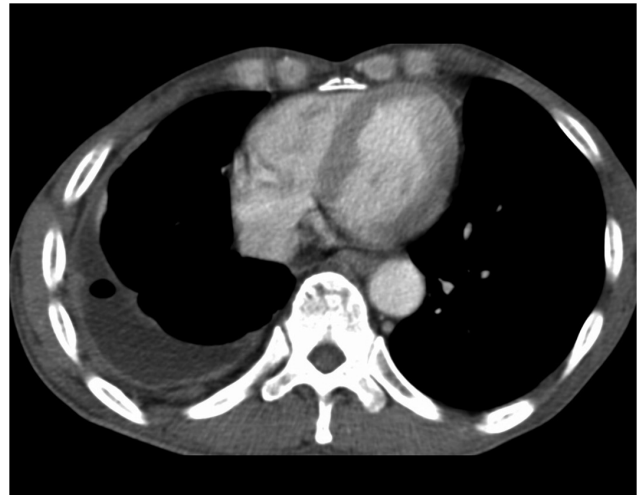


Fig. 4. A cross-sectional chest computed tomography (CT) image showing the presence of air in the pleural effusion. The right pleural effusion tends to be encapsulated, the interior is slightly heterogeneous, and the pleural effusion contains the air trapped by the septation due to the fibrin nets formed inside.

The confirmation period for pleural effusion organization was <3 months in 9.5% of the subjects. Despite having 3 points, most of the 15 subjects who took a period of ≥ 3 months to develop organization showed no changes in the pleural effusion volume in the follow-up period of 7–12 months. In certain subjects, organization took up to 108.4 months to be confirmed. For such subjects, although they were diagnosed with BAPE, pleural mesothelioma was not confirmed and they were not followed-up. Therefore, it took a long time for them to be recognized. The median observation period of the course of pleural effusion organization was 11.3 months (17.6 ± 19.3 months) (Fig. 5). Once

Table 1. Evaluation of the five diagnostic criteria for organized pleural effusion

Points	Number of cases	(%)
1 point	0 cases	(0.0%)
2 points	0 cases	(0.0%)
3 points	15 cases	(14.3%)
4 points	82 cases	(78.1%)
5 points	8 cases	(7.6%)

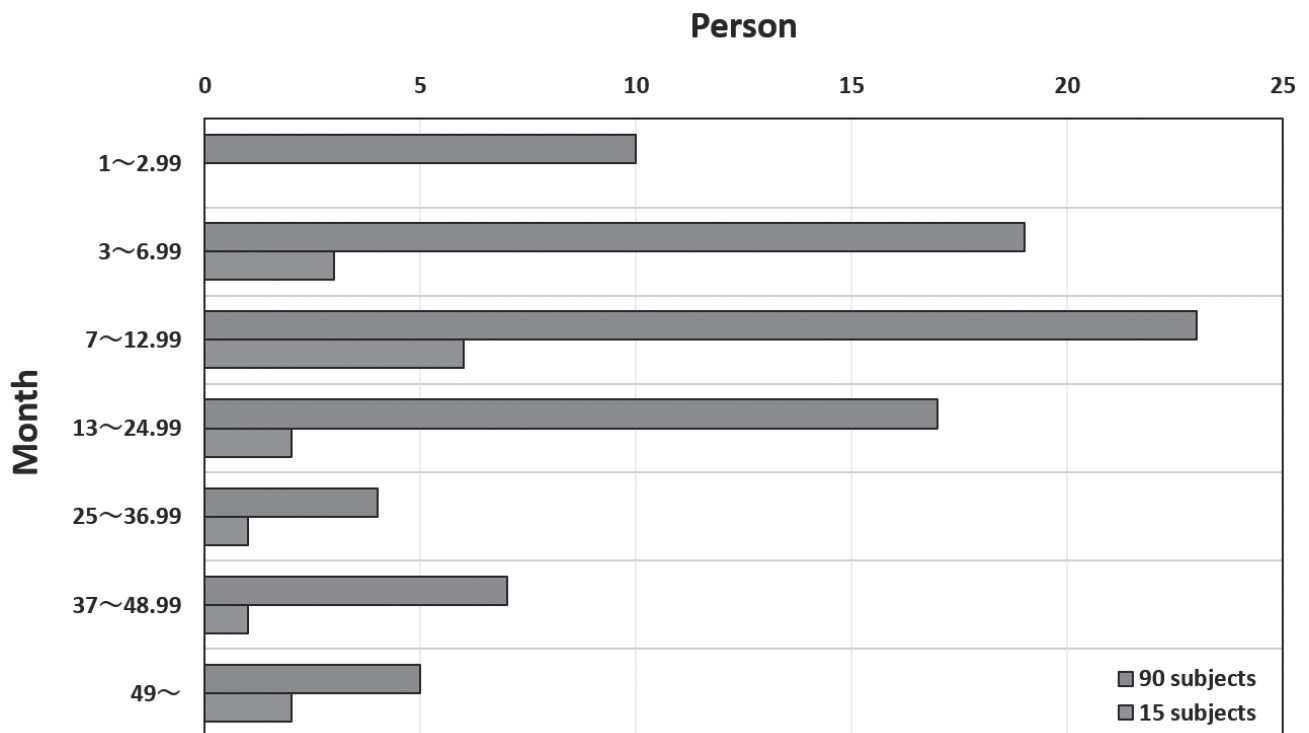


Fig. 5. Observation period following the confirmation of pleural effusion organization on chest computed tomography (CT) images. The confirmation period of organization in all 105 subjects and 15 subjects recognized by 3 points is shown. The observation period varies greatly depending on the subject.

organization was confirmed, the lung capacity did not become greater than that at the confirmation period in any case of relapsed BAPE. However, after an approximate 3-month follow-up on the organization, because the chest shrank although the organized pleural effusion volume decreased, the % vital capacity (VC) that had once dropped to <60% did not exceed 60% again any subject.

Although %VC is an indicator of restrictive ventilatory defect showing a significant respiratory functional disorder, it was 17.3%–70.3% with a mean of 43.8% ± 11.9% (median = 43.2%). Of 102 subjects whose %VC was measured, 95 subjects (93.1%) had a %VC of <60% and seven sub-

jects (6.7%) had >60%. Thirty subjects (29.4%) had a recognized %VC of 50%–59.9%, whereas 29 subjects (28.4%) had a recognized %VC of 30%–39.9%, demonstrating bimodality (Fig. 6). The seven subjects that were not recognized by %VC were recognized by the Worker's Accident Compensation Law. Five subjects had a forced expiratory volume in one second/forced VC ratio of <70% and a forced expiratory volume in one second of <50%; one subject exceeded the alveolar-arterial oxygen difference (AaDO₂) threshold value, and one subject had a partial pressure of oxygen in the arterial blood (PaO₂) of <60 Torr.

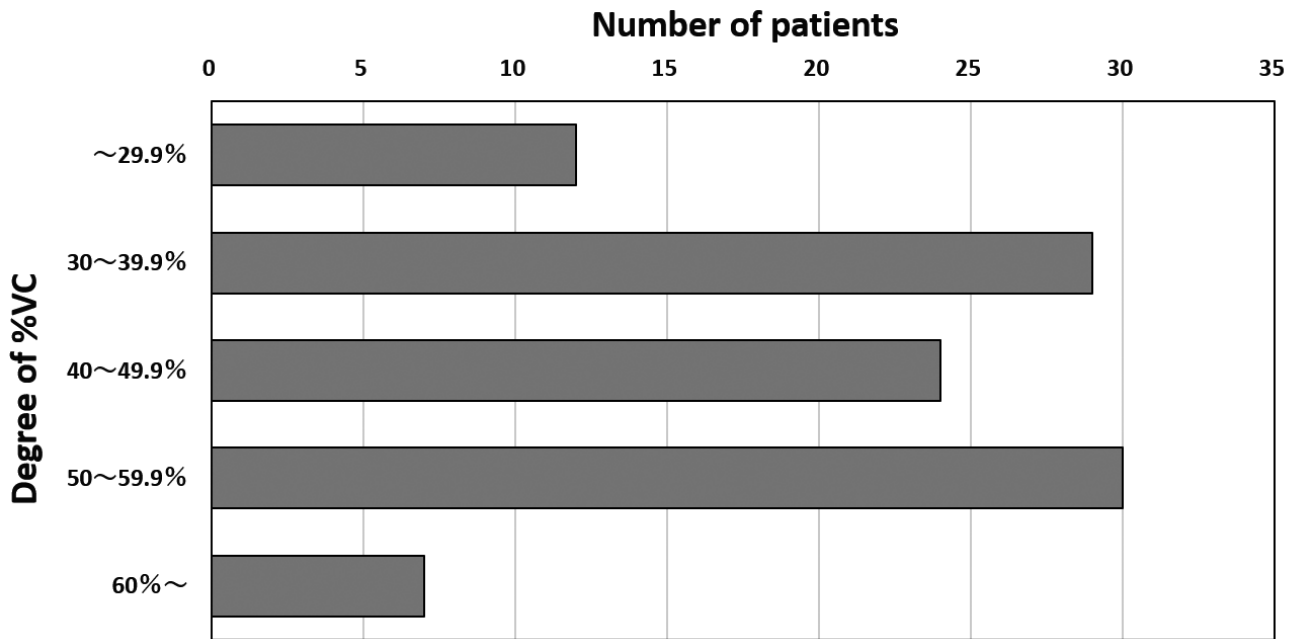


Fig. 6. The number of cases by the degree of %vital capacity (VC) in significant respiratory dysfunction in the respiratory function test.

Discussion

Benign asbestos pleural effusion that occurs due to asbestos exposure is an inflammatory disease of the visceral pleura caused by asbestos fibers, and because diffuse pleural thickening develops after BAPE, many studies have reported diffuse pleural thickening caused by BAPE^{2, 3)}.

This is a retrospective study on 105 subjects (34.8%) who were diagnosed with at least BAPE and had clinical course with the onset of pleural effusion organization. They were selected out of 302 patients with diffuse pleural thickening in Japan. Yates *et al.*⁵⁾ have reported that the transition rate from BAPE to diffuse pleural thickening was 30% in 64 cases, which is consistent with the results of our study (34.7%). However, our study was a mega study including 302 patients in Japan.

Of the five chest CT findings indicating that pleural effusion is organized without disappearing and lung re-expansion is hindered and irreversible according to the Act on Asbestos Health Damage Relief 2017, [1] heterogeneity in the pleural effusion (high absorption of the pleural effusion) and [3] presence of the “crow’s feet” sign in the pleural effusion site are the two findings showing pleural effusion organization and fibrosis of the visceral pleura; these are crucial image findings of the development of diffuse pleural thickening in BAPE. Furthermore, these findings were observed in all 105 subjects.

On the other hand, [2] declined chest capacity was observed in 93 subjects (88.8%); however, in the case of bilateral lesions, it is difficult to capture the declined chest capacity as laterality, and the findings are inconsistent for all cases. Thus, although declined chest capacity is observed, [4] the immobilization of the pleural effusion should be confirmed. However, it is difficult to determine immobilization by investigating at one time point, so pleural effusion immobilization can be determined by observing its course through CT images. Organized pleural effusion is said to be immobilized if it remains unchanged for approximately 3 months; although many cases required approximately 18 months (mean, 17.6 ± 19.3 months; median, 11.3 months), the dispersion was large. In particular, 9.5% of the subjects were diagnosed with organized pleural effusion in approximately 3 months, in accordance with the requirement of the Act on Asbestos Health Damage Relief of the Ministry of the Environment. Although [5] the presence of air in the pleural effusion was not observed in eight cases, it is an important finding that indicates immobilization.

In certain subjects, pleural effusion decreased and lung capacity increased after organization; however, when the long-term course was observed using chest CT images, no lung re-expansion due to pleural adhesion and almost no recovery in lung capacity were observed in most subjects. Therefore, the 3-month follow-up after the confirmation of pleural effusion organization was considered available. Subjects in whom the confirmation of pleural effusion im-

mobilization took some time were followed-up while still being diagnosed with BAPE despite the complication of significant respiratory functional disorder, left uncared for despite the diagnosis of BAPE, not recognized after the development of diffuse pleural thickening, and not provided long-term treatment despite exertional dyspnea.

In an ideal scenario, the appropriate pleural effusion observation period must be determined in a prospective study, but the temporal examination from BAPE to diffuse pleural thickening could be done in only a limited number of cases. In particular, because BAPE is not a target disease according to the Act on Asbestos Health Damage Relief of the Ministry of the Environment, its confirmation is difficult, but we need to confirm whether 3 months follow up of organized pleural effusion is suitable or not, using cases followed-up of BAPE approved by the Worker's Accident Compensation Law. Therefore, in the actual prospective evaluation, it is necessary to recommend and request a chest CT examination simultaneously with chest X-ray images, and it may also be necessary to supplement the periods if the chest CT images are not captured with chest X-ray images in a retrospective study.

In certain cases, as BAPE often relapses, and although pleural mesothelioma was ruled out using thoroscopic pleural biopsy, follow-ups revealed the development of diffuse pleural thickening and significant respiratory dysfunction; thus, it is necessary to perform thorough follow-ups instead of leaving the patients uncared for without reexamination because it is not a malignant tumor.

In addition, approximately half the subjects presented with unilateral lesions and the other half with bilateral lesions. In the study by Jeebun *et al.*⁶⁾, 80% of the subjects presented with unilateral lesions initially, but a 2-year follow-up revealed that in 24% of their subjects, pleural effusion accumulated in the opposite side and bilateral diffuse pleural thickening developed. In the current study, certain subjects initially presented with unilateral lesions but no significant respiratory dysfunction. They were inevitably followed-up due to the accumulation of pleural effusion in the opposite side, and eventually a respiratory dysfunction developed due to the bilateral diffuse pleural thickening, and it took a long time for some subjects to be diagnosed, although the number was small. The results of our previous study showed more cases of diffuse pleural thickening with organized pleural effusion than without pleural effusion. To that end, it is necessary to determine the requirement for organized pleural effusion and to identify diffuse pleural thickening for optimal outcomes.

On the other hand, based on the results of the respiratory

function test performed to evaluate respiratory dysfunction, 95.2% of the marked respiratory dysfunctions were recognized as restrictive defects with a %VC of <60%. In terms of the degree of %VC, a similar number of subjects with severe dysfunction and a %VC of <40% and subjects with relatively mild dysfunction with a %VC slightly <60% was observed. It was suggested that this difference in degree greatly affected the prognosis. However, based on the diagnostic criteria of the Worker's Accident Compensation Law, cases with a forced expiratory volume in one second/forced VC ratio of <70% and a forced expiratory volume in one second of <50% were also identified, and two cases were recognized based on this criterion, whereas 3 cases were recognized based on the criteria of the arterial blood gas analyses results exceeding the AaDO₂ threshold value or PaO₂ <60 Torr.

The criteria for compensation and Asbestos Health Damage Relief in Japan do not consider the dullness of costophrenic angles, which is a British criterion, but according to Fonseka *et al.*⁷⁾, even without the dullness of costophrenic angles, %VC reduced to 79.5% in unilateral diffuse pleural thickening and 66.7% in bilateral cases, leading to a respiratory compromise within the range of diffuse pleural thickening, which is the Japanese criterion. In addition, Singh *et al.*⁸⁾ reported that the movements of the diaphragm and lower pleura greatly affected the respiratory function of diffuse pleural thickening patients. Therefore, we believed that it was not necessarily crucial to assess the dullness of costophrenic angles. The mechanism of diffuse pleural thickening, a fibrosis of the visceral pleura, is believed to involve proliferation of subpleural fibroblasts induced by BAPE, and this fibrosis presumably consists of an interaction between inflammatory and epipleural mesothelial cells⁹⁾.

BAPE is the important factor to approve asbestos-induced diffuse pleural thickening, therefore it is essential to diagnose organized pleural effusion to prevent re-expansion of lung for many cases. We want to assess this requirement of the diffuse pleural thickening with BAPE by the Act on Asbestos Health Damage Relief of the Ministry of the Environment and grope the better Japanese criteria including the dullness of costophrenic angles for the diffuse pleural thickening with BAPE.

We hope that many patients will be diagnosed based on this requirement for compensation and Asbestos Health Damage Relief for organized pleural effusion stipulated in the 2017 Revision of Points to Note regarding Materials Pertaining to Medical Judgment under the Act on Asbestos Health Damage Relief of the Ministry of the Environment.

Declarations of Interest

None.

Institution at Which the Work was Performed

Research and Training Center for Asbestos-Related Diseases, Okayama, Japan

Institution and Ethics Approval and Informed Consent

Written informed consent was obtained from all patients in this study. Research and Training Center for Asbestos-Related Diseases granted approval for this study (Approval number #2) on May 14, 2020.

Acknowledgments

We thank Ms. Shiori Sato for the preparation of this manuscript.

Funding

This study was supported by Japanese Ministry of Environment, 2016 (No grant number available).

Data Statement

The data of this study are not publicly available, as we may use the data in future research.

References

- 1) Mastrangelo G, Ballarin MN, Bellini E, Bicciato F, Zannol F, Gioffrè F, Zedde A, Tessadri G, Fedeli U, Valentini F, Scoizzato L, Marangi G, Lange JH (2009) Asbestos exposure and benign asbestos diseases in 772 formerly exposed workers: dose-response relationships. *Am J Ind Med* **52**, 596–602.
- 2) McLoud TC, Woods BO, Carrington CB, Epler GR, Gaensler EA (1985) Diffuse pleural thickening in an asbestos-exposed population: prevalence and causes. *Am J Roentgenol* **144**, 9–18.
- 3) Hillerdal G (1981) Non-malignant asbestos pleural disease. *Thorax* **36**, 669–75.
- 4) Gevenois PA, de Maertelae V, Madani A, Winant C, Sergent G, De Vuyst P (1998) Asbestosis, pleural plaques and diffuse pleural thickening: three distinct benign response to asbestos exposure. *Eur Respir J* **11**, 1021–7.
- 5) Yates DH, Browne K, Stidolph PN, Neville E (1996) Asbestos-related bilateral diffuse pleural thickening: natural history of radiographic and lung function abnormalities. *Am J Resir Crit Care Med* **153**, 301–6.
- 6) Jeebun V, Stenton SC (2012) The presentation and natural history of asbestos-induced diffuse pleural thickening. *Occup Med* **62**, 266–8.
- 7) De Fonseka D, Edey A, Staddon L, Viner J, Darby M, Maskell NA (2017) The physiological consequences of different distributions of diffuse pleural thickening in CT imaging. *Br J Radiol* **90**, 20170218. doi: 10.1259/bjr.20170218. Epub 2017 Jul 14.
- 8) Singh B, Eastwood PR, Finucane KE, Panizza JA, Musk AW (1999) Effect of asbestos-related pleural fibrosis on excursion of the lower chest wall and diaphragm. *Am J Resir Crit Care Med* **160**, 1507–15.
- 9) Mussaers SE, Prele CM, Brody AR, Idell A (2004) Pathogenesis of pleural fibrosis. *Respirology* **9**, 428–40.

The diagnosis of early pneumoconiosis in dust-exposed workers: comparison of chest radiography and computed tomography

Acta Radiologica
2022, Vol. 63(7) 909–913
© The Foundation Acta Radiologica
2021

Article reuse guidelines:
sagepub.com/journals-permissions
DOI: 10.1177/02841851211022501
journals.sagepub.com/home/acr



Hideyuki Hayashi¹, Kazuto Ashizawa² , Masashi Takahashi³,
Katsuya Kato⁴, Hiroaki Arakawa⁵, Takumi Kishimoto⁶,
Yoshinori Otsuka⁷, Satoshi Noma⁸ and Sumihisa Honda⁹

Abstract

Background: Chest radiography (CR) is employed as the evaluation of pneumoconiosis; however, we sometimes encounter cases in which computed tomography (CT) is more effective in detecting subtle pathological changes or cases in which CR yields false-positive results.

Purpose: To compare CR to CT in the diagnosis of early-stage pneumoconiosis.

Material and Methods: CR and CT were performed for 132 workers with an occupational history of mining. We excluded 23 cases of arc-welder's lung. Five readers who were experienced chest radiologists or pulmonologists independently graded the pulmonary small opacities on CR of the remaining 109 cases. We then excluded 37 cases in which the CT data were not sufficient for grading. CT images of the remaining 72 cases were graded by the five readers. We also assessed the degree of pulmonary emphysema in those cases.

Results: The grade of profusion on CR (CR score) of all five readers was identical in only 5 of 109 cases (4.6%). The CR score coincided with that on CT in 40 of 72 cases (56%). The CT score was higher than that on CR in 13 cases (18%). On the other hand, the CT score was lower than that on CR in 19 cases (26%). The incidence of pulmonary emphysema was significantly higher in patients whose CR score was higher than their CT score.

Conclusion: CT is more sensitive than CR in the evaluation of early-stage pneumoconiosis. In cases with emphysema, the CR score tends to be higher in comparison to that on CT.

Keywords

Pneumoconiosis, chest radiography, computed tomography, chest, pulmonary emphysema

Date received: 3 April 2020; accepted: 10 May 2021

Introduction

Pneumoconiosis, an occupational lung disease caused by the inhalation of silica, coal particles, or asbestos, still has a serious effect on occupational health worldwide (1). Silicosis, a pneumoconiosis, is an incurable lung disease caused by the inhalation of dust containing free crystalline silica. Early recognition is important

⁴Department of Radiology, Kawasaki Medical School Hospital, Okayama, Japan

⁵Department of Radiology, Dokkyo Medical University, Tochigi, Japan

⁶Asbestos Research Center, Okayama Rosai Hospital, Okayama, Japan

⁷Department of Internal Medicine, Hokkaido Chuo Rosai Hospital, Hokkaido, Japan

⁸Department of Radiology, Tenri Hospital, Tenri, Japan

⁹Department of Public Health & Nursing, Nagasaki University Graduate School of Biomedical Sciences, Nagasaki, Japan

Corresponding author:

Kazuto Ashizawa, Department of Clinical Oncology, Unit of Translational Medicine, Nagasaki University Graduate School of Biomedical Sciences, 1-7-1 Sakamoto, Nagasaki 852-8501, Japan.

Email: ashi@nagasaki.u.ac.jp

¹Department of Radiology, Isahaya General Hospital, Nagasaki, Japan

²Department of Clinical Oncology, Nagasaki University Graduate School of Biomedical Sciences, Nagasaki, Japan

³Department of Radiology, Yujin-Yamazaki Hospital, Shiga, Japan

in the management of this disease. Early-stage pneumoconiosis is defined as profusion 0/1 to 1/1 cases on chest radiography (CR) based on the international classification of radiographs of pneumoconiosis published by International Labour Office (ILO) (2,3). Because they do not have pulmonary dysfunction, a radiological examination is essential for the diagnosis of pneumoconiosis for both clinical and epidemiological purposes (1). Although workers with possible exposure to occupational dust are screened using CR, there are some limitations in the assessment of pneumoconiosis on CR.

Computed tomography (CT) is more sensitive than CR in detecting lung parenchymal abnormalities. CR as well as CT findings in patients with silicosis have been documented, and it has been reported that discordance between the two was high, especially for CR-negative and early-stage pneumoconiosis cases (2). In addition, we sometimes encounter cases in which nodules, which are suspected on CR, are not evident on CT, especially in patients with pulmonary emphysema. The aim of the present study was to compare the CR and CT findings in the diagnosis of early-stage pneumoconiosis. Moreover, we also would like to evaluate whether the presence or degree of pulmonary emphysema is associated with the CR and CT scores.

Material and Methods

The present retrospective study was approved by the institutional review board of our hospitals, and the requirement for informed written consent was waived from all participants.

Patients

CR and CT examinations were performed for 132 workers with an occupational history of mining, who were recruited from two laborers' hospitals. Because the imaging findings of arc-welder's pneumoconiosis are different from those of silicosis (4), we excluded 23 cases of arc-welder's lung (Fig. 1). Thus, 109 individuals (109 men; age range = 48–89 years; mean age = 74.8 years) with silicosis or coal workers' pneumoconiosis were included. They included 25 smokers, 72 ex-smokers, and 12 never-smokers. None of the workers in the study had a history of pulmonary disease, such as tuberculosis, pneumonia, or lung cancer.

Interpretation of chest radiography

Posteroanterior CR was taken at full inspiration. CR images were displayed in 3-megapixel LCD medical-grade gray-scale monitor (Radiforce GS 320; Eizo, Ishikawa, Japan). Five readers, who were experienced chest radiologists (MT, KK, and SN, with 21–35 years of experience) or pulmonologists (TK and YO, with 27 and 15 years of experience, respectively) independently graded the profusion of lung abnormalities on CR of 109 cases in comparison to a set of standard radiographs provided by Ministry of Health, Labour and Welfare Labour Standards Bureau. In this set, CR findings are classified into one of seven PR (profusion) categories (PR 0, 1, 2, 3, 4A, 4B, and 4C). No radiographic signs of pneumoconiosis are graded as PR0 and those with pneumoconiotic small opacities as PR1–PR3, depending on increasing number

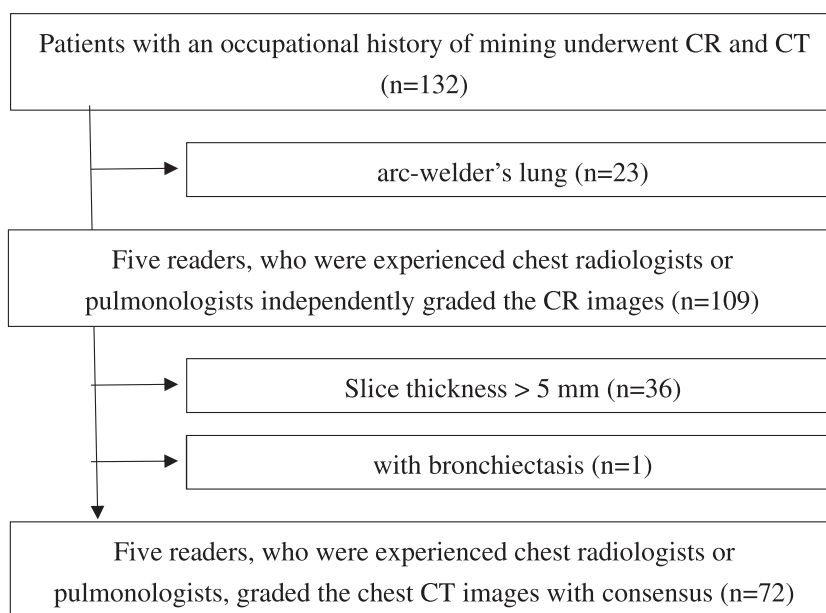


Fig. 1. Study selection process.

Table 1. Observer performance of the experienced chest radiologists or pulmonologists in the interpretation of CR images (n = 109).

CR score	5/5 agreement	4/5 agreement	3/5 agreement
0/1	4	14	11
1/0	1	7	28
1/1	0	3	14
>1/1	0	2	4
Total	5 (4.6%)	26 (24%)	57 (52%)

CR, chest radiography.

(profusion), and large opacities as PR4. Small opacities profusion is recorded on a 12-point scale from 0/- to 3/+, in which 0/- indicates no abnormality and 3/+ signifies the highest concentration of small opacities. We analyzed the observer performance of the five readers in the interpretation of CR. After the analysis of their scores (Table 1), the images from cases for which there was disagreement among the reviewers were reviewed to reach a consensus.

Interpretation of CT

All individuals were scanned in two CT scanners (TSX-302A/1A Aquilion PRIME (Toshiba Medical Systems, Tochigi, Japan) and Light Speed VCT (GE Healthcare, Chicago, IL, USA). Because of the retrospective design of this study, various CT scan protocols were used, and CT images were obtained with slice thicknesses in the range of 3–8 mm and slice intervals in the range of 5–8 mm at full inspiration. We excluded 36 cases with a slice thickness of >5 mm, and one case with marked bronchiectasis in the interpretation of CT images (Fig. 1). CT images were also displayed in 3-megapixel LCD medical-grade gray-scale monitor (Radiforce GS 320; Eizo, Ishikawa, Japan). All CT images were viewed on lung window setting (level = -700 HU; width = 1500 HU). Five readers also graded the profusion of lung abnormalities on CT images of 72 cases with consensus.

We compared the scores in both the CR and CT images. Two other experienced chest radiologists (HH and KA, with 22 and 30 years of experience, respectively) evaluated each CT image and classified the degree of emphysema into three levels: none; mild; and severe. These three levels correspond to the classification in the Fleischner Society guidelines as follows: none = none or trace; mild = mild or moderate; and severe = confluent or advanced destructive (5). The relationship between the degree of emphysema and the CR/CT scores was examined.

Table 2. Comparison of both CR and CT scores (n = 72).

CR score	CT score			
	0/1	1/0	1/1	1/<1
0/1 (n = 27)	21	5	0	1
1/0 (n = 27)	13	9	4	1
1/1 (n = 15)	3	2	8	2
1/<1 (n = 3)	0	1	0	2

CR, chest radiography; CT, computed tomography.

Table 3. Correlation between the degree of pulmonary emphysema and CR/CT scores (n = 72).

Pulmonary emphysema	CR > CT	CR = CT	CR < CT
None (n = 43)	5	26	12
Mild (n = 21)	7	13	1
Severe (n = 8)	7	1	0

CR, chest radiography; CT, computed tomography.

Data analysis

The weighted value of kappa was calculated for the comparison of CR and CT scores (Table 2). Spearman's rank correlation coefficient was calculated to assess the correlation between the degree of pulmonary emphysema and the CR/CT scores (Table 3).

Results

The observer performance in the interpretation of CR images is shown in Table 1. The scores of all five observers were identical in only 5 of 109 cases (4.6%). There were 26 cases (24%) in which the scores of four of the five observers matched. There were 57 cases (52%) in which the scores of three of the five observers matched.

A comparison of CR and chest CT according to the categories is shown in Table 2. The weighted value of the kappa coefficient between the CR and CT scores was 0.456 ($P < 0.01$). 21 out of 27 cases with a CR score of 0/1 matched the score of the CT images. Six cases with a CR score of 0/1 were scored as 1/0 (n = 5) or 1/<1 (n = 1) on CT images. Five cases with a CR score of 1/0 were scored as 1/1 (n = 4) or 1/<1 (n = 1) on CT images. Two cases with a CR score of 1/1 were scored as 1/<1 (n = 2) on CT images. Therefore, there were 13 cases in which the CT score was higher than the CR score (Fig. 2). On the other hand, there were 19 cases in which CR score was higher than the CT score (Fig. 3).

The correlation between the degree of pulmonary emphysema and the CR/CT scores is shown in Table 3. The incidence of pulmonary emphysema was significantly higher ($r = 0.503$; $P < 0.001$) in cases in which the CR score was higher than the CT score.

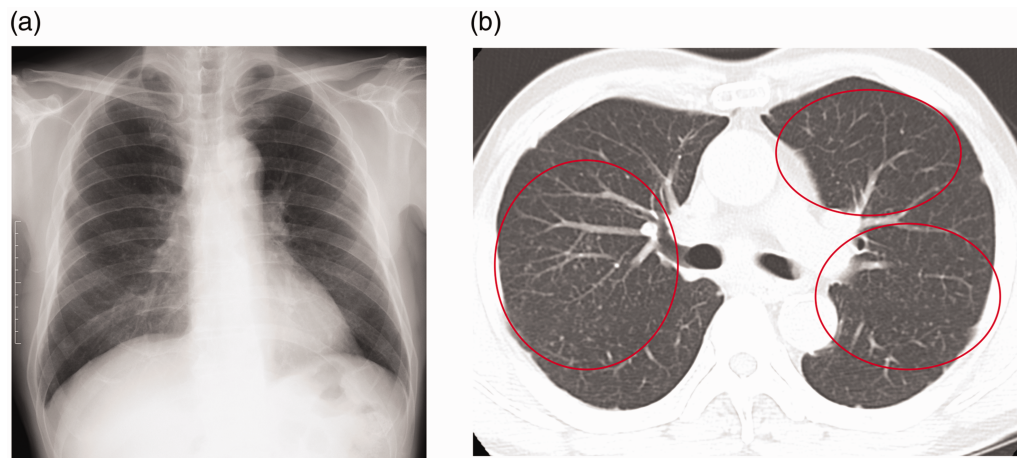


Fig. 2. (a) A 72-year-old man with an exposure duration of 30 years. Chest radiography was judged as profusion 0/1. (b) Computed tomography images revealed many small opacities in the lung parenchyma (circles).

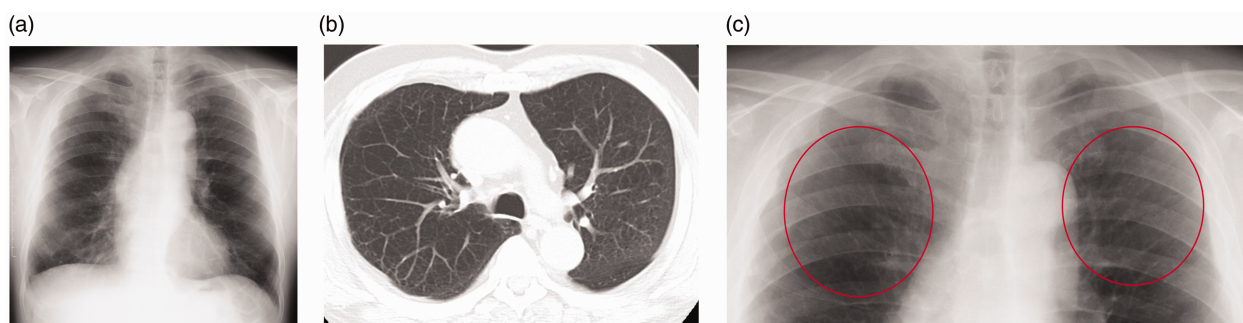


Fig. 3. (a) An 81-year-old man with an exposure duration of 34 years. CR was judged as profusion 1/1. (b) Computed tomography images revealed pulmonary emphysema with a few small opacities in the lung parenchyma. (c) Magnified image of the upper lung fields of CR (a). There appear to be small nodules in the upper lung fields (circles). CR, chest radiography.

Discussion

In the present study, CT is more sensitive than CR in the evaluation of pneumoconiosis. Pneumoconiosis is usually diagnosed based on CR. Currently the diagnosis is based on the international classification of radiographs of pneumoconiosis, published by the ILO in 1980 (3); however, CR is of limited value in cases of low-grade diffuse infiltrative lung disease (6,7). In this study, 18% (13/72) of cases had small nodular lesions that could only be detected on CT, or in which more nodules could be detected by CT. There are some cases in which tiny nodules can only be depicted on CT. Suganuma et al. (8) reported that the CR categorical classification was similar to high-resolution CT (HRCT), with the exception of category 0, in which HRCT was more sensitive.

In patients with pulmonary emphysema, the CR score tended to be higher than the CT score. Although Savranlar et al. (2) also reported that the CR categorical score was higher than the CT score in

15 of 67 patients, the reason was not shown. Patients with silicosis often have pulmonary emphysema. Bergin et al. (9) reported that pulmonary emphysema associated with silicosis was easily detected on CT. To the best of our knowledge, there are no reports on the overestimation of silicotic nodules by correlated with pulmonary emphysema.

It is difficult to diagnose pulmonary emphysema based on CR alone. Thurlbeck and Simon (10) described two different roentgenologic patterns of altered pulmonary vascularity in patients with pulmonary emphysema, namely, "arterial deficiency" and "increased marking". "Increased marking" refer to prominent vascular markings which tend to be irregular in contour. This pattern is thought to occur in patients with mild or moderate emphysema due to redistribution of blood flow, pulmonary arterial hypertension and lung overinflation. We hypothesize that the presence of "increased marking" is one of the factors associated with overestimation of tiny nodules on CR.

Although image interpretation was performed by experienced radiologists or pulmonologists in this study, there were only 5 cases (4.6%) in which all five scores of pneumoconiosis on CR matched. The diagnosis is based on the international classification of radiographs; however, the criterion is ambiguous due to the number of nodules. Since this ambiguity cannot be completely eliminated, even by CT, we are of the opinion that objective evaluation by a system such as computer-assisted diagnosis will be necessary in the future.

The present study has some limitations. First, this was a retrospective study. Second, the study population was relatively small. Third, the slice thickness of CT was relatively thick, not thin-section CT, because CT scans with thick slice thickness have been performed in the past for screening purposes at many institutions, and they are performed in some institutions in our country, even at the present time. Therefore, this limitation might influence the CT profusion score.

In conclusion, CT is more useful than CR in the evaluation of pneumoconiosis. In addition to depicting tiny nodules, we could reduce overestimation, especially in cases with pulmonary emphysema. We suggest using CT as a standard screening method to distinguish between normal and early-stage pneumoconiosis.

Acknowledgments

The authors thank Yuko Nishimoto and Tetsuhisa Nita for their helpful comments.

Declaration of conflicting interests

The authors declared no potential conflicts of interest with respect to the research, authorship, and/or publication of this article.

Funding

The authors received the following financial support for the research, authorship, and/or publication of this article: This study was supported by the Ministry of Health, Labour and Welfare Scientific Research Grant of Japan.

ORCID iD

Kazuto Ashizawa  <https://orcid.org/0000-0001-6726-1297>

References

1. Akira M. High-resolution CT in the evaluation of occupational and environmental disease. High-resolution CT of the lung II. *Radiol Clin North Am* 2002;40:43–59.
2. Savranlar A, Altin R, Mahmutyazicioglu K, et al. Comparison of chest radiography and high-resolution computed tomography findings in early and low-grade coal worker's pneumoconiosis. *Eur J Radiol* 2004;51:175–180.
3. International Labour Office. Guideline for the use of ILO international classification of radiographs of pneumoconiosis, revised ed. 31. Occupational Safety and Health Series No.2. Geneva: International Labour Office, 1980.
4. Yoshii C, Matsuyama T, Takazawa A, et al. Welder's pneumoconiosis: diagnostic usefulness of high-resolution computed tomography and ferritin determinations in bronchoalveolar lavage fluid. *Intern Med* 2002;12:1111–1117.
5. Lynch DA, Austin JHM, Hogg JC, et al. CT-definable subtypes of chronic obstructive pulmonary disease: a statement of the Fleischner Society. *Radiology* 2015;277:192–205.
6. Gevenois PA, Pichot E, Dargent F, et al. Low-grade coal worker's pneumoconiosis. Comparison of CT and chest radiography. *Acta Radiol* 1994;35:351–356.
7. Epler GR, McLoud TC, Gaensler EA, et al. Normal chest roentgenograms in chronic diffuse infiltrative lung disease. *N Engl J Med* 1978;298:934–939.
8. Suganuma N, Kusaka Y, Hosoda Y, et al. The Japanese Classification of Computed Tomography for pneumoconiosis with the ILO international classification of radiographs for pneumoconiosis. *J Occup Health* 2001;43:24–31.
9. Bergin CJ, Muller NL, Vedal S, et al. CT in silicosis: correlation with Plain Films and Pulmonary Function Tests. *AJR Am J Roentgenol* 1986;146:477–483.
10. Thurlbeck WM, Simon G. Radiographic appearance of the chest in emphysema. *AJR Am J Roentgenol* 1978;130:429–440.

Increased alpha cell to beta cell ratio in patients with pancreatic cancer

Tami Tsuchiya¹⁾, Yoshifumi Saisho^{1),2)}, Jun Inaishi^{1),3)}, Hironobu Sasaki^{1),3)}, Midori Sato¹⁾, Masaru Nishikawa¹⁾, Yohei Masugi⁴⁾, Taketo Yamada^{4),5)} and Hiroshi Itoh¹⁾

¹⁾ Division of Nephrology, Endocrinology and Metabolism, Department of Internal Medicine, Keio University School of Medicine, Tokyo 160-8582, Japan

²⁾ Saisho Diabetes Clinic, Tokyo 164-0001, Japan

³⁾ Center for Preventive Medicine, Keio University School of Medicine, Tokyo 160-8582, Japan

⁴⁾ Department of Pathology, Keio University School of Medicine, Tokyo 160-8582, Japan

⁵⁾ Department of Pathology, Saitama Medical University, Saitama 350-0495, Japan

Abstract. The development of pancreatic cancer (PC) is associated with worsening of glucose tolerance. However, there is limited information about the effects of PC on islet morphology. The aim of this study was to elucidate changes in alpha and beta cell mass in patients with PC. We enrolled 30 autopsy cases with death due to PC (9 with diabetes; DM) and 31 age- and BMI-matched autopsy cases without PC (controls, 12 with DM). Tumor-free pancreatic sections were stained for insulin and glucagon, and fractional beta cell (BCA) and alpha cell area (ACA) were quantified. In addition, expression of dedifferentiation markers, *i.e.*, ALDH1A3 and UCN3, was qualitatively evaluated. The pancreas of subjects with PC showed atrophic and fibrotic changes. There was no significant difference in BCA in subjects with PC compared to controls ($1.53 \pm 1.26\%$ vs. $0.95 \pm 0.42\%$, $p = 0.07$). However, ACA and ACA to BCA ratio were significantly higher in subjects with PC compared to controls ($2.48 \pm 2.39\%$ vs. $0.53 \pm 0.26\%$ and 1.94 ± 1.93 vs. 0.59 ± 0.26 , respectively, both $p < 0.001$). Increased ACA to BCA ratio was observed in subjects with PC irrespective of the presence of DM. Qualitative evaluation of ALDH1A3 and UCN3 expression showed no significant difference between the groups. In conclusion, in subjects with PC, alpha to beta cell mass ratio is increased, which may contribute to the increased risk of worsening glucose metabolism. Further studies are warranted to elucidate the mechanisms of increased alpha to beta cell mass in patients with PC.

Key words: Beta cell mass, Alpha cell mass, Pancreatic cancer

IN GENERAL, pancreatic cancer (PC) is a malignant disease with a poor prognosis, with a 5-year survival rate of 3–10% [1-6]. Development of PC is often associated with worsening glucose metabolism and onset of diabetes, so-called pancreatic cancer associated diabetes [7-9], while in subjects with type 2 diabetes, the risk of PC has also been shown to be 1.5 to 2 times higher than in those without diabetes [7, 8, 10, 11].

It has been reported that patients with PC exhibit insulin resistance and beta cell dysfunction [12-14], and it is speculated that a complex combination of islet blood flow dysfunction, microthrombosis and perivascular fibrosis suppresses insulin secretion dynamics and leads

to the development of diabetes [8, 15].

Previous histological studies have shown decreased beta cells and increased alpha cells in patients with PC [16, 17], while others have reported no change in beta and alpha cells in PC patients [18], and there is no certainty about the changes in endocrine cells in PC patients.

Moreover, a recent histological study has shown that the percentage of dedifferentiated beta cells was increased in non-diabetic PC patients, suggesting that paraneoplastic beta cell dysfunction precedes hyperglycemia [19]. However, there are limited data available on histological changes in the pancreatic islets in subjects with PC, and it remains unclear how PC affects beta cell mass (BCM) and alpha cell mass (ACM).

Therefore, in the present study, we aimed to elucidate the effects of PC on ACM and BCM and its effects on dedifferentiation markers in subjects with and without diabetes, using autopsy specimens.

Submitted Mar. 31, 2022; Accepted Jun. 30, 2022 as EJ22-0170
Released online in J-STAGE as advance publication Aug. 6, 2022
Correspondence to: Yoshifumi Saisho, MD, PhD, Division of Nephrology, Endocrinology and Metabolism, Department of Internal Medicine, Keio University School of Medicine, 35 Shinanomachi, Shinjuku-ku, Tokyo 160-8582, Japan.
E-mail: ysaisho@keio.jp

Materials and Methods

Subjects

The characteristics of the subjects are shown in Table 1 and Supplementary Table 1. Autopsy specimens of pancreas were obtained with the permission of the bereaved family. This study was approved by the Review Committee of the Faculty of Medicine, Keio University (approval number 20120475). Potential cases that died of PC and age- and BMI-matched cases without pancreatic disease (controls) were identified by retrospective analysis of the autopsy database of Keio University. To assess the effects of diabetes, both cases with and without diabetes were included.

Eligible cases 1) underwent a complete autopsy within 24 hours of death, 2) had available medical information prior to death, 3) were not receiving obvious glucocorticoid therapy, and 4) had sufficient size and quality of preserved tumor-free pancreatic tissue. Cases in which the pancreatic tissue was autolytic were excluded.

After reviewing about 2,000 autopsy cases from 1992 to 2017, 39 cases of PC were identified. Among them, 5 cases were excluded because of lack of pancreatic specimens and 4 cases were excluded because of insufficient quality of the specimen, resulting in inclusion of a total of 30 cases with PC (9 with diabetes; DM) in this study. One subject in the PC group was diagnosed with DM at the time of PC diagnosis; the rest had been diagnosed with type 2 DM at least 2 years prior to their PC diagnosis.

The histological type of PC in all cases was pancreatic ductal adenocarcinoma (PDAC). Among them, 4 cases were mucinous carcinoma and the rest were tubular adenocarcinoma. The location of the tumor was the pancreatic body or tail in 12 cases and the pancreatic head in 18 cases.

As controls, 31 age- and BMI-matched cases without pancreatic disease (with and without type 2 DM) were selected from the database. Of those, 14 cases died of malignancy other than PC (Supplementary Table 1). The

presence of DM was confirmed by review of medical records and autopsy reports. In 41 cases (20 PC, 21 controls), specimens were collected from the body or tail of the pancreas, and in the remaining cases, specimens were collected from the head of the pancreas.

Glycated hemoglobin (HbA1c) level within 1 year prior to death was obtained from the medical records in 36 cases (Table 1) [20]. HbA1c values were expressed as National Glycohemoglobin Standardization Program (NGSP) values [21].

Tissue processing of pancreas

The pancreas was fixed with formaldehyde at autopsy and embedded in paraffin for subsequent analysis. In cases of PC, we selected sections of tumor-free pancreatic tissue for histological analysis. Subsequently, 5- μ m sections were stained as follows: 1) hematoxylin and eosin, 2) insulin (peroxidase staining) with hematoxylin, and 3) glucagon with hematoxylin, and viewed under an optical microscope. For immunohistochemical staining, guinea pig polyclonal antibody against porcine insulin and rabbit polyclonal antibody against human glucagon were used (DAKO Japan).

As dedifferentiation markers, chromogenic immunohistochemical staining for aldehyde dehydrogenase 1 family member A3 (ALDH1A3) and urocortin 3 (UCN3) expression was evaluated using an automated staining system (Bond Max, Leica Biosystems) with a Bond Polymer Refine Detection Kit (Leica Biosystems). For primary antibodies, an anti-ALDH1A3 rabbit polyclonal antibody (dilution, 1:1000; Novus, NBP2-15339) and an anti-UCN3 rabbit monoclonal antibody (dilution, 1:200; Sigma, HPA-038281) were used.

Morphometric analysis

For quantification of beta cell area (BCA), a single cross-sectional pancreatic section of each subject was used; it was photographed using a NanoZoomer-XR slide scanner at 200 \times (20 \times objective), displayed with

Table 1 Patients' characteristics

	PC group			Controls			Total
	Total	DM (-)	DM (+)	Total	DM (-)	DM (+)	
<i>N</i> (male/female)	30 (19/11)	21 (12/9)	9 (7/2)	31 (21/10)	19 (12/7)	12 (9/3)	61 (40/21)
Age, years	68.8 \pm 9.7	68.4 \pm 10.3	69.7 \pm 8.4	65.6 \pm 7.0	63.7 \pm 6.4	68.8 \pm 7.0	67.1 \pm 8.5
BMI, kg/m ²	21.4 \pm 4.2	21.1 \pm 3.3	22.2 \pm 6.0	22.2 \pm 4.1	22.3 \pm 4.0	22.0 \pm 4.3	21.8 \pm 4.1
HbA _{1c} , % ¹⁾	6.7 \pm 1.1	5.2 \pm 0.2	7.1 \pm 0.85 ^{†‡}	6.3 \pm 1.0	5.6 \pm 0.7	7.3 \pm 0.5 ^{†‡}	6.5 \pm 1.0

Data are mean \pm SD or *n* (%). PC; pancreatic cancer, DM; diabetes.

1) HbA1c was obtained in 36 subjects.

[†] *p* < 0.05 vs. PC group without DM.

[‡] *p* < 0.05 vs. controls without DM.

NDP.view2 software (Hamamatsu Photonics, Shizuoka, Japan) and then the percentage of BCA to the total pancreas area was digitally measured using Image Pro Plus software (Media Cybernetics, Silver Spring, MD, USA). Similarly, the ratio of alpha cell area (ACA) to total pancreas area was also digitally measured, and the ratio of ACA to BCA was determined in each case. These measurements were performed by one researcher (T.T.), and the inter-observer and intra-observer coefficients of variation were approximately 6% and 5%, respectively. All measurements were performed twice, and the mean of the two measurements was used. At the time of measurement, the researcher was blinded to the PC and glucose metabolism status of each sample.

In addition, mean islet size was quantified using NDP.view2 in a randomly selected region of the pancreas containing approximately 100 islets in each case (101 ± 17 islets, 6,191 islets in total) [20, 22]. For evaluation of dedifferentiation markers, we selected 20 cases in the PC group (12 with high ACA to BCA ratio and 8 with low ACA to BCA ratio) and 10 cases in the controls (with low ACA to BCA ratio) and compared them qualitatively (Supplementary Table 2). Two researchers (T.T. and Y.M.) evaluated each slice using the same criteria under double-blind conditions. The expression of these markers within the islets was qualitatively evaluated as four levels, [none (-) to very high (+++)], depending on the degree of positive staining.

Statistical analysis

Data showing a non-normal distribution were expressed as median (interquartile range) and those

showing a normal distribution were expressed as mean \pm SD. Mann-Whitney *U* test was used to analyze differences between the two groups, and Kruskal-Wallis test was used to analyze differences between the four groups. Statistical analysis was performed using SPSS 26 software (IBM, Chicago, IL, USA). For all analyses, a value of $p < 0.05$ was regarded as significant.

Results

Subjects' characteristics

Characteristics of patients in the PC group ($n = 30$, 9 with DM) and controls ($n = 31$, 12 with DM) are shown in Table 1 and Supplementary Table 1. HbA1c levels in the DM group with and without PC were significantly higher compared to those in subjects without DM with and without PC, respectively.

Pancreatic morphology in subjects with PC

Representative microphotographs of the pancreas of subjects with and without PC are shown in Fig. 1. Atrophic and fibrotic changes of the pancreatic parenchyma were more prominent in the tumor-free pancreas of those with PC compared with the pancreas of those without PC. In contrast, islet morphology was relatively intact in those with PC compared with those without PC.

Effects of PC on alpha and beta cell mass

While there was no significant difference in BCA between subjects with and without PC ($1.53 \pm 1.26\%$ vs. $0.95 \pm 0.42\%$, $p = 0.07$) (Figs. 2 and 3a, Supplementary Table 2), ACA was significantly greater in subjects with

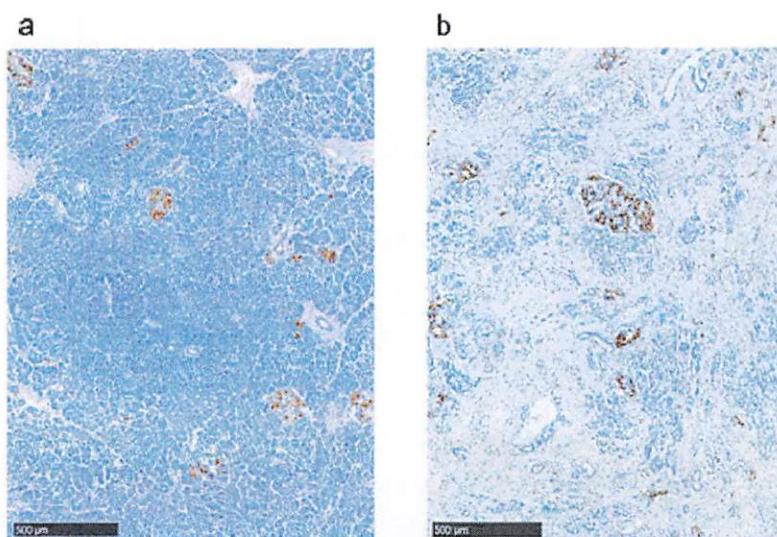


Fig. 1 Representative microphotographs of pancreas of subjects with (b) and without (a) pancreatic cancer. Tumor-free pancreatic sections were immunostained for insulin (brown) and with hematoxylin. Scale bar = 500 μ m.

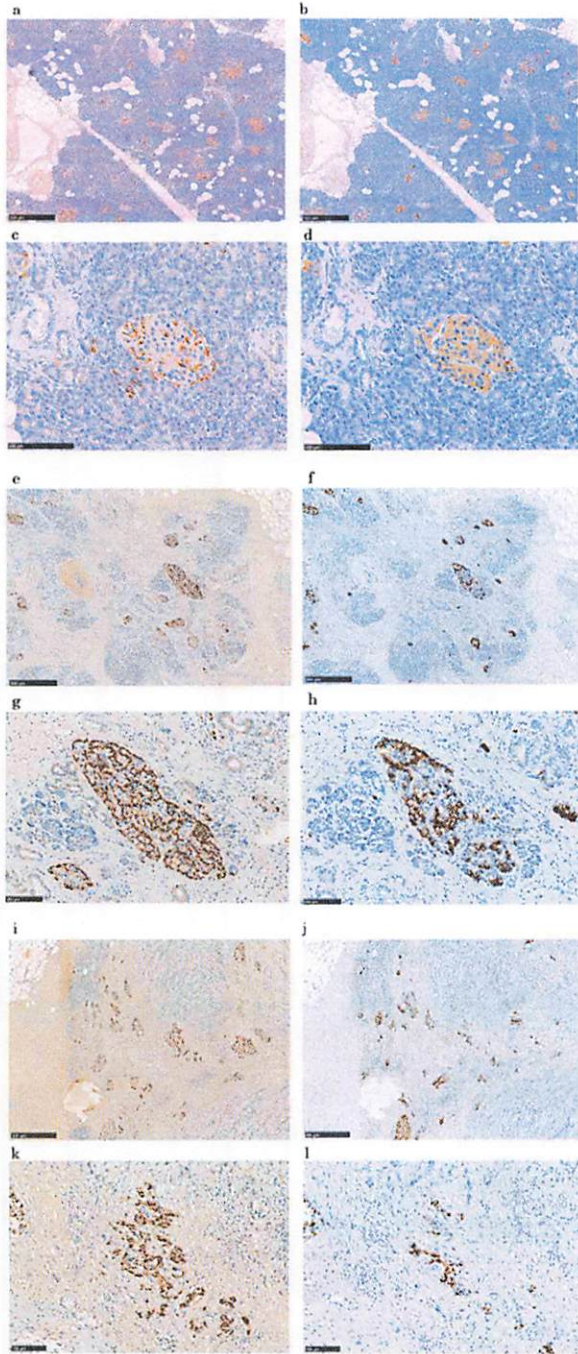


Fig. 2 Representative photomicrographs of pancreas immunostained for glucagon (brown) (a, c, e, g, i, k) or insulin (brown) (b, d, f, h, j, l) and with hematoxylin. a–d: A case without pancreatic cancer (c and d: higher power images). e–l: Cases with pancreatic cancer (g, h, k and l: higher power images). Scale bars, 500 μ m for lower power images and 100 μ m for higher power images.

PC compared with those without PC ($2.48 \pm 2.39\%$ vs. $0.53 \pm 0.26\%$, $p < 0.001$) (Fig. 3b). ACA to BCA ratio was also significantly higher in those with PC compared

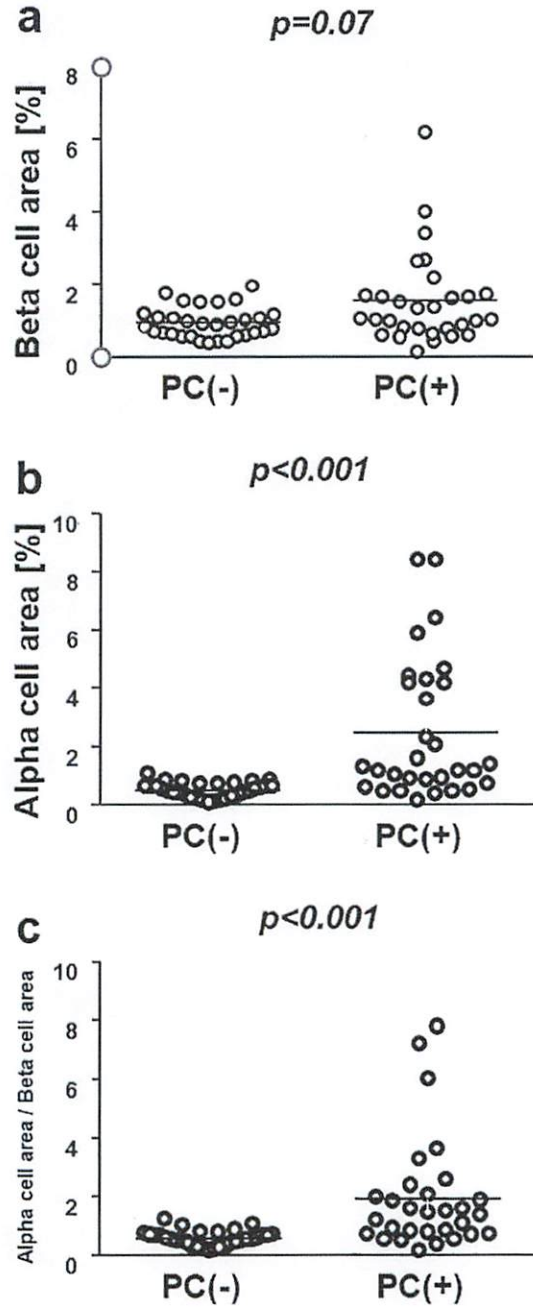


Fig. 3 Beta cell area (BCA, a), alpha cell area (ACA, b) and ACA to BCA ratio (c) in subjects with and without pancreatic cancer. Bars indicate mean.

with those without PC (1.94 ± 1.93 vs. 0.59 ± 0.26 , $p < 0.001$) (Fig. 3c). Increases in ACA and ACA to BCA ratio were observed in PC patients with and without DM, while BCA did not differ significantly between patients with and without DM or PC (Supplementary Fig. 1). Increases in ACA and ACA to BCA ratio were observed in samples from both the pancreatic head and body/tail (Supplementary Fig. 2). There was no significant

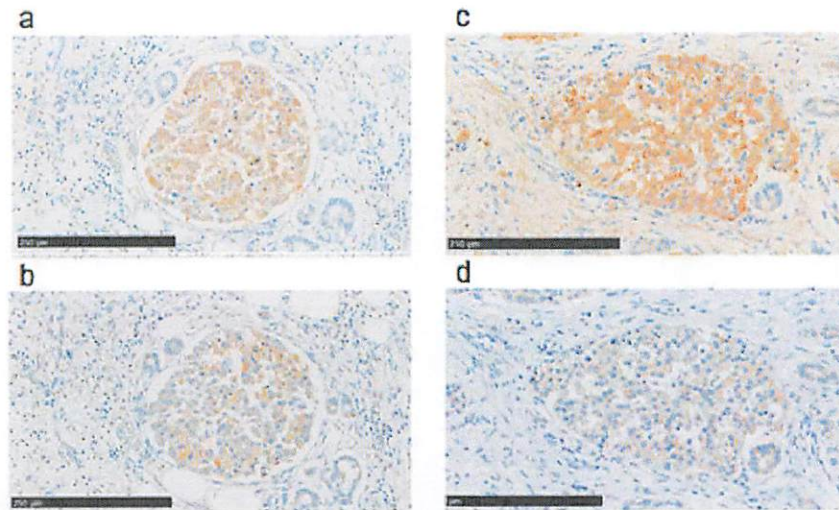


Fig. 4 Representative microphotographs of islets immunostained for ALDH1A3 (brown, a and c) or UCN3 (brown, b and d) and with hematoxylin. Subjects with (c and d) and without (a and b) pancreatic cancer. Scale bar = 250 μm .

difference in mean islet size between the groups with and without PC ($6,973 \pm 3,508$ vs. $5,819 \pm 2,180 \mu\text{m}^2$, $p = 0.25$).

Expression of dedifferentiation markers

To assess the role of dedifferentiation as a mechanism of increased ACA to BCA ratio in subjects with PC, sections of pancreas from controls and PC were stained for ALDH1A3 (Fig. 4a and 4c) and UCN3 (Fig. 4b and 4d) and the expression patterns of these markers within the islets were qualitatively evaluated (Supplementary Table 2). However, we could not find any certain relationship between the ACA to BCA ratio and the degree of staining. We also did not find any qualitatively significant difference in expression of dedifferentiation markers between subjects with and without PC.

Discussion

In this study, we report that 1) ACA and ACA to BCA ratio were increased in subjects with PC compared with those without PC, 2) an increase in ACA to BCA ratio was observed in subjects with PC irrespective of the presence or absence of DM, and 3) there was no significant change in expression of dedifferentiation markers in subjects with PC.

Type 1 and type 2 DM are both characterized by a deficit of BCM [23–26]; however, the effects of PC on BCM remain unclear. Similarly, ACA/BCA ratio has been reported to be significantly correlated with glucose metabolism indices such as fasting blood glucose level, blood glucose level 2 hours after a load, and HbA1c, but there are few reports on ACA/BCA ratio in PC [27]. In

our prior study, we reported that BCA but not ACA was reduced in subjects with PC compared with those without PC [25], while in this study, we observed no reduction in BCA but increases in ACA and ACA to BCA ratio in subjects with PC. Several reasons for this inconsistency including differences in patient characteristics between the studies can be postulated. Especially, subjects who had undergone surgical resection of PC were included in our prior study, while autopsy cases that died of PC, *i.e.*, with advanced clinical stage of PC, were included in this study. That is, the subjects in the previous study had operable early-stage cancer, whereas the patients in the present study had so-called end-stage cancer in which the cause of death was PC in all of them. Indeed, the pancreases of subjects with PC in this study were markedly atrophic and fibrotic, which are major histological changes often observed in subjects with advanced PC [19, 28]. Due to the atrophic and fibrotic changes in the exocrine pancreas, BCA and ACA expressed as fractional area to the exocrine area may be overestimated in subjects with advanced PC. In this study, thus, the increase in ACA to BCA ratio in subjects with PC suggests two possibilities; reduced BCM and/or increased ACM, although it was not possible for us to calculate the actual BCM or ACM due to the lack of information on pancreas weight in each individuals. Two of the subjects with PC in the present study had a history of surgery for PC, but when we excluded these subjects and performed the analysis, the results remained the same.

DM secondary to pancreatic cancer is associated with a reduced response of beta cells to an oral glucose load, hyperglycemic clamp, and glucagon stimulation [29–32].

Basso *et al.* conducted a glucagon-stimulation study in PC, type 1 DM, type 2 DM patients, and healthy controls to evaluate beta cell function in PC patients. They found no significant increase in C-peptide level in type 1 DM and PC patients after glucagon stimulation, but a significant increase in controls and type 2 DM patients [31].

Previous studies showed that plasma islet amyloid polypeptide level was elevated in PC patients with DM, and it was speculated that this might contribute to the pathogenesis of the disease. However, this hypothesis has not been explored further, and the mechanism of altered beta cell function remains unknown [33-35]. On the other hand, Permert *et al.* found, in a series of studies, insulin resistance in subjects with PC, which was more pronounced in subjects with DM, but was also present in normoglycemic subjects with PC [36, 37].

These results suggest that insulin resistance and altered beta cell function seen in PC patients may lead to hyperglycemia [31]. However, previous studies on the amount of beta cells in PC have not yielded consistent results. Meier *et al.* reported no significant difference in BCA between subjects with and without primary pancreatic disease, including PC, and Yoon *et al.* reported no significant difference in the relative volume of alpha- or beta-cells between patients with and without PC [18, 38]. On the other hand, Katsumichi *et al.* reported a decrease in islet size and beta cell count in subjects with PC, but the number of samples was small and as the PC group did not include subjects without DM, the influence of DM on islet morphology could not be excluded [39].

There have been previous reports showing increased plasma glucagon level in patients with PC [30, 40, 41]. Jin *et al.* reported higher plasma glucagon level, lower insulin level, and higher glucagon/insulin ratio during 75 g OGTT in patients with PC [41]. Also, Kolb *et al.* reported that there was no difference in insulin-expressing area or islet size between subjects with and without PC, but glucagon-expressing area and glucagon/insulin expression ratio were higher in PC patients [40], consistent with our findings. Schmied *et al.* reported that PC specimens also showed a significant decrease in beta cells and a significant increase in alpha cells within and around the tumor [16, 17].

Recently, Wang *et al.* reported that ALDH1A3, a marker of dedifferentiation, is highly expressed and UCN3 expression is low in PC patients [19]. ALDH1A3 is highly expressed in progenitor cells and functions as a marker of beta cell dedifferentiation. In contrast, UCN3 is a beta cell-enriched gene product and its loss is an early event in beta cell dedifferentiation in DM. Therefore, UCN3 is considered a functional maturation marker [42]. However, in this study, we did not find any significant change in expression of dedifferentiation markers in

subjects with PC, although there was no significant difference in mean islet size between the groups. Further studies are needed to clarify the role of beta cell dedifferentiation in subjects with PC.

There are limitations of this study. First, we cannot rule out the possibility that other factors such as duration and treatment of PC, cause of death and family history of DM might have influenced the results of this study. Secondly, different portions of the pancreas were sampled, although the proportion of endocrine cells has been shown to be relatively consistent regardless of the pancreatic site, except for the ventral portion of the pancreatic head [26]. Third, with respect to subjects with PC, pathological changes in pancreatic exocrine tissue may have affected endocrine tissue changes, but it is difficult to determine whether the changes in fibrosis and atrophy of the pancreatic parenchyma observed in pancreatic cancer specimens are a direct effect of PC or an effect associated with complicated pancreatitis. Finally, all the subjects in this study were Japanese, so our results may not be as relevant for other ethnic groups.

In conclusion, ACA to BCA ratio was increased in subjects with PC compared to those without PC. Since an increase in ACA to BCA ratio was observed in subjects with PC irrespective of the presence or absence of DM, a relative increase in ACM to BCM may be one of the mechanisms of worsening glucose metabolism associated with PC. Further research is needed to clarify the mechanisms of the relative increase in ACM in subjects with PC.

Acknowledgements

We thank Yuko Madokoro, Department of Pathology, Keio University School of Medicine, for technical assistance and Dr. Wendy Gray, self-employed, for editing the manuscript.

Disclosure and Management of Conflicts of Interest

None of the authors has any potential conflict of interest associated with this study.

Funding

The authors were supported by grants from the Ministry of Education, Culture, Sports, Science and Technology (Grant Nos. 20K17542 and 21K08535).

Availability of Data and Material Code Availability

The datasets generated during and/or analyzed during the current study are available from the corresponding author on reasonable request.

Code Availability

Not applicable.

Authors' Contributions

T.T. researched and analyzed the data and wrote the manuscript. Y.S. designed the study, analyzed the data and wrote the manuscript. J.I., H.S., M.S. and M.N. contributed to discussion and reviewed and edited the manuscript. Y.M. and T.Y. researched the data, contributed to discussion and reviewed and edited the manuscript. H.I. contributed to discussion and reviewed and edited the manuscript. Y.S. is the guarantor of this work and, as

such, had full access to all the data in the study and takes responsibility for the integrity of the data and the accuracy of the data analysis.

Ethics Approval

This study was carried out with the approval of the Keio University School of Medicine Ethics Committee (approval number 20120475, approval date 2022/03/28, initial approval date 2013/02/25).

Consent to Participate

Pancreatic specimens obtained at autopsy were obtained with the permission of the bereaved families.

Consent to Publication

This study was conducted with the permission of the bereaved families.

References

- Pannala R, Leirness JB, Bamlet WR, Basu A, Petersen GM. *et al.* (2008) Prevalence and clinical profile of pancreatic cancer-associated diabetes mellitus. *Gastroenterology* 134: 981–987.
- Everhart J, Wright D (1995) Diabetes mellitus as a risk factor for pancreatic cancer. A meta-analysis. *JAMA* 273: 1605–1609.
- Siegel RL, Miller KD, Fuchs HE, Jemal A (2021) Cancer statistics, 2021. *CA Cancer J Clin* 71: 7–33.
- Tanaka M, Mihaljevic AL, Probst P, Heckler M, Klaiber U, *et al.* (2019) Meta-analysis of recurrence pattern after resection for pancreatic cancer. *Br J Surg* 106: 1590–1601.
- Barros AG, Pulido CF, Machado M, Brito MJ, Couto N, *et al.* (2021) Treatment optimization of locally advanced and metastatic pancreatic cancer (Review). *Int J Oncol* 59: 110.
- Carrato A, Falcone A, Ducreux M, Valle JW, Parnaby A, *et al.* (2015) A systematic review of the burden of pancreatic cancer in Europe: real-world impact on survival, quality of life and costs. *J Gastrointest Cancer* 46: 201–211.
- Bhattamisra SK, Siang TC, Rong CY, Annan NC, Sean EHY, *et al.* (2019) Type-3c diabetes mellitus, diabetes of exocrine pancreas—an update. *Curr Diabetes Rev* 15: 382–394.
- Sah RP, Nagpal SJ, Mukhopadhyay D, Chari ST (2013) New insights into pancreatic cancer-induced paraneoplastic diabetes. *Nat Rev Gastroenterol Hepatol* 10: 423–433.
- Ogawa Y, Tanaka M, Inoue K, Yamaguchi K, Chijiwa K, *et al.* (2002) A prospective pancreatographic study of the prevalence of pancreatic carcinoma in patients with diabetes mellitus. *Cancer* 94: 2344–2349.
- Huxley R, Ansary-Moghaddam A, Berrington de González A, Barzi F, Woodward M (2005) Type-II diabetes and pancreatic cancer: a meta-analysis of 36 studies. *Br J Cancer* 92: 2076–2083.
- Pothuraju R, Rachagani S, Junker WM, Chaudhary S, Saraswathi V, *et al.* (2018) Pancreatic cancer associated with obesity and diabetes: an alternative approach for its targeting. *J Exp Clin Cancer Res* 37: 319.
- Chari ST, Zapiach M, Yadav D, Rizza RA (2005) Beta-cell function and insulin resistance evaluated by HOMA in pancreatic cancer subjects with varying degrees of glucose intolerance. *Pancreatol* 5: 229–233.
- Wolpin BM, Bao Y, Qian ZR, Wu C, Kraft P, *et al.* (2013) Hyperglycemia, insulin resistance, impaired pancreatic β -cell function, and risk of pancreatic cancer. *J Natl Cancer Inst* 105: 1027–1035.
- Javeed N, Sagar G, Dutta SK, Smyrk TC, Lau JS, *et al.* (2015) Pancreatic cancer-derived exosomes cause paraneoplastic β -cell dysfunction. *Clin Cancer Res* 21: 1722–1733.
- Hart PA, Bellin MD, Andersen DK, Bradley D, Cruz-Monserrate Z, *et al.* (2016) Type 3c (pancreatogenic) diabetes mellitus secondary to chronic pancreatitis and pancreatic cancer. *Lancet Gastroenterol Hepatol* 1: 226–237.
- Schmied BM, Ulrich AB, Matsuzaki H, Li C, Friess H, *et al.* (2000) Alteration of the Langerhans islets in pancreatic cancer patients. *Int J Pancreatol* 28: 187–197.
- Schmied BM, Ulrich A, Matsuzaki H, Li CH, Pour PM

- (1999) *In vitro* pancreatic carcinogenesis. *Ann Oncol* 10 Suppl 4: 41–45.
18. Yoon KH, Ko SH, Cho JH, Lee JM, Ahn YB, *et al.* (2003) Selective beta-cell loss and alpha-cell expansion in patients with type 2 diabetes mellitus in Korea. *J Clin Endocrinol Metab* 88: 2300–2308.
 19. Wang Y, Ni Q, Sun J, Xu M, Xie J, *et al.* (2020) Paraneoplastic β cell dedifferentiation in nondiabetic patients with pancreatic cancer. *J Clin Endocrinol Metab* 105: dgz224.
 20. Kou K, Saisho Y, Satoh S, Yamada T, Itoh H (2013) Change in β -cell mass in Japanese nondiabetic obese individuals. *J Clin Endocrinol Metab* 98: 3724–3730.
 21. Kashiwagi A, Kasuga M, Araki E, Oka Y, Hanafusa T, *et al.* (2012) International clinical harmonization of glycated hemoglobin in Japan: From Japan Diabetes Society to National Glycohemoglobin Standardization Program values. *J Diabetes Investig* 3: 39–40.
 22. Sato S, Saisho Y, Inaishi J, Kou K, Murakami R, *et al.* (2015) Effects of glucocorticoid treatment on β - and α -cell mass in Japanese adults with and without diabetes. *Diabetes* 64: 2915–2927.
 23. Saisho Y (2015) β -cell dysfunction: its critical role in prevention and management of type 2 diabetes. *World J Diabetes* 6: 109–124.
 24. Butler AE, Janson J, Bonner-Weir S, Ritzel R, Rizza RA, *et al.* (2003) Beta-cell deficit and increased beta-cell apoptosis in humans with type 2 diabetes. *Diabetes* 52: 102–110.
 25. Inaishi J, Saisho Y, Sato S, Kou K, Murakami R, *et al.* (2016) Effects of obesity and diabetes on α - and β -cell mass in surgically resected human pancreas. *J Clin Endocrinol Metab* 101: 2874–2882.
 26. Sakuraba H, Mizukami H, Yagihashi N, Wada R, Hanyu C, *et al.* (2002) Reduced beta-cell mass and expression of oxidative stress-related DNA damage in the islet of Japanese Type II diabetic patients. *Diabetologia* 45: 85–96.
 27. Inaishi J, Saisho Y, Hirakawa Y, Yoshida D, Hata J, *et al.* (2020) Association of glucose tolerance status with pancreatic β - and α -cell mass in community-based autopsy samples of Japanese individuals: the Hisayama study. *J Diabetes Investig* 11: 1197–1206.
 28. Özdemir BC, Pentcheva-Hoang T, Carstens JL, Zheng X, Wu CC, *et al.* (2014) Depletion of carcinoma-associated fibroblasts and fibrosis induces immunosuppression and accelerates pancreas cancer with reduced survival. *Cancer Cell* 25: 719–734.
 29. Cersosimo E, Pisters PW, Pesola G, McDermott K, Bajorunas D, *et al.* (1991) Insulin secretion and action in patients with pancreatic cancer. *Cancer* 67: 486–493.
 30. Schwartz SS, Zeidler A, Moossa AR, Kuku SF, Rubenstein AH (1978) A prospective study of glucose tolerance, insulin, C-peptide, and glucagon responses in patients with pancreatic carcinoma. *Am J Dig Dis* 23: 1107–1114.
 31. Basso D, Plebani M, Fogar P, Del Favero G, Briani G, *et al.* (1994) Beta-cell function in pancreatic adenocarcinoma. *Pancreas* 9: 332–335.
 32. Fan KY, Dholakia AS, Wild AT, Su Z, Hacker-Prietz A, *et al.* (2014) Baseline hemoglobin-A1c impacts clinical outcomes in patients with pancreatic cancer. *J Natl Compr Canc Netw* 12: 50–57.
 33. Permert J, Larsson J, Westermarck GT, Herrington MK, Christmansson L, *et al.* (1994) Islet amyloid polypeptide in patients with pancreatic cancer and diabetes. *N Engl J Med* 330: 313–318.
 34. Chari ST, Klee GG, Miller LJ, Raimondo M, DiMagno EP (2001) Islet amyloid polypeptide is not a satisfactory marker for detecting pancreatic cancer. *Gastroenterology* 121: 640–645.
 35. Aggarwal G, Ramachandran V, Javeed N, Arumugam T, Dutta S, *et al.* (2012) Adrenomedullin is up-regulated in patients with pancreatic cancer and causes insulin resistance in β cells and mice. *Gastroenterology* 143: 1510–1517.e1.
 36. Permert J, Ihse I, Jorfeldt L, von Schenck H, Arnqvist HJ, *et al.* (1993) Pancreatic cancer is associated with impaired glucose metabolism. *Eur J Surg* 159: 101–107.
 37. Permert J, Adrian TE, Jacobsson P, Jorfelt L, Fruin AB, *et al.* (1993) Is profound peripheral insulin resistance in patients with pancreatic cancer caused by a tumor-associated factor? *Am J Surg* 165: 61–66; discussion 66–67.
 38. Meier JJ, Breuer TG, Bonadonna RC, Tannapfel A, Uhl W, *et al.* (2012) Pancreatic diabetes manifests when beta cell area declines by approximately 65% in humans. *Diabetologia* 55: 1346–1354.
 39. Katsumichi I, Pour PM (2007) Diabetes mellitus in pancreatic cancer: is it a causal relationship? *Am J Surg* 194: S71–S75.
 40. Kolb A, Rieder S, Born D, Giese NA, Giese T, *et al.* (2009) Glucagon/insulin ratio as a potential biomarker for pancreatic cancer in patients with new-onset diabetes mellitus. *Cancer Biol Ther* 8: 1527–1533.
 41. Jin SM, Choi SH, Choi DW, Heo JS, Suh S, *et al.* (2014) Glucagon/insulin ratio in preoperative screening before pancreatic surgery: correlation with hemoglobin A1C in subjects with and without pancreatic cancer. *Endocrine* 47: 493–499.
 42. Blum B, Roose AN, Barrandon O, Maehr R, Arvanites AC, *et al.* (2014) Reversal of β cell de-differentiation by a small molecule inhibitor of the TGF β pathway. *Elife* 3: e02809.